Doctoral theses at NTNU, 2020:374

Henrik Granum

Multi-scale modelling and simulation of ductile failure in aluminium structures

Doctoral thesis

NTNU
Norwegian University of Science and Technology
Thesis for the Degree of
Philosophiae Doctor
Faculty of Engineering
Department of Structural Engineering

NTNU
Norwegian University of
Science and Technology

Henrik Granum

Multi-scale modelling and simulation of ductile failure in aluminium structures

Thesis for the Degree of Philosophiae Doctor

Trondheim, November 2020

Norwegian University of Science and Technology
Faculty of Engineering
Department of Structural Engineering

NTNU
Norwegian University of
Science and Technology

NTNU
Norwegian University of Science and Technology

Thesis for the Degree of Philosophiae Doctor

Faculty of Engineering
Department of Structural Engineering

ISBN 978-82-326-5094-1 (printed ver.)
ISBN 978-82-326-5095-8 (electronic ver.)
ISSN 2703-8084 (online)
ISSN 1503-8181 (printed ver.)

Doctoral theses at NTNU, 2020:374

Printed by NTNU Grafisk senter

Preface

This thesis is submitted in partial fulfilment of the requirements for the degree of Philosophiae Doctor in Structural Engineering at the Norwegian University of Science and Technology (NTNU). The work has been conducted at the Structural Impact Laboratory (SIMLab) at the Department of Structural Engineering, NTNU. Funding was provided by the Research Council of Norway through the FRINATEK Programme FractAl, Project No. 250553. The main supervisor has been Professor Odd Sture Hopperstad and the co-supervisor has been Professor Tore Børvik.

The thesis consists of five articles, referred to as Parts 1 to 5. Parts 1, 3 and 5 have been published in international peer-reviewed journals and Part 4 has been published in a proceedings of a national conference. Part 2 is to be submitted for possible publication in an international peer-reviewed journal. A synopsis binds the five individual parts together.

The first author has been responsible for conducting the work and preparing the manuscripts that comprise Parts 1 to 5, with a few exceptions. Adjunct Professor Ole Runar Myhr has conducted the *NaMo* analyses and contributed to the manuscripts of Parts 1 and 2 about the details of the *NaMo* results. Associate Professor David Morin performed the localization analyses and calibrated the fracture criterion presented in Part 5. He also calibrated the fracture criterion employed in Part 4. Associate Professor Vegard Aune contributed with comments and suggestions on the work in Part 3, as well as guidance with the experimental work in the SIMLab Shock Tube Facility.

Henrik Granum
Trondheim, Norway
September 1, 2020

Abstract

Due to the ever-increasing computational power available in work stations and computer clusters, the engineer of today can to a greater extent use numerical simulations in the design of structures and components. This approach may reduce the number of experiments necessary and has the potential to result in significant savings. However, the accuracy of the numerical simulation relies on an accurate description of the material behaviour, which is usually obtained from material tests or in some cases provided by the material manufacturer. In modern design of structures and components, the design may require the material to be utilized to the brink of failure. The tools used by the engineer are often not sufficient to account for this, where an accurate description of the material properties is required. Satisfactory accuracy may be achieved with finite element simulations, but some of the more complex problems require sophisticated material and/or fracture models to provide reliable results, where multiple experiments are needed for the calibration process. The numerical tools presented in this thesis can in some cases achieve this goal without the need for an extensive test programme. The mentioned numerical tools are part of a multi-scale modelling approach, whose main objective is to enable predictions of ductile failure in components and structures made of aluminium alloys with a minimum number of experiments needed for calibration purposes.

This thesis consists of five individual parts which all contain a single journal article either published (Parts 1, 3, 4 and 5) or to be submitted (Part 2) to peer-reviewed journals. The context of the articles is presented in the synopsis which links the parts together. The synopsis presents the background and motivation, a brief overview of relevant topics, objectives and scope of the thesis, and the overall conclusions and suggestions for further work.

Part 1 presents an experimental and numerical study on rectangular hollow section (RHS) profiles subjected to quasi-static axial crushing. The profiles were made of three aluminium alloys (AA6063, AA6061 and AA6110) in three heat-treatments (T6, T7 and O). The nanostructure model (NaMo) was used to predict the stress-strain curves of the alloys based on the chemical composition and thermo-mechanical history. The predicted stress-strain curves were then employed in finite element analyses of rectangular hollow section profiles subjected to quasi-static axial crushing. The explicit FE code Impetus Afea Solver was used to conduct the numerical simulations. The simulations were thus carried out without the need for material tests to calibrate the plasticity model. To evaluate the predictions, the results were compared to the experiments in terms of peak and mean force and force-displacement curves. Additional simulations were performed where the plasticity model was calibrated based on material tests and used to assess the predictions by the nanostructure model. The force-displacement curves indicated that the two approaches achieved equally accurate results when compared to the experiments. The robustness of the nanostructure model was substantiated by the variation in the chemical composition and thermo-mechanical

history between the nine material combinations, resulting in predictions that yielded equal or better results compared to the conventional approach.

In Part 2, the effect of pre-stretching on the mechanical behaviour of the aluminium alloys AA6063, AA6061 and AA6110 in temper T6 is investigated. Uniaxial tensile tests and quasi-static axial crushing tests were conducted on RHS profiles, where the profiles had been pre-stretched 0.5% and 4.0% after extrusion and prior to artificial ageing. The uniaxial tensile tests were used to investigate the effect of pre-stretching on plasticity and fracture by comparison of the stress-strain curves for the two pre-stretching levels, where digital image correlation was used to determine the fracture strain on the specimen surface. It was found that the yield stress is unaffected, while the ultimate tensile stress is somewhat lower and the failure strain is considerably higher for the profiles pre-stretched 4.0% compared to those pre-stretched 0.5%. By visual inspection of the deformed RHS profiles, less cracks were generally seen on the profiles pre-stretched 4.0%. Also, the specific energy absorption from the crushing tests is somewhat lower for the profiles pre-stretched 4.0%. The nanostructure model NaMo was used to predict the stress-strain curves of the pre-stretched and artificially aged extruded profiles and the results were compared to the experimental data. The overall experimental trends were accurately predicted by NaMo, even though the yield plateau present in some configurations was not captured. The predicted evolution of the microstructure during artificial ageing was used to gain insight into the physical mechanisms responsible for the observed stress-strain behaviour.

In Part 3, we investigated the effect of heat-treatment on the structural response of blast-loaded aluminium plates with pre-cut slits. Rolled plates of the aluminium alloy AA6016 were tested in three different heat-treatments (T4, T6 and T7) with four different pre-cut slit geometries at two different blast intensities. The thickness of the plates was 1.5 mm. The blast tests were conducted in the SIMLab Shock Tube Facility and a total of 16 tests were conducted. By varying the number and orientations of the pre-cut slits, different crack patterns and failure modes were obtained in the plates, and it was found that the blast resistance was markedly affected by the orientation and number of the defects. The plates were modelled using symmetry when available and simulations were conducted employing an uncoupled isotropic plasticity and fracture models in Abaqus/Explicit. The experiments included crack initiation and complex crack propagation and are considered valuable in evaluating the predictive capabilities of plasticity and failure models. By comparing the failure modes in the experiments and the simulations, it became evident that the model was able to predict the onset of fracture accurately, even though the subsequent crack propagation was not accurately predicted in all cases.

Part 4 presents a numerical study on blast-loaded aluminium plates with pre-cut slits. The plates were modelled in LS-DYNA using an uncoupled plasticity and fracture model with a through-thickness regularization scheme valid for shell elements. Uniaxial tensile tests were used to determine the parameters of the constitutive model by inverse modelling using the optimization tool LS-OPT and FE simulations. Plates with four different crack-like defects were considered at a load level resulting in failure and crack propagation in all tests. The plates were made of the aluminium alloy AA6016 in temper T4. The through-thickness regularization scheme allowed different mesh sizes to be employed, where four different length-to-thickness ratios of the shell

elements were investigated. Two different approaches to apply the pressures were used, one where the pressure acted normal to the surface throughout the simulation and one where the pressure "slid off" as the plate deformed. The numerical results revealed that the latter approach to model the pressure gave better agreement with the experiments. The global displacement field was accurately predicted by all mesh sizes. However, to predict initiation of failure correctly, a length-to-thickness ratio of the shell elements equal to unity was needed. Crack initiation and propagation were only predicted in the simulations with an element length-to-thickness ratio equal to $1/3$. A simulation with solid elements using three elements over the plate thickness gave similar results as the shell element simulation with the finest mesh, but at a much higher computational cost.

In Part 5, a novel calibration procedure of the modified Mohr-Coulomb (MMC) fracture model by use of localization analyses for three heat-treatments (T4, T6 and T7) of the AA6016 aluminium alloy is presented. The localization analyses employed the imperfection band approach, where metal plasticity was assigned outside the band and porous plasticity was assigned inside the band. Ductile failure was thus assumed to occur when the deformation localizes into a narrow band. This approach is presumed to be valid as strain localization is usually a strong indicator for imminent failure. The metal plasticity model was calibrated from notch tension tests by use of inverse modelling and FE simulations. The porous plasticity model was calibrated by use of localization analyses where the deformation histories from finite element simulations of notch and plane-strain tension tests were prescribed as boundary conditions. Subsequently, localization analyses were used to establish the fracture locus in stress space for proportional loading conditions and from there to determine the parameters of the MMC fracture model. Finite element simulations of notch tension and in-plane simple shear tests as well as two load cases of the modified Arcan test were used to validate the calibrated fracture model. The predictions by the simulations were in good agreement with the experimental results, even though some deviations were seen for each temper. The results demonstrated that localization analyses are a cost-effective and reliable tool for predicting ductile failure, reducing the number of mechanical tests required to calibrate the MMC fracture model to a minimum compared to the hybrid experimental-numerical approach usually applied.

Acknowledgements

First of all, I would like to express my deepest gratitude to my supervisors Professor Odd Sture Hopperstad and Professor Tore Børvik. You have truly been an inspiration to me with your attention to detail and tireless effort put into this work. Your guidance has been impeccable throughout this project and I feel honoured to be given the possibility to work with you.

The thesis would not have been the same without my wonderful colleagues at SIMLab. The fruitful working environment at SIMLab has repeatedly proven to me the importance of collaboration. It has been an enjoyable place to work, both during and outside working hours. A special thanks goes to SIMLabs' invincible duo, Dr. Joakim Johnsen and Dr. Lars Edvard Blystad Dæhli for their invaluable help and input as well as non-technical chit-chat. In particular, Dr. Johnsen's IT support has been of huge help as well as your usual mockery after a less intelligent question. There was never any danger of being overconfident when you were nearby. Nonetheless, it has been a privilege to work alongside you and I am grateful for the friendship we have developed. A special thanks must also be sent to Dr. Joakim Johnsen and Dr. Jens Kristian Holmen for sharing the computational power of your work stations with me, even though I have the feeling you sometimes regretted it. Dr. Jens Kristian Holmen is also acknowledged for splendid guidance with the IMPETUS Afea Solver. I would like to thank Associate Professor Vegard Aune for support and guidance in the study he co-authored and for assistance with the experiments conducted in the SIMLab Shock Tube Facility. I would like to thank Associate Professor David Morin for his contributions to the manuscripts he co-authored as well as general support and guidance. Adjunct Professor Ole Runar Myhr is acknowledged for his contributions with the software NaMo in the manuscripts he co-authored. Your contributions and guidance are highly appreciated. I would also like to thank the colleagues I shared office with the first few years. We had a lot of fun and the numerous discussions and chats we had are much appreciated.

The experimental work would not have been completed without the sturdy assistance from Mr. Trond Auestad and Mr. Tore Wisth, in which I am grateful for. I would also like to thank Dr. Egil Fagerholt for support with the digital image correlation analyses when needed. Hydro Aluminium is acknowledged for providing the materials used as well as assistance with the extrusion process.

Lastly, I would like to thank my friends and family for encouragement and support throughout my PhD work. Even though you did not fully understand what I worked with, you always showed interest and cheered on me. I am deeply grateful for this.

Contents

Part 2

Effect of pre-stretching on the mechanical behaviour of three artificially aged 6xxx series aluminium alloys

Part 3

Effect of heat-treatment on the structural response of blast-loaded aluminium plates with pre-cut slits

Part 4

Simulation of blast-loaded aluminium plates with crack-like defects

Part 5

Calibration of the modified Mohr-Coulomb fracture model by use of localization analyses for three tempers of an AA6016 aluminium alloys

Synopsis

1 Introduction

1.1 Motivation

Along with the development of light alloys like aluminium, magnesium and titanium alloys, a whole new set of possibilities opened up for the design of lightweight structures and components. Among these, aluminium alloys are the most widely used and an abundance of research is carried out on topics related to this material. Aluminium has numerous favourable properties like high strength-to-weight ratio, high electrical and thermal conductivity, and excellent corrosion resistance. In particular, the superior strength-to-weight ratio compared to steel made it a popular material in the early days in the aviation industry. The first human flight made by the Wright brothers in 1903 was possible due to the usage of aluminium. To reach the necessary weight of the aircraft to enable lift-off, the engine had to be built with aluminium parts. After World War II, aluminium was widely used in aviation, shipbuilding and automotive industries and was being introduced in civil engineering. As the demand for better utilization of the structural components appeared, engineers and designers turned to numerical simulations to aid the design process. The increased computational power available and new knowledge on the material's mechanical behaviour made numerical simulations a powerful tool. At the same time, new aluminium alloys with improved properties were continuously being developed and tailored to obtain the requirements in the respective industries.

In the last few decades, new and enhanced plasticity and fracture models, able to accurately predict ductile failure in complex structures and components, have been developed. In combination with the progress made on understanding the underlying physical phenomena that govern ductile failure, the reliability and versatility of the numerical models are greatly improved. Numerical simulations are included in the design process in several industries today, reducing the cost and time spent at this stage in the development. Yet, there are still mechanisms and phenomena governing ductile fracture that are not fully understood. It is reasonable to believe that the solution to many of these challenges is found on the micro- and nanoscale.

With the recently developed plasticity and fracture models, increased accuracy is usually accompanied by increased complexity. These models often have several model parameters that need to be determined based on a set of suitable material tests. A hybrid experimental-numerical approach is traditionally used, where finite element (FE) simulations are employed in the calibration process of the model parameters. This approach is robust and used with success in numerous studies. However, it requires access to modern laboratory equipment to run mechanical tests. There

are also challenges related to finding suitable experiments that meet the requirements needed to obtain an accurate calibration of the advanced plasticity and fracture models. Besides, many of the experiments require custom-made test set-ups and are complex to perform. Because of this, in practice, these models are confined to applications where cost, time and complexity are not limiting factors.

This PhD project is part of FractAl - *Microstructure-based Modelling of Ductile Fracture in Aluminium Alloys*, a FRIPRO Toppforsk project. In FractAl, the main objective is to develop and validate a novel microstructure-based modelling framework for ductile fracture in aluminium alloys. The intention is to reliably introduce multi-scale simulations in the design of aluminium structures against failure. Besides extending the fundamental understanding of the mechanisms governing ductile fracture in aluminium alloys, the microstructure-based modelling framework will make it possible for designers to tailor the properties of the alloy and analyse it under various loading conditions. This approach may be completed with a limited amount of mechanical tests, opening up for an entirely new way of designing aluminium structures against ductile failure in the future. In practice, complex plasticity and fracture models may be calibrated by use of a limited number of material tests and in some cases without any material tests at all. The microstructure-based modelling framework consists of five modules which are illustrated in Figure 1 and will be presented in more detail in Section 1.3.

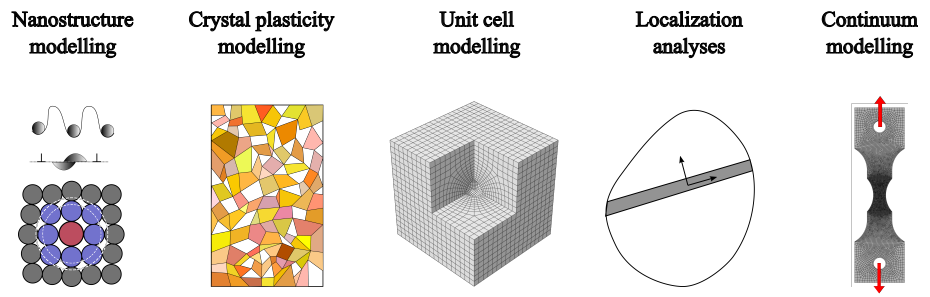

Figure 1: Illustration of the five modules that make up the modelling framework in FractAl.

1.2 Aluminium alloys

A wealth of different aluminium alloys are available for engineers today. The alloys are divided into two main classes; cast or wrought. Cast alloys are made by a casting process like sand casting, permanent mould casting, and cold or hot chamber pressure die casting. The casting process makes it possible to produce parts with complex geometries like an engine block or an automotive transmission. Wrought alloys are produced as cast ingots before they are worked. The work in this thesis is limited to wrought alloys and only this type of alloys will be considered in the following. Examples of wrought alloys are rolled plates, extruded profiles and drawn wires. The class of wrought alloys can further be divided into series designated by a number ranging from 1 to 8 followed by three numbers. This classification system, denoted the International Alloy Designation System (IADS), is given in Table 1 [1]. Each series contains different main alloying elements

that contribute to its particular mechanical properties. Common for all main alloying elements is their sufficient solubility. Other alloying elements are added in small weight percentages to maintain acceptable solubility. The importance of the alloying elements is evident, considering that high-purity aluminium only has a yield strength of around 10 MPa [1]. A 6xxx series alloy typically contains around eight alloying elements, where Mg and Si are the main alloying elements. Most of the alloying elements also introduce disadvantages that naturally limits their use. An example is Cu, which contributes to the strength in 2xxx series alloy, but at the same time makes the alloy susceptible to stress corrosion cracking [1]. As a result, the 7xxx series alloy has replaced the 2xxx series alloy in numerous applications since the former alloy is known to have sufficient resistance against stress corrosion cracking.

Table 1: International Alloys Designation System (IADS) for wrought alloys [1]

.

4-digit series	Main alloying elements	Heat-treatable
1xxx	Minimum of 99% aluminium	-
2xxx	Copper	✓
3xxx	Manganese	-
4xxx	Silicon	-
5xxx	Magnesium	-
6xxx	Magnesium and Silicon	✓
7xxx	Zinc	✓
8xxx	Others	-

As indicated by Table 1, only three of the aluminium alloy series are heat-treatable. There are five different classes of heat-treatments designated by a capital letter (F, O, H, W and T). Only the thermally treated (T) and annealed (O) temper conditions will be considered in this thesis. The temper condition T applies to an alloy that is solution heat-treated, quenched and followed by an optional heat-treatment. To distinguish between the types of heat-treatment, a number is always given after the treatment class, for example, T6 which is the peak strength condition. The annealed temper is reached if the heat-treatment is conducted at a sufficiently high temperature at a given time. An annealed alloy has low strength, but high workability and ductility, and is often required to prevent cracking in bending applications.

The 6xxx series is the most used aluminium alloy and the work in this thesis is limited to this series of wrought alloys [1]. It is considered as a medium-strength structural alloy and among the prominent properties are good weldability, corrosion resistance and immunity to stress-corrosion cracking [1]. This makes the 6xxx series alloy an optimal choice in applications like bike frames, architectural fabrication, fuselages and automotive parts to name a few. The alloys of the 6xxx series are used for the majority of extrusions, with smaller quantities being available as sheets and plates.

The main alloying elements in 6xxx series alloys are Mg and Si, and thus the series of alloys is often denoted Al-Mg-Si alloys. The amount of Mg and Si varies, but is often expressed by the

internal ratio Mg/Si. This composition is said to be balanced when Mg/Si = 1.73 as this is the ratio needed to form Mg_2Si particles during solution heat-treatment [2]. This value of the Mg/Si-ratio was for some time thought to be the optimal value until further knowledge of the precipitation sequence was gained [1]. Al-Mg-Si alloys are sometimes classified as excess-Si (Mg/Si < 1.73) or excess-Mg (Mg/Si > 1.73) alloys, based on the value of the Mg/Si-ratio. Fe is traditionally an unwanted element that is difficult to remove completely from the molten metal. The solubility of Fe is negligible and it mainly precipitates in the formation of non-soluble particles during solidification. Fe-rich intermetallics are reported to decrease the ductility significantly [3], but in some cases, a positive effect is reported [2]. Elements like Mn, Cr or Zr may be added to form dispersoids during homogenisation [1]. Mn is also found to reduce the average size of the primary particles, resulting in improved ductility [4]. Increased strength may be achieved by adding Cu, where the increased strength comes from the slightly different precipitation sequence in alloys with additions of Cu [5]. Furthermore, the presence of Cu in solid solution is presumed to improve ductility. Other elements are sometimes added in small quantities like Ti [6] and Zn [7], reported to improve the mechanical properties.

The mechanical properties of 6xxx series aluminium alloys are governed by their microstructural features. These include primary particles, dispersoids, precipitates, grain size and structure, crystallographic texture and dislocation substructure [1]. Figure 2 shows a comparison of the different particles found in the 6xxx series alloys in peak strength condition. Primary particles are large particles, typically up to some micrometers that normally contain Fe. During solidification, Fe precipitates in the formation of non-soluble particles that may transform into other phases. Common primary particles in 6xxx series alloys include α-AlFeSi and β-AlFeSi particles that form during homogenisation [2]. These particles form on grain boundaries and are typical sites for nucleation of micro-voids. During extrusion, primary particles are broken up into smaller pieces and aligned along the extrusion direction due to the large plastic deformations [8].

Dispersoids are smaller particles, typically below 0.5 micrometers, that form during homogenisation. The compounds usually consist of either Mn, Cr or Zr, which all have low solubility in aluminium. Besides retarding recrystallisation, dispersoids have been found to increase work-hardening as geometrically necessary dislocations are introduced during deformation [2]. Fine precipitates are the major contributor to strength in 6xxx series alloy [5, 9]. They form during heat-treatment and are typically below 0.1 micrometers. The strengthening effect is found to be the strongest for the β'' (Mg_5Si_6) precipitate, which is the most commonly observed precipitate in the peak strength condition, temper T6 [5].

Grain size and structure are important for the mechanical properties of an alloy. A small grain size is presumed to increase both the strength and ductility of an alloy as grain boundaries are effective obstacles for dislocations. The grain structure is typically altered by the extrusion process, where the grains become flat and elongated. The grains are said to appear as long fibres along the extrusion direction, where each fibre consists of many subgrains that have small relative misorientations. The grain size and structure is closely linked to the presence of dispersoids, as they retard recrystallisation which typically may occur during extrusion or in the following heat-treatment. In an alloy that contains dispersoids, the grain structure remains fibrous after

extrusion or heat-treatment. The grains in a recrystallised alloy are usually larger and equi-axed.

The statistical distribution of the orientation of the grains is referred to as crystallographic texture or simply texture. Texture may also be a result of working and annealing, which is typical for rolled products. In a random texture, the grains are randomly oriented and thus exhibit isotropic properties. Depending on the fraction of grains oriented in the same direction, the texture is often defined as weak or strong. During plastic deformation, individual grains may rotate and alter the texture, referred to as texture evolution. The strain ratio, often referred to as the Lankford coefficient, is a common measure of plastic anisotropy in a rolled sheet. The coefficient is a measure of the alloys propensity to thin during uniaxial tension. It is defined as the ratio of the width strain increment to thickness strain increment and is denoted R-value. An R-value > 1 means that the alloy resists thinning, which is preferable in metal forming as it enables a deeper cup to be drawn.

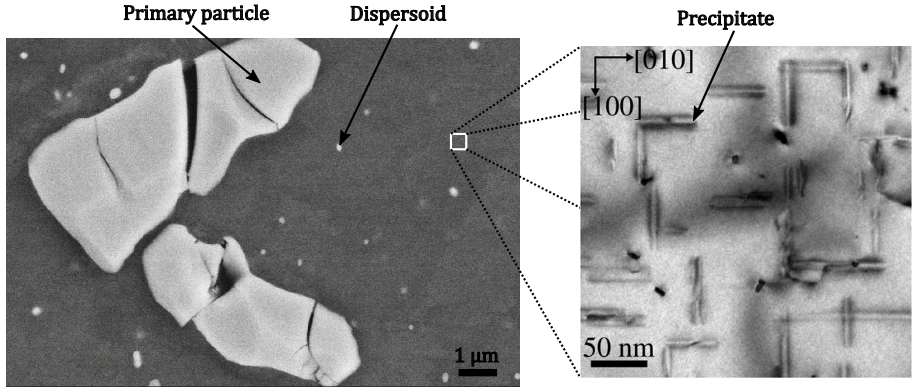

Figure 2: Comparison of the different sizes of the different particles found in 6xxx series aluminium alloys in temper T6. The images are taken from [10, 11].

The ageing precipitation sequence in most 6xxx series alloys follows the sequence presented in Equation (1) [2]. A solution heat-treatment at a relatively high temperature is required to dissolve the alloying elements, followed by rapid cooling or quenching to room temperature to obtain a supersaturated solid solution (SSSS) of these elements. The SSSS comprises both solute and vacancies, where the latter are required to form precipitates. Precipitation of atomic clusters occurs at room temperature and increases the strength of the alloy slowly with time. Three types of clusters are usually seen; Si atoms, Mg atoms and co-clusters of both Mg and Si atoms. This process is referred to as natural ageing and in most cases has a detrimental effect on the following heat-treatment [12, 13]. It is therefore customary to minimize the time at room temperature storage prior to heat-treatment or perform pre-ageing to reduce the potential for natural ageing. Clusters eventually grow into Guinier-Preston (GP) zones, which are ordered, solute rich groups of atoms that are partially coherent, meaning that they partially retain the structure of the matrix material. GP zones are normally finely dispersed with a needle shape. The GP zones are in turn replaced by a sequence of meta-stable, semi-coherent phases and eventually turn into the incoherent stable particle β, which marks the end of the sequence. The first phase is the needle-shaped β''-phase

which is the main strengthening precipitate. Further ageing results in formation of β', U1, and U2 particles [14]. These are rod-shaped precipitates, where the composition of the β' particle is close to the balanced Mg/Si-ratio (Mg/Si = 1.73). The final phase is the stable β particle (Mg_2Si) that is often seen in the overaged temper condition and contributes less to strength than the previous phases.

$$SSSS \rightarrow atomic\,clusters \rightarrow GP\,zones \rightarrow \beta'' \rightarrow \beta', U1, U2, B' \rightarrow \beta \tag{1}$$

The presence of Cu in 6xxx series alloys changes the precipitation sequence, often resulting in alloys with higher strength. The precipitation sequence is found to follow the sequence in Equation (2) [5]. It is considerably more complex than the one presented in Equation (1), where most of the precipitates have needle or plate morphologies. In alloys where the Mg content is high, the β'' phase is replaced by the disordered L-phase, known to increase the strength significantly. In an Al-Mg-Si-(Cu) alloy with excess-Si in peak strength condition, only 20-30% of the total amount of particles was found to be β'' particles [15]. The L-phase may either be lath-or needle-shaped and found to be more temperature resilient than β''. For excess-Si alloys, improved ductility has been reported for increasing Cu-content [16].

$$SSSS \rightarrow atomic\,clusters \rightarrow GP\,zones \rightarrow \beta'', Q', L, S, C, QC \rightarrow Q' \rightarrow Q \tag{2}$$

The strengthening mechanisms that occur during plastic deformation are attributed to the interaction of dislocations with various obstacles [17]. A dislocation is a line defect or irregularity within the crystal structure of the alloy that contains an abrupt change in the arrangement of atoms. The dislocations glide on a slip plane in the slip direction. The set of a slip plane and direction is denoted a slip system. Aluminium is a face-centred cubic (FCC) crystal with 12 active slip planes. The number of active slip planes to choose from usually results in a ductile behaviour, as it is likely that one of these is favourably oriented for plastic slip to take place. Precipitates are the main obstacles to the motion of dislocations in a 6xxx series alloy. Depending on the size, phase or shape of the precipitate, the dislocation may either cut trough or loop around, referred to as shearing or bypassing, respectively. A shearable precipitate that is cut by a dislocation may result in various defects inside the precipitation structure. Bypassing large, non-shearable particles is often linked to the Orowan mechanism, where the precipitate is encircled by dislocation loops. In a recent study by Christiansen et al. [9], the β'' precipitate was found to be sheared several times on different planes by dislocations during deformation. Shearing of the β'' precipitate results in increased strength while bypassing increases the dislocation density and contribute to work-hardening.

In addition to the formation of precipitates, precipitate-free zones (PFZs) adjacent to grain boundaries and dispersoids may form. These zones are relatively weak due to the absence of strengthening precipitates, but are typically stronger than pure aluminium as elements in solid solution is present. PFZs tend to form due to a vacancy and/or solute depletion close to the

dispersoids and grain boundaries. Strain localization and accelerated void nucleation and growth at particles on the grain boundary, is attributed to PFZs and may lead to intergranular fracture [18]. The width of the PFZ is closely linked to the heat-treatment and quenching, where a higher solution treatment temperature and fast quench rate results in a narrower zone [11].

There are an abundance of microstructural features that determine the mechanical properties of an aluminium alloy. Understandably, all microstructural features cannot be accounted for exactly in a numerical calculation of the mechanical properties of an aluminium alloy. The nanostructure model, which is part of the multi-scale modelling framework, has adopted various idealizations to obtain a reasonable mathematical model able to predict the stress-strain curve of a 6xxx series aluminium alloy. The model can predict the yield strength and work-hardening solely based on the chemical composition and the thermo-mechanical process. One such idealization is that the hardening precipitates (β'' and β') are assumed to be spherical, while experiments have agreed on that these are either needle- or rod-shaped, see e.g., [19]. However, this idealization has been deemed reasonable based on the mathematical treatment presented in [20], as long as the model is calibrated. In the nanostructure model, there are four contributions to the yield strength: the intrinsic yield strength of pure aluminium, the contributions from elements in solid solution, hardening precipitates and clusters, and dislocations. The elements in solid solution that contribute to the yield strength are Mg, Si, Cu and Mn. Continuously during the thermo-mechanical process, the concentration of Mg and Si is calculated at each time step to keep track of the amount of solute being tied up in precipitates and clusters. The contribution from precipitates and clusters to the yield strength is governed by the mean obstacle strength and the mean effective particle spacing in the slip plane along the bending dislocation, which are computed as described in [21]. Dislocations contribute to the yield strength if cold work is applied prior to artificial ageing. The evolution of the statistical storage and dynamic recovery of dislocations is governed by the equation proposed by Kocks and Mecking [22, 23]. The work-hardening is governed by the evolution of the total dislocation density, which is taken equal to the sum of the geometrically necessary and statistically stored dislocations. The evolution of the two dislocation densities is calculated by separate evolution equations.

1.3 The multi-scale modelling approach

The multi-scale modelling approach illustrated in Figure 1 covers the nano-, micro- and mesoscales and comprises five modules. The primary goal of this "virtual" laboratory is to provide a framework to assist the engineer in the design phase of structures by reducing the number of mechanical tests needed to predict ductile fracture in simulations. Also, the possibility to tailor the alloy to obtain the mechanical properties needed for a component or structure makes this approach a useful tool. The modules may be used individually or combined, depending on the complexity of the problem at hand and the desired accuracy of the solution. The robustness of the approach may be enhanced by increasing the number of mechanical tests to be used in the calibration process. Each module requires input to run, which is mostly obtained from the previous module. The first module relies on input that is readily available from the manufacturer of the alloy, thus no

expensive or time-consuming initial tests have to be conducted to get started.

The nanostructure model NaMo is the first module of the virtual laboratory and was developed by Myhr and co-workers [20, 21]. NaMo is a combined precipitation, yield strength and work-hardening model that can predict the yield strength and work-hardening of 6xxx series aluminium alloys, solely based on the chemical composition and the thermo-mechanical history of the alloy. Since its initial release, NaMo has received extensions to account for prolonged storage in room temperature and cold work prior to heat-treatment. The model has been successfully employed in numerous studies [24–27], where it was validated against material tests made of different alloys and heat-treatments. It has also been validated against experiments on structural components where loading conditions ranged from quasi-static crushing of profiles [28, 29] to ballistic impact of thin plates [30]. A limitation of the model is its inability to predict work-hardening for large strains. The current version of NaMo predicts saturation of the work-hardening for large strains, where numerous experiments show that the work-hardening is quasi-linear for large strains, until material damage counteracts the effect in the last stages before failure. A version of NaMo where the contribution to the work-hardening for large strains is accounted for is currently under development. The importance of the description of the work-hardening at large strains becomes evident if the NaMo model is to be paired with localization analyses. Strain localization is a phenomenon dependent on the work-hardening modulus, thus an accurate description of the work-hardening all the way to failure is essential to obtain an accurate prediction of the failure strain.

By combining NaMo with crystal plasticity theory [31], the strength, work-hardening and plastic anisotropy of an alloy can be determined. The plastic anisotropy of aluminium alloys and its evolution during plastic deformation can be modelled with good accuracy using the crystal plasticity finite element method (CP-FEM) based on the measured microstructure. In the CP-FEM, each grain of an alloy is modelled with one, several or many finite elements, and the plastic behaviour of the material is described on the slip systems within each grain. The method is computationally expensive and not yet feasible for simulations of entire structures or large structural components. However, the method has been used successfully to calculate the anisotropic yield function of textured aluminium alloys [32, 33] and to predict plastic behaviour and anisotropic hardening at large strains [34]. As a result, the CP-FEM is considered important to obtain accurate predictions on plastic flow and ductile fracture if the alloy exhibits anisotropic properties.

Unit cell modelling is a powerful tool to study the underlying mechanisms of ductile failure. Traditionally, unit cell models consist of one or several voids — with or without particles — and a matrix material. Such models have been used to analyze void nucleation, growth and coalescence as well as macroscopic localization [35–37]. Unit cell simulations have shown that the failure loci for non-proportional loading differ considerably from that of proportional load paths and that under non-proportional load paths the failure loci are not unique [36]. The latter finding implies that computational failure models based on a universal failure locus and a damage accumulation rule have limited validity for general loading scenarios. Unit cell simulations have also demonstrated the dependence of ductile fracture upon the stress state, where the influence of the Lode parameter for low values of the stress triaxiality is of particular interest. Unit cell modelling may also be used to determine model parameters of a porous plasticity model or other types of coupled damage

models. In the spirit of adopting a “virtual" laboratory, unit cell simulations are combined with anisotropic plasticity models calibrated from NaMo and crystal plasticity simulations to predict ductile fracture of anisotropic aluminium alloys.

Localization of strains in a narrow band is a well-known precursor to ductile failure. Thus, presuming that the onset of ductile failure coincides with strain localization is a valid presumption, which opens up new possibilities to determine ductile failure. Both the imperfection band approach and the bifurcation approach may be used, where a rate-dependent behaviour may be accounted for in the former. The localization module is described in its entirety in Morin et al. [38] together with the mathematical foundation. Localization analyses may be used to calibrate material parameters based on experimental tests and to predict ductile failure. Both approaches were used in this thesis, but only with the imperfection band approach. The imperfection band approach follows the work by Rice [39], were a solid body with an initial imperfection in the form of a thin, planar band is assumed to exist. Metal plasticity is usually assigned to the material outside the band and porous plasticity is assigned inside the band. The imperfection may then be introduced as e.g., pre-existing voids in the porous plasticity model. Continuity and compatibility across the band are enforced and localization is set to occur when the strain rate inside the band goes to infinity. The critical band orientation has to be searched for, where the one exhibiting the lowest ductility is critical. The capability of the module has been investigated in Morin et al. [40] where ductile failure under non-proportional loading paths was considered. The results were compared to unit cell simulations where coalescence between neighbouring voids coincided with ductile failure. The two approaches gave similar results, but the localization analyses required an order of magnitude less computational time. In Gruben et al. [41], localization analyses were used to predict ductile fracture in various experimental tests of specimens made of advanced high-strength steel. The versatility of the module is evident as it can be used to generate a cloud of failure strains in the stress space under proportional loading conditions. Complex fracture models can then be calibrated against these failure strains, which traditionally requires multiple material tests to obtain.

The multi-scale modelling approach presented above includes all ingredients needed to predict ductile failure in structures made from 6xxx series aluminium alloys. Since the results from one module are carried over as input in the next module, the possibility to accumulate errors along the path is important to be aware of. Therefore, a thorough validation of each module is important to ensure that sufficient accuracy is achieved. The goal with this modelling approach is not to replace the role that experiments play today, but rather to serve as a useful tool where the number of experiments may be reduced. Even though the necessary ingredients are present, the accuracy of the predictions still relies on a good finite element model able to describe the problem properly.

1.4 Ductile fracture

In metallic materials, the physical mechanisms governing ductile fracture are known to be nucleation, growth and coalescence of microscopic voids at various length scales [42]. The voids

nucleate at particles when the stress on the particle is sufficient to induce either particle cracking or particle-matrix decohesion. Microscopic voids may already be present in the material as a result of the manufacturing process. The microscopic voids grow due to plastic straining until they coalesce as the inter-void ligaments are subjected to plastic flow localization. According to Benzerga and Leblond [43] and Pineau et al. [44], there are three essential types of coalescence: (i) coalescence in layers by internal necking, (ii) void-sheet coalescence in a micro-shear band, and (iii) coalescence in columns denoted necklace coalescence. Among the effects that determine which type of coalescence that occurs is the underlying microstructure and the stress state. For low values of the stress triaxiality, coalescence of type (ii) and (iii) are usually seen, while for high values of stress triaxiality coalescence of type (i) is dominant. The influence of the stress triaxiality on ductile fracture is well established, where experiments and simulations have revealed a monotonic decrease in ductility for increasing values of the stress triaxiality. A more recent recognition is the influence of the deviatoric stress state, which may be represented by the Lode parameter. Experiments have shown that the influence of the Lode parameter is particularly important for low values of the stress triaxiality (e.g., [45, 46]). In a shear dominated stress state, the ductility is evidently lower than in axisymmetric stress states.

A step-by-step process of ductile failure of porous polycrystalline solids is given in Figure 3 [40]. The material consists of an incompressible matrix with particles and pre-existing voids as shown in the initial state ①. The ductile failure process is initiated by diffuse plastic flow where the growth of existing voids and nucleation of new voids occur in stage ②. Eventually, strain localization takes place in stage ③ as a result of material instability, leading to localization of the plastic flow in stage ④. At this point, the material outside the localized zone is experiencing elastic unloading and the void growth stops. Within the localized zone, the void growth accelerates until the neighbouring voids start to interact and the onset of coalescence is reached in stage ⑤. The inevitable formation of a macro-crack is the final stage where several microscopic voids coalesce and the load-carrying capacity is lost in stage ⑥. It should be noted that localization of strains can be the result of local material heterogeneities or imperfections as well as the result of a geometrical constraint. Ductile failure in the unit cell modelling framework is usually assumed to correspond to the onset of coalescence, represented by stage ⑤. In localization analyses, the onset of strain localization is set to correspond to ductile failure, represented by stage ③. The predictions based on the localization analyses are thus anticipated to be conservative. Considering that strain localization is a strong indicator of imminent failure, the validity of the approach is reasonable.

There are several approaches to model ductile fracture that vary in complexity. A common way to categorize them is on their basis, which may be either phenomenological or physically-based. In general, the phenomenological fracture models are usually less complex and more computationally effective and are often favoured for being easy to use. The physically-based models are usually more mathematically complex as physical phenomena are accounted for. Even though these models are based on physical mechanisms governing ductile failure, they are idealized and do not necessarily perform better than phenomenological models. Among the popular approaches to model ductile fracture are uncoupled fracture models, porous plasticity models, continuum

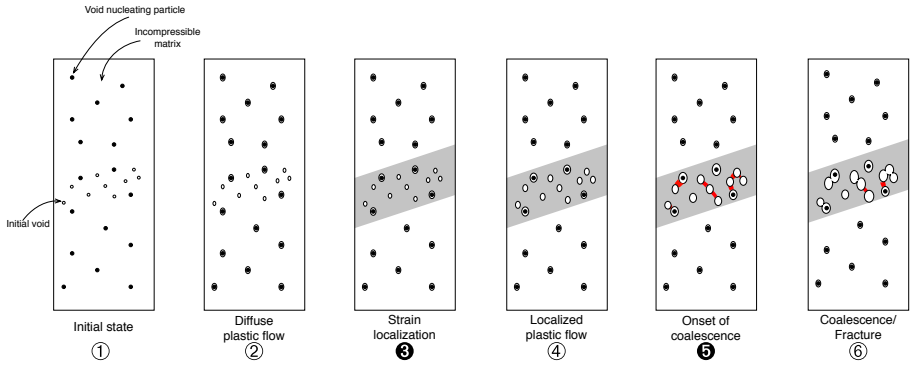

Figure 3: Illustration of the main stages in ductile failure [40]

.

damage models and forming limit curves. They all have their pros and cons which favours them in different situations within different applications. This thesis is confined to porous plasticity and uncoupled damage models, and only these two types of models will be discussed in the following.

Uncoupled damage models are among the most straightforward approaches to model ductile failure. Damage evolution is uncoupled from the constitutive equations and material degradation is thus not accounted for. Damage is simply represented by a scalar value that usually evolves with the equivalent plastic strain. This approach is favoured for use within industrial applications, where a simple and efficient calibration is important in combination with computational efficiency. The number of model parameters that need to be calibrated varies, where some popular uncoupled fracture models only have one model parameter. The accuracy of these models is not necessarily inferior to fracture models with several model parameters, but their versatility is usually limited. This means that the model may be accurate for specific stress states, but may give inaccurate results for other stress states. One such model is the Cockcroft-Latham (CL) fracture model [47], where damage evolves only for tensile stresses and is driven by the plastic work. Of the more advanced fracture models used today, many are heuristic extensions of well-known models where the dependence on the stress triaxiality and the Lode parameter is included, i.e., the modified Mohr-Coulomb (MMC) [48], extended Cockcroft-Latham (ECL) [49], extended Rice-Tracey (ERT) [49] and Hosford-Coulomb (HC) [50] models to name a few. They all include model parameters to control the dependence of the stress triaxiality and the Lode parameter. It is common to express the failure strain as a function of the stress triaxiality and the Lode parameter, or similar dimensionless measures that describe the stress state, where it may be visualized as a fracture locus [46, 48, 51]. This requires a transformation of the fracture model where proportional loading is assumed. In order to overcome this limitation, an integral-based damage accumulation framework is usually employed to account for non-proportionality [51, 52].

A hybrid numerical-experimental approach is often employed in the calibration process of these uncoupled fracture models [49, 50, 53, 54]. Finite element simulations of the tests are conducted and the stress state history is extracted from the critical elements. The equivalent plastic strain at failure in a simulation is determined based on the onset of fracture in the corresponding experiment.

The desired fracture model may be calibrated against these failure strains by e.g., a minimizing approach. The number of experiments used in the calibration depends on how many model parameters that need to be determined. Better accuracy can be achieved by using additional experiments in the calibration process. However, the calibration of the model is simplified if experiments that exhibit proportional loading paths are available. This condition is difficult to fulfil for certain stress states and imposes a challenge in the calibration process. Despite these challenges, the hybrid experimental-numerical approach has been used with success in numerous studies, see e.g., [49, 50].

Porous plasticity models are physically based and coupled in the sense that damage is incorporated in the constitutive equations. In these models, the evolution of microstructural variables is included to describe effects such as material softening due to damage evolution. The models account for physical mechanisms governing ductile fracture and are extensively used in research within the academic field. The well-known model proposed by Gurson [55] in 1977 using an upper-bound limit analysis of a rigid perfectly plastic hollow sphere, marked the birth of what is known as the Gurson model. Multiple extensions were later proposed that further enhanced the model. The most used extension of the Gurson model was introduced by Tvergaard [56, 57] where three material parameters, often referred to as the Tvergaard parameters, were included. This model is frequently referred to as the Gurson-Tvergaard model. Other notable extensions were proposed by Chu and Needleman [58] and Tvergaard and Needleman [59], where void nucleation and accelerated void growth to represent coalescence were introduced, respectively. The last few decades, numerous suggestions to enhance the model have been made, for example to account for void size effects [60] and damage due to void shearing [61] to name a few. Despite the capabilities of the different types of Gurson models, such models are seldom used outside academic research. The reason for this is linked to the dense element discretization needed to obtain reliable results and model parameters that must be determined, which limits the use within industrial applications. A challenge related to the use of porous plasticity models occurs after the onset of localization, where the loss of ellipticity of the governing field equations causes numerical problems. The use of non-local formulations like strain gradient plasticity have overcome this problem by regularizing the mathematical problem, but with this approach, a new set of challenges have arisen [62–64].

2 Objectives and scope

This PhD-thesis is part of the FRIPRO Toppforsk project *Microstructure-based Modelling of Ductile Fracture in Aluminium Alloys* (FractAl) and the objectives of the project therefore also embrace the objectives of this thesis. The project's main objective is to develop and validate a novel microstructure-based modelling framework for ductile fracture in aluminium alloys and thus introduce credible multi-scale simulations in the design of aluminium structures against ductile fracture. The intention of such a modelling framework is to minimize the need for experiments without sacrificing accuracy and thus be able to accurately predict ductile fracture in aluminium structures more effectively. The modelling framework (see Figure 1) depends on accurate predictions from the different modules in order to provide reliable predictions. Thus, the modules that make up the modelling framework must be thoroughly tested and validated to ensure adequate accuracy. In this thesis, the focus has been on testing and validating individual modules against experimental tests by use of finite element simulations. A variety of experimental tests are conducted, including typical material tests and various component tests, covering both quasi-static and dynamic loading conditions. To focus on the validation of a specific module, the remaining ingredients in the FE simulation are kept according to standard, well-known guidelines. Alloys and heat-treatments that exhibit widely different material properties have been tested in an attempt to assess the framework's ability to handle alloys with different strength, work-hardening and ductility. Also, the experiments alone contribute to knowledge about ductile fracture of aluminium alloys.

Specific objectives are summarized as follows:

- Conduct experiments that serve as a basis of comparison for the numerical simulations. The experiments should include material tests that cover different stress states and component tests where both quasi-static and dynamic loading conditions are included. These experiments set requirements for the constitutive equations and the finite element models used to simulate the response.

- Assess the predictive capabilities of the nanostructure model NaMo. The validity of the stress-strain curves predicted by NaMo is important to examine as it is the foundation of the modelling framework. Thus, employing the stress-strain curves in numerical simulations of the experiments is vital to obtain an assessment of the predictions. Also, a direct comparison to experimentally obtained stress-strain curves is considered important to detect trends.

- Conduct localization analyses under proportional loading conditions to obtain a set of failure strains covering the stress space. Localization analyses should also be employed to calibrate the porous plasticity model based on selected experiments. A suitable fracture model should

then be calibrated against the obtained failure strains and used in numerical simulations to assess the predictive capabilities.

The scope of this work contains several limitations. Being part of a larger project, important aspects addressed by other researchers in the project are not covered in this thesis. As emphasized in the objectives, to best assess the performance of a module in the microstructure-based modelling framework, the possible sources of error have to be kept to a minimum. This is best achieved by keeping the models simple and introduce as few uncertainties as necessary. For example, anisotropy is disregarded throughout this thesis even though some of the alloys investigated exhibited anisotropic behaviour. The nanostructure model NaMo, which is a vital part of the multi-scale modelling framework, is limited to 6xxx series alloy. This limitation is not seen as a disadvantage as it makes sense to focus on a specific series of alloy when validating the framework. The focus has been on assessing the capabilities of individual modules of the framework by comparison against experimental results. A wealth of experiments and benchmark tests are required to cover all the details of the framework and is considered out of scope in this work.

3 Summary

3.1 Part 1

[1] Granum, H., Myhr, O. R., Børvik, T., Hopperstad, O. S. (2018). *Nanostructure-based finite element analyses of aluminium profiles subjected to quasi-static axial crushing.* Thin-Walled Structures 131, 769-781.

Part 1 presents an experimental and numerical study on aluminium profiles subjected to quasi-static axial crushing. The rectangular hollow section (RHS) profiles were made of the aluminium alloys AA6063, AA6061 and AA6110 in tempers T6, T7 and O, resulting in nine different material configurations. This gave materials with widely different material properties such as strength, work-hardening and ductility. The profiles were extruded as RHS profiles with cross-section 37 mm $\times$ 29 mm and an initial wall thickness of 2.8 mm. The profiles were cut to lengths of 100 mm with a geometrical trigger to ensure good repeatability and symmetric progressive folding. Three tests on each material configuration were conducted with a cross-head velocity of 30 mm/min to a total deformation of 67 mm. The scatter in mean and peak force between repeated tests was less than 2% and 3%, respectively.

The stress-strain curves were predicted by the nanostructure model NaMo based on the thermo-mechanical histories and the chemical compositions, and employed in finite element simulations of the RHS profiles. The results from the finite element analyses were validated against the experimental results in terms of force-displacement curves and the peak and mean forces. The numerical results were thus obtained without any calibration of the constitutive relation based on mechanical tests. To put emphasis on the performance of the nanostructure model, three fully integrated cubic 64-node hexahedron elements with third-order shape functions, available in the Impetus FE code, were employed through the thickness in the finite element model. A separate study to investigate the effect of the friction on the simulated behaviour of the profiles was conducted. To assess the predictive capabilities of the nanostructure model, stress-strain curves were also calibrated based on uniaxial tension tests and used in simulations of the RHS profiles. This opened up the possibility to compare the two numerical approaches against each other and the experimental results. By comparison of the force-displacement curves, it was found that the results based on the nanostructure model were as accurate as the results based on material tests. By visual inspection of the deformed profiles, excellent agreement was found between the numerical simulations based on the nanostructure model and the experimental tests. The results suggest that the nanostructure model can be used with confidence in the design of energy absorbing structural components made of 6xxx aluminium alloys.

3.2 Part 2

[2] Granum, H., Myhr, O. R., Børvik T., Hopperstad, O. S. (2020). *Effect of pre-stretching on the mechanical behaviour of three artificially aged 6xxx series aluminium alloys.* To be submitted for possible journal publication.

In Part 2, the effect of pre-stretching on the mechaincal behaviour of the aluminium alloys AA6063, AA6061 and AA6110 in temper T6 is investigated. Uniaxial tensile tests and quasi-static axial crushing tests were conducted on rectangular hollow section (RHS) profiles, where the profiles had been pre-stretched 0.5% and 4.0% after extrusion and prior to artificial ageing. The RHS profiles had similar dimensions to the ones investigated in Part 1, where the profiles pre-stretched 0.5% were presented. The uniaxial tensile tests were used to investigate the effect of pre-stretching on plasticity and fracture by comparison of the stress-strain curves for the two pre-stretching levels, where digital image correlation was used to determine the fracture strain on the specimen surface. It was found that the yield stress and ultimate tensile stress are somewhat lower for the profiles pre-stretched 4.0%, while the failure strain was considerably higher compared to those pre-stretched 0.5%. Some of the uniaxial tensile tests exhibited a distinct yield plateau, which was analysed by Kocks-Mecking plots. By visual inspection of the deformed RHS profiles, less cracks were generally seen on the profiles pre-stretched 4.0%. Also, the specific energy absorption from the crushing tests is somewhat lower for the profiles pre-stretched 4.0%.

The nanostructure model NaMo was used to predict the stress-strain curves of the pre-stretched and artificially aged extruded profiles and the results were compared to the experimental data. The overall experimental trends were accurately predicted by NaMo, even though the yield plateau present in some configurations was not captured. The predicted evolution of the microstructure during artificial ageing was used to gain insight into the physical mechanisms responsible for the observed stress-strain behaviour. It was found that the contribution from the dislocations to the yield stress was balanced out by the lower contribution by precipitates in the 4.0% pre-stretched materials compared to the 0.5% pre-stretched materials. The dislocation density in the AA6061 alloy pre-stretched 4.0% was about two times higher than for the corresponding alloy pre-stretched 0.5%. It was found that the dislocations generated during the pre-stretching had a slightly negative effect on the alloy's ability to work-harden.

3.3 Part 3

[3] Granum, H., Aune, V., Børvik, T., Hopperstad, O. S. (2019). *Effect of heat-treatment on the structural response of blast-loaded aluminium plates with pre-cut slits.* International Journal of Impact Engineering 132, 103306.

In Part 3, both an experimental and numerical study on 1.5 mm thick aluminium plates with pre-cut slits subjected to blast loading is presented. The experimental programme included 16

blast tests and 27 uniaxial tensile tests on the alloy AA6016 in tempers T4, T6 and T7. The blast tests were conducted in the SIMLab Shock Tube Facility (SSTF) which is a steel tube where air pressure is built up in a compartment and released when the desired air-pressure is achieved. The plate was mounted by two clamping frames at the other end of the tube with bolts in an attempt to achieve fixed boundary conditions. The blast exposed area on the plate coincided with the internal cross-section of the tube, viz. 0.3 m $\times$ 0.3 m. Pressure sensors upstream the tube monitored the incident and reflected pressure and were used to calculate the velocity of the incoming shock front. Two high-speed cameras were positioned in a stereovision setup, recording the blast event at a resolution of 768 $\times$ 800 pixels. The cameras were upgraded during the test period, thus some tests were recorded at 24 000 fps and some at 37 000 fps. Four different pre-cut slit geometries were investigated at two different firing pressures for temper T4. Two of the pre-ut slit geometries were selected for the tests in tempers T6 and T7, also conducted at two firing pressures. Triplicate uniaxial tensile tests were conducted in the 0°, 45°and 90°directions with respect to the rolling direction. Lankford coefficients were calculated and revealed that the alloy exhibits moderate anisotropy in plastic flow, where the tendency for thinning is stronger than for isotropic materials.

The blast tests were studied by use of 3D-DIC, high-speed images and 3D-scan of the plates after testing. The effect of the slit geometry was investigated for the temper T4 plates, where a marked difference in blast performance was seen. Both the number and orientation of the slits influenced the blast performance and it was difficult to pinpoint which of the two parameters was most detrimental for the plate. The effect of the heat-treatment was evident as the crack propagation and blast resistance were significantly influenced. However, the failure mode of the plate did not change particularly. The speed of propagating cracks and the degree of damage were in general higher for plates in temper T6 than for the plates in tempers T4 and T7. Thus, the higher strength of the plates in temper T6 did not compensate for the reduced ductility compared with the plates in tempers T4 and T7 regarding blast protection.

A finite element model of the blast-exposed area was modelled in Abaqus, with 8-node brick elements with reduced integration and hourglass control. Three elements over the thickness were used with a characteristic element length of 0.5 mm. Two-fold in-plane symmetry was utilized when the initial geometry of the plate allowed for it. The meshing technique was investigated, were both a randomly oriented sweep mesh and a structured mesh were used. The blast load was applied as a tabulated pressure, where the pressure-time histories were taken from massive plate tests with pressure sensors mounted directly on the plate. A modified Johnson-Cook constitutive relation and the Cockcroft-Latham fracture model were used to describe the plasticity and fracture behaviour. Fracture of the plate was modelled by element erosion where elements were removed from the mesh when critical damage was reached in the integration point. The uniaxial tensile tests were used in the calibration of the constitutive relation, where representative tests in the rolling direction were employed. By use of 3D-DIC, displacement profiles from the experiments were obtained and compared to numerically obtained displacement profiles. The results showed good agreement between the displacement profiles for selected points in time, suggesting that the numerical model can accurately describe the plasticity in the problem. The numerical simulations accurately predicted the time and position where fracture initiated and the degree of damage.

However, some failure modes were not predicted correctly. By inspection of the stress state in a plate where the failure mode was incorrectly predicted, a marginal difference of the stress state was observed between propagating and stagnating cracks. This suggests that a more enhanced fracture model could possibly have been able to predict the correct failure mode.

3.4 Part 4

[4] Granum, H., Morin, D., Børvik, T., Hopperstad, O. S. (2019). *Simulation of blast-loaded aluminium plates with crack-like defects.* In: Proceedings of MekIT'19 - 10th National Conference on Computational Mechanics, 149-164.

Part 4 presents a numerical study of the 1.5 mm thick AA6016 aluminium plates with pre-cut slits subjected to blast-loading presented in Part 3. Only the plates in temper T4 tested at the highest load intensity were considered. The plates have different crack-like defects to facilitate crack propagation as the failure mode and they all experienced crack initiation and propagation. The numerical simulations were conducted in the explicit solver of LS-DYNA where shell elements with reduced integration and five integration points through the thickness were used. The element size was varied where four different length-to-thickness ratios ranging from $1/3$ to 5 were investigated. The meshes were generated using a sweep technique to obtain a random orientation. This resulted in approximately 450 000 elements and below 2000 for the smallest and largest element sizes, respectively. The blast load was applied as a tabulated uniform pressure, where the pressure-time history was obtained from a blast test on a massive steel plate with pressure sensors mounted directly on the plate surface. In addition to the built-in pressure definition in LS-DYNA, a user-defined subroutine was employed where the magnitude of the applied pressure decreased as the angle between the initial load direction and the normal of the shell elements increased. Failure was handled by element erosion.

The constitutive model consisted of an isotropic yield surface, isotropic hardening and the associated flow rule. A fracture model that comprises a through-thickness damage regularization scheme was used to model failure in the plates. Here, the contribution to damage is divided into two parts responsible for pure membrane loading and pure bending. The regularization scheme allows different sizes of the mesh to be investigated without the need for individual calibrations of the fracture model for each element size. The numerical results revealed that the pressure definition is important in cases where the plate deforms in a petal mode. When compared to the experiments, the user-defined pressure formulation provided better agreement than the built-in pressure definition. The results with the different mesh sizes revealed evident differences with respect to the predicted failure mode. Only the finest mesh was able to predict both crack initiation and propagation with sufficient accuracy. Crack initiation was captured correctly by the second finest mesh also, but the crack was arrested shortly after initiation. When comparing the simulation with the finest mesh to a solid element simulation with similar characteristic element size, the two approaches provide similar results. However, the computational time was much higher for the solid element model.

3.5 Part 5

[5] Granum, H., Morin, D., Børvik, T., Hopperstad, O. S. (2020). *Calibration of the modified Mohr-Coulomb fracture criterion by use of localization analyses for three heat treatments of an AA6016 aluminium alloy.* International Journal of Mechanical Sciences 192 (2021) 106122.

In Part 5, a novel calibration procedure of the modified Mohr-Coulomb (MMC) fracture model by use of localization analyses is presented. The study is an experimental and numerical study on three different tempers (T4, T6 and T7) of the aluminium alloy AA6016. The experimental part consisted of uniaxial tension, notch tension with two different notch radii, plane-strain tension, in-plane simple shear tests and two load cases of the modified Arcan test. The specimens were cut from plates of the same material as used in Parts 3 and 4. All tests were carried out with the longitudinal axis along the rolling direction. A speckle pattern was spray-painted on the in-plane surface of the specimens to enable 2D-DIC and three tests per test configuration were conducted. The two loading cases of the modified Arcan test consisted of a tension mode and a mixed-mode loading. The experiments served as a basis for calibration and validation of the numerical study.

The localization analyses employed the imperfection band approach, where metal plasticity was assigned outside the band and porous plasticity was assigned inside the band. The stress and strain rates inside the band were allowed to be different from their values outside the band. However, continuing equilibrium and compatibility across the imperfection band were enforced and localization was set to occur when the strain rate inside the band became infinite. The metal plasticity model was calibrated by inverse modelling of a notch tension test using FE simulations and LS-OPT. The porous plasticity model was calibrated by use of localization analyses where the deformation gradient was extracted from the critical element in notch tension and plane-strain tension simulations and assigned as a boundary condition in the localization analyses. With the metal and porous plasticity models calibrated, localization analyses with proportional loading paths were conducted to obtain failure strains covering the stress space. The parameters of the MMC fracture model were then optimized against the obtained failure strains.

The tests not used to calibrate the plasticity models were used in the validation of the MMC fracture model. The results from simulations of the NT3, NT10, PST and ISS tests were compared to the experiments in terms of force-displacement and logarithmic strain-displacement curves. The results from the NT3, NT10 and PST simulations were in good agreement, but the response curves for the ISS tests deviated already at yielding. The reason for these deviations is linked to the texture of the alloy. Crack initiation and propagation were accurately captured in all but one Arcan test. By comparing the predicted strain fields of selected Arcan tests to the ones obtained by use of DIC, the qualitative trends are similar. The results suggest that the use of localization analyses to calibrate fracture models is an effective and well-suited tool for design of components and structures of metallic materials, where the need for an extensive test programme could be reduced.

Conference contributions

[6] Granum, H., Aune, V., Børvik, T., Hopperstad, O. S. (2018). *Aluminium plates with pre-formed slits subjected to blast loading*. EPJ Web Conferences 183, 01032.

4 Concluding remarks and further work

This PhD-thesis has focused on the modelling and simulation of ductile fracture in 6xxx series aluminium alloys. An integral part of the work has been devoted to performing experiments and numerical simulations in order to evaluate and validate individual modules of the modelling framework of the FractAl project. In the work of assessing the capabilities of the modules in the modelling framework, it is important to choose a diverse test programme to avoid biased and spurious results. Emphasis has been put on testing alloys with varying heat-treatments, yielding widely different properties in terms of strength, work-hardening and ductility. The modules tested in this work include the nanostructure model NaMo and localization analyses. Various FE solvers have been used in the numerical simulations, utilizing the advantages and specific features of each software. The research methodology has been according to standard practice where emphasis has been put on obtaining an objective comparison of the experimental and numerical results. Reasonable assumptions have been introduced when deemed necessary and simplifications made to achieve an adequate computational cost of the simulations. These simplifications and modifications are also needed to limit the possible sources of error in the simulations. To assess the quality of the FE models and obtain a broader basis of comparison for the modelling framework, numerical simulations where the plasticity and fracture models are calibrated based on experiments are conducted. As with all numerical simulations, an appropriate FE model and constitutive relations are essential to obtain trustworthy results and the importance of this is unchanged regardless of the calibration approach.

Overall, the performance of NaMo and the localization analyses was satisfactory, where accurate predictions on plasticity and fracture were obtained. The results indicate that the two modules provide satisfactory accuracy of the predictions when compared to experiments. The performance of the modules is particularly impressive if cost and time are included in the evaluation. It must be emphasized that the intention with the modelling framework is not to replace the role that calibration experiments have today, but rather serve as an additional tool. Besides extending our fundamental understanding of ductile fracture in aluminium alloys, the modelling framework opens up an entirely new way of designing aluminium structures against ductile fracture. The results presented in this work suggest that the goal of being able to predict ductile fracture in aluminium structures without the need for an extensive test programme is one step closer.

Based on the insight and knowledge gained on the capabilities of the individual modules in this work and by co-workers of the FractAl project, the next step now is to employ the complete modelling framework. The extensive experimental database that is built up during the project provides a solid basis of comparison for the numerical results. In the assessment of the complete modelling framework, the calibration may be conducted entirely based on predictions or aided by a reduced amount of experiments. This task is suggested for further work.

Additional suggestions for further work are:

- The simulations of the profiles in Part 1 could be extended to account for plastic anisotropy by conducting polycrystal plasticity simulations based on the initial microstructure. By combining polycrystal plasticity simulations with the nanostructure model, the yield strength, work-hardening and plastic anisotropy may be accurately predicted in the numerical simulations.
- The numerical simulations in Part 1 could be extended to account for ductile fracture by conducting localization analyses. Comparison against the deformed profiles may be used to reveal if fracture is correctly initiated in the simulations.
- A natural extension to Part 2 is to investigate further the modifications introduced to NaMo to gain insight into the yield plateau phenomenon and the subsequent work-hardening seen in some of the tensile tests. A transmission electron microscopy study would provide useful information to investigate the microstructural features of the different pre-stretch combinations.
- Perform numerical simulations with the plasticity and fracture models calibrated in Part 5 on the plates subjected to blast loading in Part 3. Considering that the correct failure mode was not predicted for all plates in the numerical study in Part 3, the more complex fracture model presented in Part 5 may be able to predict the correct failure mode.
- The numerical study in Part 4 could be extended to the full test programme presented in Part 3 to obtain a better evaluation of the FE model and the constitutive relations. By including different tempers, firing pressures, number and orientation of the crack-like defects, a more comprehensive evaluation of the capabilities of the numerical simulations presented in Part 3 is possible.
- A natural extension to Part 5 is to calibrate the fracture model with the traditional hybrid experimental-numerical approach and conduct numerical simulations of the experiments. Comparison between the results from the two calibration approaches would be useful to evaluate the two calibrated fracture models' ability to predict ductile fracture.
- The porous plasticity model is an important ingredient in the localization analyses where the accuracy of the results from the latter rely on an accurate description of the former. Different procedures to calibrate the porous plasticity model should be investigated in an attempt to find the optimal procedure. Also, different heuristic extensions to the porous plasticity model should be investigated to see how they affect the results of the localization analyses.

Bibliography

[1] Polmear, I. J. *Light Alloys: From traditional Alloys to Nanocrystals*. Fourth edition. Elsevier Ltd. (Butterworth-Heinemann), 2006.

[2] Remøe, M. S., Marthinsen, K., Westermann, I., Pedersen, K., Røyset, J., and C., Marioara. "The effect of alloying elements on the ductility of Al-Mg-Si alloys". *Materials Science & Engineering A* 693 (2017), pp. 60–72.

[3] Ji, S., Yang, W., Gao, F., Watson, D., and Fan, Z. "Effect of iron on the microstructure and mechanical property of Al-Mg-Si-Mn and Al-Mg-Si diecast alloys." *Materials Science and Engineering: A* 564 (2012), pp. 130–139.

[4] Poole, W. J., Wang, X., Embury, J. D., and Lloyd, D. J. "The effect of manganese on the microstructure and tensile response of an Al- Mg-Si alloy". *Materials Science & Engineering A* 755 (2019), pp. 307–317.

[5] Andersen, S. J., Marioara, C., Friis, J., Wenner, S., and R., Holmestad. "Precipitates in aluminium alloys". *Advances in Physics: X* 3 (2018), p. 1479984.

[6] Ji, S. X., Watson, D., Wang, Y., White, M., and Fan, Z. Y. "Effect of Ti Addition on Mechanical Properties of High Pressure Die Cast Al-Mg-Si Alloys". *Light Metals Technology 2013*. Vol. 765. Materials Science Forum. Trans Tech Publications Ltd, 2013, pp. 23–27.

[7] Li, L., Ji, S., Zhu, Q., Wang, Y., Dong, X., Yang, W., Midson, S., and Kang, Y. "Effect of Zn concentration on the microstructure and mechanical properties of Al-Mg-Si-Zn alloys processed by gravity die casting." *Metallurgical and Materials Transactions A* 49 (2018), pp. 3247–3256.

[8] Pedersen, K. O., Westermann, I., Furu, T., Børvik, T., and Hopperstad, O. S. "Influence of microstructure on work-hardening and ductile fracture of aluminium alloys". *Materials and Design* 70 (2015), pp. 31–44.

[9] Christiansen, E., Marioara, C., Holmedal, B., Hopperstad, O. S., and Holmestad, R. "Nano-scale characterisation of sheared β'' precipitates in a deformed Al-Mg-Si alloy." *Scientific reports* 9 (2019), p. 17446.

[10] Frodal, B. H., Pedersen, K. O., Børvik, T., and Hopperstad, O. S. "Influence of pre-compression on the ductility of AA6xxx aluminium alloys". *International Journal of Fracture* 206.2 (2017), pp. 131–149.

[11] Frodal, B. H., Christiansen, E., Myhr, O. R., and Hopperstad, O. S. "The role of quench rate on the plastic flow and fracture of three aluminium alloys with different grain structure and texture". *International Journal of Engineering Science* 150 (2020), p. 103257.

[12] Murayama, M. and Hono, K. “Pre-precipitate clusters and precipitation processes in Al-Mg-Si alloys.” *Acta Materiala* 47.5 (1999), pp. 1537–1548.

[13] Pogatscher, S., Antrekowitsch, H., Leitner, H., Ebner, T., and Uggowitzer, P. J. “Mechanisms controlling the artificial aging of Al-Mg-Si alloys.” *Acta Materiala* 59.9 (2011), pp. 3352–3363.

[14] Matsuda, K., Sakaguchi, Y., Miyata, Y., Uetani, Y., Sato, T., Kamio, A., and Ikeno, S. “Precipitation sequence of various kinds of metastable phases in Al-1.0mass% Mg2Si-0.4mass% Si alloy”. *Journal of Materials Science* 35 (2000), pp. 1573–4803.

[15] Marioara, C. D., Andersen, S. J., Stene, T. N., Hasting, H., Walmsley, J., Van Helvoort, A. T. J., and Holmestad, R. “The effect of Cu on precipitation in Al–Mg–Si alloys”. *Philosophical Magazine* 87 (23 2007), pp. 3385–3413.

[16] Kato, Y., Hisayuki, K., Sakaguchi, M., and Higashi, K. “Effect of Alloy Elements on Microstructures and Mechanical Properties in Al-Mg-Si Alloys”. *ICAA13 Pittsburgh*. Springer International Publishing, 2012, pp. 1521–1526.

[17] Shewmon, P.G. *Transformations in Metals*. Materials Science and Engineering Series. McGraw-Hill, 1969.

[18] Christiansen, E., Marioara, C., Marthinsen, K., Hopperstad, O. S., and Holmestad, R. “Lattice rotations in precipitate free zones in an Al-Mg-Si alloy.” *Materials Characterization* 144 (2018), pp. 522–531.

[19] Teichmann, K., Marioara, C. D., Andersen, S. J., and Marthinsen, K. “The effect of preaging deformation on the precipitation behavior of an Al-Mg-Si alloy”. *Metallurgical and Materials Transaction A: Physical Metallurgy and Materials Science* 43.11 (2012), pp. 4006–4014.

[20] Myhr, O. R., Grong, Ø., and Schäfer, C. “An Extended Age-Hardening Model for Al-Mg-Si Alloys Incorporating the Room-Temperature Storage and Cold Deformation Process Stages”. *Metallurgical and Materials Transactions A: Physical Metallurgy and Materials Science* 46.12 (2015), pp. 6018–6039.

[21] Myhr, O. R., Grong, Ø., and Pedersen, K. O. “A combined precipitation, yield strength, and work hardening model for Al-Mg-Si alloys”. *Metallurgical and Materials Transactions A: Physical Metallurgy and Materials Science* 41.9 (2010), pp. 2276–2289.

[22] Kocks, U. F. “Laws for Work-Hardening and Low-Temperature Creep.” *Journal of Engineering Materials and Technology* 98.1 (1976), pp. 76–85.

[23] Mecking, H. and Kocks, U. F. “Kinetics of flow and strain-hardening.” *Acta Metallurgica* 29 (11 1981), pp. 1865–1875.

[24] Engler, O., Schäfer, C., and Myhr, O. R. “Effect of natural ageing and pre-straining on strength and anisotropy in aluminium alloy AA 6016”. *Materials Science and Engineering A* 639 (2015), pp. 65–74.

[25] Myhr, O R, Hopperstad, O. S., and Børvik, T. “A Combined Precipitation , Yield Stress , and Work Hardening Model for Al-Mg-Si Alloys Incorporating the Effects of Strain Rate and Temperature”. *Metallurgical and Materials Transactions A* 49.8 (2018), pp. 3592–3609.

[26] Khadyko, M., Myhr, O. R., and Hopperstad, O. S. "Mechanics of Materials Work hardening and plastic anisotropy of naturally and artificially aged aluminium alloy AA6063". *Mechanics of Materials* 136.February (2019), p. 103069.

[27] Johnsen, J., Holmen, J. K., Myhr, O. R., Hopperstad, O. S., and Børvik, T. "A nano-scale material model applied in finite element analysis of aluminium plates under impact loading". *Computational Materials Science* 79 (2013), pp. 724–735.

[28] Hoang, N. H., Hopperstad, O. S., Myhr, O. R., Marioara, C., and Langseth, M. "An improved nano-scale material model applied in axial-crushing analyses of square hollow section aluminium profiles". *Thin-Walled Structures* 92 (2015), pp. 93–103.

[29] Granum, H., Myhr, O. R., Børvik, T., and Hopperstad, O. S. "Nanostructure-based finite element analyses of aluminium profiles subjected to quasi-static axial crushing". *Thin-Walled Structures* 131 (2018), pp. 769–781.

[30] Holmen, J. K., Børvik, T., Myhr, O. R., Fjær, H. G., and Hopperstad, O. S. "Perforation of welded aluminum components: Microstructure-based modeling and experimental validation". *International Journal of Impact Engineering* 84 (2015), pp. 96–107.

[31] Khadyko, M., Myhr, O. R., Dumoulin, S., and Hopperstad, O. S. "A microstructure-based yield stress and work-hardening model for textured 6xxx aluminium alloys". *Philosophical Magazine* 96.11 (2016), pp. 1047–1072.

[32] Frodal, B. H., Dæhli, L. E. B., Børvik, T., and Hopperstad, O. S. "Modelling and simulation of ductile failure in textured aluminium alloys subjected to compression-tension loading." *International Journal of Plasticity* 118 (2019), pp. 36–69.

[33] Khadyko, M., Dumoulin, S., Cailletaud, G., and Hopperstad, O. S. "Latent hardening and plastic anisotropy evolution on AA6060 aluminium alloy." *International Journal of Plasticity* 76 (2016), pp. 51–74.

[34] Khadyko, M., Dumoulin, S., Børvik, T., and Hopperstad, O. S. "An experimental-numerical method to determine the work-hardening of anisotropic ductile materials at large strains." *International Journal of Mechanical Sciences* 88 (2014), pp. 25–36.

[35] Needleman, A. "Void Growth in an Elastic-Plastic Medium". *Journal of Applied Mechanics* 39.4 (1972), pp. 964–970.

[36] Dæhli, L. E. B., Børvik, T., and Hopperstad, O. S. "Influence of loading path on ductile fracture of tensile specimens made from aluminium alloys". *International Journal of Solids and Structures* (2015), pp. 1–18.

[37] Dæhli, L. E. B., Faleskog, J., Børvik, T., and Hopperstad, O. S. "Unit cell simulations and porous plasticity modelling for strongly anisotropic FCC metals". *European Journal of Mechanics, A/Solids* 65 (2017), pp. 360–383.

[38] Morin, D., Hopperstad, O. S., and Benallal, A. "On the description of ductile fracture in metals by the strain localization theory". *International Journal of Fracture* 209.1 (2018), pp. 27–51.

[39] Rice, J. R. “The localization of plastic deformation”. *Theoretical and Applied Mechanics (Proceedings of the 14th International Congress on Theoretical and Applied Mechancs, Delft, 1976)*. Vol. 1. North-Holland Publishing Co, 2012, pp. 207–220.

[40] Morin, D., Dæhli, L. E. B., Børvik, T., Hopperstad, O. S., and Benallal, A. “Numerical study of ductile failure under non-proportional loading”. *European Journal of Mechanics A/Solids* 74.7491 (2019), pp. 221–241.

[41] Gruben, G., Morin, D., Langseth, M, and Hopperstad, O. S. “Strain localization and ductile fracture in advanced high-strength steel sheets”. *European Journal of Mechanics A/Solids* 61 (2017), pp. 315–329.

[42] Anderson, T. L. *Fracture Mechanics: Fundamentals and Applications*. Third edition. CRC press, Taylor & Francis Group, 2005.

[43] Benzerga, A. A. and Leblond, J. B. “Ductile Fracture by Void Growth to Coalescence”. *Advances in Applied Mechanics* 44 (2010), pp. 169–305.

[44] Pineau, A., Benzerga, A. A., and Pardoen, T. “Failure of metals I: Brittle and ductile fracture”. *Acta Materialia* 107 (2016), pp. 424–483.

[45] Barsoum, I. and Faleskog, J. “Rupture mechanisms in combined tension and shear—Experiments.” *International Journal of Solid and Structures* 44.6 (2007), pp. 1768–1786.

[46] Bao, Y. and Wierzbicki, T. “On fracture locus in the equivalent strain and stress triaxiality space.” *International Journal of Mechanical Sciences* 40 (1 2004), pp. 81–98.

[47] Cockcroft, M. G. and Latham, D. J. “Ductility and the workability of metals”. *Journal of the Institute of Metals* 96 (1968), pp. 33–39.

[48] Bai, Y. and Wierzbicki, T. “Application of extended Mohr-Coulomb criterion to ductile fracture.” *International Journal of Fracture* 161 (2010), pp. 1–20.

[49] Gruben, G., Hopperstad, O. S., and Børvik, T. “Evaluation of uncoupled ductile fracture criteria for the dual-phase steel Docol 600DL.” *International Journal of Mechanical Sciences* 62 (2012), pp. 133–146.

[50] Mohr, D. and Marcadet, S. J. “Micromechanically-motivated phenomenological Hosford-Coulomb model for predicting ductile fracture initiation at low stress triaxialities”. *International Journal of Solids and Structures* 67-68 (2015), pp. 40–55.

[51] Butcher, C. and Abedini, A. “On Phenomenological Failure Loci of Metals under Constant Stress States of Combined Tension and Shear: Issues of Coaxiality and Non-Uniqueness.” *Metals* 9 (2019), p. 1052.

[52] Papasidero, J., Doquet, V., and D., Mohr. “Ductile fracture of aluminum 2024-T351 under proportional and non-proportional multi-axial loading: Bao–Wierzbicki results revisited.” *International Journal of Solids and Structures* 69-70 (2015), pp. 459–474.

[53] Dunand, M. and Mohr, D. “Hybrid experimental–numerical analysis of basic ductile fracture experiments for sheet metals.” *International Journal of Solids and Structures* 47 (9 2010), pp. 1130–1143.

[54] Mohr, D. and Henn, S. “Calibration of Stress-triaxiality Dependent Crack Formation Criteria: A New Hybrid Experimental–Numerical Method.” *Experimental Mechanics* 47 (2007), pp. 805–820.

[55] Gurson, A. L. “Continuum Theory of Ductile Rupture by Void Nucleation and Growth: Part I—Yield Criteria and Flow Rules for Porous Ductile Media”. *Journal of Engineering Materials and Technology* 99.1 (1977), pp. 2–15.

[56] Tvergaard, V. “Influence of voids on shear band instabilities under plane strain conditions”. *International Journal of Fracture* 17.4 (1981), pp. 389–407.

[57] Tvergaard, V. “On localization in ductile materials containing spherical voids”. *International Journal of Fracture* 18.4 (1982), pp. 237–252.

[58] Chu, C. C. and Needleman, A. “Void Nucleation Effects in Biaxially Stretched Sheets”. *Journal of Engineering Materials and Technology* 102.3 (1980), pp. 249–256.

[59] Tvergaard, V. and Needleman, A. “Analysis of the Cup-Cone Round Tensile Fracture”. *Acta Metallurgica* 32.1 (1984), pp. 157–169.

[60] Monchiet, V. and Bonnet, G. “A Gurson-type model accounting for void size effects”. *International Journal of Solids and Structures* 50.2 (2013), pp. 320–327.

[61] Nahshon, K. and Hutchinson, J. W. “Modification of the Gurson Model for shear failure”. *European Journal of Mechanics, A/Solids* 27.1 (2008), pp. 1–17.

[62] Fleck, N., Muller, G. M., Ashby, M. F., and Hutchinson, J. W. “Strain gradient plasticity: Theory and experiment.” *Acta Metallurgica et Materialia* 42 (2 1994), pp. 475–487.

[63] Fleck, N. and Hutchinson, J. W. “Strain Gradient Plasticity.” *Advances in Applied Mechanics* 33 (1997), pp. 295–361.

[64] Fleck, N. and Hutchinson, J. W. “A reformulation of strain gradient plasticity.” *Journal of the Mechanics and Physics of Solids* 49 (10 2001), pp. 2245–2271.

Part 1

Henrik Granum, Ole Runar Myhr, Tore Børvik,
Odd Sture Hopperstad

Nanostructure-based finite element analyses of aluminium profiles subjected to quasi-static axial crushing

Thin-Walled Structures 131 (2018) 769-781

Thin-Walled Structures 131 (2018) 769–781

Contents lists available at ScienceDirect

Thin-Walled Structures

journal homepage: www.elsevier.com/locate/tws

Full length article

Nanostructure-based finite element analyses of aluminium profiles subjected to quasi-static axial crushing

Henrik Granum[a,*], Ole Runar Myhr[a,b,c], Tore Børvik[a,c], Odd Sture Hopperstad[a,c]

[a] Structural Impact Laboratory (SIMLab), Norwegian University of Science and Technology, N-7491 Trondheim, Norway
[b] Hydro Aluminium, Research and Technology Development (RTD), NO-6601 Sunndalsøra, Norway
[c] Centre for Advanced Structural Analysis (CASA), NTNU, NO-7491 Trondheim, Norway

ARTICLE INFO

Keywords:
Aluminium alloys
Nanoscale model
Energy absorption
Crashworthiness
Finite element analysis

ABSTRACT

In this study, a nanostructure model is used to predict the stress-strain curves of the aluminium alloys AA6063, AA6061 and AA6110 in T6, T7 and O tempers based on the chemical composition and the thermo-mechanical history. The predicted stress-strain curves are then employed in finite element analyses of rectangular hollow section (RHS) profiles of the same materials subjected to axial quasi-static crushing. Thus, the simulations are performed without any calibration of the plasticity model based on material tests. In addition, simulations with the material model calibrated from tensile tests on the same materials are performed for comparison. An experimental programme of the RHS profiles is conducted for validation purposes and compared to the numerical results in terms of the force-displacement curves and the peak and mean forces. To put emphasis on the performance of the nanostructure model, a refined solid element model is used to capture accurately the deformed geometry during axial crushing. A separate study is conducted to investigate the effect of friction on the simulated behaviour of the profiles. The numerical and experimental force-displacement curves display good agreement with deviations in the mean absolute percentage error (MAPE) of the peak and mean force less than 10% and 8%, respectively. By visual inspection of the deformed profiles, excellent agreement is found between the numerical simulations and the experimental tests. The results suggest that the nanostructure model can be used with confidence in design of energy absorbing structural components made of 6xxx aluminium alloys.

1. Introduction

Aluminium is favourable in a number of engineering applications due to its low weight-to-stiffness ratio. Among the many applications are automotive, offshore, protective and aerospace structures. Aluminium alloys have also entered into new application areas during the last several decades due to the development of new alloys with improved properties, often replacing steel as the preferred material. From an environmental point of view, the recyclability of aluminium compared to steel makes it favourable as a future-oriented construction material. In the automotive industry, the introduction of aluminium components has contributed to lower the CO_2 emission and fuel consumption due to weight savings. Other advantageous properties of aluminium include high corrosion resistance, and high electrical and thermal conductivity. Aluminium alloys with specific properties are often required and the possibility to tailor an alloy to given properties would be beneficial.

In 6xxx alloys, the yield strength and the work hardening depend on the chemical composition and the thermo-mechanical history. Nanostructure models able to predict the flow stress from the chemical composition and the thermo-mechanical history of 6xxx alloys have been under development for the last few decades. By use of such models, flow stress curves can be obtained without carrying out any mechanical tests and thus enable simulation-based design of structures made of 6xxx alloys.

The nanostructure model NaMo, which was developed for 6xxx alloys by Myhr et al. [1], has been used with success in different applications on a variety of different alloys. Johnsen et al. [2] conducted ballistic impact experiments on the wrought AA6070 in four different temper conditions. The stress-strain behaviour was predicted by NaMo and used in non-linear finite element simulations with good correlation to the experimental tests. The ballistic limit velocity and the flow stress curves were reported with a maximum deviation of less than 10% between the numerical and experimental results. Holmen et al. [3]

* Corresponding author.
E-mail address: henrik.granum@ntnu.no (H. Granum).
URL: http://www.ntnu.edu/kt/fractal (H. Granum).

https://doi.org/10.1016/j.tws.2018.07.034
Received 1 March 2018; Received in revised form 5 June 2018; Accepted 17 July 2018

Table 1
Chemical composition of the different alloys in wt%.

	Si	Mg	Fe	Mn	Ti	Zn	Cu	Cr	Al
AA6063	0.512	0.470	0.206	0.047	0.006	0.003	0.001	0.001	Balance
AA6061	0.621	0.903	0.209	0.038	0.106	0.054	0.204	0.060	Balance
AA6110	0.720	0.828	0.196	0.506	0.026	0.003	0.203	0.157	Balance

conducted experiments on MIG-welded AA6082-T6 extrusions struck by small-arms bullets. A spatial distribution of the stress-strain behaviour at ambient temperature was determined by NaMo from the chemical composition, artificial ageing history and welding procedure. The resulting flow stress curves were functions of the distance from the weld centre line and used in a 3D finite element model to investigate the effect of the heat affected zone (HAZ) on the ballistic properties. The numerical simulations were found to be in good correspondence with the experimental results and the ballistic limit velocities were within 10% of the experimental ones. In Hoang et al. [4], square hollow section AA6060 profiles subjected to quasi-static axial crushing were investigated. The profiles were artificially aged to three different tempers using two different cooling rates after solution heat treatment. The flow stress curves were predicted by NaMo, where the incubation time was included in the simulations by a new feature in the model, and good agreement between the experimental and numerical results was reported. Engler et al. [5] investigated the effect of natural ageing and pre-straining on the strength and anisotropy of AA6016. Tensile tests with varying room temperature storage time and pre-straining were conducted to obtain stress-strain curves for the alloy-temper combinations. Corresponding stress-strain curves were calculated by NaMo and compared to the experimentally obtained ones. It was reported that the curves predicted by NaMo captured the main trends, even though they consistently underestimated the flow stress compared with the measured values.

Crashworthiness of aluminium profiles has been studied extensively in recent years, both experimentally and numerically. The strive to optimize the energy absorbing capability during car crashes has led to studies on a variety of geometries and materials. Zhang et al. [6] studied axial crushing of square multi-cell columns of AA6060-T4. It was found that by introducing internal webs to the columns, the energy absorption capability was improved when comparing plain columns of equal weight. An increased energy absorption efficiency of 50% was reported by substituting a single-cell column with a 3×3 column of equal weight. In Zhang et al. [7], square AA6061-O tubes with graded thickness subjected to quasi-static axial loading were investigated experimentally and numerically. Two types of thickness distributions were tested and the results showed that introducing a thickness gradient to a tube might increase the energy absorption capability significantly and an increase in mean force of up to 35% compared to non-graded tubes was reported. However, the problems of material fracture and mode switch were addressed as a potential effect of too excessive grading. The numerical simulations reflected the trends seen in the experiments, and the deviation was less than 16%. Optimization of the tubes was performed by use of the response surface methodology (RSM) to obtain an optimal cross-section for a square tube. Results showed that increasing the wall-thickness in the corners increased the energy absorption capability. Sun et al. [8] studied the energy absorption capability of multi-corner profiles of AA6060 subjected to dynamic axial impact. It was shown numerically that increasing the number and size of corners in a profile had an effect on the energy absorption capability and that multi-corner profiles increased the crushing force efficiency with 12% compared to square tubes of equal weight. Aluminium alloy profiles have also been studied extensively in combination with foam fillers and other reinforcements, see e.g. [9–15].

The main objective of this study is to investigate the accuracy of the nanostructure model NaMo for a range of alloy-temper combinations by employing the predicted stress-strain curves in nonlinear finite element (FE) simulations of RHS profiles subjected to quasi-static axial crushing. To evaluate the accuracy of the flow stress curves predicted by NaMo for application in design of energy absorbing structures, tensile tests and quasi-static axial crushing tests are performed for the same array of alloy-temper combinations. Section 2 presents the alloys and heat treatments, the tensile tests and the axial crushing tests, whereas Section 3 gives an overview of the nanostructure model NaMo and presents the calculated flow stress curves for all combinations of alloy and heat treatment. In Section 4, the FE model of the axial crushing test and the numerical results, obtained with the IMPETUS Afea Solver [16], are presented. The numerical results are discussed in Section 5, and the main observations and conclusions are summarized in Section 6.

2. Experimental study

2.1. Alloys and heat treatments

Three different 6xxx aluminium alloys are investigated in this study: AA6063, AA6061 and AA6110. The alloys were provided by Hydro Aluminium and received as billets with 95 mm diameter and 200 mm length. The chemical composition of the alloys is given in Table 1. The casting length was roughly 1.5 m and the casting conditions were according to standard guidelines for the designated alloys. Prior to extrusion, the ingots were homogenized at 575 °C with a heating rate of 200 °C per hour from room temperature and held for 2 h 15 min before cooling to room temperature at 400 °C per hour. The profiles were extruded as RHS profiles with a wall thickness of 2.8 mm and a cross-section of 37 mm × 29 mm (see Fig. 1), corresponding to a reduction ratio of about 19. The billets were pre-heated to 500 °C before extrusion and the extruded profiles were water-quenched about 0.5 m from the outlet of the die. Approximately the first half meter of the extruded profile for each new alloy was discarded due to possible contaminants in the press. After a short ramp-up time, the ram speed was held constant at 12.1 mm/s for AA6063 and 6.1 mm/s for AA6061 and AA6110. Afterwards, the profiles were cut into lengths of 175 cm and cold-deformed 0.5% by stretching between 1 and 4 h after extrusion. The profiles were then stored at room temperature for 48 h followed by artificial ageing at 185 °C for 8 h to obtain the peak strength temper T6. Selected profiles were further artificially aged to obtain the over-aged temper T7 and the soft annealed temper O, by holding at 185 °C for another 168 h and at 410 °C for 4 h, respectively. Having full control of the chemical composition and the details in the thermo-mechanical history of the material is important for the predictions of the nanostructure model NaMo presented in Section 3.

The profiles were cut into lengths of 100 mm with a geometrical trigger on the two long sides, as shown in Fig. 1, using wire erosion to ensure good repeatability and symmetric progressive folding. This type of geometrical trigger was used with success in Ref. [17] and was accordingly adopted for this study. Prior to testing, the wall thickness of the profiles was measured at various positions and the profiles were weighed.

2.2. Tensile tests

Uniaxial tensile tests were conducted for all nine alloy-temper combinations, using specimens taken from each of the four walls of the

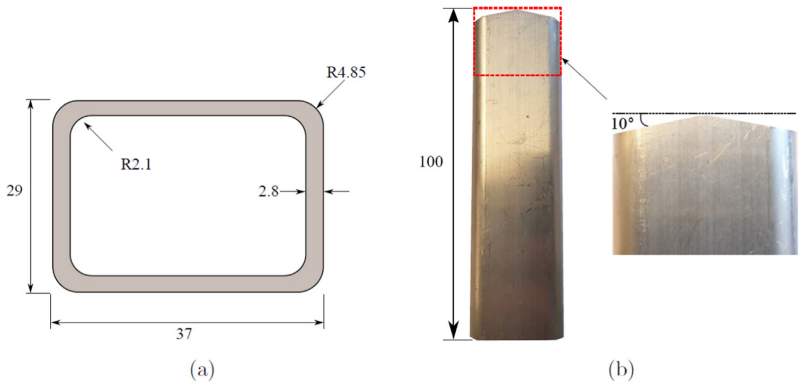

Fig. 1. (a) Nominal cross-sectional geometry of profile and (b) visualization of the geometrical trigger used in the tests. Measures not specified are in mm.

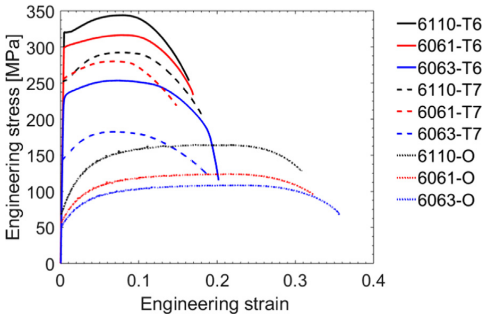

Fig. 2. Engineering stress-strain curves for the nine alloy-temper combinations from tensile tests.

profiles along the extrusion direction. The dog-bone specimens had a gauge length of 20 mm and an initial thickness of 2.8 mm, i.e., similar to the wall thickness of the profile. The tensile tests were conducted in an Instron 5985 series universal testing machine at ambient temperature with a 5 kN load cell at an initial strain rate of $5 \times 10^{-4} s^{-1}$. The force was continuously measured by the load cell and the displacement of the gauge section was tracked using digital image correlation (DIC) by a virtual extensometer. To enable the specimen for DIC, a speckle pattern was spray-painted on the gauge section and a Prosilica GC2450 camera oriented perpendicular to the gauge surface captured pictures at a resolution of 2448 × 802 pixels. The pictures from the camera and the measurements from the load cell were synchronized, operating at 2 fps. The spread among three corresponding tests was insignificant and the test experiencing median force level within an alloy-temper combination was chosen as representative test for calibration of the flow stress curves. The representative engineering stress-strain curves for all alloy-temper combinations are displayed in Fig. 2. The large variation in strength and work hardening capacity between the different alloy-temper combinations is evident with yield strengths ranging from around 50 MPa to more than 300 MPa and tensile strengths between 100 MPa and 350 MPa.

An FE model of the tensile specimen was made in Abaqus/Standard with 8-node trilinear brick elements with reduced integration. The model had six elements over the thickness, which gave an element size just below 0.5 mm. The material behaviour was represented by a rate-insensitive J_2-plasticity model, including the von Mises yield criterion, the associated flow rule and isotropic hardening. The flow stress σ_f was defined by

$$\sigma_f(\varepsilon_p) = \sigma_0 + \sum_{i=1}^{2} Q_i(1 - \exp(-C_i\varepsilon_p)) \quad (1)$$

where σ_0 is the initial yield stress, Q_i and C_i are parameters in the two-term Voce hardening rule, and ε_p is the equivalent plastic strain. As the aim of this study is to predict the overall behaviour of the profiles during axial crushing, represented by the peak force, energy absorption and folding pattern, it was found appropriate to neglect the plastic anisotropy of the extruded profiles and to use the von Mises yield function. However, in studies of formability, plastic forming or ductile fracture of extruded aluminium profiles, the high-exponent Hershey yield function [18] is deemed more appropriate for materials with random texture and a high-exponent, linear transformation-based anisotropic yield criterion, like the Yld2004-18p criterion proposed by Barlat and co-workers [19], for textured materials.

The optimization tool LS-OPT was used to calibrate the hardening parameters (Q_i, C_i) by running sequential simulations on the same model with different input data. The engineering stress-strain curves from the representative tests shown in Fig. 2 were calculated for each alloy-temper combination by use of a 16 mm virtual extensometer in the DIC software. This provides us with engineering stress-strain curves valid until failure, which were used as target curves in the optimization. An initial calibration of the hardening parameters up to necking was done in a spreadsheet and used as starting values for the optimization. A genetic algorithm was applied for the optimization and 100 equidistant regression points were used to ensure good fit in all parts of the curve. The optimal values of the hardening parameters were found by minimizing the mean square error between the simulated and experimental curves all the way to failure. The obtained parameters are given in Table 2, whereas the flow stress curves to 20% plastic strain are depicted in Fig. 3. It is seen that AA6110 has the highest strength for all tempers closely followed by AA6061, whereas AA6063 has the lowest

Table 2
Parameters of the two-term Voce rule for the calibrated flow stress curves from tests.

Alloy	Temper	σ_0 (MPa)	Q_1 (MPa)	C_1	Q_2 (MPa)	C_2
AA6063	T6	233.0	40.0	19.9	34.7	5.0
	T7	142.0	46.0	39.4	24.0	9.1
	O	50.2	46.7	38.2	81.9	2.8
AA6061	T6	298.2	51.1	13.6	18.4	13.1
	T7	254.5	40.1	19.1	19.7	28.6
	O	56.3	47.9	42.1	80.2	4.4
AA6110	T6	320.4	43.3	18.7	30.6	12.7
	T7	251.3	64.5	19.4	19.2	22.1
	O	68.0	92.6	32.8	144.9	1.6

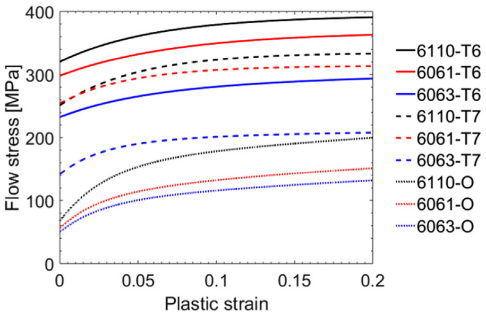

Fig. 3. Flow stress curves to 20% plastic strain for the nine alloy-temper combinations based on tensile tests and optimization using FE analysis.

strength of the three alloys. For a given alloy, temper O exhibits the lowest yield strength and highest work hardening, whereas temper T6 exhibits the highest yield strength and lowest work hardening. Temper T7 falls in-between the peak aged T6 condition and the soft annealed O condition.

2.3. Axial crushing tests

The crushing experiments were performed in an Instron 5985 series 250 kN testing machine at ambient temperature. The velocity of the cross-head was set to 30 mm/min and the profiles were deformed 67 mm. Two Prosilica GC2450 cameras operating at 5 fps with a resolution of 2448 × 1600 pixels captured the deformation from different angles. The axial force and displacement histories were recorded during the experiments. The profiles were placed directly on the level steel platen below the load cell, and no effort was put into constraining the boundary. The three alloys were all tested in the three temper conditions obtained, resulting in nine different alloy-temper combinations. The test for each alloy-temper combinations was repeated two times, resulting in a total of 27 tests.

The force-displacement curves from the experiments are given in Fig. 4, and the progress of an AA6063-T7 test is shown in Fig. 5. From the force-displacement curves it is seen that the repeatability for the different alloy-temper combinations is excellent due to the geometrical trigger shown in Fig. 1b. Some minor discrepancies are found between some repetitions at certain displacements, but the overall repeatability is deemed excellent. The scatter between repeated tests was less than 3% in peak force and less than 2% in mean force. The force-displacement curves for AA6110-T7 and AA6061-T7 seem to coincide, while the differences in the T6 temper are seen to be small between these two alloys. However, a notable difference is obtained in the O temper condition, where AA6110 is considerably higher in strength than AA6061. In general, the AA6063 alloy has notably lower strength than the other alloys for the different temper conditions, but the overall behaviour is similar as the force-displacement curves are shifted compared to the other alloys. All tests for T6 and T7 temper give four peaks in the force-displacement curves, while the tests for O temper give three fully developed peaks. As seen in Fig. 5, the folding pattern for the AA6063-T7 experiment is symmetric and progressive. The first fold is initiated near the top of the profile confirming that the geometrical trigger works as desired, and the number of folds is coinciding with the number of peaks in the force-displacement curves. By visual inspection of the folded profiles, minor cracks were found in some corners for AA6061-T6 and AA6110-T6, while the other seven alloy-temper combinations have no indication of cracks. This is consistent with the presumption that the T6 temper is less ductile than the T7 and O tempers, and that higher strength comes at the cost of lower ductility.

3. Nanostructure model (NaMo)

The nanostructure model NaMo [1,20] is a nanoscale material model composed of three interacting sub-models: a precipitation model, a yield strength model and a work hardening model. NaMo is developed for all 6xxx alloys and the present version is thoroughly validated against experimental data from hot- and cold-rolled AA6005 plates as well as extrusions of AA6060 and AA6005. The model is calibrated once against these experimental data, and no further calibration is needed between simulations. The software is integrated in a computer code with a graphical user interface. Fig. 6 describes the course of the program and the contributions from the different sub-models. The input to the model is the chemical composition of the alloy and the thermo-mechanical history, which are employed in the precipitation model. The output from the precipitation model is then given as input to the yield strength model and the work hardening model, which combined give the complete flow stress curve at room temperature, assuming isotropic material behaviour. The version used in this paper is an extended version, including the combined effect of cold deformation and prolonged room temperature storage on the subsequent response of artificial ageing, referred to as NaMo version 2 [20].

In the precipitation model, the evolution of the hardening precipitates by nucleation, growth or dissolution and coarsening is computed. There are three governing components in the precipitation model: 1) a nucleation law that predicts the number of stable nuclei forming at each time step, 2) a rate law that calculates the dissolution or growth rate of each discrete particle size class, and 3) a continuity equation that keeps track of the amount of solute being tied up in precipitates. In the present model, two different particle size distributions (PSDs) are calculated to represent different types of precipitates and clusters that tend to form in different temperature regions during thermo-mechanical processing, as determined by the individual nucleation laws that are associated with each PSD.

The first PSD is for β'' and β' particles which are nucleated during artificial ageing, while the second is for clusters which form during natural ageing. The two PSDs are linked together by the continuity equation. This leads to a complex balance between the two PSDs since the particles in each distribution consume solute as they grow. The consequence is that one PSD tends to evolve on the expense of the other at a given temperature. This is typically the case when clusters formed by natural ageing dissolve during the subsequent artificial ageing heat treatment, as hardening β'' and β' particles form. An example of this is shown in Fig. 7a for AA6061 after the T6 ageing heat treatment. At this stage of the ageing, the two PSDs co-exist, even though the one for clusters is about to disappear completely since the clusters are too small to be stable at an ageing temperature of 185 °C. Hence, after the T6 heat treatment, the predicted number density of clusters is only $\sim 10^{18}$ $\#/m^3$, compared with $\sim 10^{22}$ $\#/m^3$ for β'' and β' particles. Prolonged ageing corresponding to the overaged (T7) condition, or ageing at a higher temperature to give the O temper leads to complete dissolution of the clusters formed at room temperature, and only the PSD for β'' and β' particles survives. A comparison of this PSD for the three temper conditions T6, T7 and O is shown in Fig. 7b. From the figure, it is evident that the mean radius increases and the overall number density decreases when going from the T6 to the T7 and eventually to the O condition. The mean particle radius for the two extreme conditions, i.e., T6 and O, is 5.2 nm and 126 nm, respectively. Plots of the resulting PSDs for the remaining alloys, i.e., AA6063 and AA6110, show qualitatively similar trends as the ones for AA6061 in Fig. 7, and are therefore not presented here for brevity.

The predicted PSDs in Fig. 7 are input to the yield strength and work hardening models, as illustrated in Fig. 6. In this figure, the columns in the PSD correspond to a certain number density within a specific particle radius class. Beyond a critical particle radius, the particles are assumed non-shearable by dislocations. This is obviously unreasonable for clusters from a physically point of view, since they are fully coherent

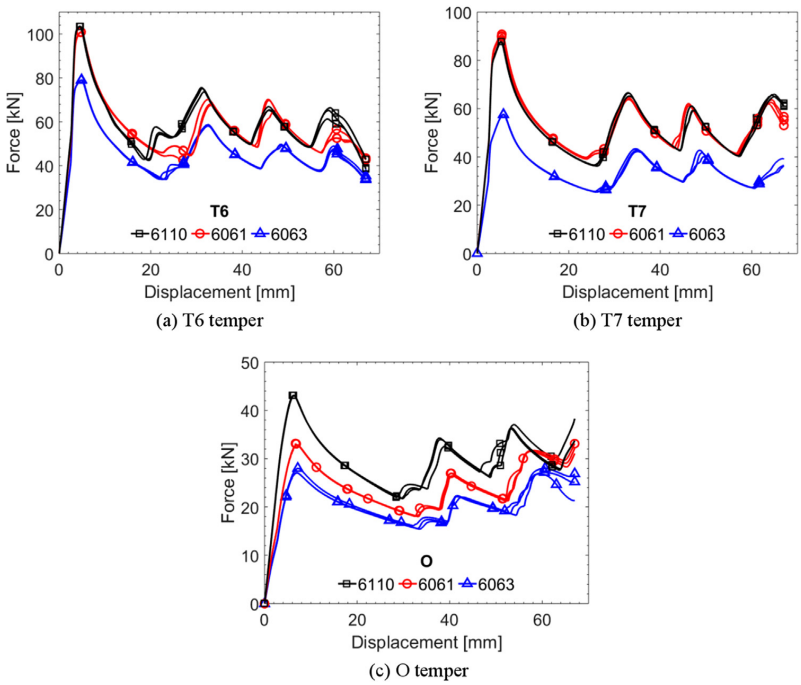

Fig. 4. Force-displacement curves from the axial crushing tests for the different alloy-temper combinations.

with the aluminium matrix and cannot be bypassed by the dislocations. The critical particle radius will in this case be hypothetical and is only used as a scaling parameter in the yield strength model as explained in Ref. [20]. The PSDs change continuously during natural and artificial ageing, and the associated parameters are extracted and transferred to the yield strength and work hardening model at each time step of the simulation, as illustrated in Fig. 6.

In the yield strength model, the overall macroscopic flow stress is given as

$$\sigma_f(\varepsilon_p) = \sigma_i + \sigma_p + \sigma_{ss} + \sigma_d(\varepsilon_p) \tag{2}$$

where σ_i corresponds to the intrinsic yield strength of pure aluminium, σ_p is the overall precipitation hardening contribution, σ_{ss} is the contribution from alloying elements in solid solution, and σ_d is the contribution from dislocation hardening as a function of the plastic strain. The precipitation hardening contribution σ_p is calculated using the following relationship:

$$\sigma_p = \frac{M\bar{F}}{bl} \tag{3}$$

where M is the Taylor factor, b is the magnitude of the Burgers vector, $\bar{F}$ is the mean obstacle strength, and l is the effective particle spacing in the slip plane along the bending dislocation. Both $\bar{F}$ and l are explicitly defined by the PSD as explained in Ref. [20]. Eq. (3) therefore represents a direct coupling between the precipitation model and the yield strength model. The overall strength contribution from particles, σ_p, contains the contributions from the two particle size distributions described above. These two strength contributions are denoted σ_{p1} and σ_{p2}, where the former represents clusters, and the latter metastable β'' and β' particles. σ_p is given by the following expression:

$$\sigma_p = \sqrt{\sigma_{p1}^2 + \sigma_{p2}^2} \tag{4}$$

In this equation, σ_{p1} and σ_{p2} are both calculated from Eq. (3) using individual values for $\bar{F}$ and l representing each of the two particle size distributions. The contribution from elements in solid solution to the flow stress, i.e., σ_{ss} in Eq. (2), is calculated as follows:

$$\sigma_{ss} = \sum_i k_i C_i^{2/3} \tag{5}$$

Here, C_i is the concentration of a specific element in solid solution and k_i is the corresponding scaling factor for the relevant elements with

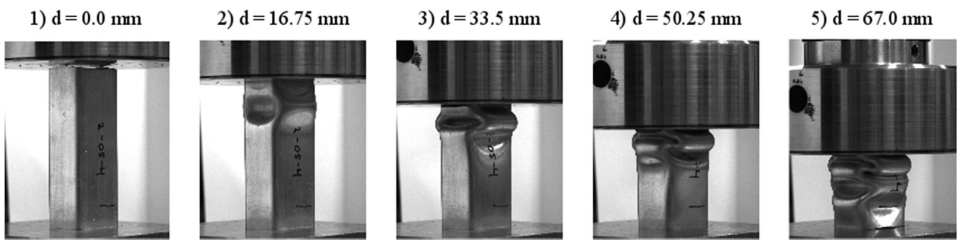

Fig. 5. Deformation patterns from a test on an AA6063-T7 profile.

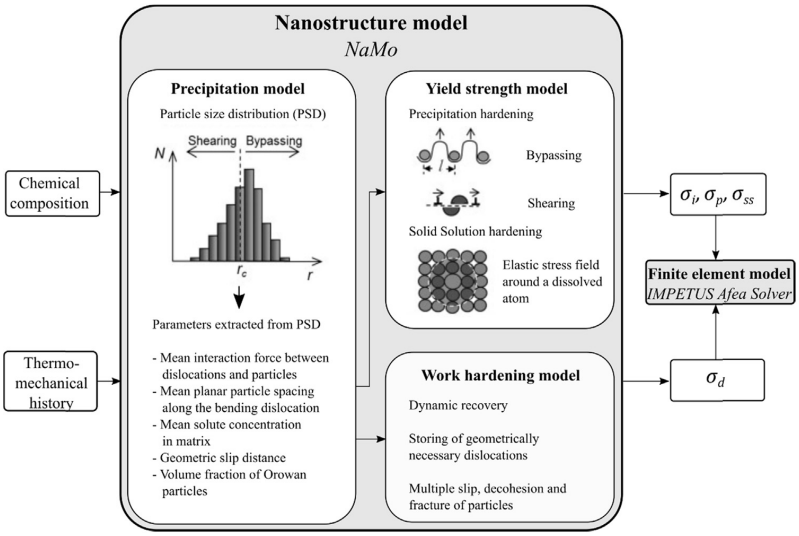

Fig. 6. Outline of NaMo [3].

values given in Ref. [20]. For the elements Mg and Si, the solid solution concentrations, i.e., C_{Mg} and C_{Si}, vary during a heat treatment depending on the volume fraction of clusters and metastable particles.

The final term in Eq. (2), σ_d , represents the contribution from dislocations to the flow stress as calculated by the work hardening model. Two types of dislocations are considered: the statistically stored dislocations that are assumed to form anywhere in the material, and the geometrically necessary dislocations that are assumed to form close to large, non-shearable particles. The corresponding dislocation densities are denoted ρ_s and ρ_g, respectively, and the total dislocation density ρ is assumed to be the sum of the two. The resulting contribution from the dislocations to the flow stress, σ_d, is given by the following equation:

$$\sigma_d = \alpha M \mu b \sqrt{\rho_s + \rho_g} \tag{6}$$

where α is a constant with a value close to 0.3, and μ is the shear modulus.

For the statistically stored dislocations, the Kocks-Mecking relationship is used

$$\frac{d\rho_s}{d\varepsilon_p} = k_1 \sqrt{\rho_s} - k_2 \rho_s \tag{7}$$

Here, k_1 is a constant being characteristic for the material under consideration, whereas the parameter k_2 determines the rate of the dynamic recovery during plastic deformation. The parameter k_2 depends on the solute content of the alloy according to the following relation:

$$k_2 = k_1 \frac{\alpha M \mu b}{k_3 (C_{ss})^{\frac{3}{4}}} \tag{8}$$

In this equation, k_3 is a parameter which expresses the influence of solutes on k_2, and C_{ss} is an effective solid solution concentration, which includes a weighted overall effect of Mg and Si in solid solution on the dynamic recovery rate based on experiments.

The work hardening model predicts the evolution of dislocation densities ρ_s and ρ_g by evolution laws. A somewhat crude approximation in NaMo is that all particles are assumed to be spherical. Hardening precipitates like β'' and β' are either needle- or rod-shaped in Al-Mg-Si alloys. However, due to the initial calibration of the model, it can be argued that the assumption is reasonable based on the mathematical treatment provided in Ref. [20]. For geometrically necessary dislocations, the resulting dislocation density ρ_g depends on the magnitude of the geometric slip distance λ_g, which is a measure of how far the

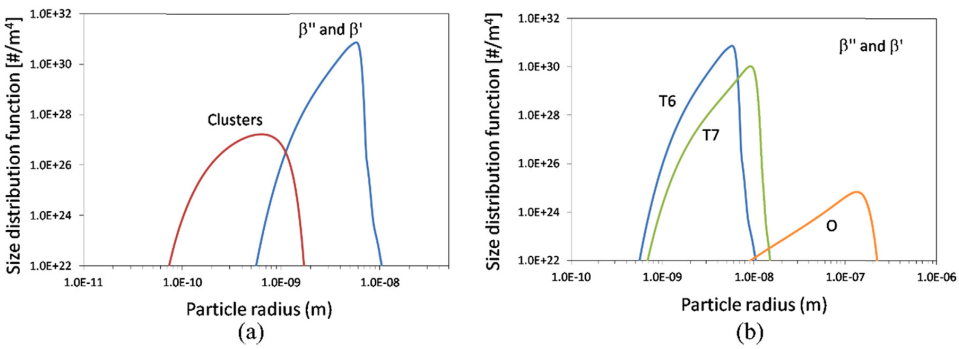

Fig. 7. Predicted PSDs from NaMo for AA6061 showing (a) two co-existing PSDs for clusters and β'' and β' after T6 ageing, and (b) comparison of the PSD for β'' and β' for tempers T6, T7 and O.

dislocations move before they are stored around the non-shearable particles that are dispersed within the material [21]. Thus, λ_g is a characteristic of the microstructure related to the type and distribution of the hardening precipitates in the material, and can be extracted from a given particle size distribution by the following expression:

$$\lambda_g = \left(8 \sum_{r=r_c}^{r=\infty} r_i^2 N_i \right)^{-1} \tag{9}$$

Here, N_i is the number of particles per unit volume within the size class r_i of the particle size distribution, and r_c is the critical radius above which the particles are bypassed by the dislocations and not sheared. Since only particles larger than r_c are capable of storing geometrically necessary dislocations, the work hardening model requires that the volume fraction of these particles f_o is estimated from the PSD containing the metastable β'' and β' particles as follows:

$$f_o = \sum_{r=r_c}^{r=\infty} \frac{4}{3} \pi r_i^3 N_i \tag{10}$$

When λ_g and f_o are known from Eqs. (9) and (10) above, ρ_g can be predicted as described in Ref. [1]. The net contribution from dislocation hardening σ_d is calculated from a response equation as a function of the equivalent plastic strain ε_p as follows:

$$\sigma_d(\varepsilon_p) = \alpha M \mu b \sqrt{\left(\frac{k_1}{k_2}\right)^2 \left(1 - \exp\left(-\frac{k_2 \varepsilon_p}{2}\right)\right)^2 + \rho_{g,s}^{\text{ref}} \frac{\lambda_g^{\text{ref}}}{\lambda_g} \frac{\min(\varepsilon_p, \varepsilon_c)}{\varepsilon_c^{\text{ref}}}} \tag{11}$$

Here, index ref means a chosen reference alloy, and λ_g and λ_g^{ref} are geometric slip distances as defined in Eq. (9). The parameters ε_c and $\varepsilon_c^{\text{ref}}$ are critical values of the equivalent plastic strain defining the saturation values for storing of geometrically necessary dislocations, which corresponds to a dislocation density $\rho_{g,s}^{\text{ref}}$ for the reference alloy. The reader is referred to Refs. [1,20] for further details.

The flow stress curves of the different alloy-temper combinations predicted by NaMo were used to fit the parameters σ_0, Q_i and C_i of the work hardening rule in Eq. (1). The resulting hardening parameters are compiled in Table 3. It was found sufficient to use only one term in the Voce hardening rule for all but one alloy-temper combination for the NaMo curves, while in the calibration based on the tensile tests, two terms were needed to obtain adequate fits for all alloy-temper combinations. The flow stress curves from NaMo and the fitted curves (using the parameters in Table 3) are presented in Fig. 8. The somewhat abrupt saturation point seen in the NaMo curves for the T6 and T7 tempers in Fig. 8 is caused by the saturation of the density of geometrically necessary dislocations, cf. Eq. (11). However, the smoothly fitted curves are used in the subsequent FE simulations and the slope discontinuity is thus avoided.

To obtain a quantitative comparison of the flow stress curves obtained based on the tensile tests and the NaMo calculations, scatter plots depicting the flow stress at 0.2% plastic strain (i.e., the 0.2% proof stress) and the flow stress at 20% plastic strain are presented in Fig. 9.

Table 3
Parameters of the two-term Voce hardening rule for the NaMo-based flow stress curves.

Alloy	Temper	σ_0 (MPa)	Q_1 (MPa)	C_1	Q_2 (MPa)	C_2
AA6063	T6	232.5	4.5	298.0	57.8	21.0
	T7	138.6	49.0	35.4	–	–
	O	49.8	73.7	17.8	–	–
AA6061	T6	280.8	60.7	30.3	–	–
	T7	205.7	48.9	43.2	–	–
	O	70.5	73.7	18.0	–	–
AA6110	T6	312.2	60.8	30.9	–	–
	T7	234.6	48.8	44.8	–	–
	O	96.0	73.7	18.0	–	–

The first plot, Fig. 9a, illustrates the accuracy of the yield stress predicted with NaMo, whereas the second plot, Fig. 9b, gives a measure of how well the work hardening is predicted. The scatter plots show that NaMo gives faithful predictions of the yield stress, even if the yield stress for AA6061-T7 is considerably underestimated. The predictions of the flow stress at 20% plastic strain is slightly more accurate even though NaMo tends to underestimate the work hardening for a majority of the alloy-temper combinations. The mean absolute percentage error (MAPE) in the predicted yield stress and flow stress at 20% plastic strain is 12% and 9%, respectively, which is deemed satisfactory as the predictions are made only based on chemical composition and heat treatment.

4. Numerical simulations

4.1. Finite element model

The explicit FE code IMPETUS Afea Solver [16] was used to simulate the quasi-static axial crushing of the RHS profiles. The material behaviour was represented by a rate-insensitive J_2-plasticity model, including the von Mises yield criterion, the associated flow rule and isotropic hardening. The flow stress curve is defined by Eq. (1) with parameters given either in Table 2 or Table 3. The remaining material parameters are taken as nominal values for aluminium from the literature: Young's modulus, $E = 70000$ MPa, Poisson's ratio, $\nu = 0.3$, and density, $\rho = 2700$ kg/m^3.

The FE model consists of three parts: a rigid bottom plate, a rigid top plate and the profile, as shown in Fig. 10a. By utilizing the symmetry of the problem, only a quarter of the profile was modelled according to the geometry presented in Fig. 1. Assuming symmetric folding, this is a viable approach saving computational time and is employed in similar studies, see e.g. [4,7,11,12]. In previous numerical studies on axial crushing of profiles, see e.g. [4,7], three linear solid elements through the wall thickness were found to be sufficient. In this study, three fully integrated cubic 64-node hexahedron elements with third-order shape functions were employed through the wall thickness, known to be excellent in highly non-linear problems [16]. This gives an effective node spacing of approximately 0.3 mm, resulting in 10 nodes over the wall thickness. The through-thickness mesh is shown in Fig. 10b. A thorough description of the applied higher order elements can be found in Holmen et al. [22]. A total of 11 118 elements and 348 244 nodes were employed in the quarter model. By employing a high-resolution mesh, the intention is to create an FE model that is sufficiently accurate to minimize the discretization errors and thus enable validation of the NaMo simulations. Prior to testing, the profiles were weighed and measured, allowing us to model the profile with the actual geometry obtained after the profiles were stretched 0.5%. This resulted in an average wall thickness of 2.75 mm and an average weight of 83.8 g. The mass of the profile in the FE model was 83.9 g.

A gap of 0.1 mm was introduced between both the bottom and top plate and the profile to ensure no initial contact between the parts. The bottom plate was fixed against displacement and rotations, while the top plate was given a prescribed displacement of 67.2 mm towards the profile, resulting in axial loading. Both the bottom and top plates were modelled as rigid parts, requiring only the density as material input, which for steel was set to $\rho = 7850$ kg/m^3. The displacement was smoothly ramped up by a built-in feature in the FE code to a maximum velocity of 4.4 m/s to avoid inertia effects, and the energy balance was carefully checked to make sure that the kinetic energy was considerably lower than the internal energy, below 1% in all simulations. Contact was taken care of by a penalty based node-to-surface algorithm, where Coulomb friction was specified in the contact. Both contact between the plates and the profile and self-contact of the profile walls were taken into consideration. Based on earlier studies on aluminium profiles subjected to axial loading, e.g. [4,23–25], the Coulomb friction coefficient is usually chosen in the range between 0.2 and 0.3 for quasi-static

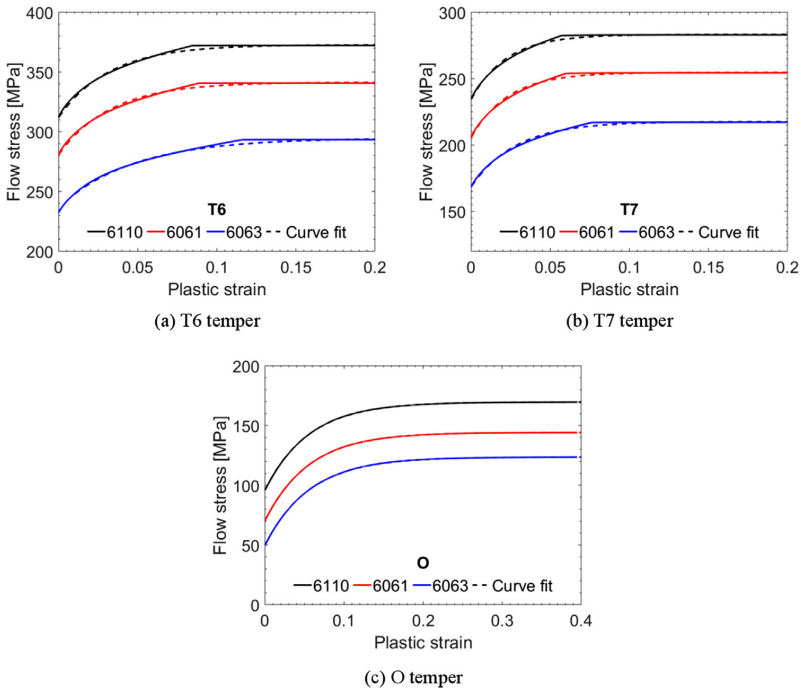

Fig. 8. Flow stress curves from NaMo simulations and fitted curves used in the FE analyses for the three alloys in temper (a) T6, (b) T7 and (c) O.

analyses. In the current study, the frictional coefficient was initially set to 0.2 for contact between the profile and the rigid plates, while the self-contact between profile walls was initially set to 0.5. The friction coefficient is difficult to determine accurately, and a sensitivity study was conducted to investigate the influence it has on the results. Even though some of the tests experienced minor cracking in the corners, it was decided to omit failure modelling in this study. This was mainly done because NaMo does not provide enough information to calibrate a failure criterion.

4.2. Numerical results

Fig. 11 shows the effect friction between the rigid parts and the profile has on the force-displacement curve for AA6061-T6 where the flow stress curve from NaMo was employed. It is evident that altering the friction coefficient slightly modifies the force-displacement curve. Especially around 20 mm displacement, a low friction coefficient results in a peak more prominent than in the experiments. A higher friction coefficient recreates this part of the force-displacement curve better. However, the last peak is better reproduced with a low friction coefficient. By inspection of the curves it is seen that all the tested friction

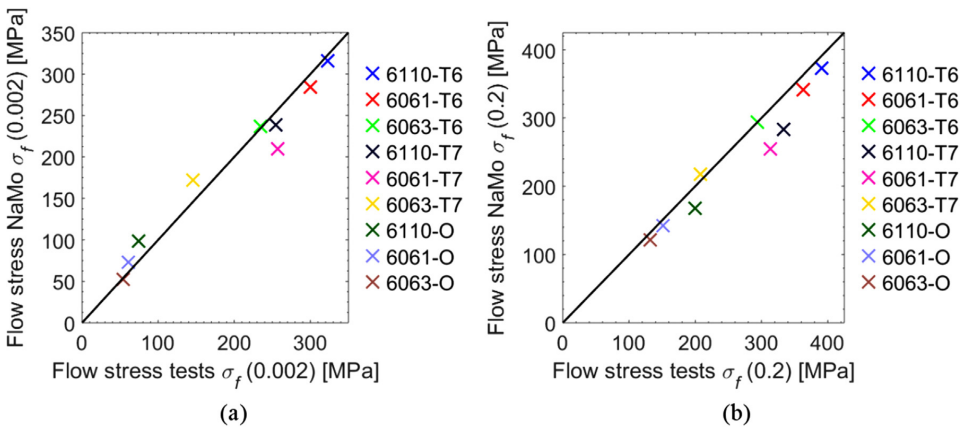

Fig. 9. Scatter plots of (a) flow stress at 0.2% plastic strain, i.e., $\sigma_f(0.002)$, and (b) flow stress at 20% plastic strain, i.e., $\sigma_f(0.2)$, based on tensile tests and NaMo simulations.

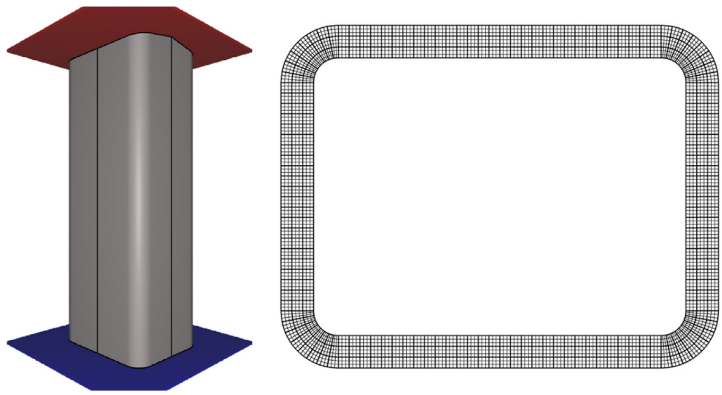

Fig. 10. (a) FE model of the profile, the top plate and the bottom plate, (b) through thickness mesh of FE model.

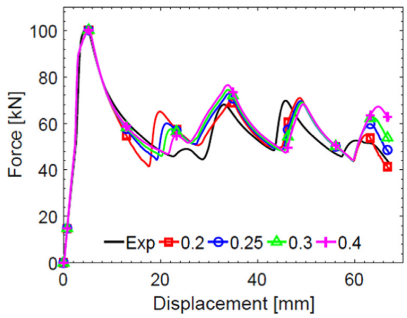

Fig. 11. Force-displacement curves for the different friction coefficients between rigid parts and profile for AA6061-T6.

coefficients provide acceptable results, and the recommendation of setting the coefficient in the range of 0.2–0.3 seems reasonable. Altering the friction coefficient for the self-contact between the profile walls showed negligible effect on the resulting force-displacement curve. Based on the results from the sensitivity study and recommendations from earlier studies, the friction coefficient between the rigid parts was changed to 0.3, while keeping the initial coefficient of 0.5 for the self-contact between profile walls for the rest of the study.

Fig. 12–14 compare the force-displacement curves from all the experiments and simulations, where the flow stress curve was based on either NaMo calculations or tensile tests. The shapes of the simulated force-displacement curves from both approaches are in good correspondence with the experimental curves, and it is evident that the FE model captures the overall behaviour. In five of the cases, the results from the two simulations are better matched to each other than with the experimental data. Somewhat surprisingly, the simulations with the flow stress curve based on tensile tests only comply better with the experimental data for two of the nine alloy-temper combinations. The simulations with the flow stress curve based on NaMo calculations give better agreement with the experimental results for two of the alloy-temper combinations. As the force-displacement curves from the crush test in Fig. 4 displayed similar curves for AA6061-T7 and AA6110-T7, while the flow stress curves calculated by NaMo predicted a clear difference between these two alloy-temper combinations, it was expected that one of these simulations would be less accurate. Of the two simulations based on NaMo that are less accurate, one is overestimating the force level while the other one is underestimating it. Both sets of simulations predict the correct number of force peaks with the peaks occurring at approximately the same displacements as in the experiments.

The peak and mean forces from the experiments and simulations are plotted against each other in Fig. 15. The simulations with flow stress curve based on tensile tests yield consistent results, i.e., the simulated peak and mean forces are consistently somewhat higher than the experimental ones. Also the simulations based on NaMo data overestimate the peak and mean forces in most cases, except for AA6061-T7 and AA6110-T7 where the predicted forces are somewhat lower than the

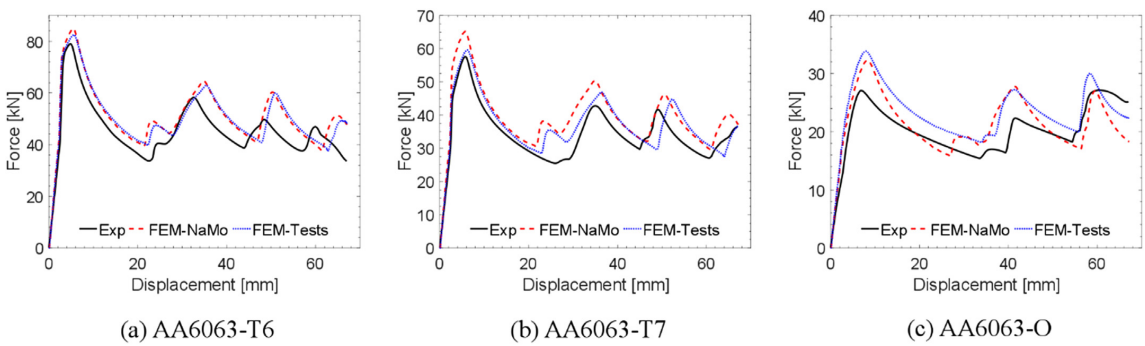

Fig. 12. Force-displacement curves from experiments and FE simulations for AA6063.

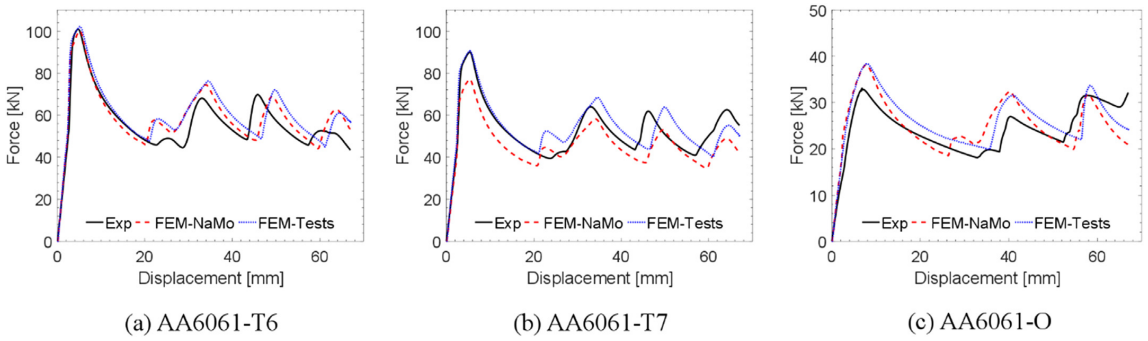

Fig. 13. Force-displacement curves from experiments and FE simulations for AA6061.

experimental ones. However, there is a distinct correlation between the accuracy in the simulated mean and peak forces for the two approaches. In the simulations based on NaMo data, the largest difference in peak force is 19%, 14% and 8% for O, T7 and T6 temper, respectively, and the MAPE of the peak force is below 10%. With flow stress curve based on tensile tests, the largest difference in peak force is 6% for both T6 and T7 temper and 25% for O temper, while the MAPE is again below 10%. This is best visualized in Fig. 12–14. The largest difference in mean force is about 16% for AA6063-T7 in the simulations based on NaMo data, while four alloy-temper combinations have a difference less than 5% and the MAPE of the mean force is less than 8%. The corresponding results for simulations based on tensile tests is about 18% as the largest difference, while only one alloy-temper combination has a difference less than 5% and the MAPE of the mean force is 10%. In summary, the overall accuracy is equally good for the NaMo-based simulations as for those based on tensile tests.

5. Discussion

In Fig. 16, the deformed RHS profile of an AA6061-T6 experiment is compared to the corresponding deformed FE mesh from a simulation based on NaMo data at given displacements. In total, five evenly spaced displacements are chosen, including the first and last frame. A plot marking these points on the force-displacement curve is given in Fig. 17. The simulation is seen to capture the correct folding mode throughout the deformation and the conformity with the experiment is deemed excellent from this viewpoint. At a displacement $d = 16.75$ mm, the initiation of the first fold is recreated and developed correctly into the second fold at $d = 33.5$ mm. This is in accordance with the good conformity in the force-displacement curves up to this point. However, by inspection of Fig. 16 and Fig. 17 at a displacement $d = 50.25$ mm, it is evident that the simulation is diverging slightly from the experiment. The third fold is just commenced in the simulation, while in the experiment the third fold is already collapsing. This delayed response is seen to initiate during the development of the second peak, where the difference in force magnitude allegedly contributes to this. The difference is assumed related to the work hardening as the aforementioned sensitivity study on the friction coefficient shows that friction has marginal influence on delaying the folding pattern. Despite the discrepancies in the force-displacement curve at the final deformation, the agreement is qualitatively good. In the bottom fold in the experiment, a crack is seen in the corner, which is not present in the simulation since a failure criterion is omitted. However, the incipient fracture is seen to have negligible influence on the global response, coinciding with the findings in Ref. [26].

Among the uncertainties introduced in the FE model, friction between the rigid parts and the profile is an important one which is difficult to determine. Fig. 16 showed an excellent agreement between experiment and simulation with respect to the folding pattern seen from the side. In Fig. 18, the bottom of the deformed profiles is seen from below, showing a comparison between the experimental and numerical results obtained with NaMo data. The shapes vary considerably from the T6 temper to the O temper, and even though one could argue that the trends are captured by the numerical model, discrepancies are seen, especially for the O temper. In the simulations of the O temper, the profiles are collapsing more than what is observed in the corresponding experiments. By visual inspection of the folding process, one can see that the bottom of the profile remains rectangular until approximately the last 10 mm of deformation. It is presumed that the discrepancies in this part of the force-displacement curves are reflected in the discrepancies in the deformation patterns of the bottom part of the profile. Discrepancies are also seen for AA6063-T6 and AA6110-T6 where the

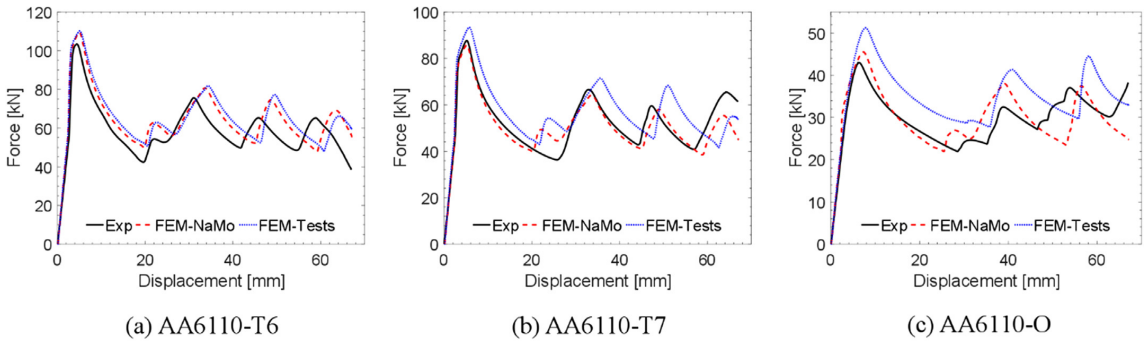

Fig. 14. Force-displacement curves from experiments and FE simulations for AA6110.

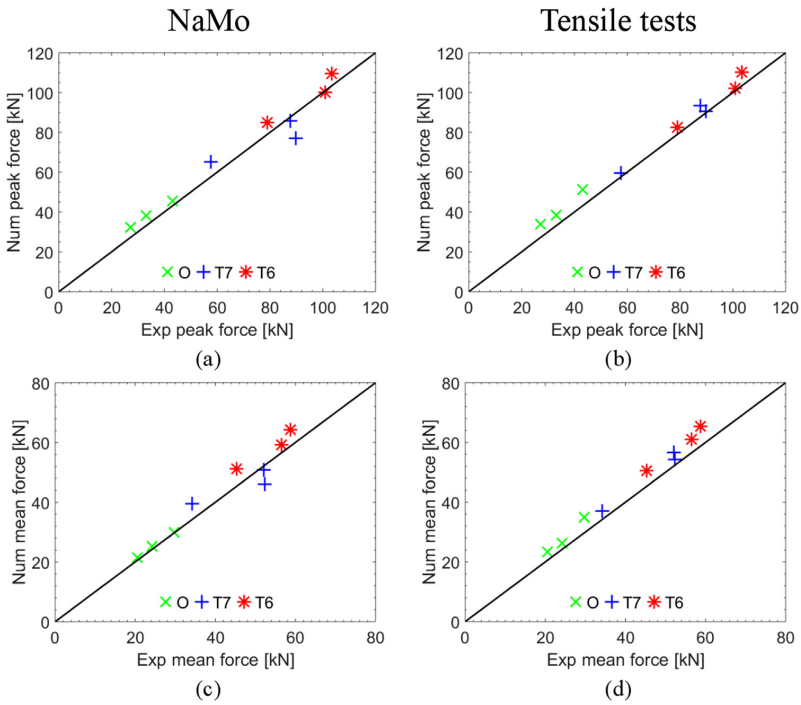

Fig. 15. Scatter plots of (a) peak force from experiments and simulations using NaMo data and (b) with simulations using data from tensile tests. Scatter plots of (c) mean force from experiments and simulations using NaMo data and (d) with simulations using data from tensile tests.

profile is seen to collapse more in the experiment than in the simulation. It is expected that the discrepancy in the folding pattern of the profiles is a result of the combined effects from inaccurate description of the friction between the rigid parts and the profile, and the predicted flow stress by NaMo. However, simulations based on the tensile tests did not give particularly better results for this problem. Based on the quantitative comparisons between the experiments and the simulations it is hard to imagine that there exists a constant friction coefficient reproducing the bottom shape of all the nine alloy-temper combinations correctly.

It should be pointed out that the almost perfect match between the experimental and numerical results with NaMo data for some alloy-temper combinations may be somewhat coincidental, keeping in mind that a number of assumptions have been made in the entirely numerically obtained results. In addition, the fact that the simulation of the RHS profile introduces a number of interfering factors may contribute

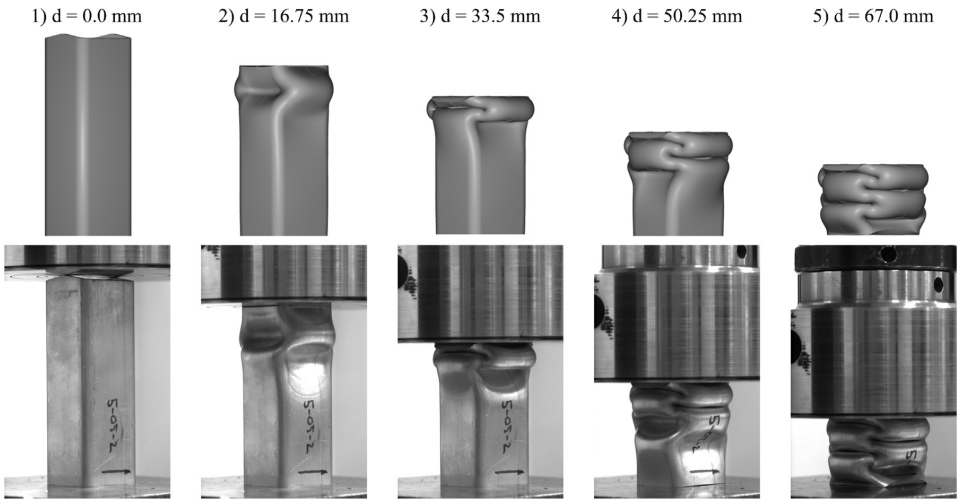

Fig. 16. Comparison of deformation patterns in experiment and simulation with NaMo data of AA6061-T6.

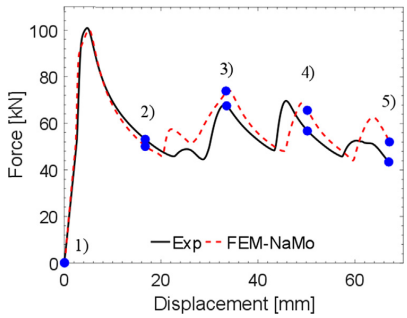

Fig. 17. Comparison of force-displacement curves between experiment and simulation with NaMo data of AA6061-T6 where the markers conform with the displacements in Fig. 16.

to balance out potential errors caused by NaMo. Especially in the mean force calculations, some discrepancies are seen to neutralize each other and thus give better results than expected. However, when considering the crushing of the RHS profiles, the results provided by the use of NaMo are as accurate as those obtained based on tensile tests, suggesting that other factors than the accuracy of the flow stress curve are as crucial for the actual problem. One can justify the use of NaMo for this application provided that the energy absorption and folding process are of main interest and that failure plays an insignificant role.

6. Concluding remarks

In this paper, nanostructure-based FE simulations of quasi-static axial crushing of rectangular hollow section profiles made of AA6063, AA6061 and AA6110 in tempers T6, T7 and O have been evaluated. The nanostructure model NaMo was employed to obtain the flow stress curves, where the chemical composition and thermo-mechanical history are used as input. The flow stress curves were then transferred to the IMPETUS Afea Solver used to simulate the quasi-static axial crushing tests. A refined finite element model was employed to reduce discretization errors and enable validation of the NaMo simulations. To evaluate NaMo for the actual application, tensile tests were conducted to obtain calibrated flow stress curves and these were employed in additional simulations of the quasi-static axial crushing tests. For validation purposes, an experimental program on crushing of RHS profiles was conducted with two repetitions of each alloy-temper combination, resulting in 27 tests. The parallel tests demonstrated excellent repeatability, which was substantiated by the conformity in the force-displacement curves.

When comparing the numerical results obtained with NaMo data to the experimental results, provided as force-displacement curves, peak and mean force scatter plots, an excellent overall agreement was found, taking into consideration that no experimental data were used to calibrate the material model. Excellent agreement was also found by visual inspection of the deformation of the profiles. However, some discrepancies were observed when inspecting the bottom part of the profiles seen from below, indicating among others that friction between the rigid parts and the profile may not be correctly described for all alloy-temper combinations by a constant friction coefficient. The performance of the FE model was deemed good as the number and magnitude of peaks in the force-displacement curves were adequately predicted, combined with the excellent correspondence in the deformation process. The simulations with flow stress curves based on tensile test data exhibited about the same level of accuracy as those based on NaMo data. The MAPE of the peak force was about 10% for the two sets of simulations, while the MAPE of the mean force was around 8% and 10% for the simulations based on NaMo data and tensile test data, respectively.

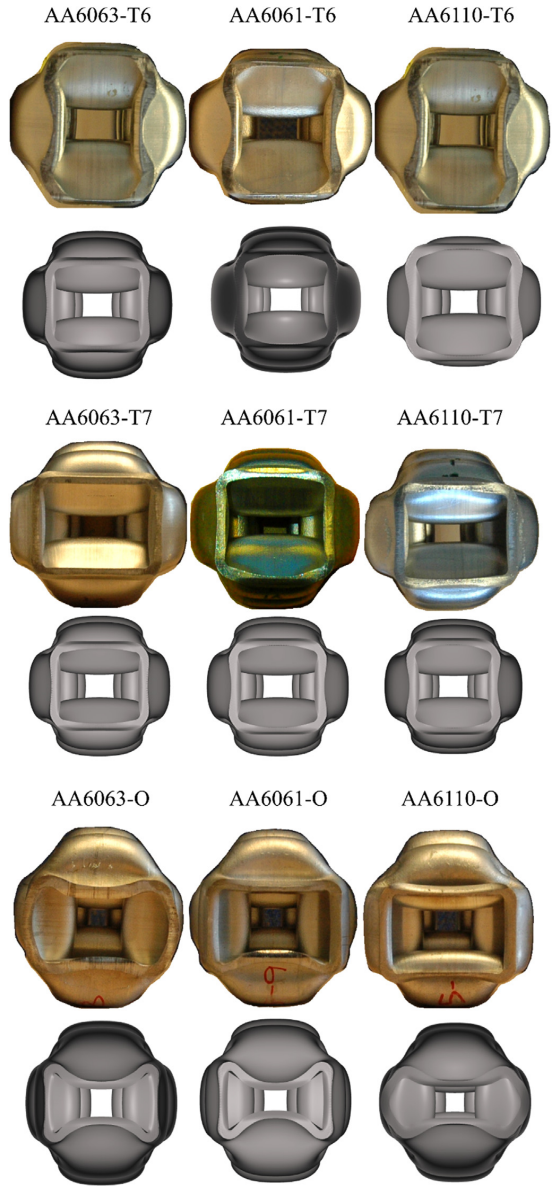

Fig. 18. Comparison of the deformation patterns of the bottom part of the profiles in experiments and simulations (based on NaMo data) as seen from below.

The performance of the nanostructure model NaMo has been assessed in this study. The results show that we can predict quasi-static axial crushing of RHS profiles made of AA6xxx aluminium alloys with good accuracy, without carrying out a single material test. The robustness of the model is verified by employing materials with different chemical composition and thermo-mechanical history. The capability of the model to predict the material behaviour of an alloy based on its chemical composition and the thermo-mechanical history, makes it useful for developing tailored alloys and reducing the need for

expensive and time-consuming test programs in design of aluminium structures made of 6xxx alloys.

Acknowledgments

The authors gratefully appreciate the financial support from NTNU and the Research Council of Norway through the FRINATEK Programme, Project No. 250553 (FractAl). The authors would like to thank Mr. Trond Auestad for managing the experimental tests and Mr. Eivind Sogn Kjus and Mr. Espen Solhjem for their contribution in the experimental work. The authors would also like to thank Dr. Ulf Tundal from Hydro Aluminium, Mr. Martin Lefstad and Mr. Arne Gellein from SINTEF Materials and Chemistry for their contribution with the extrusion of the profiles. Lastly, the authors would like to thank Ms. Helen Langeng from SINTEF for conducting the artificial ageing of the profiles.

References

[1] O.R. Myhr, O. Grong, K.O. Pedersen, A combined precipitation, yield strength, and work harden-ing model for Al-Mg-Si alloys, Metall. Mater. Trans. A: Phys. Metall. Mater. Sci. 41 (9) (2010) 2276–2289.
[2] J. Johnsen, J.K. Holmen, O.R. Myhr, O.S. Hopperstad, T. Børvik, A nano-scale material model applied in finite element analysis of aluminium plates under impact loading, Comput. Mater. Sci. 79 (2013) 724–735.
[3] J.K. Holmen, T. Børvik, O.R. Myhr, H.G. Fjær, O.S. Hopperstad, Perforation of welded aluminum components: microstructure-based modeling and experimental validation, Int. J. Impact Eng. 84 (2015) 96–107.
[4] N.H. Hoang, O.S. Hopperstad, O.R. Myhr, C. Marioara, M. Langseth, An improved nano-scale material model applied in axial-crushing analyses of square hollow section aluminium profiles, Thin- Walled Struct. 92 (2015) 93–103.
[5] O. Engler, C. Schäfer, O.R. Myhr, Effect of natural ageing and pre-straining on strength and anisotropy in aluminium alloy AA 6016, Mater. Sci. Eng. A 639 (2015) 65–74.
[6] X. Zhang, G. Cheng, H. Zhang, Theoretical prediction and numerical simulation of multi-cell square thin-walled structures, Thin-Walled Struct. 44 (11) (2006) 1185–1191.
[7] X. Zhang, Z. Wen, H. Zhang, Axial crushing and optimal design of square tubes with graded thickness, Thin-Walled Struct. 84 (2014) 263–274.
[8] H. Sun, J. Wang, G. Shen, P. Hu, Energy absorption of aluminum alloy thin-walled tubes under axial impact, J. Mech. Sci. Technol. 30 (7) (2016) 3105–3111.
[9] A. Hanssen, M. Langseth, O.S. Hopperstad, Static and dynamic crushing of circular aluminium extrusions with aluminium foam filler, Int. J. Impact Eng. 24 (5) (2000) 475–507.
[10] T. Børvik, O.S. Hopperstad, A. Reyes, M. Langseth, G. Solomos, T. Dyngeland T, Empty and foam-filled circular aluminium tubes subjected to axial and oblique quasi-static loading, Int. J. Crashworthiness 8 (5) (2003) 481–494.
[11] X. Zhang, G. Cheng, A comparative study of energy absorption characteristics of foam-filled and multi-cell square columns, Int. J. Impact Eng. 34 (11) (2007) 1739–1752.
[12] M. Langseth, O.S. Hopperstad, A. Hanssen, Crash behaviour of thin-walled aluminium members, Thin-Walled Struct. 32 (1–3) (1998) 127–150.
[13] H. Zarei, M. Kröger, Crashworthiness optimization of empty and filled aluminium crash boxes, Int. J. Crashworthiness 12 (3) (2007) 255–264.
[14] M. Costas, D. Morin, M. Langseth, L. Romera, J. Díaz, Axial crushing of aluminum extrusions filled with PET foam and GFRP. An experimental investigation, Thin-Walled Struct. 99 (2016) 45–57.
[15] M. Costas, D. Morin, M. Langseth, J. Díaz, L. Romera, Static crushing of aluminium tubes filled with PET foam and a GFRP skeleton. Numerical modelling and multi-objective optimization, Int. J. Mech. Sci. 131–132 (2017) 205–217.
[16] IMPETUS Afea AS, IMPETUS Afea Solver, ⟨http://www.impetus-afea.com/⟩ [cited 16/08-2017].
[17] T. Tryland, T. Berstad, Keep the material model simple with input from elements that predict the correct deformation mode, in: Proceedings of the 10th European LS-DYNA Conference, Würzburg, Germany.
[18] A.V. Hershey, The plasticity of an isotropic aggregate of anisotropic face centered cubic crystals, J. Appl. Mech. 21 (3) (1954) 241–249.
[19] F. Barlat, H. Aretz, J.W. Yoon, M.E. Karabin, J.C. Brem, R.E. Dick, Linear transformation-based anisotropic yield functions, Int. J. Plast. 21 (5) (2005) 1009–1039.
[20] O.R. Myhr, O. Grong, C. Schäfer, An extended age-hardening model for Al-Mg-Si alloys incorporating the room-temperature storage and cold deformation process stages, Metall. Mater. Trans. A: Phys. Metall. Mater. Sci. 46 (12) (2015) 6018–6039.
[21] M.F. Ashby, The deformation of plastically non-homogeneous materials, Philos. Mag. 21 (8) (1970) 399–424.
[22] J.K. Holmen, J. Johnsen, O.S. Hopperstad, T. Børvik, Influence of fragmentation on the capacity of aluminum alloy plates subjected to ballistic impact, Eur. J. Mech. A/Solids 55 (2016) 221–233.
[23] X.W. Zhang, H. Su, T.X. Yu, Energy absorption of an axially crushed square tube with a buckling initiator, Int. J. Impact Eng. 36 (3) (2009) 402–417.
[24] M. Langseth, O.S. Hopperstad, T. Berstad, Crashworthiness of aluminium extrusions: validation of numerical simulation, effect of mass ratio and impact velocity, Int. J. Impact Eng. 22 (9–10) (1999) 829–854.
[25] D. Karagiozova, G.N. Nurick, S. Chung Kim Yuen, Energy absorption of aluminium alloy circular and square tubes under an axial explosive load, Thin-Walled Struct. 43 (6) (2005) 956–982.
[26] M. Langseth, O.S. Hopperstad, Static and dynamic axial crushing of square thin-walled aluminium extrusions, Int. J. Impact Eng. 18 (96) (1996) 949–968.

Part 2

Henrik Granum, Ole Runar Myhr, Tore Børvik,
Odd Sture Hopperstad

Effect of pre-stretching on the mechanical behaviour of three artificially aged 6xxx series aluminium alloys

To be submitted for possible journal publication

Part 3

Henrik Granum, Vegard Aune, Tore Børvik,
Odd Sture Hopperstad

Effect of heat-treatment on the structural response of blast-loaded aluminium plates with pre-cut slits

International Journal of Impact Engineering 132 (2019) 103306

International Journal of Impact Engineering 132 (2019) 103306

Contents lists available at ScienceDirect

International Journal of Impact Engineering

journal homepage: www.elsevier.com/locate/ijimpeng

Effect of heat-treatment on the structural response of blast-loaded aluminium plates with pre-cut slits

Henrik Granum[a,*], Vegard Aune[a,b], Tore Børvik[a,b], Odd Sture Hopperstad[a,b]

[a] Structural Impact Laboratory (SIMLab), Department of Structural Engineering, NTNU, Norwegian University of Science and Technology, Trondheim, Norway
[b] Centre for Advanced Structural Analysis (CASA), NTNU, Trondheim, Norway

ARTICLE INFO

Keywords:
Shock tube tests
AA6016
Crack propagation
Ductile fracture
Numerical simulations

ABSTRACT

This study investigates the structural response of blast-loaded aluminium plates with pre-cut slits. The 1.5 mm thick plates were tested after three different heat-treatments and with four different pre-cut slit geometries at two different blast intensities in a shock tube facility. By varying the number and orientations of the pre-cut slits, different crack patterns and failure modes were obtained in the plates, and it was found that the blast resistance of the plate was markedly affected by the design of the defects. The heat-treatments of the aluminium plates resulted in materials with different strength, work-hardening capacity and ductility, which made it possible to study the influence of these material characteristics on the structural behaviour. It was found that the heat-treatment affected the crack propagation and thus the blast resistance of the plates, whereas the failure mode was not significantly altered. High-speed cameras synchronised with pressure sensors recorded the blast event, and were together with 3D-DIC measurements and 3D-scans used to reveal the dynamic response of the plates. Quasi-static tensile tests were conducted to calibrate the parameters of the modified Johnson-Cook constitutive model and the Cockcroft–Latham failure criterion. Finite element models of the plates were made in Abaqus/Explicit and used in a sensitivity study to investigate the influence of element size and meshing technique on the predictions of crack propagation. Based on the sensitivity study, simulations of the blast experiments were performed using a randomly generated mesh of hexahedral solid elements with a characteristic element size of 0.5 mm. The finite element simulations were able to predict the initiation of failure correctly, even though the subsequent crack propagation was not accurately predicted in all cases.

1. Introduction

Considerable research already exists on metallic plates subjected to blast loading. However, the literature on blast-resistance of metallic plates with geometrical defects is rather scarce. Among the different blast events, the one where the blast load is accompanied with fragments is assumed to be the most detrimental [1,2]. These fragments may perforate the structure, and thereby reduce the capacity significantly. This combined effect is important to include in the design of blast-resistant structures. A possible way to investigate this problem is to inflict damage to the structure prior to the blast load, in an attempt to mimic the effect of perforation by fragments. In addition to this geometrical effect, the dynamic response of blast-loaded plates may be highly dependent on material properties such as strength, work-hardening capacity and ductility. With this as a background, the main objective of this study is to investigate the structural response of blast-loaded aluminium plates with different geometrical defects and heat-treatments.

Rakvåg et al. [3] subjected steel plates with four different pre-cut hole geometries, i.e., squares, circles, diamonds and slits, to blast loading. The pressure magnitudes in these tests were not sufficient to initiate fracture in the plates, but revealed a difference in the deflection of the plates for the different pre-cut geometries. Lagrangian and coupled Eulerian–Lagrangian finite element (FE) simulations were conducted to study the fluid-structure interaction (FSI) effect. The Lagrangian FE simulations were overall in good agreement with the tests, but the deformation in the vicinity of the pre-cut holes was not accurately predicted. By including the FSI effect in the coupled FE simulations, the local deformation increased compared to the Lagrangian FE simulations, and revealed that the pressure around the pre-cut holes was higher than for the rest of the plate. The FE simulations further showed that the configuration with pre-cut slits resulted in twice as high levels of equivalent plastic strain locally as the configuration with circular holes. This suggested that plates with pre-cut slits were more

* Corresponding author.
E-mail address: henrik.granum@ntnu.no (H. Granum).

https://doi.org/10.1016/j.ijimpeng.2019.05.020
Received 5 February 2019; Received in revised form 19 May 2019; Accepted 19 May 2019
Available online 20 May 2019
0734-743X/

susceptible to fracture than the other pre-cut geometries tested. Li et al. [4] subjected plates with three different pre-cut hole geometries to blast loads from different charges of TNT. For two of the configurations (square and circular holes), no fracture was observed in any of the tests, while for the configuration with diamond-shaped holes, fracture was observed in all tests. This substantiates the conjecture by Rakvåg et al. [3] that the shape of the pre-cut holes is important for fracture. Aune et al. [5] studied steel plates with and without pre-cut square holes subjected to blast loading. The plates were tested at four different pressure magnitudes, resulting in no fracture at the lowest pressure and complete failure at the highest pressure for the plates with pre-cut holes. In the tests at the two intermediate pressures, cracks initiated at the corners of the holes and propagated towards the centre and the corners of the plate. For the plates without pre-cut holes, fracture was not found in any of the tests at these pressures. Lagrangian FE simulations with a refined mesh were able to predict the damage evolution, but the plate deflection was overestimated in some cases. Zhang et al. [6] investigated I-core sandwich panels subjected to combined blast and fragment loading. Pre-fabricated fragments and high explosives were used to generate the load, and the results were compared to tests where only high explosives were used. It was reported that the damage caused by the combined blast and fragment loading was more severe and led to perforations of the panels, reducing the capacity sufficiently to enable tearing as the failure mode.

Mode I tearing of ductile metal plates has been studied in e.g. [7] by use of a cohesive zone model, accounting for the dependence of the cohesive tearing energy on the failure process. The results demonstrated that the model was able to capture initiation and propagation of a crack in a 10 mm thick AA5083 H116 edge-notched plate. El-Naaman and Nielsen [8] focused on the fracture surface of ductile metal sheets subjected to tearing, where two different specimens were tested under global mode I loading. Emphasis was put on understanding the alternating slant fracture phenomenon, which was observed in some tests. The physical mechanisms governing the different fracture modes were assumed to be the interplay between the initial porosity, the void nucleation/growth rate and the necking process.

The literature on blast-loaded plates mostly focuses on the loading and/or the structural response, while effects related to the material properties of the target are rarely studied in detail. McDonald et al. [9] and Langdon et al. [10] studied the behaviour of different steel plates subjected to localized blast loading. The strength and ductility of the materials differed considerably and the plates were tested with varying thicknesses and planar dimensions. The tests were done using high explosives where the charge mass, diameter and stand-off distance were varied to obtain different load conditions. Ductility was pointed out as an important property to prevent rupture of the plates and the results suggested that there was a correlation between energy absorbing capability, fracture mode and blast performance. However, they were not successful in correlating material properties with the rupture strength.

In contrast to blast loading, the effects of material properties for ballistic impact have been studied in numerous cases. Børvik et al. [11] showed that the ballistic limit velocity is a linear function of the yield strength for steel targets, while Holmen et al. [12] showed that strength is the governing material parameter regarding perforation resistance for aluminium plates when struck by small-arms bullets. This was explained by the highly localized process taking place when a small-arms bullet perforates a target plate. However, studies with larger projectiles at lower velocities suggest that there is a combined dependence of both strength and ductility (see e.g. [13] and [14]), and under certain conditions materials with lower strength and higher ductility may perform better than materials with higher strength and lower ductility [15]. Granum et al. [16] studied quasi-static axial crushing of aluminium profiles made of three different alloys in three different temper conditions, where strength, ductility and work-hardening varied among the alloys and tempers. The energy absorbing capability was found to mainly depend on the strength of the material. However, ductility is important to avoid peeling and fragmentation of the component which will reduce the energy dissipation.

In this study, the structural response of AA6016 aluminium plates with different pre-cut slits and heat-treatments subjected to blast loading was investigated experimentally and numerically. By varying the number and orientation of the pre-cut slits, different crack patterns and failure modes were obtained in the plates. The heat-treatment of the aluminium plates to tempers T4, T6 and T7 gave materials with different strength, work-hardening capacity and ductility, and thus the influence of these material characteristics on the structural response could be investigated. In the experiments, high-speed imaging, digital image correlation and 3D scanning were used to unveil the displacement fields, crack propagation and failure modes of the plates. Explicit finite element simulations of all the tests were performed with Abaqus/Explicit using solid elements to discretise the geometry. The mesh size and meshing technique were investigated in a sensitivity study. The modified Johnson-Cook model was used to describe the elastic-thermoviscoplastic behaviour of the aluminium alloy, whereas damage evolution and fracture were modelled by the Cockcroft–Latham criterion combined with element erosion. Uniaxial tensile tests were conducted to calibrate the parameters of the material model for each temper. In the numerical study, the main emphasis was put on the simulation model's ability to predict the crack propagation and the failure modes observed in the experiments.

2. Materials

The received plates had dimensions 625 mm × 625 mm × 1.5 mm. They were cut from larger rolled and heat-treatable AA6016 plates produced and delivered by Hydro Aluminium Rolled Products. The chemical composition of the alloy is given in Table 1. The AA6016 alloy is much used by the automotive industry due to its good formability, good strength and high corrosion resistance. It is particularly suited for car-body components where long and high temperature paint-bake cycles may occur [17]. The plates were received in three different tempers, i.e., the naturally aged T4 temper and the artificially aged T6 and T7 tempers. To obtain the T4 temper, the material was solution heat-treated at 530 °C, forced air cooled, pre-baked at 80 °C and finally naturally aged to a substantially stable condition. The peak strength T6 temper was obtained by aging at 185 °C for five hours and the overaged T7 temper by aging at 205 °C for 24 hours after solution heat-treatment and forced air cooling.

A plate in each temper was used to manufacture specimens for tensile tests. Dog-bone specimens with 70 mm length, 12.5 mm width and 1.5 mm thickness of the gauge section were cut from the plates with orientations 0°, 45° and 90° to the rolling direction. A sketch of the geometry of the specimen can be found in [18]. The thickness of each specimen was measured at three different positions along the gauge section. Three tests for each temper and orientation were conducted, resulting in a total of 27 tensile tests. The tensile tests were conducted in an Instron 5982 universal testing machine with a 100 kN load cell at an initial strain rate of 5×10^{-4} s^{-1}. The force was recorded by the load

Table 1
The chemical composition of AA6016 in wt%.

Si	Mg	Fe	Cu	Mn	Cr	Zn	Ti	Al
1.3160	0.3490	0.1617	0.0081	0.0702	0.0025	0.0084	0.0175	Balance

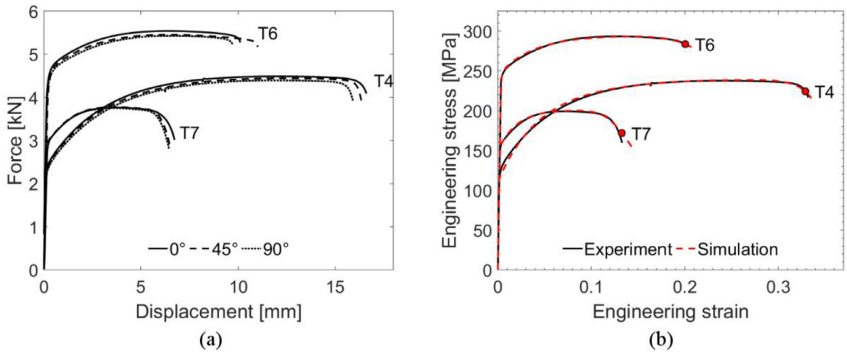

Fig. 1. (a) Force–displacement curves from representative tests in each direction, and (b) engineering stress-strain curves from experiments and simulations. .

cell and a camera oriented perpendicularly to the specimen captured pictures synchronized with the force measurements at 1 Hz. All specimens were spray-painted with a speckle pattern to enable 2D-DIC to track displacements by use of the in-house DIC-code eCorr [19], and the elongation was measured by use of a virtual extensometer with a length of approximately 50 mm.

The force–displacement curves until fracture from representative tests in the three directions are shown in Fig. 1(a). Negligible anisotropy is seen with respect to the flow stress, while the elongation to fracture is found to vary both within and between directions. Ductility is as expected seen to vary between the three heat-treatments, visualized by the drop in stress level at the tail of the curves. The calibration of the hardening parameters was based on the representative test in the rolling direction for each temper. Plots of the engineering stress-strain curves from the experimental tests and the simulations are shown in Fig. 1(b), where the circle denotes the assumed point of fracture based on the experimental results. The details of the calibration of the constitutive relation and the failure criterion used in the finite element simulations are given in Section 5.2.

As evident from Fig. 1(a), the flow stress was practically the same in the tensile tests in the 0˚, 45˚ and 90˚ directions of a given temper, with a maximum deviation of 3%, which implies that the strength anisotropy of the rolled AA6016 alloy is negligible. To evaluate the anisotropy in plastic flow, the Lankford coefficients R_α were calculated for each of the tensile tests, where α denotes the angle with respect to the rolling direction. A virtual extensometer was employed in the post-processing of the DIC results to measure the strain in the width direction of the specimen and the Lankford coefficient was calculated by assuming plastic incompressibility. Obtained Lankford coefficients are listed in Table 2, where they reveal some variation in the plastic flow with tensile direction. The Lankford coefficient is consistently somewhat higher in the rolling direction than in the two other directions, but less than unity in all cases. These results indicate that the material has a moderate anisotropy in plastic flow, where the tendency for plate thinning is stronger than for isotropic materials.

Diffuse necking in the tensile tests in the rolling direction was found to occur at plastic strains of 0.216, 0.119 and 0.066 for tempers T4, T6 and T7, respectively. The Considère criterion, given as $\mathrm{d}\sigma/\mathrm{d}\varepsilon^p = \sigma$, predicts diffuse necking at plastic strains of 0.239, 0.135 and 0.079 based on calibrated flow stress curves for the same tempers. Accordingly, the Considère criterion is seen to consistently overestimate the strain at diffuse necking for the actual materials. However, it is seen from Fig. 1(b) that the engineering stress-strain curves are described with good accuracy also in the post-necking region by the calibrated plasticity model.

Table 2
Lankford coefficient R_α from representative tensile tests.

	R_0	R_{45}	R_{90}
T4	0.58	0.45	0.44
T6	0.69	0.48	0.55
T7	0.77	0.57	0.62

3. Blast tests

3.1. SIMLab Shock Tube Facility

The blast testing of the aluminium plates was conducted in the SIMLab Shock Tube Facility (SSTF) at NTNU. A detailed description of the SSTF as well as an evaluation of the facility can be found in Aune et al. [20], while a general overview of the SSTF and its components is shown in Fig. 2. The tube is made of stainless steel and is divided into three main parts. At the left end, a high-pressure chamber denoted the driver section is located, which by use of removable aluminium inserts has a length of 0.77 m in this study. The driver section is divided from the rest of the tube by the firing section, which consists of several intermediate chambers separated by diaphragms. A 16.20 m long low-pressure chamber denoted the driven section follows the firing section, and the test specimen is mounted at the right end of this section. The intention of the multiple chambers in the firing section is to create a step-wise pressure gradient between the driver and driven sections. The pressure in the driver section is then released by a controlled venting of the intermediate chamber closest to the driver section, causing the diaphragms to rupture one after the other. By keeping the length of the driver section short compared to the driven section, the resulting pressure waves will take on the characteristic form of a blast wave similar to that in a free-field air blast explosion [20,21].

The test specimen is attached to the flange of the tube by use of two clamping frames and twelve M24 bolts, see Fig. 3(a), in an attempt to achieve fixed boundary conditions. All plates tested were mounted with the rolling direction vertically. The planar shock wave impacts the plate where the exposed area corresponds to the internal cross-section of the driven section, viz. 0.3 m × 0.3 m. Upstream the driven section, two pressure sensors denoted Sensor 1 and Sensor 2 are located 0.245 m and 0.345 m from the test specimen, respectively. These sensors are used to measure the velocity of the incoming shock front and to estimate the reflected pressure-time history on the target during testing. The test specimen is surrounded by a dump tank with windows on each side, allowing high-speed cameras to record the test. Two Phantom v1610 high-speed cameras were positioned in a stereovision setup, recording the blast event at 24 000 fps with an image size of 768 × 800 pixels. The testing was conducted in two parts, and prior to the second part the high-speed cameras were upgraded to Phantom v2511. In the subsequent tests, the events were recorded at 37 000 fps. The images were

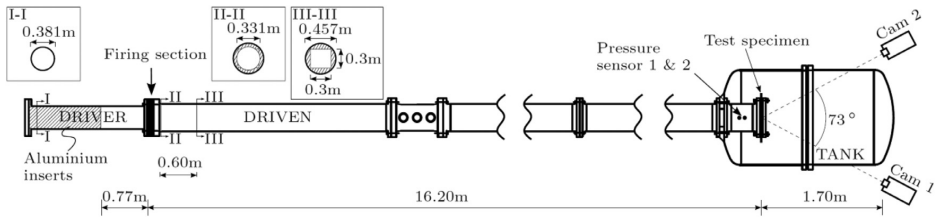

Fig. 2. Overview of the SIMLab Shock Tube Facility (SSTF) [5,20].

synchronized with the pressure-time measurements from Sensor 1 and Sensor 2 in all tests. Three-dimensional digital image correlation (3D-DIC) analyses were conducted using the high-speed camera images and the in-house DIC code eCorr [19]. The stereovision setup was calibrated prior to testing by a pre-calibrated cylinder with a diameter of 80 mm and a checkerboard pattern printed on the surface. In total, five pictures with varying position of the cylinder were used in the calibration process. Out-of-plane displacements were calculated based on the image sets from the synchronized cameras, comparing the relative displacement of the plate at the deformed state to an undeformed reference state. A detailed description of the calibration procedure is found in [20]. Prior to each test, the plate was spray-painted with a speckle pattern required for the DIC analyses. A template was used to apply a black speckle pattern with a size distribution in the range of 2–4 mm, equivalent to 3.4–6.7 pixels. The axial movement of the entire tube was also measured by 3D-DIC and accounted for in the results from the DIC measurements of the plates.

3.2. Blast test programme

The experiments in part one of the blast test programme consisted of plates in temper T4 tested at firing pressures of 1.0 and 1.5 MPa. Four different slit geometries with a width of 0.1 mm were pre-cut in the plates by use of wire erosion before testing. The heat that arises during wire erosion may locally affect the material properties near the slits, but this effect is assumed small and will not be considered in the following. The different slit geometries are shown in Fig. 3(b). The objective was to investigate the influence of the slit geometry on the structural response and failure mode of the plates. Based on that, two of the tested geometries were selected for part two of the study. In this part, plates with the selected slit geometry in tempers T6 and T7 were tested at similar firing pressures. The objective was to study the influence of strength, work-hardening capacity and ductility on the structural response and failure mode of the plates. An overview of the blast test programme is shown in Table 3, where each test is given an abbreviation used in the rest of the study. A total of 16 blast tests were conducted, 8 in each part. The abbreviation reads X–Y–Z–W in which X denotes the temper, Y provides the number of slits, Z represents the orientation of the slits and W indicates the intended firing pressure in MPa in the driver section. Note that Y is omitted in the cases of only one slit in the centre of the plates.

Table 3
Overview of the blast test programme.

Firing pressure [MPa]				
1.0	T4-4-HV-1.0	T4–4-45-1.0 T6-4-45-1.0 T7-4-45-1.0	T4-HV-1.0	T4-22.5–1.0 T6-22.5-1.0 T7-22.5-1.0
1.5	T4-4-HV-1.5	T4-4-45-1.5 T6-4-45-1.5 T7-4-45-1.5	T4-HV-1.5	T4-22.5-1.5 T6-22.5-1.5 T7-22.5-1.5

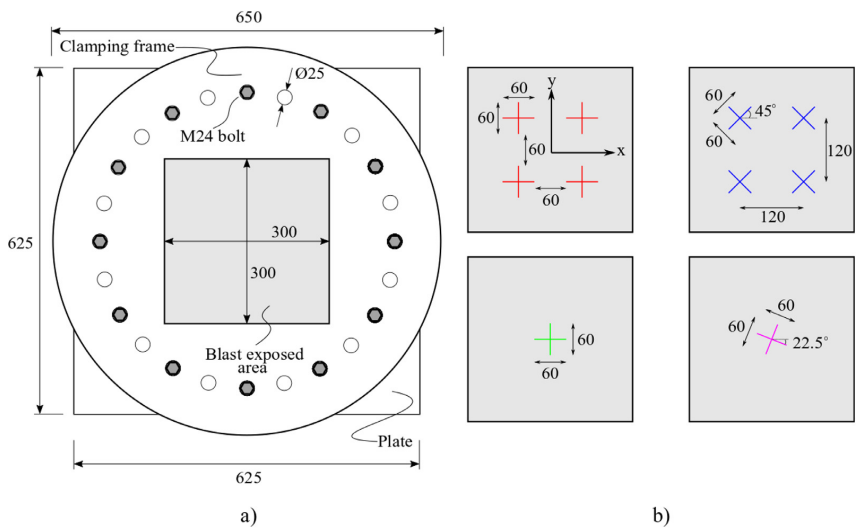

Fig. 3. Sketch of (a) plate and clamping frame, and (b) blast exposed area of the plates depicting the four pre-cut slit(s) geometries. Measures are in mm.

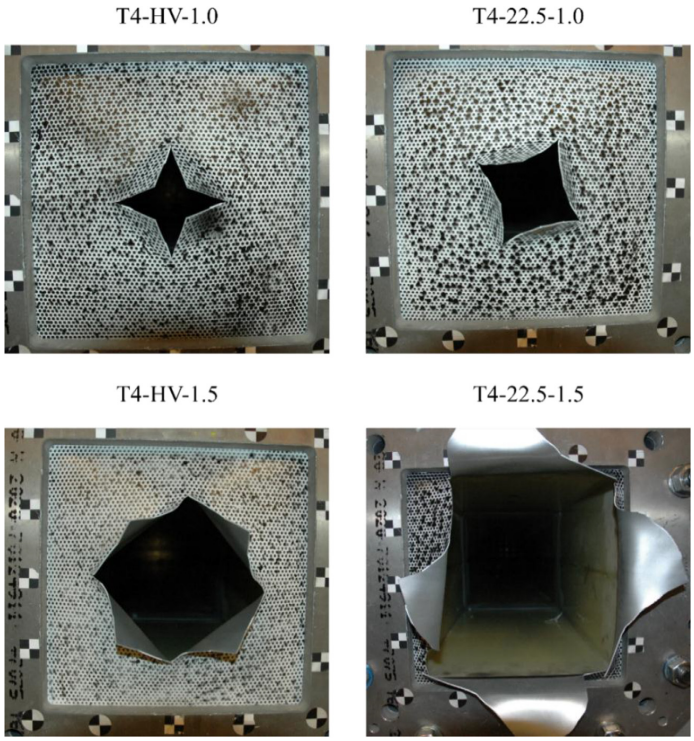

Fig. 4. Deformed state of plates in temper T4 with one slit after testing.

4. Experimental results

4.1. Effect of slit geometry

Fig. 4 shows the final deformed state of the plates in temper T4 with only one slit at the two firing pressures. By inspection it is evident that the plate with the slit rotated 22.5° experienced more fracture and crack propagation than the plate where the slit was oriented along the horizontal and vertical axes. The difference is less pronounced at the lowest firing pressure, where both slit configurations experienced minor crack propagation along the slit directions. However, for the highest firing pressure there is a clear difference, where the integrity of the plate is completely lost in the T4-22.5-1.5 test. The crack paths are curved and seemingly seeking towards the corners of the plate, resulting in complete failure of this plate. These crack paths are assumed affected both by the geometry and the boundary conditions of the plate. In the T4-HV-1.5 test, the cracks are seen to propagate along the slit directions in a similar way as for the lower firing pressure. However, compared to the T4-22.5-1.5 test the cracks are arrested before complete rupture is reached. In all tests, the slits in the pre-cut plates deform into petals, where flaps in the vicinity of the slits are folded and the pressure is partially vented through the resulting opening.

In Fig. 5, the deformed state of the plates with four slits is shown 1.5 ms after impact of the blast wave. Three of the four tests are close to complete rupture, while the last only experienced minor crack propagation. The effect of the orientation of the slits seems negligible at the highest firing pressure, considering that both plates experienced complete failure. However, there is a considerable difference at the lowest firing pressure. The failure patterns for the two T4-4-HV tests are similar, where the cracks propagated in the slit directions. The main differences between these two tests based on the observations in Fig. 5 are the slightly more extended cracks in the T4-4-HV-1.5 test and the out of plane displacement of the centre square of the plate. In both tests the failure pattern is the same, where the centre square of the plate is torn out and the remainder of the plate is folded around the clamping frame. In contrast, the two T4-4-45 tests exhibit differences between the two firing pressures. For the lowest firing pressure, only minor crack propagation and petal formation around the slits are observed, whereas for the highest firing pressure cracks propagate between the slits, resulting in the centre part of the plate being torn out, forming a cross. Cracks propagate from the slits oriented towards the corners of the plate all the way to the boundary, and the remainder of the plate is folded around the clamping frame. In the T4-4-45-1.0 test, both curved and straight crack paths are seen, and no symmetry or system of the crack paths was found. However, the T4-4-45-1.5 test exhibits an approximate doubly symmetric failure mode. From a blast protective view, the fragment from the ejected part of the plate in the T4-4-HV tests could be highly dangerous. In this respect, the slit geometry in the T4-4-45 tests is preferable.

Based on these results, it is difficult to conclude on what is most detrimental of increasing the number of slits or changing their orientation, as both these changes proved to have a distinct impact on the response. When the slits are oriented along the horizontal and vertical axes, the results suggest that increasing the number of slits is more detrimental and increases the amount of damage in the plate. However, changing the orientation of the slits is also observed to play an important role, independent of the number of slits.

The pressure-time histories measured by the sensor closest to the plate (Sensor 1) are plotted along with corresponding data from tests on a massive steel plate (from Aune et al. [20]) in Figs. 6 and 7 for a firing pressure of 1.0 MPa and 1.5 MPa, respectively. Sensor 1 is positioned 245 mm upstream the test specimen (Fig. 2), measuring both the

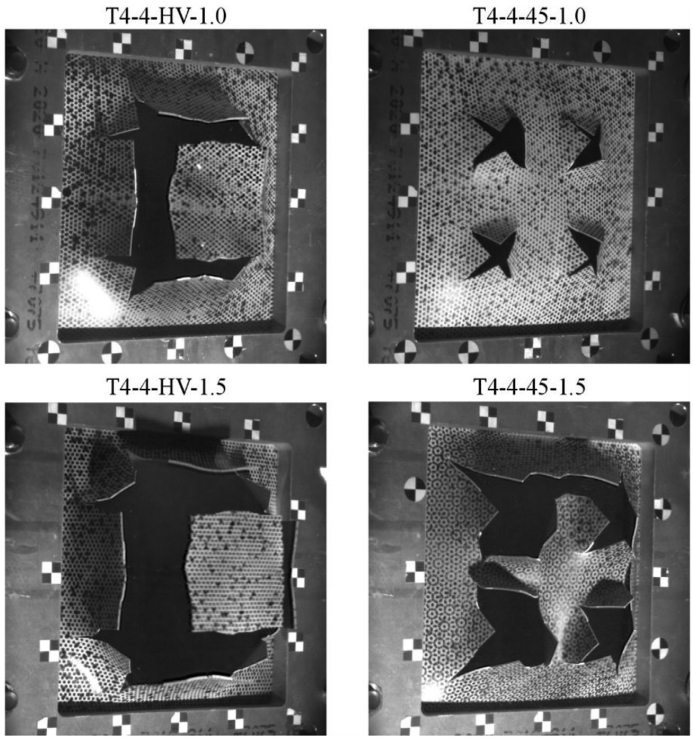

Fig. 5. Deformed state of plates in temper T4 with four slits at 1.5 ms after impact.

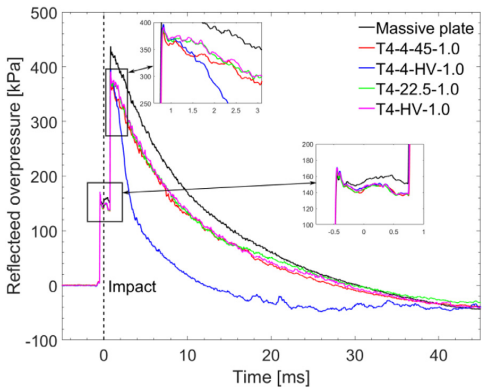

Fig. 6. Pressure-time histories from Sensor 1 for the tests of plates in temper T4 with firing pressure of 1.0 MPa compared with corresponding massive plate test from Aune et al. [20]. The dashed line indicates the time of impact by the blast wave on the plates.

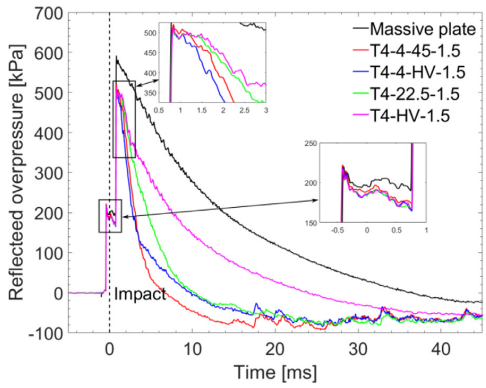

Fig. 7. Pressure-time histories from Sensor 1 for the tests of plates in temper T4 with firing pressure of 1.5 MPa compared with corresponding massive plate test from Aune et al. [20]. The dashed line indicates the time of impact by the blast wave on the plates.

incident and reflected shock waves. All data were filtered using a low-pass Butterworth filter of 2nd-order with a cut-off frequency of 0.05 s^{-1} to remove noise in the recordings without altering the characteristic shape of the pressure profiles. Note also that the pressure-time loading in these tests are in the dynamic regime, indicating that the peak pressure is the critical load parameter. As illustrated in the subplots in the figures, the incident waves are nearly identical at similar firing pressures, proving the repeatability of the test setup. The peak reflected pressures are also similar. However, the pressure is in general higher for the massive plate tests compared to the others due to FSI effects. This was also observed by Aune et al. [5] for steel plates with pre-cut holes. As expected, the reflected pressures vary among the different geometries, which is related to the varying structural response of the plates and FSI effects. For a firing pressure of 1.0 MPa, the T4-4-HV-1.0 test stands out as the reflected pressure drops significantly compared to the other tests, which show a similar decay of the pressure over time. This is related to complete failure of the plate in the T4-4-HV-1.0 test, where the pressure build-up in front of the plate is fully vented into the dump

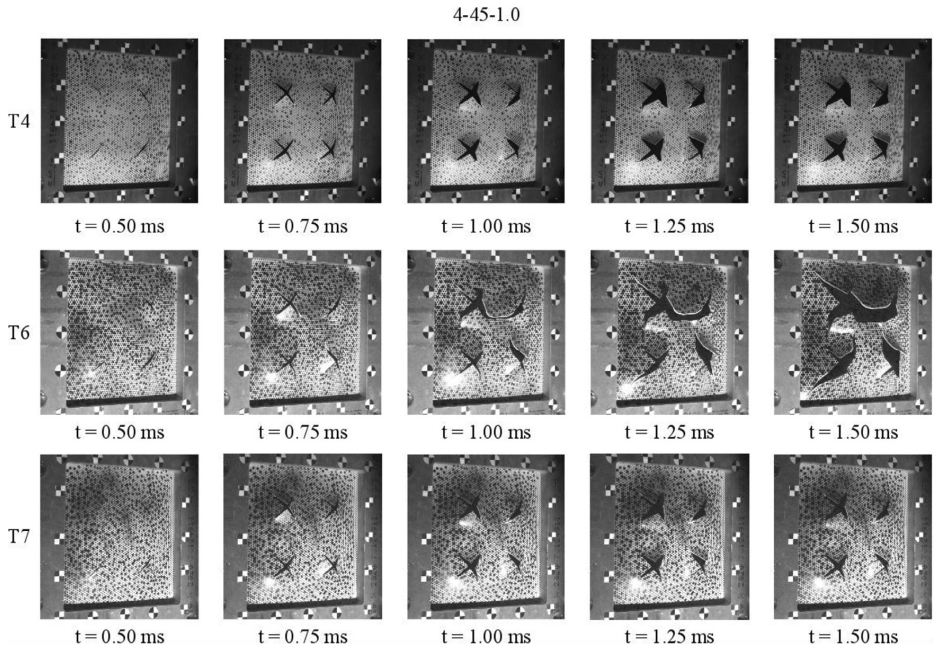

Fig. 8. Image series from the 4-45-1.0 tests at selected points in time.

tank. For the remaining three tests, it is seen that the pressure-time curves are shifted compared to the massive plate test, indicating that even though an opening in the plate is created by folding of the flaps, most of the pressure is reflected from the remaining surface of the plate. In the T4-4-HV-1.0 test, the pressure goes below atmospheric pressure at around $t = 0.10$ ms due to rarefaction waves, resulting in a suction in the opposite direction. Among the tests at a firing pressure of 1.5 MPa, the T4-HV-1.5 test stands out as the shape of the curve is comparable to the massive plate test, only shifted (Fig. 7). This means that the plate appears to behave similarly as a plate without pre-cut holes and most of the pressure is reflected, even though a substantial part of the original surface is gone. This test is the only one where the cracks did not propagate all the way to the boundary, which apparently is vital for the pressure to be ventilated into the dump tank.

4.2. Effect of temper

Image series from tests on plates with different tempers are shown in Figs. 8–11 at selected points in time. In general, the plates in tempers T4 and T7 showed similar behaviour in the four different cases. These tempers are closer in strength and ductility compared with the T6 temper that has higher strength and lower ductility, as will be shown in Section 5.2.

The slit geometry demonstrating the largest difference between the tempers is found in tests 4-45-1.0 (Fig. 8), where only the plate in temper T6 experiences complete failure. The deformation is similar up to $t = 0.75$ ms, but then an incipient crack in the horizontal direction between the two upper slits is seen for the T6 temper, which is not present in tests involving the other tempers. As the horizontal crack merges the upper pair of slits, the centre part of the plate is torn out and cracks propagate towards the corners of the plate. The plates in tempers T4 and T7 exhibit a petal deformation around the slits towards the end of the tests, but no prominent crack propagation is observed.

In the 4-45-1.5 (Fig. 9), 22.5–1.0 (Fig. 10) and 22.5–1.5 (Fig. 11) tests, all three tempers gave similar global response, but there are differences in terms of crack propagation between them. In the 4-45-1.5 tests (Fig. 9), the failure mode is similar among the tests and all plates experience complete failure. Based on the high-speed camera images, cracks initiate in all tests at $t = 0.5$ ms after impact by the blast wave. At $t = 0.75$ ms (not shown for brevity), two propagating cracks have merged for the plate in temper T6 between the two upper slits, while the plates tested in tempers T4 and T7 mostly experience petal formation around the slits. Even at $t = 1.00$ ms, no cracks have propagated enough to merge for the plates in tempers T4 and T7, while for the plate in temper T6 another pair of propagating cracks have merged between the slits on the right-hand side. The same trend is also observed for the cracks propagating along the diagonal towards the corners of the plate, where it is clearly seen that the cracks in the plate in temper T6 are longer than in the plates in tempers T4 and T7 at this point in time. At $t = 1.25$ ms after impact of the blast wave, the plates in all three tempers have at least one pair of merged cracks and the centre cross is close to being torn out. The differences between the three tempers are less pronounced at this point in time, except for the cracks propagating along the diagonals toward the corners of the plate. The plates in tempers T4 and T7 seem to be more resistant against fracture, even though at $t = 2.00$ ms the response is nearly identical between the tests.

Some of the trends observed for the 4-45-1.5 tests are also seen in the 22.5-1.0 tests (Fig. 10). Based on the high-speed camera images, cracks have initiated at $t \approx 0.60$ ms after impact by the blast wave in all tests. In the T6-22.5-1.0 test, the plate was mistakenly mounted so that the slit was oriented in a positive angle as opposed to the other tests with this geometry. This might have altered the results slightly and the results are therefore not emphasized as much with respect to the observed trends. However, by assuming an isotropic material, this implies loading the plate from the opposite side compared to the negative slit orientation. This geometry gave the least difference in response among the tests in this part of the study. The cracks are observed to propagate equally for all tempers at the selected points in time and the final deformation is similar from an overall point of view. Also in the 22.5-1.5 tests (Fig. 11) the crack propagation is initiated at $t \approx 0.60$ ms for all

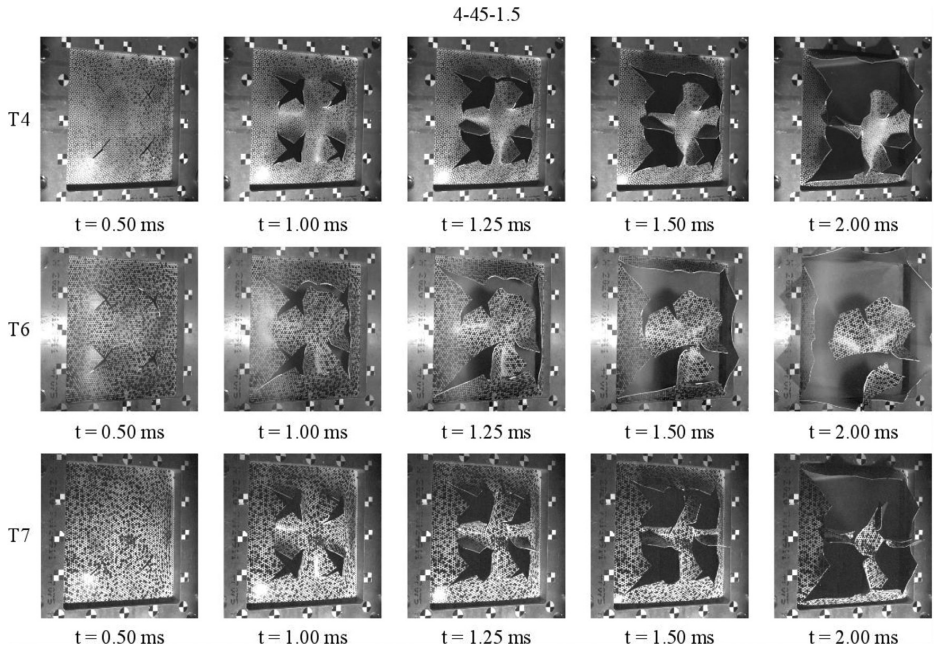

Fig. 9. Image series from the 4-45-1.5 tests at selected points in time.

tempers, but already at $t = 1.00$ ms the cracks are considerably longer in the plate in temper T6 than in the plates in tempers T4 and T7. This difference increases towards the end of the tests, suggesting that the speed of the propagating cracks is higher for the plate in temper T6 than for the plates in tempers T4 and T7. By inspection of the high-speed camera images, a difference in the crack propagation between the plates in tempers T4 and T7 is observed, where the speed of the propagating cracks is slightly lower in the former. The main reason for this is believed to be the high work-hardening capacity of AA6016 in temper T4 (see Fig. 1).

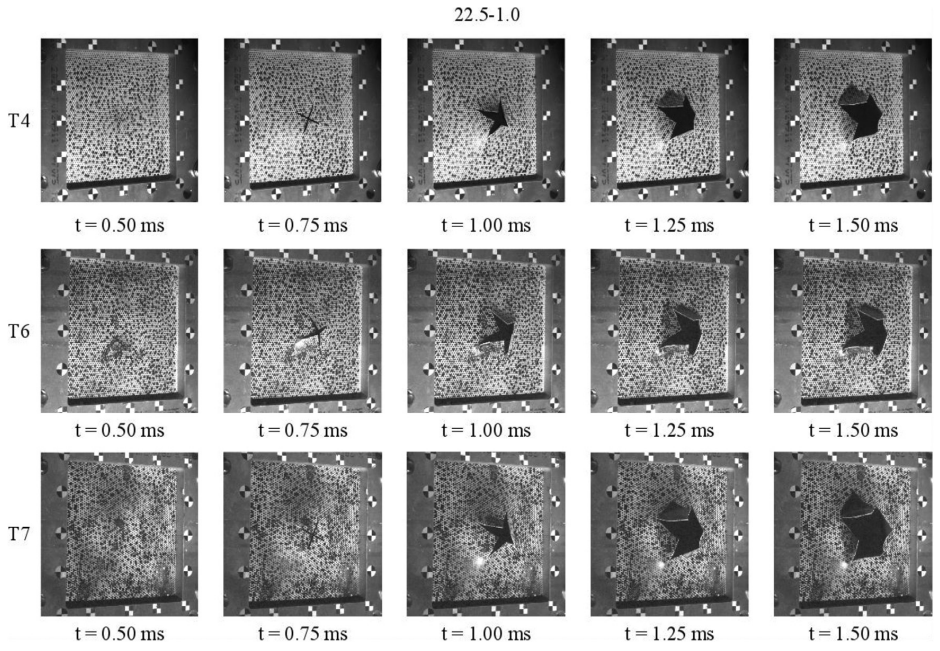

Fig. 10. Image series from the 22.5-1.0 tests at selected points in time.

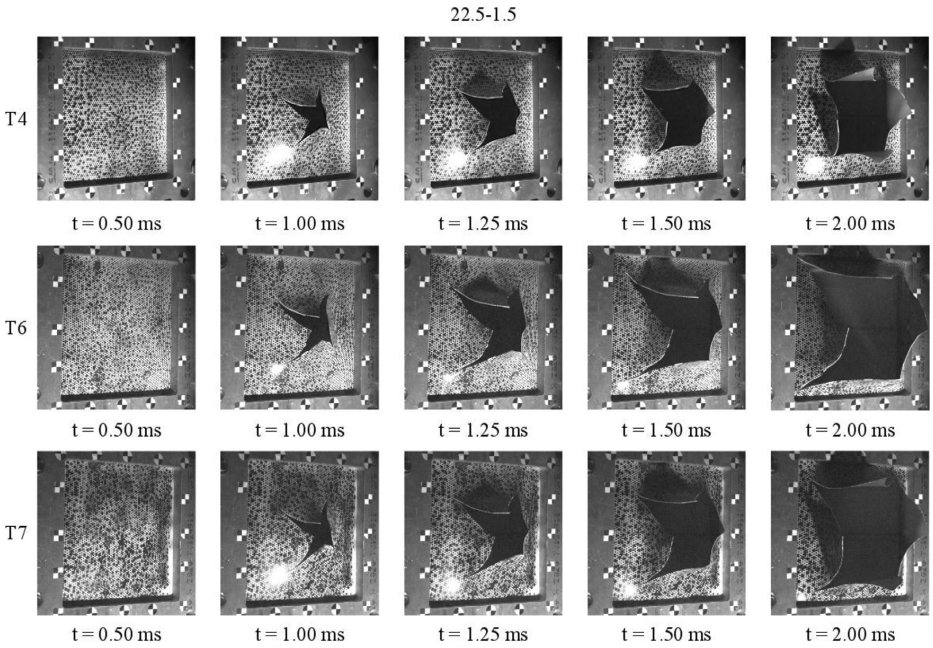

Fig. 11. Image series from the 22.5-1.5 tests at selected points in time.

In all tests experiencing fracture, a slant fracture surface was observed, making a 45° angle with the thickness direction of the plate. In some tests, the alternating slant fracture phenomenon was observed, where the slanted crack irregularly alternated between the two possible shear bands forming in front of the crack tip [8].

4.3. 3D-scan and 3D-DIC

A ROMER Absolute Arm 7252SI, consisting of a probe and a laser scanner, was used to scan the plates not experiencing complete failure during testing. The probe was used to define the coordinate axes, while the laser was used to scan the plates. The data were processed by the software PC-DMIS and exported as point clouds and stereo-lithographic files. In Fig. 12, 3D-scans of the three 22.5-1.0 tests are compared to each other in terms of front and side images as well as contour plots of the displacement fields. Despite the incorrect orientation of the slit in the T6-22.5-1.0 test, the results can still be compared to the other test results. By inspection of the images, one can see that the shape of the opening differs between the tests. For the plate in temper T7, the opening resembles a square, while for the plates in the two other tempers the flaps have not folded as much, and the opening has more of a star shape. In the plate in temper T6, the crack paths are more curved than in the plates in tempers T4 and T7, where the crack paths are in the directions of the slits. The length of the cracks was measured, revealing that the plate in temper T6 has the longest crack paths with an average length of 48.5 mm, while the plates in tempers T7 and T4 have average crack lengths of 41.8 mm and 39.5 mm, respectively. When seen from the side, the plates in tempers T4 and T7 clearly experienced more global deformation than the plate in temper T6, where the deformation is mainly localized near the slits. This is substantiated by the contour plots of the deformation fields. For better comparison, the range of the colour bar is the same for all the contour plots, and displacements beyond 20 mm have the same colour; hence the large areas in dark red.

Fig. 13 displays the 3D-scans of the plates from the T4-HV-1.0, T4-22.5-1.0 and T4-HV-1.5 tests. The same global response is observed for the T4-HV-1.0 and T4-22.5-1.0 tests, namely a nearly linear increase in deformation from the boundary towards the centre of the plate. The plate in the T4-22.5-1.0 test folded more around the slits than the plate in the T4-HV-1.0 test, where the opening at the centre of the plate is more prominent. This is substantiated by the average length of the crack paths, which was 39.5 mm for the plate in test T4-22.5-1.0 and 26.3 mm for the plate in test T4-HV-1.0. The effect of increasing the firing pressure is evident for the T4-HV tests, in which a larger opening and an increased global deformation of the plate are seen for the highest firing pressure. The average crack length is 73 mm for the plate in test T4-HV-1.5, i.e., almost three times longer than for the plate in test T4-HV-1.0.

Displacement profiles across the centre of the plate were obtained using 3D-DIC in the tests which did not rupture completely, i.e., tests T4-4-45-1.0 and T7-4-45-1.0. The results are plotted in Fig. 14 at selected points in time. From the figure it is seen that the displacement is initiated at the boundary and moves towards the centre of the plate. The displacement is consistently larger for the plate in temper T4 than for the plate in temper T7, and this difference increases throughout the test. At the end of the tests, the difference in mid-point deflection is above 7 mm, resulting in a relative percentage difference of 27.3%. The same observation is made from the 3D-scan of the same plates, shown in Fig. 15, where the difference in global deformation between the plates is evident. By inspection of the contour plots, one can see that the flaps next to the slits pointing towards the centre of the plate are more deformed than the others. This is also to some extent observed in the side image of the plates. The average crack lengths are 14.3 mm for the plate in temper T4 and 10.4 mm for the plate in temper T7. However, the difference in length between the longest and the shortest crack within a plate is substantial for these two plates, i.e., 16 mm and 13 mm for the plates in tempers T4 and T7, respectively. This is related to the varying deformation of the flaps, where the cracks propagating from the slits pointing towards the centre of the plate are consistently longer than the other cracks.

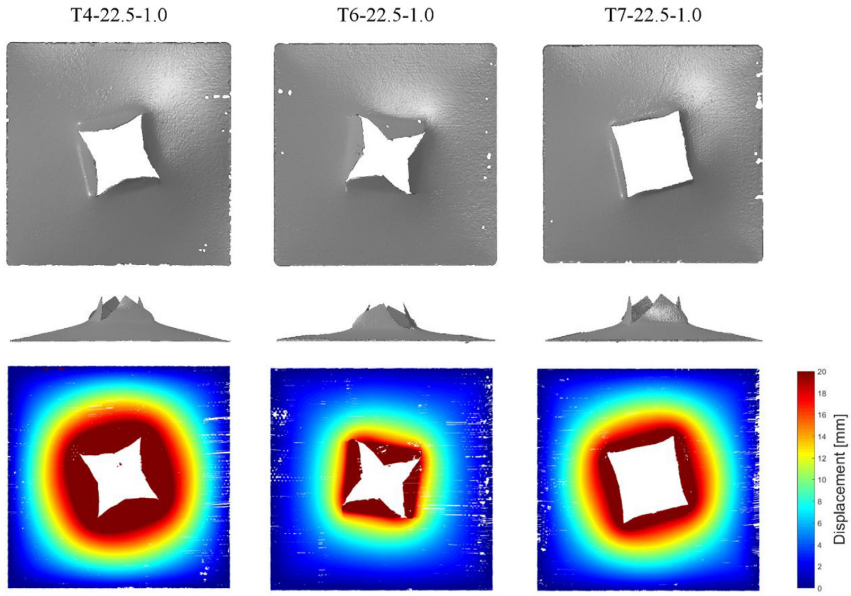

Fig. 12. 3D-scans of the deformed plates from the 22.5-1.0 tests: front image (top), side image (middle) and displacement field (bottom).

5. Finite element model

5.1. Material description

The material behaviour is described by a modified version of the Johnson-Cook constitutive model [22], where plasticity is defined by the von Mises yield criterion, the associated flow rule, and a constitutive relation in the plastic domain given as [23]

$$\sigma_{eq} = (\sigma_0 + R(p))(1 + \dot{p}^*)^c(1 - T^{*m}) \quad (1)$$

where σ_{eq} is the von Mises equivalent stress, σ_0 is the yield stress, R is the hardening variable, p is the von Mises equivalent plastic strain, $\dot{p}^* = \dot{p}/\dot{p}_0$ is a dimensionless plastic strain rate, and $\dot{p}_0$ is a user-defined reference strain rate. The homologous temperature is given as

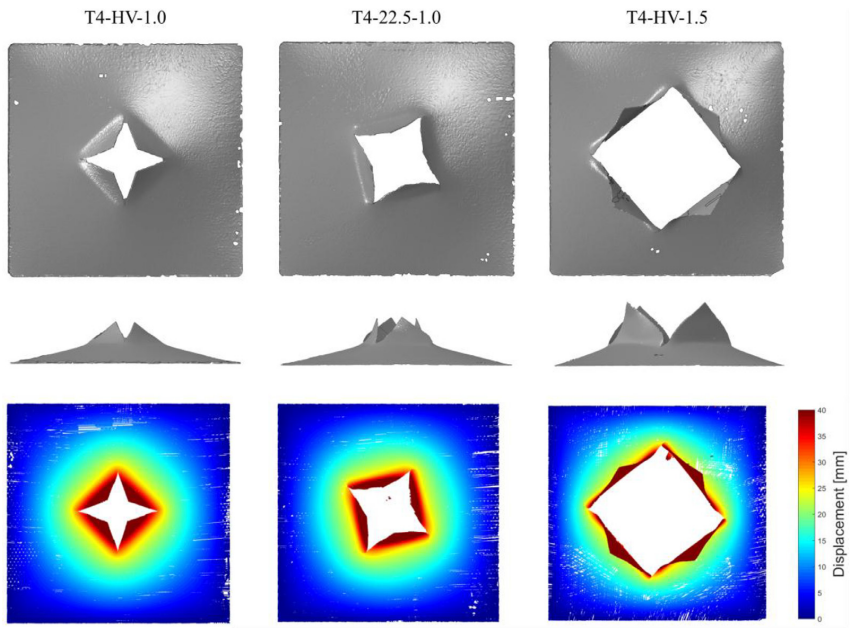

Fig. 13. 3D-scans of deformed plates in temper T4: front image (top), side image (middle) and displacement field (bottom).

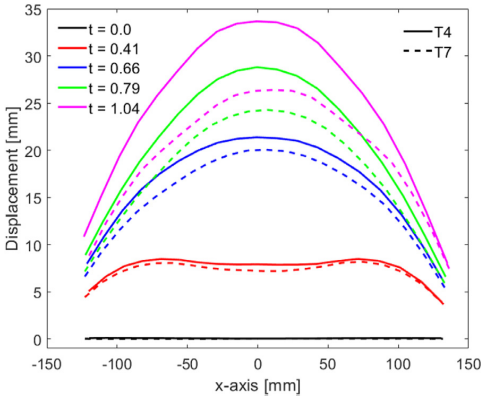

Fig. 14. Displacement profiles from the 4-45-1.0 tests on plates in tempers T4 and T7 at selected points in time. The times are given in ms.

$T^* = (T - T_r)/(T_m - T_r)$, where T is the temperature, T_r is the ambient temperature and T_m is the melting temperature of the material. The model parameters c and m govern the rate sensitivity and thermal softening of the material, respectively. The hardening variable is defined by an extended Voce hardening rule on the form

$$R(p) = \sum_{i=1}^{3} R_i(p) = \sum_{i=1}^{3} Q_i(1 - \exp(-C_i p)) \tag{2}$$

where R_i are hardening terms that saturate at different levels of plastic strain. The hardening parameters Q_i and C_i represent the saturation value and the rate of saturation of the hardening term R_i, i.e., a high value of C_i implies that the maximum value Q_i is reached at a low strain level and vice versa. It is assumed here that $C_1 \geq C_2 \geq C_3$, so that the R_1 saturates at the lowest strain level, R_2 at an intermediate strain level, and R_3 at a high strain level. The change in temperature due to adiabatic heating is calculated as

$$\dot{T} = \frac{\chi}{\rho c_p}\sigma_{eq}\dot{p} \tag{3}$$

where ρ is the density, c_p is the specific heat and χ is the Taylor–Quinney coefficient.

Ductile fracture is modelled by the uncoupled damage evolution rule proposed by Cockcroft and Latham [24], which reads

$$D = \frac{1}{W_c}\int_0^p \sigma_I \, \mathrm{dp} = \frac{1}{W_c}\int_0^p \left\langle \sigma^* + \frac{3 - L}{3\sqrt{3 + L^2}} \right\rangle \sigma_{eq} \, \mathrm{dp} \leq 1 \tag{4}$$

where D is the damage variable, W_c is the fracture parameter, σ_I is the major principal stress and $\langle \cdot \rangle$ are the Macaulay brackets: $x = \max(x, 0)$. According to the Cockcroft–Latham criterion, damage evolves for tensile stresses and is driven by the plastic work amplified by a factor depending on the stress state. Fracture occurs when D reaches unity. In the definition of the damage variable, the major principal stress σ_I has been expressed in terms of the von Mises equivalent stress σ_{eq}, the stress triaxiality σ^* and the Lode parameter L, where the latter two stress invariants are defined by

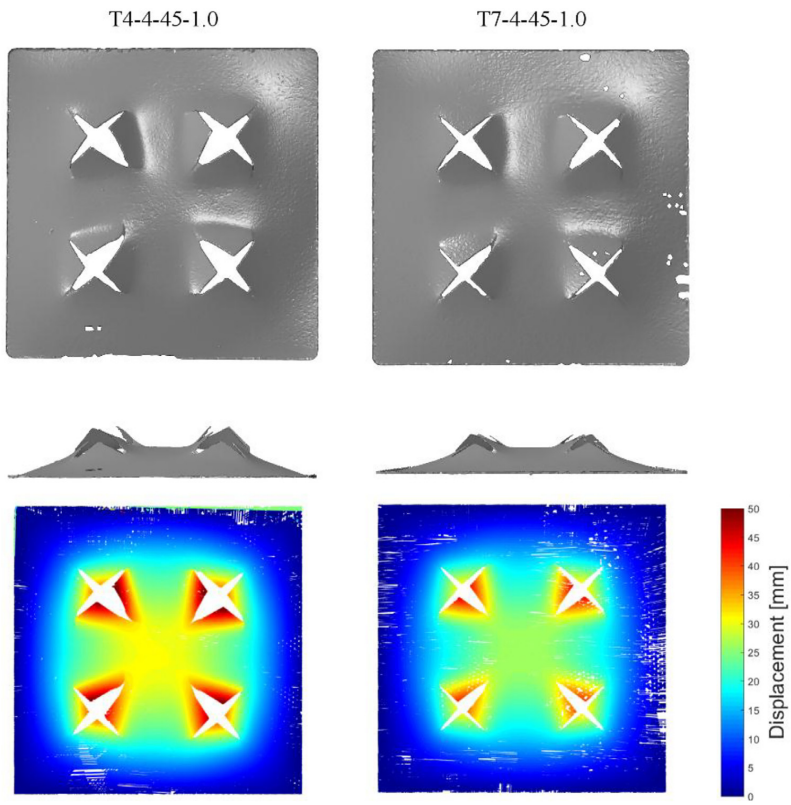

Fig. 15. 3D-scans of deformed plates in temper T4 and T7 from the 4-45-1.0 tests: front image (top), side image (middle) and displacement field (bottom).

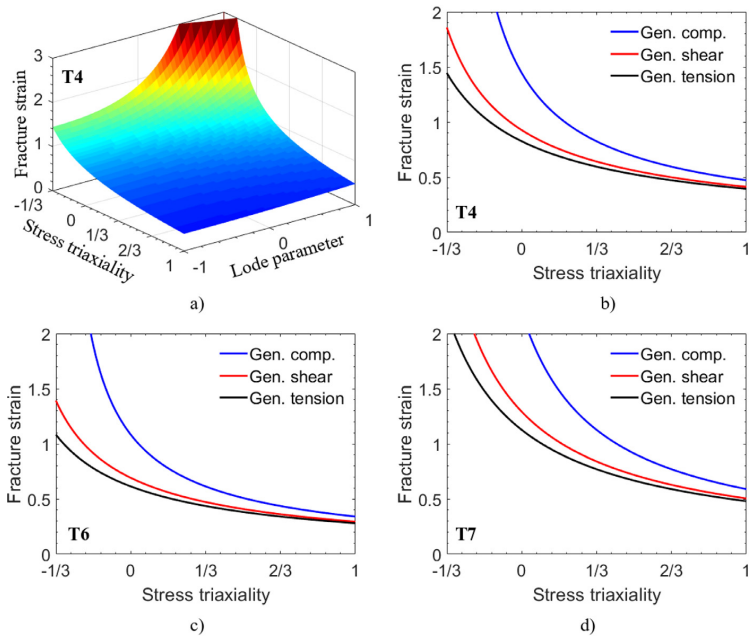

Fig. 16. a) Fracture surface $p_f = p_f(\sigma^*, L)$ of the Cockcroft–Latham failure criterion as a function of the stress state in terms of stress triaxiality, σ^*, and Lode parameter, L, for temper T4 and b) - d) fracture loci $p_f = p_f(\sigma^*)$ at selected values of the Lode parameter: generalized tension, $L = +1$, generalized shear, $L = 0$, and generalized tension, $L = -1$ for tempers T4, T6 and T7, respectively.

$$\sigma^* = \frac{\sigma_H}{\sigma_{eq}}, \quad L = \frac{2\sigma_{II} - \sigma_I - \sigma_{III}}{\sigma_I - \sigma_{III}} \tag{5}$$

In Eq. (5), $\sigma_I \geq \sigma_{II} \geq \sigma_{III}$ are the ordered principal stresses and $\sigma_H = (\sigma_I + \sigma_{II} + \sigma_{III})/3$ is the hydrostatic stress.

Assuming constant values of the stress triaxiality σ^* and the Lode parameter L, quasi-static loading conditions ($\dot{p} \ll \dot{p}_0$) and ambient temperature ($T = T_r$), a fracture surface $p_f = p_f(\sigma^*, L)$ can be computed based on the damage evolution rule in Eq. (4). The fracture surface is plotted in Fig. 16(a), while Fig. 16(b-d) shows fracture loci $p_f = p_f(\sigma^*)$ for three values of the Lode parameter for the three tempers. The plotted fracture surface is based on the calibrated parameters for AA6016 in temper T4, which will be discussed in the next section. The topology of the fracture surface shows that for a given stress triaxiality σ^*, the highest and lowest values of the fracture strain p_f are obtained for generalized compression ($L = +1$) and generalized tension ($L = -1$), respectively, with generalized shear ($L = 0$) giving intermediate values. It is further seen that for a constant value of the Lode parameter L, the fracture strain p_f decreases monotonically with increasing stress triaxiality. Finally, we note that as W_c is here taken to be constant, the fracture strain p_f increases for increasing temperature (lower stress level) and decreases for increasing strain rate (higher stress level) according to the damage evolution rule in Eq. (4) combined with the modified Johnson-Cook plasticity model in Eqs. (1)–(3).

5.2. Calibration of model parameters

First, an initial estimate of the parameters (Q_1, C_1) and (Q_2, C_2) of the two first terms R_1 and R_2 of the hardening variable R was obtained for the three tempers in a spreadsheet based on a least square curve fit to the experimental flow stress curves (see Fig. 17) up to necking. Only a representative test in the rolling direction was used in the calibration, and the parameters (Q_3, C_3) of the third hardening term R_3 were set to zero. Second, an FE model of the dog-bone specimen used in the tensile

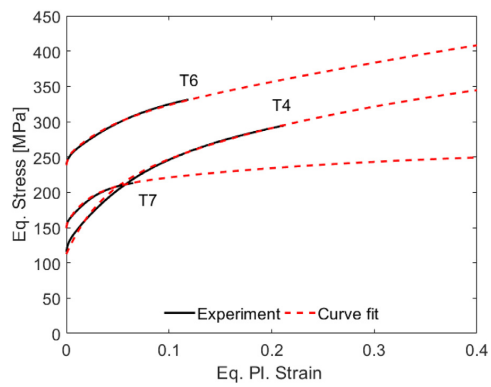

Fig. 17. Experimental and calibrated flow stress curves in terms of the equivalent stress σ_{eq} and the equivalent plastic strain p based on the uniaxial tensile tests up to necking.

tests was made in Abaqus/Standard. Symmetry was exploited so that only one quarter of the specimen was modelled to save computational time. The mesh consisted of 8-node trilinear bricks with reduced integration and hourglass control. The size of the elements in the gauge region was 0.1875 mm, giving eight elements over the thickness. Calibration of the hardening parameters was done by the optimization tool LS-OPT [25], where sequential simulations on the same model were run with different choices of the hardening parameters. The parameters obtained from the initial curve fit up to necking were used as starting values. In the optimization process, the parameters (Q_1, C_1) of the first term R_1 were fixed, while the parameters (Q_2, C_2) and (Q_3, C_3) of the two remaining terms R_2 and R_3 were allowed to change. The measured

Table 4
Model parameters for the AA6016 plates in the three tempers.

Temper	σ_0 (MPa)	Q_1 (MPa)	C_1	Q_2 (MPa)	C_2	Q_3 (MPa)	C_3	W_c (MPa)
T4	112.46	78.64	32.80	109.80	4.94	325.69	0.50	181.82
T6	238.25	11.18	539.62	46.32	24.71	398.37	0.83	155.05
T7	149.20	5.89	1989.17	47.32	48.47	60.36	3.73	186.08

Table 5
Material constants for aluminium alloys taken from the literature.

E (GPa)	ν	ρ (kg/m^3)	$\dot{p}_0$ (s^{-1})	c	T_r (K)	T_m (K)	m	c_p (J/kgK)	χ
70	0.3	2700	5×10^{-4}	0.001	293	923	1.0	910	0.9

Table 6
Parameters of the Friedlander equation determined from the pressure measurements from massive plate tests [20].

Test	$P_{r,\ max}$ [kPa]	t_{d+} [ms]	b
M-1.0	446.2	35.4	1.571
M-1.5	606.6	44.1	2.025

engineering stress-strain curves to fracture were used as target curves in the optimization (Fig. 1(b)). A genetic algorithm in LS-OPT was applied in the optimization, where 100 equidistant regression points were used in the calculation of the mean square error to ensure a good fit in all parts of the engineering stress-strain curve. The hardening parameters were found by minimizing the mean square error and are given in Table 4. The experimental and calibrated flow stress curves up to necking are plotted in Fig. 17, whereas Fig. 1(b) shows the experimental and simulated engineering stress-strain curves for the three tempers. Good agreement is also found in the post-necking part of the engineering stress-strain curve, which indicates that the extrapolation of the flow stress curve beyond necking shown in Fig. 17 is sufficiently accurate.

The Cockcroft–Latham failure criterion was also calibrated based on numerical simulations of the tensile tests. The FE model was identical to the one used in the calibration of the extended Voce hardening rule, except for the characteristic element size that was increased to 0.5 mm, coinciding with the mesh size used in the subsequent blast simulations. The equivalent plastic strain p was extracted from the element exposed to the largest plastic strain in the simulations. This element was in the through-thickness centre of the specimen, which was also the element that exhibited the highest value of the damage variable D. The fracture strain p_f was determined based on the measured force–displacement curves, where the point of fracture was set to match the anticipated point of fracture from the experimental curve, as visualized in Fig. 1(b). The fracture parameter W_c was calculated based on the stress and plastic strain history in the critical element as

$$W_c = \int_0^{p_f} \sigma_1 \, \mathrm{d}p \tag{6}$$

The resulting values of the fracture parameter W_c are compiled in Table 4 for all three tempers, showing that tempers T4 and T7 have significantly better ductility than temper T6, which has the highest strength. The slight deviation in elongation to fracture between the three repeat tests indicates some uncertainty in the calibrated value of W_c, which could affect the numerical results obtained in the simulations of the blast tests. The fracture strain p_f obtained in the simulation of the tension test was 0.59, 0.44 and 0.77 for tempers T4, T6 and T7, respectively, which quantifies the difference in ductility between the three materials.

The strain-rate sensitivity of AA6016 was not examined in this study, but the rate sensitivity of 6xxx aluminium alloys has been extensively studied in the literature. The degree of strain-rate sensitivity has been reported to increase for decreasing material strength or for increasing purity [26]. Chen et al. [27] studied the strain rate sensitivity of extruded AA6082 and AA6060 in temper T6 at strain rates up to 1000 s^{-1}. Calibration of the strain rate parameter c resulted in values of 0.0015 and 0.0038 for the two alloys, respectively, which implies that the strain rate sensitivity is practically negligible. Vilamosa et al. [28] studied three 6xxx alloys at various strain rates and temperatures. A low strain-rate sensitivity was reported for the tested alloys at room temperature, substantiating the findings in [27]. Based on these findings, the strain-rate parameter c was set to 0.001 in all simulations in this study. The reference strain rate was set to $\dot{p}_0 = 5 \times 10^{-4}$ s^{-1}, coinciding with the initial strain rate in the uniaxial tensile tests. The parameter controlling the thermal softening m was set to 1, indicating a linear reduction in strength with increasing temperature. The effect of including adiabatic heating was investigated by also running simulations assuming isothermal conditions, and the effect was found to be minor in this particular study. All material parameters used in the simulations are presented in Tables 4 and 5, where the parameters not calibrated from the tensile tests are taken from the literature as standard values for aluminium.

5.3. Simulation procedures

The FE simulations of the plates subjected to blast loading were

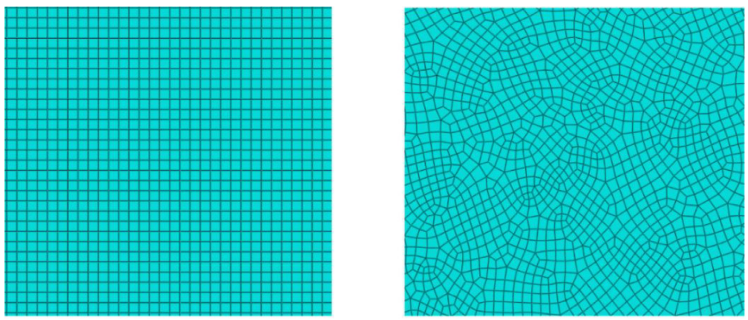

Fig. 18. A segment of a structured mesh (left) and a random mesh (right) used in the numerical simulations.

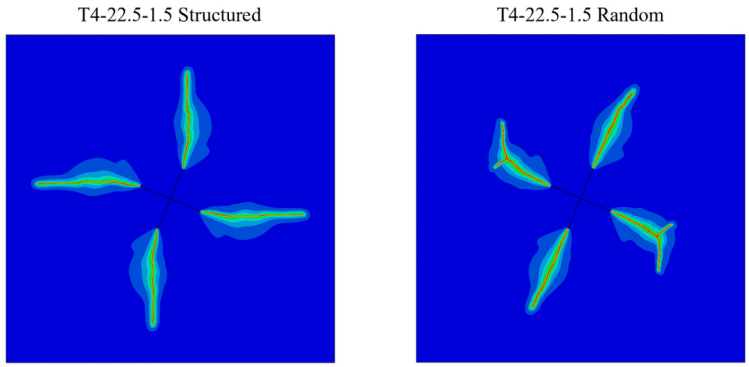

Fig. 19. Damage evolution in simulation of test T4-22.5-1.5 with a structured mesh (left) and a random mesh (right).

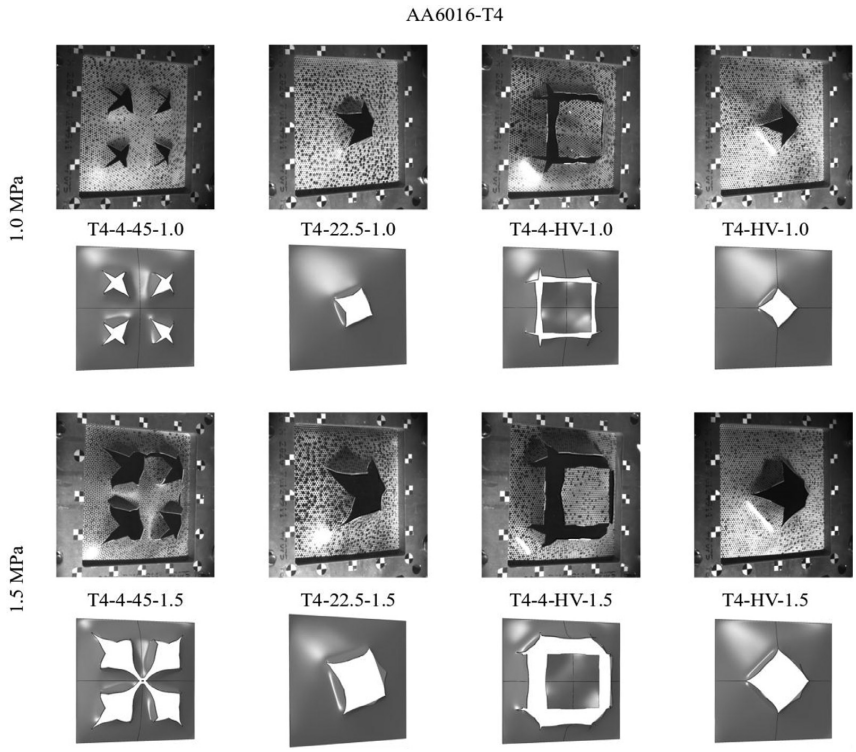

Fig. 20. Comparison between experiments and simulations of plates in temper T4. All images are taken 1.25 ms after impact by the blast wave.

conducted using Abaqus/Explicit. A user-defined subroutine (VUMAT) was employed to include the modified Johnson-Cook constitutive relation and the Cockcroft–Latham failure criterion in the solver. To save computational time and keep the complexity of the model reasonable, only the blast loaded area of the plate was modelled. The outer boundary of the plate was fixed against displacements to mimic the effect of the clamping plates. The simulations were run with 8-node brick elements with reduced integration and hourglass control. A random generated sweep mesh and a structured mesh, both with a characteristic element length of 0.5 mm, were used in the simulations, resulting in three elements over the plate thickness. Two-fold in-plane symmetry was utilized when the initial geometry of the plate allowed for it. The quarter model consisted of about 270 000 elements, while the full model involved roughly 1 000 000 elements. The slits were modelled star-shaped, where each end-point of the slits was modelled with a single node. The width of the slit then increased towards the centre to 0.1 mm. This modelling option has the advantage of making the meshing of the plate more feasible as well as avoiding bad aspect ratios and distortions of elements near the slits. Contact was omitted as only the blast exposed area was modelled and self-contact only occurred at the very last part of the deformation process in some few simulations.

The blast load was applied as a tabulated pressure, where the pressure-time histories were taken from massive plate tests, having

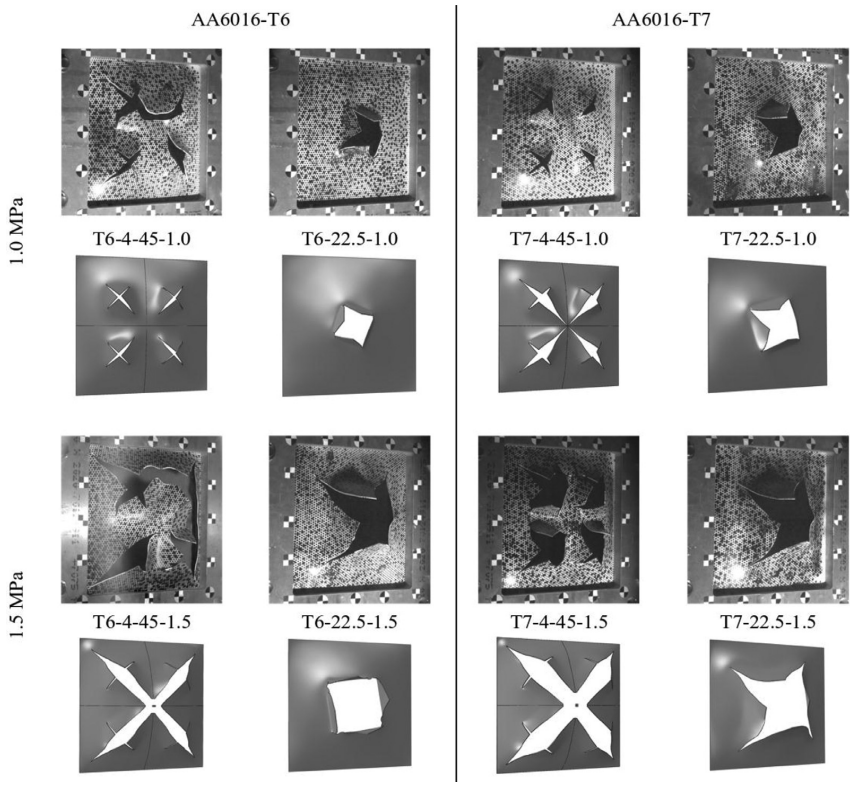

Fig. 21. Comparison between experiments and simulations of plates in tempers T6 and T7. All images are taken 1.25 ms after impact by the blast wave.

pressure sensors mounted directly on the plate [20]. These pressure-time histories were used to determine the parameters of the modified Friedlander equation, given as

$$P_r(t) = P_{r,max}\left(1 - \frac{t - t_a}{t_{d+}}\right)\exp\left(\frac{-b(t - t_a)}{t_{d+}}\right),\ t_a \le t \le t_{d+} \tag{7}$$

where $P_{r,\ max}$ is the peak reflected overpressure, t_a is the time of arrival of the blast wave at the plate, t_{d+} is the duration of the positive phase, and b is the exponential decay coefficient. The parameters of the Friedlander equation were obtained by Aune et al. [20] and are given in Table 6. Fracture of the plate was modelled by element erosion, and elements were removed from the mesh when the damage variable D in the integration point reached unity.

6. Numerical results

6.1. Parameter study

An initial mesh sensitivity study was conducted to ensure that the discretization of the plate was sufficient. The number of elements over the thickness was varied from three to six, using an element aspect ratio close to unity. Three elements over the thickness proved to give sufficient accuracy at an acceptable computational cost and was used in the rest of the study. However, analyses with a refined mesh were run in cases where the initial model struggled to replicate the experiment, to investigate if this resolved the discrepancies.

Additionally, the design of the element mesh was investigated, where both a structured and a randomly generated mesh were applied. The difference between the two meshes with a characteristic element size of 0.5 mm is depicted in Fig. 18. Since element erosion is used to describe fracture in the plates, the design of the mesh plays a significant role in determining the crack path. In simulations with a structured mesh, it was evident that the propagating cracks were aligned with the mesh. This proved to be especially important when the slits were not aligned with the mesh, resulting in a higher resistance against crack propagation than when the slits were aligned. Fig. 19 shows how the mesh designs in Fig. 18 affect the damage evolution and crack propagation in the plate when plotted on the undeformed geometry. Here, a red colour indicates a failed element. Overall, it was found that the desired crack path could to some extent be achieved by altering the mesh. The best way to minimize this effect of element erosion is to refine the mesh sufficiently, but this is not feasible as the computational cost becomes too high. Thus, in an attempt to avoid the mesh design effect and to ensure trustworthy results, a randomly generated mesh was used in this study.

6.2. Blast simulation results

A comparison between experiments and simulations for plates in temper T4 is shown in Fig. 20. All images are taken 1.25 ms after impact by the blast wave. By inspecting the figure, it is evident that the numerical model is able to replicate most of the tests with reasonable accuracy. However, if studied in detail, some discrepancies are found. The simulation of test T4-4-45-1.5 deviates the most from the experiment, where the failure mode is incorrectly predicted. The mesh dependence was investigated by running a simulation where the mesh was refined to six elements over the thickness, resulting in a characteristic element size of 0.25 mm and almost 2.7 million elements. However, the

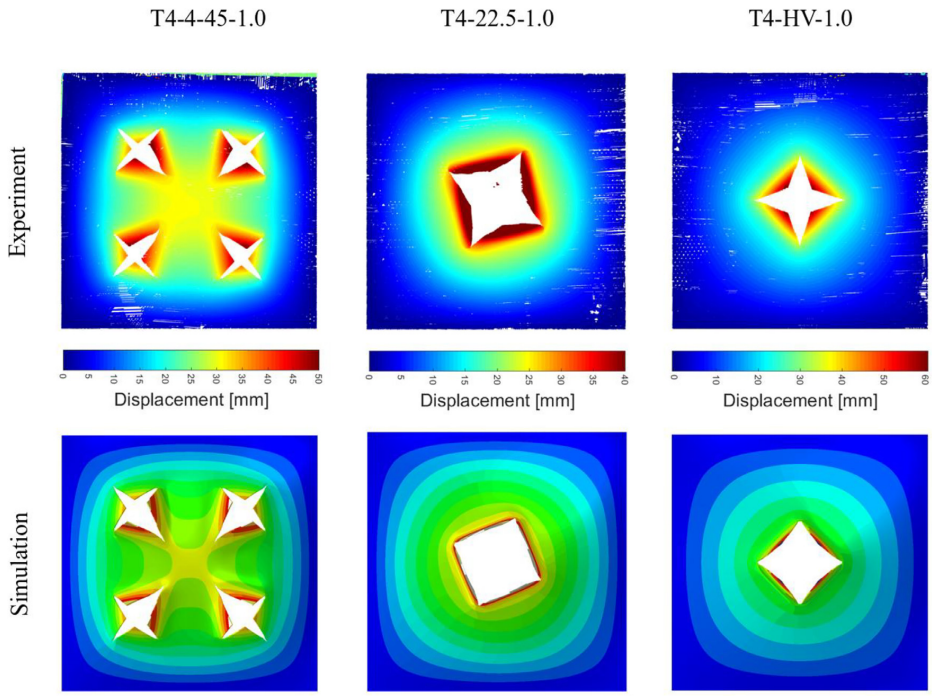

Fig. 22. Contour plots of the displacement field from available experiments and simulations of plates in temper T4.

same failure mode was predicted as in the coarser mesh, and only marginal differences were observed between the two simulations. In the Lagrangian FE simulations applied here, the pressure from the blast wave was applied perpendicularly to the front surface of the plate, independent of its displacement, which implies that the pressure loading is overestimated as the plate fails and undergoes large displacements. In the experiments, the pressure is vented into the dump tank when the plate fails and the resultant pressure load on the plate is reduced. In simulations with the highest firing pressure, this artificial overloading is the main source of error, as it accumulates error as the plate deforms. This is especially evident in the last frames of the simulations, where the flaps have folded considerably more than in the experiment. If a flap is sufficiently deformed, one may end up in a situation where the load is acting in the opposite direction of the initial blast load. To enable more accurate prediction of the final shape of the plates, one possibility is to perform fully coupled FSI simulations. Another approach could be to manipulate the pressure load to only account for the component in the initial blast load direction.

Fig. 21 compares the deformed configurations of the plates in tempers T6 and T7 obtained in the experiments and simulations for firing pressures of 1.0 and 1.5 MPa. The simulation of test T6-4-45-1.0 was not able to predict the failure mode that occurred in the experiment, and only minor cracking was seen in the simulation. The cracks in the simulation propagated in the directions of the diagonals, similar to what was observed in the simulation of test T4-4-45-1.0. Cracks initiated at the same point in time in both the simulation and experiment, but already at $t = 1.00$ ms discrepancies were observed as two propagating cracks had merged in the experiment but not in the simulation. The simulation of test T6-22.5-1.0 was, on the other hand, in good agreement with the experiment, where the flaps were folded at the correct point in time. As already mentioned, the failure pattern in the experiments of tests T4-4-45-1.5 and T6-4-45-1.5 were similar, and once again the simulation of the latter test gave a different failure mode than what was observed in the experiment. In the simulation, cracks propagated along the diagonals of the plate and the petals were folded around each side of the plate. In the experiment, indications of crack propagation along the diagonals towards the centre of the plate were seen, but the growth of these cracks were halted as cracks propagated between the slits, resulting in the centre of the plate being torn out with the shape of a cross. When comparing the simulations of tests T6-4-45-1.5 and T4-4-45-1.5, the difference in velocity of the growing cracks is correctly predicted, where in the latter the plate is seemingly more resistant to crack propagation. Among the three tests in the 4-45-1.5 plate configuration, the structural response between tempers T4 and T7 was similar. However, simulations of the same tests predict that the response between tempers T6 and T7 were similar. In the simulation of test T6-22.5-1.5, the response was well predicted up to $t = 1.00$ ms, but then the cracks were arrested while the flaps continued to fold and a peeling type of failure was seen at $t = 2.00$ ms. Further, rupture was not predicted in the simulation of test T6-4-45-1.0, while too much fracture was predicted in the simulation of test T7-4-45-1.0. Fracture was predicted in the simulation of test T7-4-45-1.5, but with the same incorrect failure mode as observed in the simulation of tests T6-4-45-1.5 and T4-4-45-1.5. In general, the numerical model did not succeed to predict the correct failure mode for any of the plates with this geometry except for test T4-4-45-1.0. This suggests that the numerical model is not able to capture all the physical mechanisms governing the failure of the plates. On the other hand, the numerical simulations were in good agreement with the experiments for tests T7-22.5-1.0 and T7-22.5-1.5, where the structural response was well predicted at all points in time. In particular, the resemblance between experiment and simulation of test T7-22.5-1.5 is excellent, where the curved crack path was accurately predicted. However, the plates are in general more folded towards the end of the simulations compared to the experiments, which is expected due to the definition of the pressure load used throughout these simulations. The plastic work in the simulations further support the observations

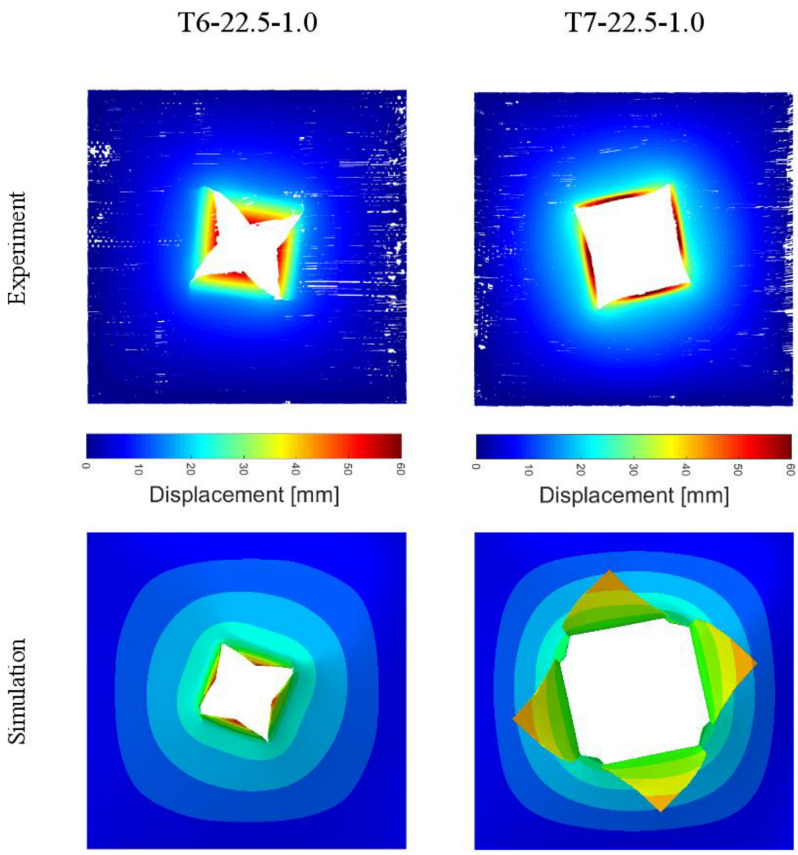

Fig. 23. Contour plots of the displacement field from experiments and simulations of tests T6-22.5-1.0 and T7-22.5-1.0.

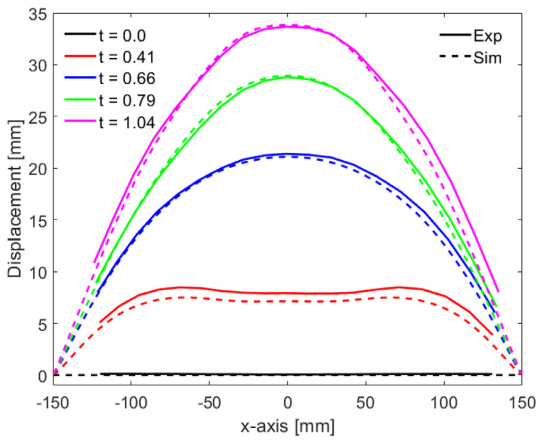

Fig. 24. Displacement profiles from experiments and simulation of test T4-4-45-1.0 at five different points in time. The times are given in ms.

made throughout this study, namely that the same slit geometry and pressure load gives approximately the same values of plastic work for tempers T4 and T7, while the value for temper T6 is substantially lower. The difference is also larger for the higher pressure load than for the lower. For the plates in temper T4, the 4-45 geometry is seen to give the highest value of plastic work, closely followed by the 4-HV geometry. Further, a higher number of slits seems to dissipate more plastic work than a lower number.

Contour plots of the displacement fields from available experiments and simulations of the plates in temper T4 are shown in Fig. 22. The plates with only one slit show more global deformation in the simulations than in the experiments. One should have in mind that the last frame from the simulation is two milliseconds after the blast wave has impacted the plate, and the plate is still moving at this point due to elastic vibrations. The elastic vibrations are relatively small, but they will have an impact on the contour plot. This effect is expected to be larger for higher firing pressures. The agreement between the experiment and simulation of test T4-4-45-1.0 is good, and the trends seen experimentally were well predicted. A comparison of the experiment and simulation of test T4-HV-1.5 is not shown, as the definition of the pressure load in the simulation resulted in self-contact between the flaps and the remainder of the plate at the final part of the deformation process.

Contour plots of the displacement fields from experiments and simulations of tests T6-22.5-1.0 and T7-22.5-1.0 are shown in Fig. 23. The results for tests T6-4-45 and T7-4-45 are omitted since either the experiments or the simulations experienced complete failure. Like the results for the plates in temper T4 in Fig. 22, the simulations of the plates in tempers T6 and T7 gave more global deformation than what was seen in the experiments. The discrepancies in the simulation of test

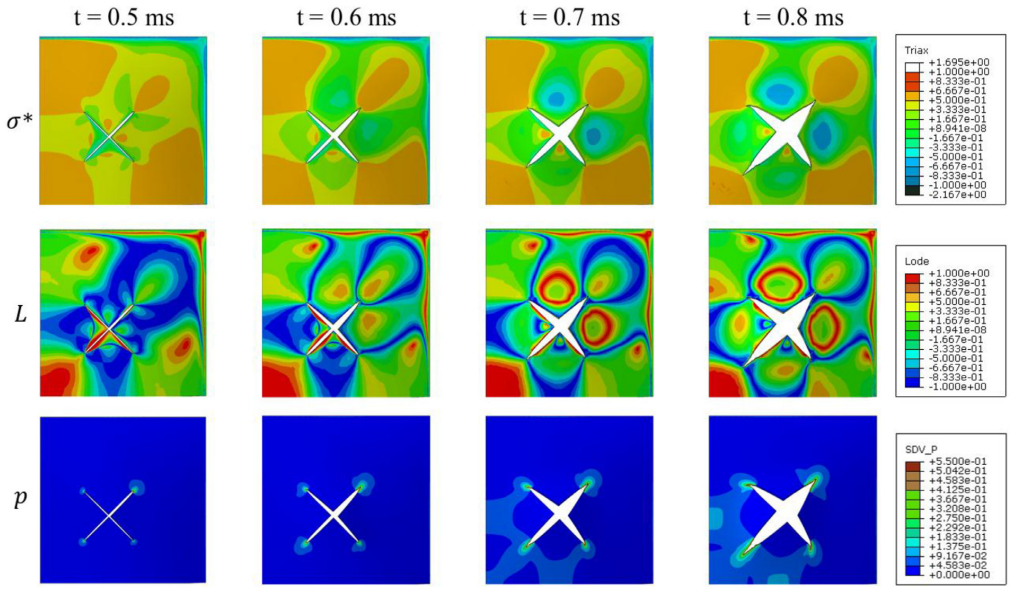

Fig. 25. Predicted contour plots of the stress triaxiality, Lode parameter and equivalent plastic strain for a quarter of the plate from test T4-4-45-1.5 at selected points in time.

T7-22.5-1.0 are due to the definition of the pressure load discussed earlier, which affects the deformation of the plate in the later stages of the loading process. However, the overall agreement between the experiments and the simulations is reasonable.

To further investigate how well the plastic deformation of the plates is predicted numerically, a cross-section along the horizontal axis in the middle of the plate is extracted from both the experiment and the simulation of test T4-4-45-1.0 at five different points in time and plotted in Fig. 24. The response is accurately predicted to initiate at the boundary of the plate, and the displacement profile is as seen correct at $t = 0.41$ ms. The agreement between the experiment and simulation is excellent all the way to $t = 1.04$ ms, which is the maximum displacement of the plate in the test. Both the experiment and the simulation showed minor crack propagation, supposed to have negligible influence on the global response. It is evident that the numerical model can describe the plasticity in the problem. This comparison is unavailable for tempers T6 and T7, as complete failure occurred in either the experiment or the simulation of the tests.

Contour plots of the stress triaxiality σ^*, the Lode parameter L, and the equivalent plastic strain p from the simulation of test T4-4-45-1.5 are presented for the upper right quarter of the plate in Fig. 25. The plots are extracted at times between $t = 0.50$ ms and $t = 0.80$ ms, and show the evolution of the first cracks. By inspection of these plots one can see that the cracks are propagating in elements with a stress triaxiality between 0.5 and 0.67 and a Lode parameter around zero, suggesting that these elements are in a stress state close to plane strain tension. The equivalent plastic strain is accumulating in front of the slits, and cracks are seen to propagate from all of them. Between $t = 0.70$ ms and $t = 0.80$ ms the crack propagation becomes critical along the diagonals of the plate, while it stagnates in the other directions. The stress state in front of the four slits is comparable, even though the cracks only propagate along those aligned with the diagonal. To predict the same failure mode as seen in the experiment of this plate, the cracks would have to propagate along the two opposite slits as well. By inspecting the figure one can see that the cracks from these slits are deflecting along the horizontal and vertical axes of the plate as observed in the experiment, before they stagnate. The marginal difference in stress state between the propagating and the stagnating cracks suggests that a more enhanced failure criterion could have been able to predict the correct failure mode for this geometry.

7. Conclusions

An experimental and numerical study on the structural response of 1.5 mm thick AA6016 aluminium plates in tempers T4, T6 and T7 with geometrical defects subjected to blast loading has been presented. The blast tests were divided into two main parts, both conducted in a shock tube facility. Part one of the study consisted of eight tests on plates in temper T4 with four different pre-cut slit geometries at two different firing pressures, while part two consisted of eight tests on plates in tempers T6 and T7 with two of the pre-cut slit geometries from part one using the same firing pressures. High-speed cameras synchronized with pressure sensors near the plates were used to study the structural response during blast loading. 3D-DIC was employed to extract the displacement fields during testing, and selected plates were 3D-scanned to visualize the permanent damage. Uniaxial tensile tests were conducted in directions 0°, 45° and 90° with respect to the rolling direction of the plate for each temper, amounting to 27 tests in total. The tensile tests exhibited a moderately anisotropic plastic behaviour for the three tempers of the rolled AA6016 plates, while the elongation to fracture within each temper displayed small variations. Numerical simulations were carried out using a modified Johnson-Cook plasticity model and the Cockcroft–Latham failure criterion. Element erosion was used to remove failed elements, while the blast load was applied as a pressure-time curve on the plate surface. Possible FSI-effects were not included in these simulations. A refined solid element mesh with a characteristic element size of 0.5 mm was generated using a sweep meshing technique.

The main findings from the study can be summarized as follows:

- By changing the number and orientation of the pre-cut slits, the failure mode and the blast resistance of the plates were markedly affected.
- By changing the heat-treatment, and thereby the strength, work-

hardening capacity and ductility of the plate material, the crack propagation and blast resistance were significantly influenced, whereas the failure mode of the plate did not change significantly.
- Crack initiation occurred at similar points in time independent of the heat-treatment of the plate, whereas the speed of the propagating cracks and the degree of damage were higher for plates in temper T6 than in the plates in tempers T4 and T7. Thus, the higher strength of the plates in temper T6 did not compensate for the reduced ductility compared with the plates in tempers T4 and T7 regarding blast protection.
- The numerical simulations accurately predicted initiation of failure and the degree of damage, but some of the failure modes were not predicted correctly.

Acknowledgements

The authors gratefully appreciate the financial support from NTNU and the Research Council of Norway through the FRINATEK Programme, Project no. 250553 (FractAl), and from the Norwegian Ministry of Justice and Public Security. The authors would also like to thank Mr. Trond Auestad at SIMLab, NTNU, for assistance with accomplishing the experimental programme, and Dr. Olaf Engler at Hydro Aluminium Rolled Products in Bonn, Germany, for providing the materials.

References

[1] Nyström U, Gylltoft K. Numerical studies of the combined effects of blast and fragment loading. Int J Impact Eng 2009;36(8):995–1005.
[2] Grisaro HY, Dancygier AN. Characteristics of combined blast and fragments loading. Int J Impact Eng 2018;116:51–64.
[3] Rakvåg KG, Underwood NJ, Schleyer GK, Børvik T, Hopperstad OS. Transient pressure loading of clamped metallic plates with pre-formed holes. Int J Impact Eng 2013;53:44–55.
[4] Li Y, Weiguo W, Haiqing Z, Zhen W, Zhipeng D. The influence of different pre-formed holes on the dynamic response of square plates under air-blast loading. Eng Fail Anal 2017;78:122–33.
[5] Aune V, Valsamos G, Casadei F, Langseth M, Børvik T. On the dynamic response of blast-loaded steel plates with and without pre-formed holes. Int J Impact Eng 2017;108:27–46.
[6] Zhang C, Cheng Y, Zhang P, Duan X, Liu J, Li Y. Numerical investigation of the response of I-core sandwich panels subjected to combined blast and fragment loading. Eng Struct 2017;151:459–71.
[7] Woelke PB, Shields MD, Hutchinson JW. Cohesive zone modeling and calibration for mode I tearing of large ductile plates. Eng Fract Mech 2015;147:293–305.
[8] El-Naaman SA, Nielsen KL. Observations on Mode I ductile tearing in sheet metals. Eur J Mech A/Solids 2013;42:54–62.
[9] McDonald B, Bornstein H, Langdon GS, Curry R, Daliri A, Orifici AC. Experimental response of high strength steels to localized blast loading. Int J Impact Eng 2018;115:106–19.
[10] Langdon GS, Lee WC, Louca LA. The influence of material type on the response of plates to air-blast loading. Int J Impact Eng 2015;78:150–60.
[11] Børvik T, Dey S, Clausen A. H. Perforation resistance of five different high-strength steel plates subjected to small-arms projectiles. Int J Impact Eng 2009;36:948–64.
[12] Holmen JK, Johnsen J, Hopperstad OS, Børvik T. Influence of fragmentation on the capacity of aluminum alloy plates subjected to ballistic impact. Eur J Mech A/Solids 2016;55:221–33.
[13] Forrestal MJ, Børvik T, Warren TL. Perforation of 7075-T651 aluminum armor plates with 7.62mm APM2 bullets. Exp Mech 2010;50(8):1245–51.
[14] Holmen JK, Johnsen J, Jupp S, Hopperstad OS, Børvik T. Effects of heat treatment on the ballistic properties of AA6070 aluminium alloy. Int J Impact Eng 2013;57:119–33.
[15] Dey S, Børvik T, Hopperstad OS, Leinum JR, Langseth M. The effect of target strength on the perforation of steel plates using three different projectile nose shapes. Int J Impact Eng 2004;30(8–9):1005–38.
[16] Granum H, Myhr OR, Børvik T, Hopperstad OS. Nanostructure-based finite element analyses of aluminium profiles subjected to quasi-static axial crushing. Thin Walled Struct 2018;131:769–81.
[17] Engler O, Schäfer C, Myhr O. R. Effect of natural ageing and pre-straining on strength and anisotropy in aluminium alloy AA6016. Mater Sci Eng 2015;639:65–74.
[18] Gruben G, Hopperstad OS, Børvik T. Simulation of ductile crack propagation in dual-phase steel. Int J Fract 2013;180(1):1–22.
[19] https://www.ntnu.edu/kt/ecorr[cited: 07.05.2019].
[20] Aune V, Fagerholt E, Langseth M, Børvik T. A shock tube facility to generate blast loading on structures. Int J Prot Struct 2016;7(3):340–66.
[21] Tasissa AF, Hautefeuille M, Fitek JH, Radovitzky RA. On the formation of Friedlander waves on a compressed-gas-driven shock tube. Proc R Soc A 2016;472:20150611.
[22] Johnson G. R, Cook W.H.A constitutive model and data for metals subjected to large strains, high strain rates and high temperatures. Proceedings of the 7th international symposium on ballistics1983: 541–547.
[23] Børvik T, Hopperstad OS, Berstad T, Langseth M. A computational model of viscoplasticity and ductile damage for impact and penetration. Eur J Mech A/Solids 2001;20(5):685–712.
[24] Cockcroft MG, Latham DJ. Ductility and workability of metals. J Inst Met 1968;96:33–9.
[25] Livermore Software Technology Corporation, LS-OPT, Version 5.2.1, 2016.
[26] Zukas JA, Nicholas T, Swift HF. Impact dynamics. Krieger Publishing Company; 1992.
[27] Chen Y, Pedersen KO, Clausen AH, Hopperstad OS. An experimental study on the dynamic fracture of extruded AA6xxx and AA7xxx aluminium alloys. Mater Sci Eng A 2009;523(1–2):253–62.
[28] Vilamosa V, Clausen AH, Børvik T, Skjervold SR, Hopperstad OS. Behaviour of Al-Mg-Si alloys at a wide range of temperatures and strain rates. Int J Impact Eng 2015;86:223–39.

Part 4

Henrik Granum, David Morin, Tore Børvik,
Odd Sture Hopperstad

Simulation of blast-loaded aluminium plates with crack-like defects

In: Proceedings of MekIT'19 - 10th National Conference on Computational Mechanics (2019)
149-164

10. National Conference on Computational Mechanics
MekIT'19
B. Skallerud and H I Andersson (Eds)

SIMULATION OF BLAST-LOADED ALUMINIUM PLATES WITH CRACK-LIKE DEFECTS

Henrik Granum[1], **David Morin**[1,2], **Tore Børvik**[1,2], **Odd Sture Hopperstad**[1,2]

[1]Structural Impact Laboratory (SIMLab), Department of Structural Engineering, Norwegian University of Science and Technology (NTNU), Trondheim, Norway

[2]Centre for Advanced Structural Analysis (CASA), NTNU, Trondheim, Norway

Key words: Computational mechanics, Shell elements, Ductile failure, Through-thickness regularization

Abstract. This paper presents a numerical study on the response of blast-loaded AA6016 T4 aluminium plates with crack-like defects. Explicit finite element simulations were performed with LS-DYNA, using an uncoupled plasticity and fracture model with through-thickness damage regularization valid for shell elements. Uniaxial tensile tests are used to determine the parameters of the constitutive model by inverse modelling. Four different crack-like defects are considered at a load level resulting in failure and crack propagation in all the plates. The simulation results obtained with different mesh sizes are evaluated against experiments conducted in a shock tube facility. The shell element model is able to predict failure and crack propagation with good accuracy for the finest mesh, i.e., shell elements with length-to-thickness ratio of 1/3, while the accuracy decreases rapidly as the mesh size is increased.

1 INTRODUCTION

When modelling structural problems using the finite element method (FEM), shell elements have been the standard in industrial applications due to their superior computational efficiency compared to solid elements. They benefit from a versatile formulation and are especially suitable for structures where two dimensions are much larger than the third one. Even though shell elements provide good results in the elastic and plastic domains, predicting failure and crack propagation has always been a challenge. Local necking is often a precursor to failure in thin-walled structures. In the necking process, the local stress state of the plate changes from plane stress to a three-dimensional stress state. Computationally efficient simulations often require large element sizes, which makes it difficult to capture strain localization. This is due to the local characteristic of a necking process, where a coarse spatial discretization in a simulation will even out the strain gradients. To overcome the aforementioned problems, different empirical relationships have

been proposed in an attempt to couple the failure strain to the element size. However, many of the proposed regularization models are limited to membrane loading. This is a problem due to the lower ductility exhibited by a plate in stretching compared to bending, linked to the local neck which is formed in a membrane dominated problem. To account for this challenge, the damage evolution due to stretching and bending should be accounted for in problems involving combined loading actions. The uncoupled plasticity and fracture model used in this study was proposed by Costas et al. [1] and comprises a through-thickness damage regularization scheme valid for shell elements. The model has been validated against experiments on a two-chamber extruded profile of the aluminium alloy AA6005 T6 subjected to quasi-static and dynamic axial crushing and quasi-static three-point bending. The results showed that the model was able to predict failure in tests involving both local necking and severe bending of the material. The mesh sensitivity was found to be reduced with the proposed scheme, providing a more realistic prediction of the local necking. The simple calibration of the model from a single tensile test using two-dimensional digital image correlation (2D-DIC) and inverse modelling makes it suitable for industrial applications.

Numerical simulations of ductile failure using shell elements have been presented in a number of studies (see e.g. [2, 3, 4]). Woelke et al. [5] investigated an idealized ship grounding scenario where both phenomenological damage and cohesive zone models for ductile failure were evaluated. Stiffened and unstiffened steel plates, where the loading was dominated by biaxial stretching, were considered. Both models were able to reproduce the experimentally observed behaviour, despite the differences between them. Pack and Mohr [6] proposed the concept of Domain of Shell-to-Solid Equivalence (DSSE) to account for the onset of localized necking with shell elements. Marciniak-Kuczynski type of localization analyses were used in the calibration of the model and combined with the Hosford-Coulomb fracture initiation model. The proposed model was validated against five different tests on DP780 steel, and the displacement at fracture was successfully predicted in all the tests. The authors emphasized that the DSSE concept should be confined to the domain where the plane-stress assumption of the shell element solution is meaningful. Morin et al. [7] investigated the behaviour and failure of stiffened aluminium panels subjected to quasi-static and low-velocity impact loading conditions. A regularized failure criterion was employed and the effect of mesh size was investigated. The numerical results showed a good correlation with the experiments for the fine meshes, while the larger meshes failed to initiate and propagate cracks as observed in the experiments. The mesh dependence was reduced by employing the regularization model, where five different length-to-thickness ratios were employed.

Blast-loaded aluminium plates with crack-like defects presented in [8] are investigated numerically in this study. This is done using an uncoupled plasticity and fracture model with through-thickness damage regularization. A simplified finite element model of the blast test set-up is made with shell elements, and the numerical results are evaluated against blast tests conducted in a shock tube facility on 1.5 mm thick AA6016 T4 plates

with four different configurations of crack-like defects. The effect of varying the mesh size is investigated, where the in-plane dimensions of the elements varied from 1/3 to 5 times the thickness of the plate.

2 MATERIAL AND EXPERIMENTAL WORK

The material considered in this study is the aluminium alloy AA6016 in temper T4, which is an Al-Mg-Si alloy often used in the automotive industry. The material was delivered as 1.5 mm thick sheets with in-plane dimensions 625 mm × 625 mm by Hydro Aluminium Rolled Products in Bonn, Germany. The chemical composition of the alloy as provided by the supplier is given in Table 1.

Table 1: Chemical composition of AA6016 in wt%.

Si	Mg	Fe	Cu	Mn	Cr	Zn	Ti	Al
1.3160	0.3490	0.1617	0.0081	0.0702	0.0025	0.0084	0.0175	Balance

Uniaxial tensile tests were carried out on specimens with tensile axis at 0°, 45° and 90° to the rolling direction of the sheet, see Granum et al. [8]. The tests revealed a slight difference in elongation to failure with the tensile direction and minor scatter was observed between the repeat tests. The flow stress was practically independent of the tensile direction. In contrast, the Lankford coefficient, defined as the ratio of the plastic strain in the width direction to that in the thickness direction, was consistently higher in the rolling direction than in the other two directions, but always less than unity. The material exhibits a moderate plastic anisotropy, where the tendency for thinning is stronger than for an isotropic material.

The blast tests were conducted in the SIMLab Shock Tube Facility at NTNU [9]. The test program, setup and experimental results are presented in Granum et al. [8], and the reader is referred to this article for details. In total, four different initial defect geometries were tested with peak pressure at impact of the blast wave approximately equal to 600 kPa. The clamping of the plate in the shock tube and the different plate configurations are shown in Figure 1, where each plate configuration is given an abbreviation on the form X-Y, where X is the number of defects and Y indicates the orientation of the defect(s). These abbreviations are used in the rest of this study. The defects were cut with wire erosion as thin slits with an approximate width of 0.1 mm. The blast event was recorded by two synchronized Phantom v1610 high-speed cameras positioned in a stereovision setup, recording at 24 000 fps with an image resolution of 768 × 800 pixels.

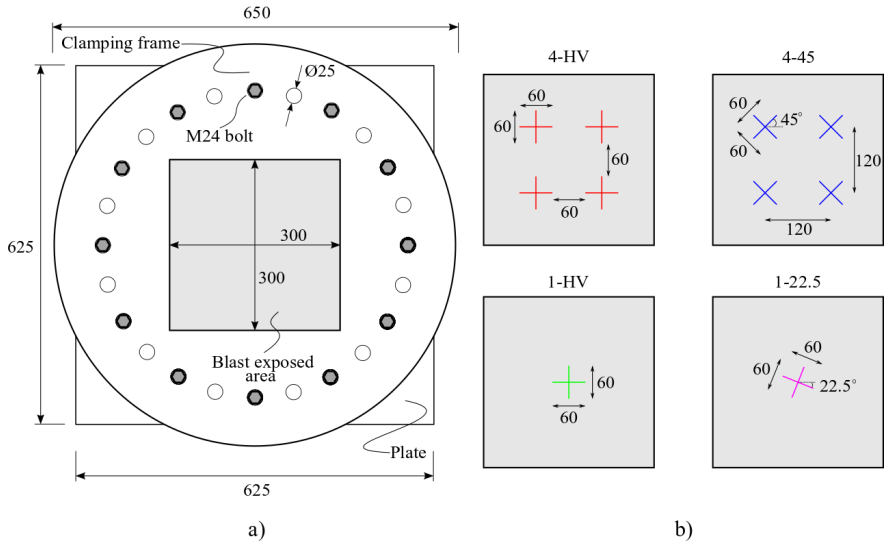

Figure 1: Sketch of a) plate and clamping frame, and b) blast exposed area of the plates depicting the four different initial defect geometries. Measurements are in mm.

3 MATERIAL MODELLING

3.1 Constitutive model

Even though the plate material exhibits moderate plastic anisotropy, the assumption of isotropic material behaviour was employed for simplicity in the constitutive modelling. The yield surface was defined by the high-exponent Hershey-Hosford yield function [10, 11], which has been shown to be suitable for isotropic Face Centered Cubic (FCC) and Body Centered Cubic (BCC) materials. The yield surface is expressed as

$$f = \varphi(\boldsymbol{\sigma}) - (\sigma_0 + R) = 0 \tag{1}$$

where φ is the equivalent stress, $\boldsymbol{\sigma}$ is the stress tensor, σ_0 is the initial yield stress and R is the isotropic hardening variable. A rate-independent formulation was selected due to the low rate sensitivity reported for 6000-series aluminium alloys [12]. Also the temperature dependence was omitted, as this proved to give negligible differences in the results [8]. The Hershey-Hosford equivalent stress is expressed as

$$\varphi(\boldsymbol{\sigma}) = \left[\frac{1}{2}\left(|\sigma_1 - \sigma_2|^m + |\sigma_2 - \sigma_3|^m + |\sigma_3 - \sigma_1|^m\right)\right]^{\frac{1}{m}} \tag{2}$$

where σ_1, σ_2 and σ_3 are the principal stresses and m is a parameter controlling the curvature of the yield surface. Studies on FCC materials like aluminium alloys suggest

to set m equal to 8, based on polycrystal plasticity calculations [13]. This value was adopted without further investigation in this study. The hardening variable is given by the extended Voce hardening rule on the form

$$R(p) = \sum_{i=1}^{3} R_i(p) = \sum_{i=1}^{3} Q_i(1 - \exp(-C_i p)) \tag{3}$$

where R_i are hardening terms that saturate at different levels of equivalent plastic strain p, and Q_i and C_i represent the saturation value and the rate of saturation of the hardening term R_i, respectively.

3.2 Failure model

Failure was modelled by the Cockcroft-Latham failure criterion [14]. Accordingly, the damage variable D is defined as

$$D = \frac{1}{W_C} \int \langle \sigma_I \rangle \mathrm{d}p \leq 1 \tag{4}$$

where W_C is the fracture parameter, σ_I is the major principal stress and $\langle \cdot \rangle$ are the Macaulay brackets, defined as $\langle \sigma_I \rangle = \frac{1}{2}(|\sigma_I| + \sigma_I)$. The failure criterion has been modified as proposed by Costas et al. [1] where the fracture parameter W_C is divided into two parts responsible for pure membrane loading and pure bending. The reader is referred to Costas et al. [1] for a detailed description of the modified failure criterion. The fracture parameter W_C^b governing pure bending is retrieved from a finite element simulation of a tensile test using a fine solid element mesh. By conducting similar simulations with shell elements, the fracture parameter governing membrane loading W_C^m is obtained for a range of element sizes. The influence of element size is then included by making W_C^m a function of the element's aspect ratio l_e/t_e, where l_e is the element length and t_e is the initial thickness of the plate [7]

$$W_C^m = W_C^l + (W_C^s - W_C^l) \cdot \exp\left(-c \cdot \left(\frac{l_e}{t_e} - 1\right)\right) \tag{5}$$

where W_C^l is the fracture parameter for large shell elements, W_C^s is the fracture parameter for an element with aspect ratio equal to unity, and c is a model parameter. In elements subjected to combined membrane loading and bending, the fracture parameter is calculated as

$$W_C = \Omega W_C^b + (1 - \Omega) W_C^m \tag{6}$$

where Ω is a deformation mode indicator determining the relative amount of membrane loading and bending an element is subjected to. The deformation mode indicator is defined by the through-thickness plastic strain as

$$\Omega = \frac{1}{2} \frac{\left|\varepsilon_{\mathrm{p},33}^{\mathrm{T}} - \varepsilon_{\mathrm{p},33}^{\mathrm{B}}\right|}{\max\left\{\left|\varepsilon_{\mathrm{p},33}^{\mathrm{T}}\right|, \left|\varepsilon_{\mathrm{p},33}^{\mathrm{B}}\right|\right\}} \tag{7}$$

where $\varepsilon_{\mathrm{p},33}^{\mathrm{T}}$ and $\varepsilon_{\mathrm{p},33}^{\mathrm{B}}$ are the through-thickness plastic strains at the top and bottom integration point of the shell element, respectively. This gives $\Omega = 1$ for pure bending and $\Omega = 0$ for pure membrane loading.

3.3 Parameter identification

The yield stress σ_0 and the hardening parameters Q_i and C_i were calibrated based on a representative tensile test in the rolling direction of the sheet. An initial estimate of the hardening parameters was obtained in a spreadsheet, using the true stress-strain curve up to necking. A finite element model of the tensile test was made in Abaqus/Standard, where only 1/8 of the specimen was modelled, assuming isotropic material behaviour. The gauge section was modelled with solid elements with characteristic element size of 0.15 mm, resulting in 10 elements over the thickness. Reduced integration with hourglass control was employed. An extensometer of length 50 mm was used to extract displacements from the simulation, coinciding with the virtual extensometer used to extract displacements from the DIC. Inverse modelling by use of the optimization tool LS-OPT was used to improve the accuracy of the hardening parameters, where sequential simulations on the same model with different values of the hardening parameters were conducted. The engineering stress-strain curve obtained from the test was used as the target curve, and the mean squared error between the target curve and the simulated curve was calculated and used in the optimization. The result of the optimization is shown in Figure 2 a) in terms of the force-displacement curves from the representative tests and the simulation, where the marker illustrates the assumed point of failure in the simulation. The figure demonstrates good agreement between the experiments and the simulation all the way to failure. The equivalent stress-equivalent plastic strain curve from the experiment is plotted up to necking in Figure 2 b) together with the calibrated flow stress curve. The moderate anisotropy exhibited by the material suggests that the fit may not be as good when plotted against test data in the other tensile directions.

The calibrated material parameters for the extended Voce hardening rule are presented in Table 2. The elastic material properties were taken as standard values for aluminium: Young's modulus $E = 70000$ MPa and Possion's ratio $\nu = 0.3$. The failure parameter governing bending W_C^b was obtained from a simulation using a fine solid element mesh and estimated to $W_C^b = 245.2$ MPa. In Costas et al. [1], the failure parameter governing membrane loading W_C^m was obtained by use of a virtual extensometer to extract DIC measurements at different length-to-thickness ratios l_e/t_e of a uniaxial tensile test. In this study, W_C^m was found by use of a finite element simulation of the uniaxial tensile test with a refined solid element mesh. Vectors of different length l_e spanned across the neck were used to extract elongations. These elongations were then applied as boundary conditions

to a single shell element simulation with the same element size l_e until the point where fracture occurred in the test. The fracture parameters W_C^m for the different element sizes l_e were found by numerical integration. The obtained fracture parameters then served as discrete points which Equation (5) was curve fitted to, where the optimized parameters came out as $W_C^l = 79.1$ MPa, $W_C^s = 116.1$ MPa and $c = 0.36$.

Table 2: Parameters for the extended Voce hardening rule for AA6016 T4.

σ_0 [MPa]	Q_1 [MPa]	C_1	Q_2 [MPa]	C_2	Q_3 [MPa]	C_3
112.5	78.6	32.80	109.8	4.9	325.7	0.5

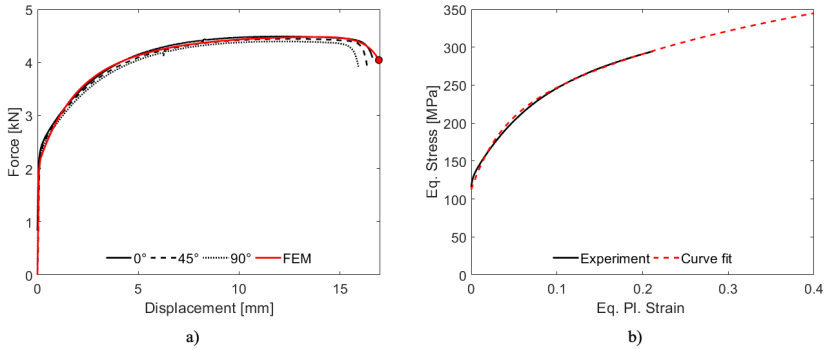

Figure 2: a) Force-displacement curves from representative tests in each direction together with the curve from the calibrated FE model, and b) experimental and calibrated flow stress curves in terms of the equivalent stress and equivalent plastic strain.

4 NUMERICAL RESULTS

4.1 Finite element model

The numerical simulations of the blast-loaded plates were conducted in the explicit solver of LS-DYNA. The edge of the plate was fixed in an attempt to mimic the effect of the clamping frames in the test setup. Shell elements with reduced integration and five integration points through the thickness were used, denoted type 2 in LS-DYNA. This is a Belytschko-Lin-Tsay shell formulation which is based on the Reissner-Mindlin kinematic assumption [15]. Four different length-to-thickness ratios of the shell elements were used in the model ($l_e/t_e = 1/3, 1, 3, 5$). A sweep meshing technique was used to

obtain a random mesh, resulting in approximately 450 000 elements for l_e/t_e equal to 1/3 and below 2000 elements for l_e/t_e equal to 5. The slits were modelled star shaped, resulting in a single node at each slit end to simplify the meshing of the plate.

The blast load was obtained from blast tests on a massive steel plate, where pressure sensors mounted directly on the plate recorded the loading [9], and applied to the AA6016 T4 plates as a tabulated uniform pressure-time curve. In addition to the built-in pressure definition in LS-DYNA, a user-defined subroutine was employed where the magnitude of the applied pressure was multiplied by the cosine of the angle between the initial load direction and the normal of the shell element. This allowed the pressure to "slide off" as the plate deformed, preventing situations where the pressure pointed in the opposite direction of the initial pressure load. Failure was handled by element erosion, where the stress tensor is set to zero in all integration points when the damage variable D is equal to unity in two integration points on either side of the mid through-thickness integration point.

4.2 Results and discussion

The effect of updating the pressure magnitude as described above in the simulations was significant for some defect geometries. In Figure 3, this effect is shown for the 1-HV configuration with l_e/t_e equal to 1. The "flaps" in the simulation with the original pressure formulation have folded considerably and the pressure on the flaps is pointing in the opposite direction of the initial loading direction in the last part of the simulation due to the Lagrangian description of the loading. In the simulation with the updated pressure formulation, the pressure "slides off" as the flaps deform in a petal mode, i.e., the pressure is reduced with the rotation of the shell normal. By comparing the two approaches to the corresponding experiment also shown in the figure, it is concluded that the correct behaviour is somewhere in-between the two approaches, yet much closer to the updated pressure formulation. However, to properly account for fluid-structure interactions, coupled Eulerian-Lagrangian simulations are needed, increasing the complexity and computational cost of the simulations significantly.

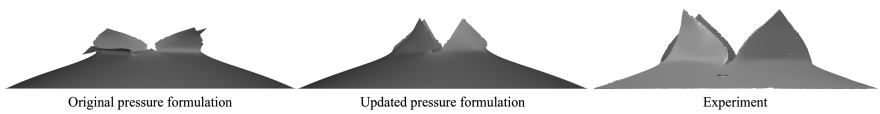

Figure 3: The effect of the two pressure formulations on a plate with a slit oriented along the plate axis compared to the corresponding experiment.

Image series comparing the 1-22.5 simulations to the experiment are shown in Figure 4 at selected points in time, where $t = 0$ indicates the time of impact of the blast load. Similar trends were seen for the other geometries and they are omitted for brevity. In the

experiment, cracks propagate from the slit ends towards the corner of the plate and the flaps deform in a petal mode. As expected, the discretization of the mesh is important when modelling failure and crack propagation. For a length-to-thickness ratio $l_e/t_e = 5$, no failure or cracking is seen as the flaps just deform in a petal mode. The plastic zones in front of the slit ends are smeared out over the coarse elements, preventing the failure criterion to be triggered. In the simulation with $l_e/t_e = 3$, the overall response is similar to the coarsest model. However, failure initiation is predicted, but the mesh discretization is not fine enough for the cracks to propagate. Failure of two elements in front of each slit end resulted in a substantial increase in the crack width and led to the sudden arrest of the crack. First in the simulation with $l_e/t_e = 1$ crack propagation is predicted, where the experimental behaviour up to $t = 1.00$ ms is accurately recreated. The cracks are arrested at $t = 1.25$ ms and the flaps fold in a petal mode. Further reduction of the length-to-thickness ratio to $l_e/t_e = 1/3$ proved to enhance the results even more. Shell elements with smaller in-plane dimension than the thickness are usually not recommended and the results should be evaluated carefully. However, the smaller in-plane element size makes the width of the crack narrower when an element is eroded, which is advantageous for the crack to propagate. Eventually, the cracks are arrested slightly prematurely compared to the experiment, but the agreement up to $t = 1.50$ ms is deemed good.

The last frame from the four 1-22.5 simulations is shown from the side in Figure 5. From the figure it is evident that the global displacement is predicted equally well in the simulations with $l_e/t_e = 5$ and $l_e/t_e = 1$. Even though the amount of crack propagation varies between these simulation, the final shape of the plates is almost identical. However, in the simulation with $l_e/t_e = 1/3$, the flaps have folded considerably and there is a significant opening of the plate. As seen from the image series in Figure 4, this simulation gives the most accurate failure mode when compared to the experiment.

The simulations with the different length-to-thickness ratios are compared to the experiments at $t = 2.0$ ms in Figure 6. The simulations with $l_e/t_e = 5$ are not able to capture failure in any of the four configurations due to the coarse discretization. Contour plot of the damage variable D shows that $D = 0.76$ in the most critical element, substantiating the difficulty to capture localization of plastic strain with a coarse mesh. Even with $l_e/t_e = 3$ the predictive capability of the model is insufficient. The two elements in front of the slit ends for the 1-HV and 1-22.5 configurations have failed in these simulations, but no crack propagation is observed. For the 4-HV and 4-45 configurations, no failure is observed, even though the damage variable D is close to unity in the elements in front of the slits in the 4-HV simulation. For $l_e/t_e = 1$, the 4-HV simulation is in good agreement with the experiment, where the centre part of the plate is correctly ejected from the rest of the plate. However, the 4-45 simulation is not able to predict crack propagation particularly well and the agreement with the experiment is less good. The 1-HV and 1-22.5 configurations are predicted with acceptable accuracy. The simulations with the finest mesh ($l_e/t_e = 1/3$) were able to replicate the experiments with reasonable accuracy for all configurations, where the crack propagation is especially impressive in

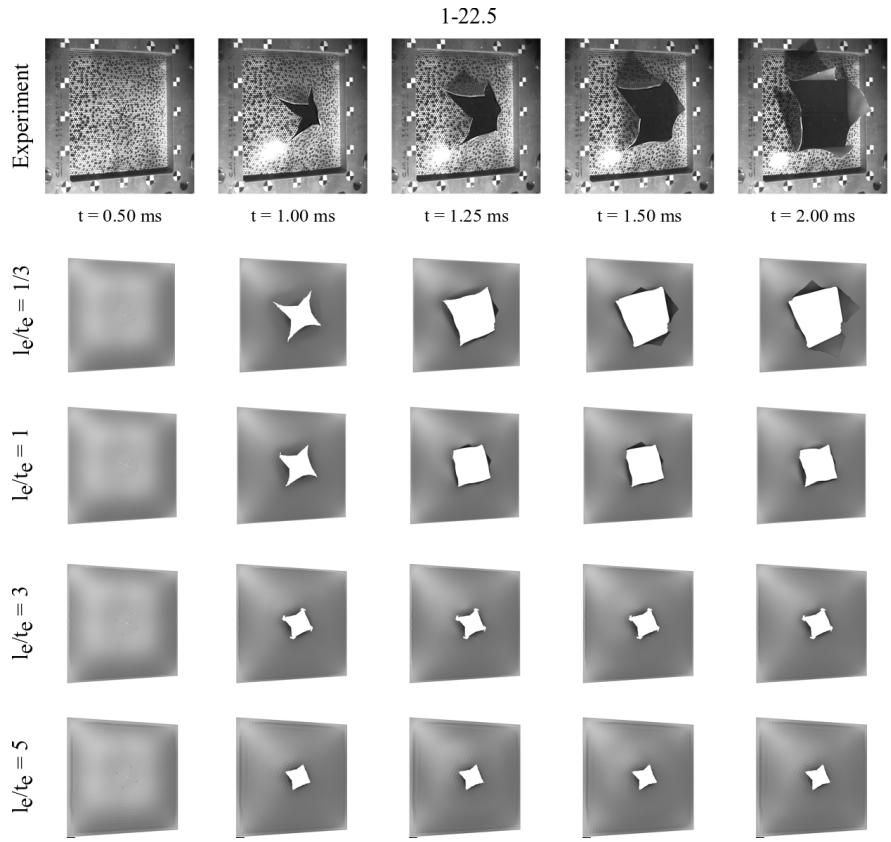

Figure 4: Image series from test 1-22.5 and corresponding simulations with different length-to-thickness ratios (l_e/t_e) at selected points in time.

Figure 5: Side view of 1-22.5 simulations with different length-to-thickness ratios (l_e/t_e).

the 4-HV and 4-45 simulations. The cracks were arrested slightly too early in the 1-HV and 1-22.5 simulations, but the overall response was predicted. The crack propagation in the simulations was always less than what was seen in the experiment apart from the 4-HV simulation. In many structural applications, the occurrence of failure is of interest,

which the two finest meshes were able to predict with satisfying accuracy. However, if crack propagation is of interest, only the finest mesh is able to give reliable results.

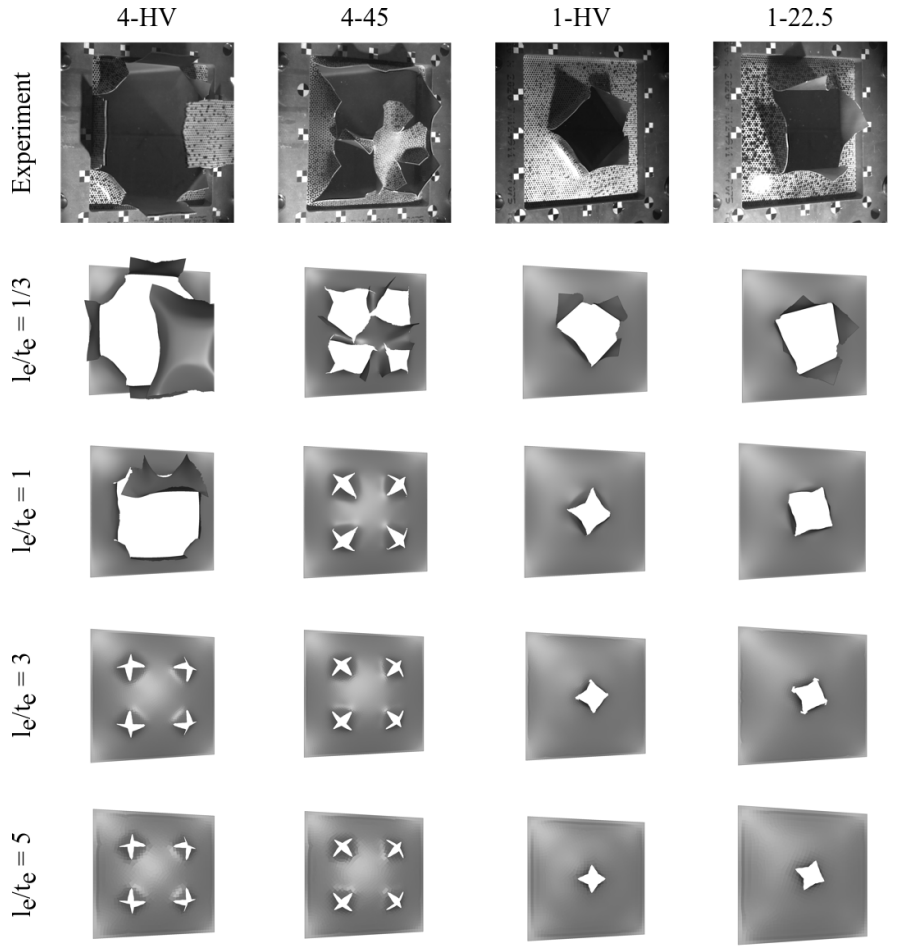

Figure 6: Comparison of tests and simulations with different length-to-thickness ratios (l_e/t_e) at $t = 2.0$ ms.

Figure 7 shows a contour plot of the deformation mode indicator Ω given in Equation (7) for simulations with $l_e/t_e = 1$ at $t = 1.25$ ms. The figure shows that the loading is dominated by membrane actions, but near the defects and the boundary there are areas with mixed loading. Such a thin plate is not expected to have particularly high bending

stiffness compared to the membrane capacity. In front of the cracks, the deformation mode indicator is close to zero in all simulations, indicating pure membrane loading. However, the 4-HV and 4-45 simulations exhibit areas near the defects where the deformation mode varies and significant bending is observed. On the other hand, in the 1-HV and 1-22.5 simulations the loading is mostly membrane dominated near the slits. The corners are the most confined part of the plate, as seen by the bending dominated loading in this region.

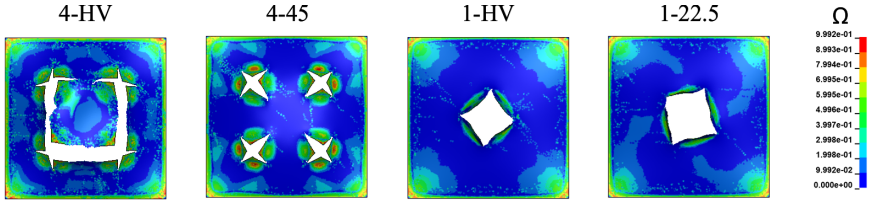

Figure 7: Contour plots of the deformation mode indicator Ω for simulations with $l_e/t_e = 1$ at $t = 1.25$ ms.

In modelling of ductile failure and crack propagation, solid elements are usually the preferred option as long as it is computationally feasible. The simulation time with shell elements ranged from 17 seconds for $l_e/t_e = 5$ to above 13 hours for $l_e/t_e = 1/3$ using 8 cores on an Intel Xeon Gold 5120 CPU. To assess the efficiency of the shell element model, a comparison to a solid element model with the same in-plane dimension as the finest shell model was conducted. The characteristic element size was set to 0.5 mm, resulting in three elements over the thickness and around 1 000 000 elements in total. The model was equivalent to the shell element model apart from the modelling of failure, where the standard Cockcroft-Latham failure criterion was employed (Equation (4)). The simulation time was approximately 6 hours on 28 cores, making the computational cost about 60 % more expensive than for the finest shell element model. The results from the two simulations are compared to the experiment in Figure 8 at selected points in time. By inspection of the figure, the shell element model gives similar results as the solid element simulation. The same trend is observed as in the shell element mode, where the propagating cracks were arrested too early compared to the experiment. However, Granum et al. [8] showed that the solid element model overall gave satisfactory results with regards to fracture initiation and crack propagation for various geometries and materials.

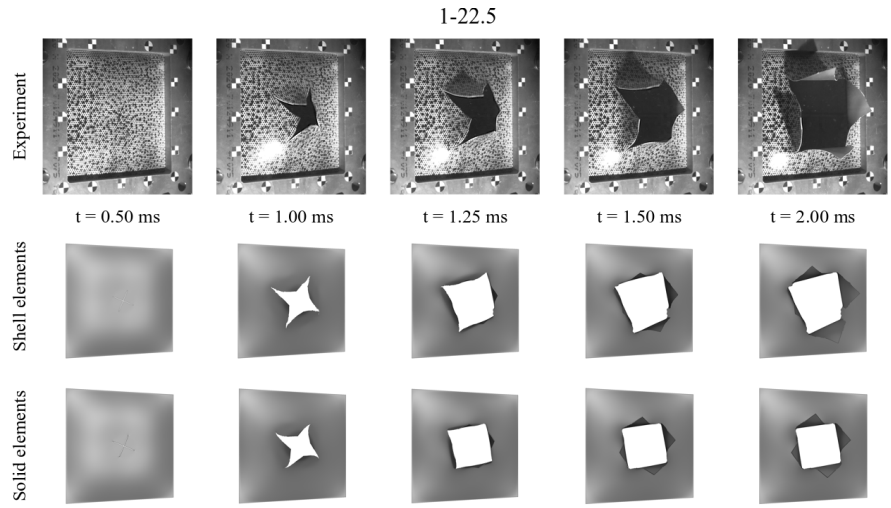

Figure 8: Comparison of a shell element simulation ($l_e/t_e = 1/3$) and a solid element simulation to test 1-22.5 at selected points in time.

5 Conclusions

The behaviour of aluminium plates with crack-like defects subjected to blast loading was investigated numerically and compared to experiments presented by Granum et al. [8]. The finite element analyses employed an uncoupled plasticity and fracture model with through-thickness damage regularization developed for shell elements. The conclusions from the study are summarized in the following.

- The simulated global displacement field of the plates was similar for all mesh sizes.
- A length-to-thickness ratio of the shell elements equal to unity was sufficient to describe initiation of failure in the simulations.
- Initiation and crack propagation were only predicted in the simulations with the finest mesh, i.e., a length-to-thickness ratio of the shell elements equal to 1/3.
- A simulation with solid elements using three elements over the plate thickness gave similar results as the shell element simulation with the finest mesh, but at a higher computational cost.

Acknowledgements

The authors appreciate the financial support from NTNU and the Research Council of Norway through the FRINATEK Programme, Project No. 250553 (FractAl). The

authors would also like to thank Dr. Olaf Engler at Hydro Aluminium Rolled Products in Bonn, Germany, for providing the materials.

REFERENCES

[1] Costas, M., Morin, D., Hopperstad, O.S., Børvik, T. and Langseth, M. A through-thickness damage regularization scheme for shell elements subjected to severe bending and membrane deformations. Journal of the Mechanics and Physics of Solids 123 (2019) 190-206.

[2] Alsos, H.S., Amdahl J. and Hopperstad, O.S. On the resistance to penetration of stiffened plates, Part II: Numerical analysis. International Journal of Impact Engineering 36 (2009) 875-887.

[3] Storheim, M., Alsos, H.S., Hopperstad, O.S and Amdahl J. A damage-based failure model for coarsely meshed shell structures. International Journal of Impact Engineering 83 (2015) 59-75.

[4] Simonsen, B.C. and Törnqvist R. Experimental and numerical modelling of ductile crack propagation in large-scale shell structures. Marine Structures 17 (2004) 1-27.

[5] Woelke, P.B., Shields, M.D., Abboud N.N. and Hutchinson J.W. Simulations of ductile fracture in an idealized ship grounding scenario using phenomenological damage and cohesive zone models. Computational Materials Science 80 (2013) 79-95.

[6] Pack, K. and Mohr, D. Combined necking & fracture model to predict ductile failure with shell finite elements. Engineering Fracture Mechanics 182 (2017) 32-51.

[7] Morin, D., Kaarstad, B.L., Skajaa, B., Hopperstad, O.S. and Langseth, M. Testing and modelling of stiffened aluminium panels subjected to quasi-static and low-velocity impact loading. International Journal of Impact Engineering 110 (2017) 97-111.

[8] Granum, H., Aune, V., Børvik T. and Hopperstad O.S. Effect of heat-treatment of the structural response of blast-loaded aluminium plates with pre-cut slits. International Journal of Impact Engineering 132 (2019) 103306.

[9] Aune, V., Fagerholt, E., Langseth, M. and Børvik, T. A shock tube facility to generate blast loading on structures. International Journal of Protective Structures 7 (2016) 340-366.

[10] Hershey, A.V. The plasticity of an isotropic aggregate of anisotropic face centred cubic crystals. Journal of Applied Mechanics 76 (1954) 241-9.

[11] Hosford, W.F. A generalized isotropic yield criterion. Journal of Applied Mechanics 39 (1972) 607-9.

[12] Vilamosa, V., Clausen, A.H., Børvik, T, Skjervold S.R. and Hopperstad O.S. Behaviour of Al-Mg-Si alloys at a wide range of temperatures and strain rates. International Journal of Impact Engineering 86 (2015) 223-239.

[13] Hosford, W.F. On the crystallographic basis of yield criterion. Textures and Microstructures 26-27 (1996) 479-493.

[14] Cockcroft, M. and Latham D. Ductility and workability of metals. Journal of the Institute of Metals 96 (1968) 33-9.

[15] Belytschko, T., Lin, J.I. and Tsay, C.S. Explicit algorithms for nonlinear dynamics of shells. Computer Methods in Applied Mechanics and Engineering 42 (2) (1984) 225-251.

Part 5

Henrik Granum, David Morin, Tore Børvik,
Odd Sture Hopperstad

Calibration of the modified Mohr-Coulomb fracture model by use of localization analyses for three tempers of an AA6016 aluminium alloy

International Journal of Mechanical Sciences 192 (2021) 106122

International Journal of Mechanical Sciences 192 (2021) 106122

Contents lists available at ScienceDirect

International Journal of Mechanical Sciences

journal homepage: www.elsevier.com/locate/ijmecsci

Calibration of the modified Mohr-Coulomb fracture model by use of localization analyses for three tempers of an AA6016 aluminium alloy

Henrik Granum[a,*], David Morin[a,b], Tore Børvik[a,b], Odd Sture Hopperstad[a,b]

[a] Structural Impact Laboratory (SIMLab), Department of Structural Engineering, NTNU – Norwegian University of Science and Technology, Trondheim, Norway
[b] Centre for Advanced Structural Analysis (CASA), NTNU, Trondheim, Norway

ARTICLE INFO

Keywords:
Ductile fracture
AA6016
Uncoupled damage
Crack propagation
Numerical simulations

ABSTRACT

This paper presents a novel calibration procedure of the modified Mohr-Coulomb (MMC) fracture model by use of localization analyses and applies it for three tempers of an AA6016 aluminium alloy. The localization analyses employ the imperfection band approach, where metal plasticity is assigned outside the band and porous plasticity is assigned inside the band. Ductile failure is thus assumed to occur when the deformation localizes into a narrow band. The metal plasticity model is calibrated from notch tension tests using inverse finite element modelling. The porous plasticity model is calibrated by use of localization analyses where the deformation histories from finite element simulations of notch and plane-strain tension tests are prescribed as boundary conditions. Subsequently, localization analyses are used to establish the failure locus in stress space for proportional loading conditions and thus to determine the parameters of the MMC fracture model. Finite element simulations of notch tension and in-plane simple shear tests as well as two load cases of the modified Arcan test are used to validate the calibrated fracture model. The predictions by the simulations are in good agreement with the experiments, even though some deviations are seen for each temper. The results demonstrate that localization analyses are a cost-effective and reliable tool for predicting ductile failure, reducing the number of mechanical tests required to calibrate the MMC fracture model compared to the hybrid experimental-numerical approach usually applied.

1. Introduction

Modelling and simulation of ductile fracture in metallic materials is an active research field where significant progress has been made over the last decades. This research is important since industries like the automotive industry want to utilize the materials to the brink of failure. Thus, the demand for accurate predictions of fracture by numerical simulations is increasing. Reliable design of structural components against ductile fracture requires a robust numerical framework able to accurately describe the damage and fracture properties of the material. In many lightweight metals, which have received special attention by the automotive industry in recent years, strength and ductility are inversely proportional properties. As strength is often favoured in this case, the ductility imposes a great challenge in design of safety components of such materials.

Nucleation, growth and coalescence of microscopic voids at various length scales is known to be the physical mechanism governing ductile failure. Studies have agreed that the stress state affects the ductility of a metallic material [1–3]. The influence of the hydrostatic stress state was discovered early and has since been included in several fracture models. More recently, the influence of the deviatoric stress state on ductility has been proven through experiments, see [4], for example. This led to proposals of both new and modified versions of existing fracture models to incorporate this dependence. A variety of approaches to model ductile fracture are currently available. Notable mentions are porous plasticity, continuum damage models, forming limit curves and uncoupled damage models. The latter approach is popular due to its simplicity, where the damage evolution is uncoupled from the constitutive equation in contrast to porous plasticity and continuum damage models. Material degradation is thus not accounted for and the damage is merely represented by a scalar variable. This comes with the advantage that the fracture model may be calibrated independently of the plasticity model, simplifying the identification of model parameters significantly. The uncoupled fracture models are usually presented on locus form where the failure strain is defined by the stress state. By this approach, the validity of the failure strain is confined to proportional loading paths. Damage is often accumulated by an integral-based approach where damage evolves with increments of the equivalent plastic strain over the plastic strain path. By employing such a damage accumulation approach, the model is justified in the literature to be valid in simulations involving

* Corresponding author. URL: https://www.ntnu.edu/kt/fractal.
E-mail address: henrik.granum@ntnu.no (H. Granum).
URL: http://www.ntnu.edu/kt/fractal (H. Granum)

https://doi.org/10.1016/j.ijmecsci.2020.106122
Received 29 June 2020; Received in revised form 15 September 2020; Accepted 27 September 2020
Available online 2 October 2020

non-proportional loading paths [5]. However, the extension of this type of model to non-proportional loading is found by Benzerga et al. [6] to be in contradiction with micromechanical observations, and therefore questionable.

Fracture models that incorporate stress triaxiality and Lode parameter dependence usually have the disadvantage of a comprehensive calibration scheme, requiring multiple model parameters to be calibrated from different types of mechanical tests. Often a hybrid experimental-numerical approach is employed, where the stress and strain histories are extracted from the critical element in a finite element simulation of the test. The optimal set of parameters is then found by comparing the curves from the simulations to those of the experiments. The accuracy of this approach relies on experiments that cover a range of stress states and exhibit close to proportional loading paths all the way to fracture. The latter requirement is difficult to fulfil for most stress states. As an alternative to this approach, localization analyses may be used to predict ductile failure. An underlying assumption here is that strain localization is a precursor to failure, and thus may be regarded as the onset of fracture. Mechanical tests are then only needed to calibrate the constitutive equations used in the localization analyses and there is no requirement for proportional loading paths. Morin et al. [7] combined unit cell simulations and localization analyses to predict failure of a steel under non-proportional loading. The numerical results were validated against experimental results reported by Basu and Benzerga [8] and found to be in good agreement. The versatility and effectiveness of the localization analyses were demonstrated by Morin et al. [9] where failure loci of metals were generated from localization analyses and applied to an advanced high-strength steel subjected to proportional loading paths. The results were evaluated against 3D unit cell analyses by Dunand and Mohr [10] and proven to give comparable results in a fraction of the computational time. Gruben et al. [11] applied an experimental-numerical approach to determine the strain localization and ductile fracture of two dual-phase steels. Four tests that covered stress states from simple shear to equi-biaxial tension were conducted. Numerical simulations of the tests were performed, and the failure strains were estimated by comparison to the experimental data. Localization analyses by use of the imperfection band approach were conducted to predict the onset of localization. The results indicated that the localization analyses provided conservative values of the failure strains and that the stress state inside the band tends to move towards a generalized shear state prior to localization. Bergo et al. [12] used unit cell simulations and localization analyses to calibrate failure loci for three different steels. The study was confined to generalized tension stress states and thus only the dependence on stress triaxiality was included. The uncoupled plasticity and fracture models were calibrated based on a single uniaxial tension test and micromechanical simulations using unit cells, metal and porous plasticity and localization theory. The predicted ductility was somewhat conservative for Weldox 460E and non-conservative for Weldox 900E, but accurate for Weldox 700E. It was emphasized that the accuracy of the localization analyses relies heavily on an accurate calibration of the porous plasticity model. However, it was noted that this approach is well suited to reduce the experimental programme required to calibrate fracture models.

Wierzbicki et al. [13], Li et al. [14], Gruben et al. [15] and Bai et al. [16] have all presented studies comparing the predictive capabilities of different uncoupled fracture criteria for various steels and aluminium alloys. Several of the criteria evaluated are heuristic extensions of well-known criteria like the Mohr-Coulomb (MC), Cockcroft-Latham (CL), Rice-Tracey (RT) and Wilkins criteria to name a few. As Wierzbicki et al. [13] pointed out, the quality of a fracture criterion intended for industrial application may be roughly measured by the performance and the cost. Here, performance is defined by the accuracy of simulations compared to experimental tests, while the cost is related to the number of mechanical tests needed to calibrate the model and the complexity related to this. Among the criteria with only one mechanical test required for calibration is the CL criterion. It has been used with success in many studies and is favoured by many for its simplicity and versatility [17,18]. However, it is evident that the criterion has its limitations as it postulates lower ductility in generalized tension than in generalized shear for low and moderate stress triaxiality. The modified Mohr-Coulomb (MMC) fracture model was proposed by Bai and Wierzbicki [19], where parameters used to control both the dependence of the stress triaxiality and the Lode parameter were introduced. The model provides a monotonic decrease in ductility for increasing stress triaxiality, which is coupled with an asymmetric function of the Lode parameter. The model has been proposed in various versions and is extensively used in the literature. Bai and Wierzbicki [19] calibrated the MMC fracture model for an AA2024 T351 aluminium alloy and a TRIP690 steel, and validated it against various mechanical tests. Accurate predictions of fracture initiation were obtained, but it was noted that the predictions were less accurate in generalized tension. Dunand and Mohr [20] investigated the predictive capability of the MMC fracture model by comparing predictions to fracture experiments on TRIP780 steel. Nine different experiments were used in the comparison covering wide ranges of stress triaxiality and Lode parameter. Fracture initiation was correctly predicted in all simulations of the tests. It was suggested that the underlying physics of the fracture model is of less importance than its mathematical flexibility, implying that even though phenomenological fracture models are motivated by micromechanical observations, their ability to fit experimental data is a superior characteristic. However, a fracture model with high flexibility allows erroneous calibration and requires detailed knowledge by the user.

A modification of the MMC fracture model denoted the Hosford-Coulomb (HC) fracture model was proposed by Mohr and Marcadet [5], where the von Mises equivalent stress was replaced by the Hosford equivalent stress in combination with the normal stress acting on the plane of maximum shear. The HC fracture model is based on the extensive study on 3D unit cells by Dunand and Mohr [10], thus it has a micromechanical foundation in contrast to the MMC fracture model. The HC fracture model was presented on locus form, and damage accumulation was taken care of by an integral-based approach. Fracture experiments on three different steels were conducted and three experiments were used to calibrate the fracture criterion. When compared against the experiments, the simulations showed good agreement for the three materials and fracture was accurately predicted in all cases. Gorji and Mohr [21] and Zhang et al. [22] investigated ductile fracture in the aluminium alloy AA6016. In Gorji and Mohr [21], the HC fracture model was employed in combination with an anisotropic plasticity model to predict shear fracture in deep drawing tests. Eight cup drawing experiments were used in the calibration process to increase the robustness of the fracture model. The results show that the plasticity and fracture models can predict the location and the onset of fracture with good accuracy. In Zhang et al. [22], an anisotropic Drucker yield function and a fracture criterion proposed by Lou et al. [23] were employed, where a simple shear test and two notch tension tests with different radii were used in the calibration of the fracture criterion. By comparing the experiments to the simulations it was found that the onset of fracture was accurately predicted in tests ranging from simple shear to uniaxial tension.

In the present study, we apply an isotropic plasticity and fracture model to predict ductile fracture in various experiments, where specimens are taken from AA6016 aluminium alloy sheets in three different tempers. The MMC fracture model was selected and calibrated by use of localization analyses based on two mechanical tests. The study is a natural extension to the work by Bergo et al. [12] where a stress triaxiality dependant fracture model was investigated together with an isotropic plasticity model. The aim of the study is to assess the accuracy of the calibrated MMC fracture model by comparison against mechanical tests, where the model's ability to predict fracture initiation and crack propagation is evaluated for a range of stress states. The results demonstrate that the use of localization analyses to calibrate a fracture model has

Table 1
The chemical composition of AA6016 in wt%.

Si	Mg	Fe	Cu	Mn	Cr	Zn	Ti	Al
1.3160	0.3490	0.1617	0.0081	0.0702	0.0025	0.0084	0.0175	Balance

the potential to be a cost-effective and accurate way of predicting ductile fracture and crack propagation.

2. Materials and mechanical tests

2.1. Materials

Experiments were conducted on three different tempers of the aluminium alloy AA6016. The materials were delivered as 1.5 mm thick plates with in-plane dimensions 625 mm × 625 mm in tempers T4, T6 and T7 by Hydro Aluminium Rolled Products in Bonn. This alloy is mainly used in the automotive industry as outer body panels due to its excellent surface quality, good formability, and high strength. To obtain the various tempers, all plates were first solution heat-treated at 530 °C before being air quenched to reach temper T4. Tempers T6 and T7 were then obtained for some of the plates by artificial ageing for 5 h at 185 °C and for 24 h at 205 °C, respectively. The chemical composition of the alloy is given in Table 1. The yield strength of the tempers ranges from about 135 MPa for T4 to 245 MPa for T6, and the ultimate tensile strength ranges from roughly 200 MPa for T7 to just below 300 MPa for T6. All mechanical tests were carried out with the longitudinal axis along the rolling direction, unless specified otherwise. The initial thickness of all specimens was measured and found to be similar to the nominal plate thickness of 1.5 mm. An Instron 5985 series universal testing machine was used in all tests, where the force was measured by a 30 kN load cell attached to the actuator. A Prosilica GC2450 camera orientated perpendicular to the in-plane axes of the specimen captured images from all tests. All specimens were spray-painted with a speckle pattern to enable 2D digital image correlation (2D-DIC) by use of the in-house software eCorr [24].

2.2. Uniaxial tension tests

In Granum et al. [25], uniaxial tension tests in three different directions with respect to the rolling direction (0°, 45° and 90°) of the plates were conducted. Additional uniaxial tension tests in the rolling direction of the plate were conducted only for temper T4 in conjunction with the material test programme presented in this study. This was done to monitor the natural ageing that occurs in temper T4 under prolonged room temperature storage, resulting in solute clustering. This effect is known to slightly strengthen the alloy. The specimen had a gauge length of 70 mm and a width of 12.5 mm, and is depicted in Fig. 1a). The tests were conducted with a crosshead velocity of 2.1 mm/min, resulting in an initial strain rate of 5×10^{-4} s^{-1} in the gauge region. A virtual extensometer with an initial length of 60 mm was used to extract displacements by use of 2D-DIC.

2.3. Notch tension tests

Notch tension tests in the rolling direction with two different notch radii were conducted, with geometry inspired by the specimens used in Erice et al. [26]. The two specimens are denoted NT10 and NT3, and the geometries are depicted in Fig. 1b) and Fig. 1c), respectively. The NT10 specimen had a notch radius of 10 mm, while the NT3 specimen had a notch radius of 3.35 mm. The minimum width of the notch was 5 mm for both geometries. The specimens were tested with a crosshead velocity of 0.6 mm/min. Force measurement from the load cell and images from the camera were recorded at 2 Hz. Two sets of virtual extensometers available in eCorr were used in the post-processing of the experiments, one global and one local. The initial length of the global and local virtual extensometers was 15 mm and 2 mm, respectively, for both test geometries and the virtual extensometers were placed centric to the notch radius.

2.4. Plane-strain tension tests

The geometry of the plane-strain tension (PST) specimen is depicted in Fig. 1d). It had a length of 100 mm and a width of 40 mm. The opening of the notch was 10 mm and the width at the narrowest point inside the notch was measured to 17.33 mm. The force was measured by the load cell and images were taken by the camera at 2 Hz. The tests were conducted with mechanical clamps, where the clamped region on each side of the gauge was approximately 40 mm × 35 mm. Prior to testing, the clamped regions of the specimen were sanded down to ensure good grip between the clamps and the specimen. The tests were conducted with a crosshead velocity of 0.4 mm/min. Two global virtual extensometers with an initial length of 10 mm positioned approximately 16 mm from the centre of the notch were used to extract the displacements in the DIC calculations. The displacements from two virtual extensometers in eCorr were used to ensure that no rotations were enforced during loading. A local virtual extensometer with a gauge length of 2 mm placed centric across the notch was used to obtain local measurements from the tests.

2.5. In-plane simple shear tests

The in-plane simple shear (ISS) specimen had a gauge length of 5 mm and the geometry is depicted in Fig. 1e). The tests were conducted with a crosshead velocity of 0.15 mm/min in an attempt to obtain an initial strain rate in the gauge region of 5×10^{-4} s^{-1}. A virtual extensometer in eCorr spanning across the gauge region with an initial length of 10.05 mm was used to extract displacements. A camera aimed perpendicular to the in-plane surface captured images and force measurements were recorded by the load cell, both at 1 Hz.

2.6. Modified Arcan tests

Six modified Arcan specimens were cut from a plate of each temper. The geometry of the specimen is given in Fig. 1f). The specimen was clamped by four loading brackets using 12 M6-bolts as shown in Fig. 2. Two different load cases were applied by altering the loading direction β; three with $\beta = 90^{\circ}$ and three with $\beta = 45^{\circ}$ as shown in Fig. 2a) and Fig. 2b), respectively. All tests were conducted with a crosshead velocity of 1 mm/min, similar to those carried out in [27]. The tests are abbreviated "Arcanβ" to distinguish between the two load cases. In the Arcan90 tests, the specimen is loaded in a tension mode where the load axis coincides with the specimen's longitudinal axis. The pin connecting the mounting brackets to the test machine allows the mounting brackets and specimen to rotate when loaded, enabling the specimen to tear open. In the Arcan45 tests, the specimen is subjected to a mixed-mode loading. The width at the narrowest point in the gauge section was measured to 32 mm with negligible variations between the specimens. A virtual extensometer of initial length 10.5 mm spanning across the notch along the longitudinal axis of the specimen in eCorr was used to extract displacements by use of 2D-DIC.

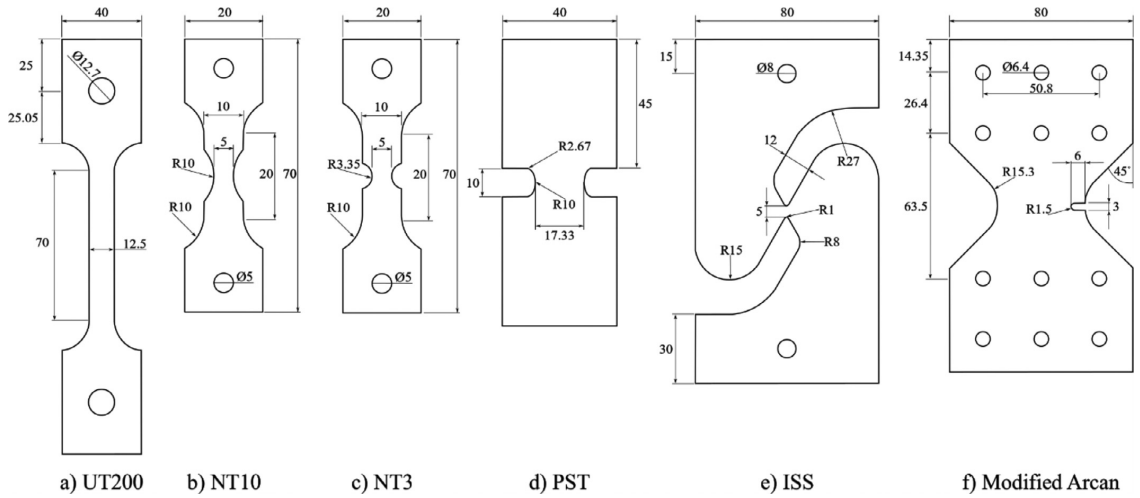

Fig. 1. Geometry of test specimens with measures in mm: a) uniaxial tension, b) and c) notch tension, d) plane-strain tension, e) in-plane simple shear and f) modified Arcan.

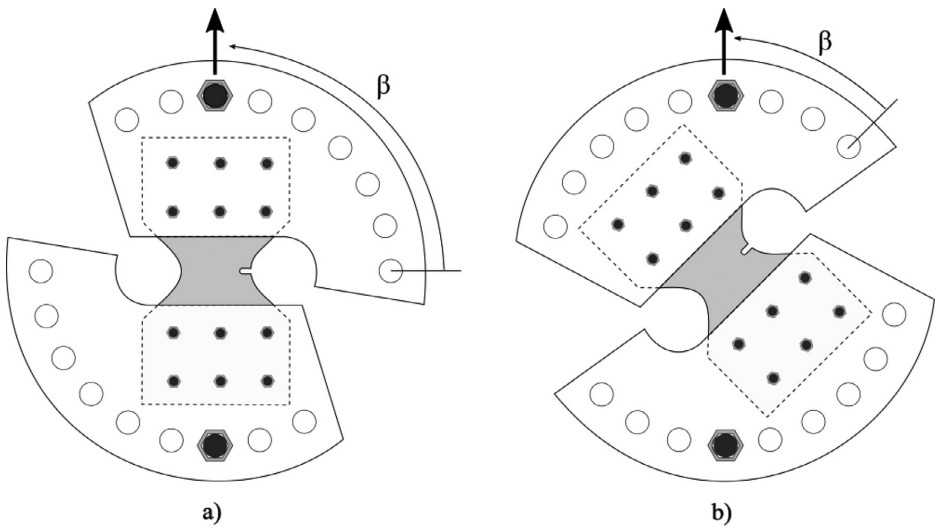

Fig. 2. Test setup of a modified Arcan specimen with a) $\beta = 90^{\circ}$ and b) $\beta = 45^{\circ}$

3. Experimental results

3.1. Uniaxial tension tests

Engineering stress-strain curves of representative tests from Granum et al. [25] are plotted in Fig. 3a). A slight variation in elongation at fracture between the different tensile directions is seen for each of the tempers, while the flow stress showed a maximum deviation of 3%. The Lankford coefficients R_α were calculated for all tension tests and are listed in Table 2, where α denotes the angle with respect to the rolling direction. All coefficients are below unity and somewhat higher in the rolling direction. The similarity in flow stress between the three directions suggests that the alloy exhibits isotropic properties with respect to strength and strain hardening. However, the Lankford coefficients suggest that the material is prone to thinning and exhibits moderate anisotropy in plastic flow. The equivalent strain at the onset of fracture was found by use of DIC where a characteristic element size of 0.57 mm was used. Multiple DIC simulations with a slightly shifted position of the mesh were conducted to avoid results biased by the DIC mesh. For the tests in the rolling direction, the average logarithmic fracture strain came out as 0.70, 0.33 and 0.73 for tempers T4, T6 and T7, respectively.

Table 2
Lankford coefficients R_α for representative tension tests.

Temper	R_0	R_{45}	R_{90}
T4	0.58	0.45	0.44
T6	0.69	0.48	0.55
T7	0.77	0.57	0.62

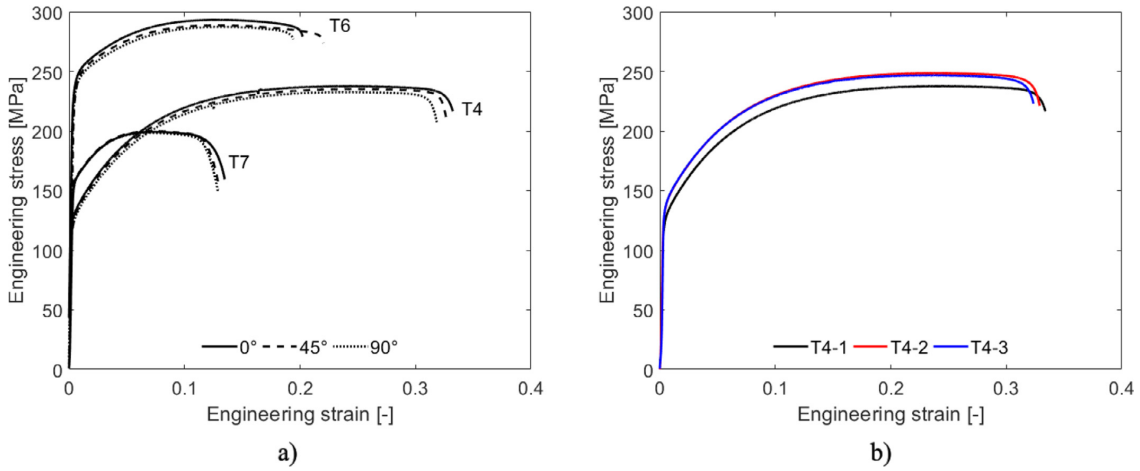

Fig. 3. Engineering stress-strain curves from: a) representative tests presented in Granum et al. [25] and b) representative tests in temper T4 conducted in conjunction with the mechanical tests to monitor the effect of natural ageing.

These values represent the strain where fracture initiates at the surface of the specimen.

The engineering stress-strain curves for three sets of temper T4 tests are presented in Fig. 3b). The T4–1 curve is a representative test in the rolling direction from Fig. 3a). T4–2 is a test conducted in conjunction with the modified Arcan tests and T4–3 is a test conducted in conjunction with the plane-strain tension and in-plane simple shear tests. The numbering of the tests indicates the order they were performed in, i.e., the T4–1 test was conducted at an earlier point in time than the T4–2 test, which was performed prior to the T4–3 test. It is seen that natural ageing increases the strength as the T4–2 and T4–3 curves are shifted upwards compared to the T4–1 curve. However, the natural ageing seems to have reached saturation when the Arcan tests were done, as the difference between the T4–2 and T4–3 curves is negligible. This effect was also investigated by Engler et al. [28] for the same material and the reader is referred to this work for a thorough discussion of this phenomenon. Due to the negligible differences between the T4–2 and T4–3 curves, the need for multiple calibrations of the plasticity model for this temper was deemed unnecessary.

3.2. Notch tension tests

The experimental results from the NT10 and NT3 tests are shown in Fig. 4. The repeatability of the notch tension tests was excellent, and thus only one test per configuration is plotted. The displacement was extracted from the global virtual extensometer while the logarithmic strain is calculated from the displacement measured by the local virtual extensometer. The force levels between the two test geometries are similar while the displacements are slightly larger for the largest notch radius. The local strain is also seen to be higher in the tests with the largest notch radius. This is expected as the sharper notch radius confines the gauge section more than the larger notch radius, resulting in higher stress triaxialities within this region.

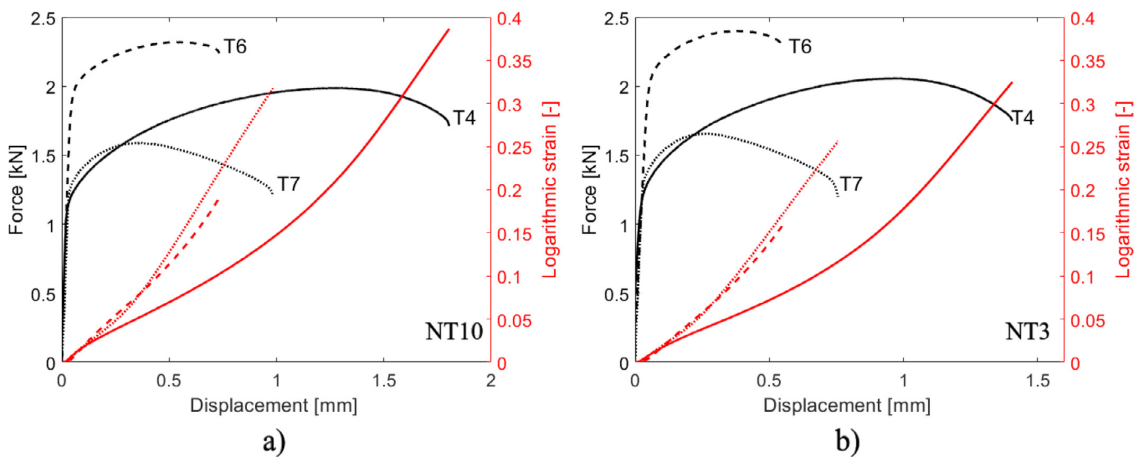

Fig. 4. Experimental results from the a) NT10 and b) NT3 tests in terms of force-displacement and logarithmic strain-displacement curves.

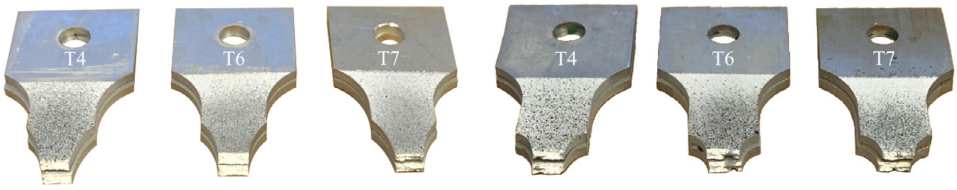

Fig. 5. Fracture surfaces of a) NT10 and b) NT3 tests for the three tempers.

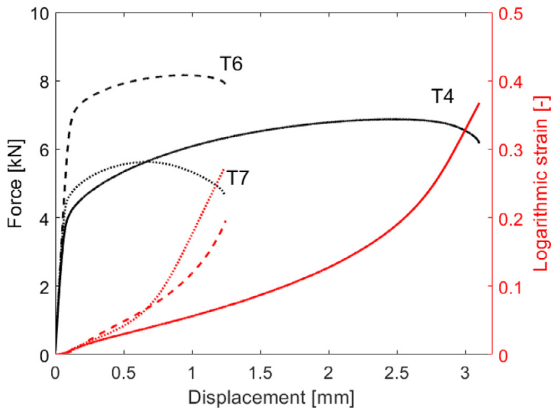

Fig. 6. Force-displacement and logarithmic strain-displacement curves from plane-strain tension (PST) tests.

Fractured specimens from the six different notch tension tests were examined by visual inspection and are shown in Fig. 5. Only one test per configuration is shown as negligible differences were seen between fracture surfaces of repeated tests. A slant fracture surface was found for all tests, even though some NT3 tests displayed rough shear lips. In general, the fracture surfaces were rougher for temper T7 than for tempers T4 and T6, and shear lips were more prominent in the NT3 tests than in the NT10 tests.

3.3. Plane-strain tension tests

The force-displacement and logarithmic strain-displacement curves from representative plane-strain tension tests are shown in Fig. 6. Duplicate tests are not shown due to the excellent repeatability. The results are in accordance with the trends seen for the notch tension tests, where the most prominent difference being the similarity in elongation at fracture between tempers T6 and T7. The fracture initiated in the centre of the specimen for all tests and propagated in a straight line towards the free edges, perpendicular to the loading direction as seen in Fig. 7. For the tests in temper T6, the crack propagated instantly resulting in a sudden loss of load-carrying capacity, while the tests in temper T4 exhibited slightly slower crack propagation. Only the T6–3 test experienced complete fracture, where the specimen was pulled apart. In the rest of the tests, the force level dropped below a threshold limit at which the test was stopped automatically. For the tests in temper T7, the crack propagated slowly and it took approximately 40 s from initiation to completion. By inspection of the fractured T6–3 specimen shown in Fig. 7, a slant fracture surface was observed, where the crack was seen to flip to the other admissible shear band.

3.4. In-plane simple shear tests

The force-displacement curves from the shear tests are shown to the left in Fig. 8 where the numbered markers coincide with the numbered images on the right-hand side. Owing to slight scatter, results from all repeat tests are presented. The strain fields obtained by 2D-DIC reveal that strains localized in a thin band across the gauge section in all tests (not shown for brevity). By inspection of the images, fracture seemingly occurred simultaneously within this band, as the origin of fracture initiation was difficult to pinpoint exactly. In-plane rotations were observed in all tests, resulting in an angle of the localized deformation band compared to the loading direction, as evident from the images in Fig. 8. The angle of the band with respect to the loading direction was similar between repetitions and tempers. The drop in the force-displacement curves, particularly for temper T7, is presumed to occur due to the combined effect of material softening and area reduction in the localized deformation band. The shear tests indicated that temper T7 has superior ductility compared to tempers T4 and T6, and the high ductility makes it difficult to pinpoint the onset of fracture in the temper T7 tests. By inspection of the images, the onset of fracture is anticipated to occur somewhere between point 2 and 3 in the representative force-displacement curve for temper T7 in Fig. 8. All specimens displayed a smooth and flat fracture surface through the thickness, and there were negligible differences among repetitions and tempers.

3.5. Modified Arcan tests

The force-displacement curves from the modified Arcan45 and Arcan90 tests are shown in Fig. 9a) and Fig. 9b), respectively. Overall, the trends are in accordance with the other mechanical tests presented showing that temper T6 gives the highest peak force followed in turn by tempers T4 and T7. The peak forces are consistently higher in the Arcan90 tests than in the Arcan45 tests, and the ratio between the peak forces in the two load cases is almost identical amongst the tempers. The displacement at peak force is smaller in the Arcan45 tests than in the Arcan90 tests, but the final displacement is larger in the former. This is linked to the crack paths being longer in the Arcan45 tests than in the Arcan90 tests, especially for tempers T4 and T6. As Fig. 9b) indicates, the Arcan90-T6 test experienced a sudden loss of load-carrying capacity as the crack propagated instantly across the specimen between two images of the test. Even though temper T7 is the most ductile alloy condition, the tests in temper T4 exhibits the largest displacements. This is linked to the combination of adequate strength, work-hardening and ductility in temper T4, which seems to be more favourable than the high ductility and low work-hardening seen for temper T7 in these tests.

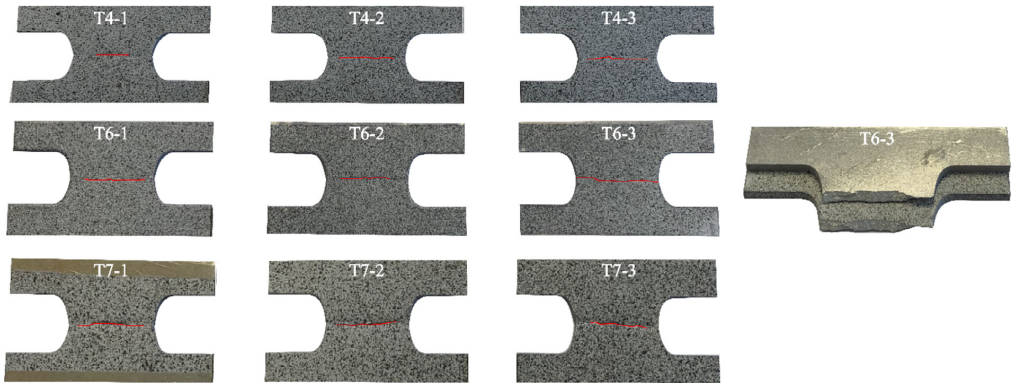

Fig. 7. Fractured plane-strain tension specimens and fracture surface of test specimen T6–3. The red lines on the pictures indicate the crack path. (For interpretation of the references to colour in this figure legend, the reader is referred to the web version of this article.)

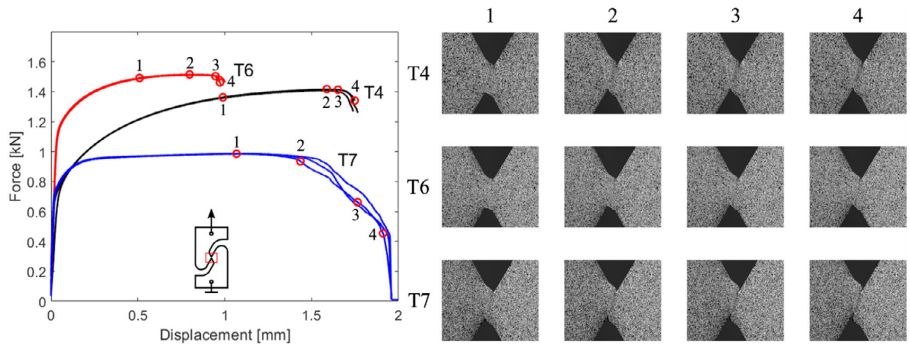

Fig. 8. Force-displacement curves from the in-plane simple shear (ISS) tests where the numbered markers coincide with the images on the right-hand side.

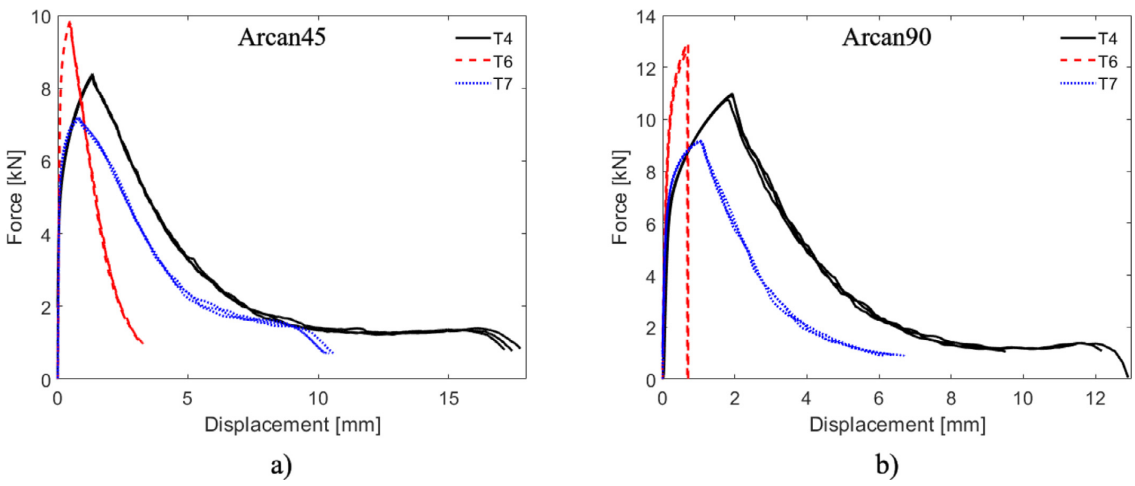

Fig. 9. Force-displacement curves from a) the Arcan45 tests and b) the Arcan90 tests.

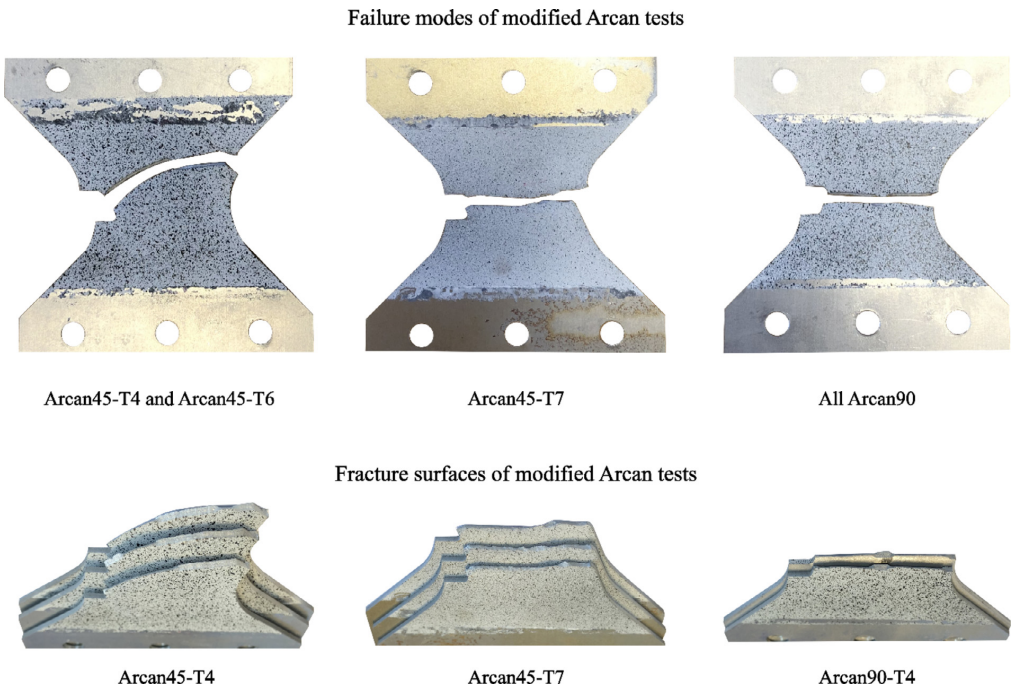

Fig. 10. Fractured specimens showing the different fracture modes of the modified Arcan tests with corresponding fracture surfaces.

Fractured specimens from the modified Arcan tests are shown in Fig. 10. In the upper part of the figure, the three different fracture modes observed in the tests are displayed. A curved crack path was observed in both the Arcan45-T4 and the Arcan45-T6 tests. In the Arcan45-T6 tests, the crack was arrested approximately 10 mm from the edge and the tests were stopped as the force level dropped below a lower threshold. In the Arcan45-T4 tests, the crack was arrested approximately 5 mm from the edge when stopped, but during the dismantling of the specimens from the loading brackets, the specimens were pulled apart. By inspection of the fracture surfaces from the Arcan45-T4 tests, all three tests exhibited the alternating slant fracture phenomenon. The crack initiated and propagated in a slant fracture mode until arrested. By inspection of the Arcan45-T6 specimen, the fracture initiated in a V-mode and propagated in this mode for approximately 3 mm before it transitioned to a slant fracture mode. The alternating slant fracture phenomenon was not observed in any of these tests. The V-mode was also seen in Gruben et al. [29] for Arcan45 specimens made of Docol 600DL steel. In the Arcan45-T7 tests, fracture initiated in a V-mode within the same area as for the Arcan45-T4 and Arcan45-T6 tests, and the crack initially followed a similar curved path. However, the crack path deflected abruptly after a few millimetres and propagated perpendicularly to the longitudinal axis of the specimen as shown in Fig. 10. The fracture surfaces were rough with evident shear lips. All the Arcan90 tests exhibited a similar crack path for all three tempers, but differences in the fracture surfaces were seen. In the Arcan90-T4 tests, the fracture initiated and propagated in a slant fracture mode where the crack was seen to flip abruptly throughout the deformation in all tests. One of the Arcan90-T6 tests initiated in a V-mode before a transition to slant fracture was seen, while the two others initiated in a slant fracture mode. Both the Arcan90-T4 and Arcan90-T6 tests showed a smooth fracture surface, while the Arcan90-T7 tests had a rougher fracture surface, similar to what was seen in the Arcan45-T7 tests.

4. Modelling and simulation

4.1. Stress state parameters

Any admissible stress state can be expressed by the three ordered principal stresses $\sigma_1 \geq \sigma_2 \geq \sigma_3$ given by

$$\sigma_1 = \frac{2}{3}\sigma_{\mathrm{vM}} \cos(\theta) + \sigma_{\mathrm{h}} \tag{1a}$$

$$\sigma_2 = \frac{2}{3}\sigma_{\mathrm{vM}} \cos\left(\theta - \frac{2\pi}{3}\right) + \sigma_{\mathrm{h}} \tag{1b}$$

$$\sigma_3 = \frac{2}{3}\sigma_{\mathrm{vM}} \cos\left(\theta + \frac{2\pi}{3}\right) + \sigma_{\mathrm{h}} \tag{1c}$$

where $0 \leq \theta \leq \frac{\pi}{6}$ is the deviatoric angle, $\sigma_{\mathrm{vM}} = \sqrt{3J_2}$ is the von Mises equivalent stress, and $\sigma_{\mathrm{h}} = I_1/3$ is the hydrostatic stress. Here, J_2 and I_1 are the second principal deviatoric stress invariant and the first principal stress invariant, respectively. The stress state may be conveniently described by the stress triaxiality T and the Lode parameter L. The stress triaxiality is defined as the ratio between the hydrostatic stress σ_{h} and the von Mises equivalent stress σ_{vM}, viz.

$$T = \frac{\sigma_{\mathrm{h}}}{\sigma_{\mathrm{vM}}} \tag{2}$$

The Lode parameter describes the deviatoric stress state, and is defined either in terms of the deviatoric angle θ or the ordered principal stresses (σ_1,σ_2,σ_3) as

$$L = \sqrt{3}\tan\left(\theta - \frac{\pi}{6}\right) = \frac{2\sigma_2 - \sigma_1 - \sigma_3}{\sigma_1 - \sigma_3} \tag{3}$$

The range of the Lode parameter is $L \in [-1, +1]$, where $L = -1$, 0 and + 1 represent states of generalized tension, generalized shear and generalized compression, respectively.

4.2. Plasticity model

The constitutive relation is given by the high-exponent yield surface proposed by Hershey [30] and Hosford [31], the associated flow rule and an extended Voce hardening rule. Even though the material exhibits moderate plastic anisotropy according to the Lankford coefficient, an isotropic plasticity model is applied. The equivalent stress is given by the principal stresses as

$$\sigma_{\text{eq}} = \left(\frac{1}{2}\left(|\sigma_1 - \sigma_2|^a + |\sigma_2 - \sigma_3|^a + |\sigma_3 - \sigma_1|^a\right)\right)^{\frac{1}{a}} \tag{4}$$

where a is a parameter controlling the curvature of the yield surface. This parameter is set to $a = 8$ in this study as suggested by Hosford [32] based on polycrystal plasticity calculations. The yield function is expressed as

$$\phi = \sigma_{\text{eq}} - \sigma_{\text{M}} = \sigma_{\text{eq}} - \left(\sigma_0 + R(p)\right) \leq 0 \tag{5}$$

where σ_{M} is the matrix material flow stress, σ_0 is the yield stress, R is the hardening variable and p is the equivalent plastic strain. The hardening variable is defined by an extended Voce hardening rule on the form

$$R(p) = \sum_{i=1}^{3} R_i(p) = \sum_{i=1}^{3} Q_i\left(1 - \exp\left(-C_i p\right)\right) \tag{6}$$

where R_i are hardening terms that saturate at different levels of plastic strain. The hardening parameters Q_i and C_i work in pair controlling the strain hardening of the material.

4.3. MMC fracture model

Fracture in the simulations is governed by a modified Mohr-Coulomb fracture model. The version of the Mohr-Coulomb model used in this study was inspired by the one proposed by Bai and Wierzbicki [19]. They transformed the original model into locus form where the failure strain $\bar{\varepsilon}_{\text{f}}$, i.e., the equivalent plastic strain at failure, was defined in terms of the stress triaxiality T and the Lode angle parameter $\bar{\theta}$. The latter is a normalized parameter of the Lode angle and is within the range $\bar{\theta} \in [-1, +1]$. In this study, the Lode parameter L is used instead of the Lode angle parameter $\bar{\theta}$, and the expression for the failure strain $\bar{\varepsilon}_{\text{f}}$ is then given as [19]

$$\bar{\varepsilon}_{\text{f}}\,(L,T) = \left\{ \frac{K}{\hat{C}_2}\left[\hat{C}_3 + \frac{\sqrt{3}}{2-\sqrt{3}}\left(\hat{C}_4^* - \hat{C}_3\right)\left(\sec\left(\frac{-L\pi}{6}\right) - 1\right)\right] \times \left[\sqrt{\frac{1+\hat{C}_1^2}{3}}\cos\left(\frac{-L\pi}{6}\right) + \hat{C}_1\left(T + \frac{1}{3}\sin\left(\frac{-L\pi}{6}\right)\right)\right]\right\}^{-\frac{1}{n}} \tag{7}$$

where

$$\hat{C}_4^* = \begin{cases} 1 & \text{for} \quad -1 \leq L \leq 0 \\ \hat{C}_4 & \text{for} \quad 0 < L \leq 1 \end{cases} \tag{8}$$

The model has six parameters that must be calibrated: $\hat{C}_1$ governs the pressure dependence; $\hat{C}_2$ and K control the overall ductility; $\hat{C}_3$ determines the Lode parameter dependence; $\hat{C}_4$ governs the asymmetry of the failure locus between states of generalized tension and compression; and increasing values of n shift the ductility upwards and decrease the stress triaxiality and Lode parameter dependence [19].

Damage is introduced by the damage variable D which is set to evolve with increments of the equivalent plastic strain p, given as

$$D(p) = \int_0^p \frac{\mathrm{d}p}{\bar{\varepsilon}_{\text{f}}(L,T)} \tag{9}$$

The material is undamaged in its initial configuration, i.e., $D = 0$, and fracture initiates when $D = 1$. Whereas the failure locus is valid for proportional loading only, the damage accumulation rule is assumed to account for non-proportional load paths in an approximate way.

4.4. Finite element modelling

The finite element (FE) simulations of the mechanical tests used in the calibration process were conducted with the implicit solver of Abaqus [33] with displacement-controlled loading. All simulations with the MMC fracture model were conducted using the explicit solver of Abaqus with velocity-controlled loading. The specimens were discretized by use of 8-node linear brick elements with selective reduced integration, denoted C3D8 in Abaqus. Fracture is modelled by element erosion, where elements are removed when D in Eq. (9) reaches unity. In the simulations of the NT3, NT10 and PST tests, three symmetry planes were utilized, and the reduced models were optimized with respect to the number of elements. The validity of the reduced models with optimized mesh design was verified against selected simulations of the full specimen with a dense, uniform mesh. The differences in the predicted crack initiation and propagation between simulations with the optimized and uniform mesh designs were negligible. The maximum time step in the implicit simulations was selected so that each simulation had around 200 increments. All simulations were conducted with 5 elements over the half-thickness and an in-plane discretization in the gauge region with a characteristic element size of 0.15 mm. This resulted in initially cubic-shaped elements in the gauge region.

An in-plane view of the FE models with the mesh depicted on the initial geometry of the specimens is shown in Fig. 11. In all simulations, except for the simulations of the PST tests, the load was assigned to a reference node positioned in the centre of the pinhole. An MPC beam constraint was used to connect the reference node to the element set on the boundary of the specimen, to mimic the effect of a pin pulling the specimen. This is visualized by the red lines and the blue reference nodes in Fig. 11. This approach limits the number of elements in the FE models significantly and presumes that the omitted part moves as a rigid body. Also, the rotations induced by the pinned link is recognized in this modelling approach by allowing the reference node to rotate in-plane. In the simulation of the PST test, the clamped area was assumed to behave as a rigid body and thus omitted in the model. The boundary conditions were thus assigned to the edges bordering to the clamped regions of the model. The ISS and modified Arcan test specimens were modelled according to Fig. 11d)-e), where only through-thickness symmetry was utilized. In the ISS model, two reference nodes connected to the edges of the specimen were applied to allow for in-plane rotations. In the modified Arcan model, the part of the specimen gripped by the clamping frame was presumed to move as a rigid body and was thus omitted from the model. In-plane rotations were accounted for by inserting reference nodes coinciding with the centre of the two loading pins shown in Fig. 2. The reference nodes were connected to the edges of the specimen by an MPC beam constraint. This approach simplifies the model substantially and enables feasible computational times with the desired discretization. In all explicit simulations, the velocity was ramped up over the first 10% of the simulation time, and the energy balance was carefully checked to ensure quasi-static loading conditions.

4.5. Localization analyses

The localization analyses were conducted using the imperfection band approach, following the work by Rice [34]. A detailed description of the approach used in this study can be found in Morin et al. [9], and only a brief overview is given herein. A solid, homogenous body that is homogeneously deformed is considered. Within this body, a thin planar band is assumed to exist where stress and strain rates are allowed to be different from their values outside the band. However, continuing equilibrium and compatibility across the imperfection band are enforced. The normal to the band is denoted $\boldsymbol{n}$ and a sketch of a solid body with a planar band is depicted in Fig. 13. Localization is set to occur when the strain rate inside the band becomes infinite. The critical orientation of the band is not known on beforehand and localization analyses covering a range of band orientations must be conducted to find the one

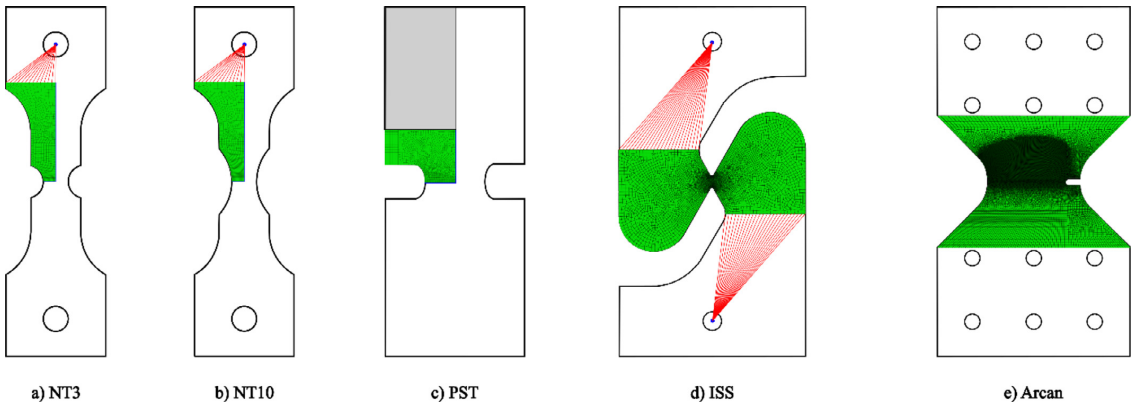

Fig. 11. Finite element meshes of test specimen: a) NT3, b) NT10, c) PST, d) ISS and e) modified Arcan.

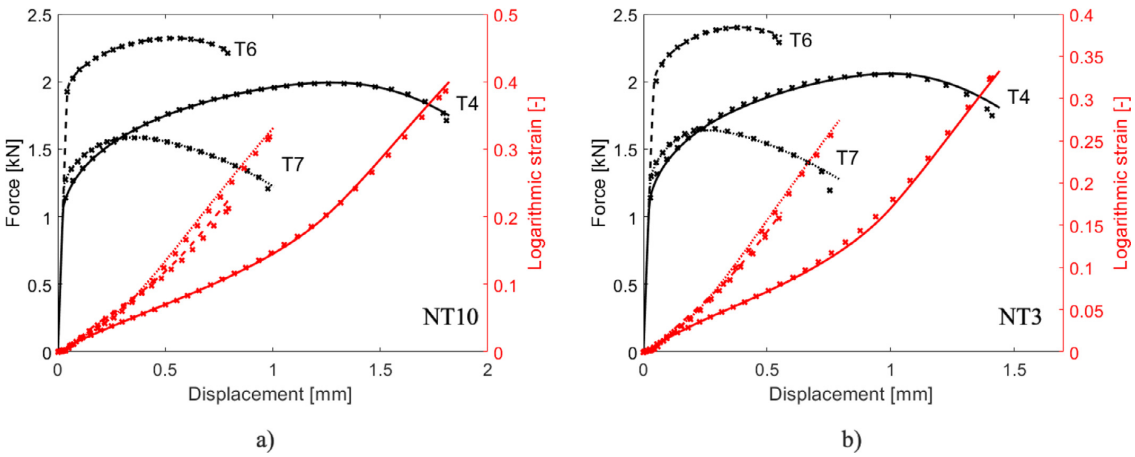

Fig. 12. Experimental (crosses) and numerical force-displacement and logarithmic strain-displacement curves of the three tempers for a): NT10 and b): NT3.

exhibiting the lowest ductility. The failure strain is taken as the equivalent plastic strain outside of the imperfection band at localization inside the band.

The solid body is governed by the plasticity model described in Section 4.2. Inside the band, a porous plasticity model is used to represent the material behaviour, which enables a simple approach to introduce an imperfection by nucleation and growth of voids. The heuristic extension of the Gurson-Tvergaard model [35,36] proposed by Dæhli et al. [37] is adopted, where the yield condition is given by

$$\Phi = \left(\frac{\sigma_{\mathrm{eq}}}{\sigma_{\mathrm{M}}}\right)^2 + 2q_1 f \cosh\left(\frac{3q_2}{2}\frac{\sigma_{\mathrm{h}}}{\sigma_{\mathrm{M}}}\right) - \left(1 + q_3 f^2\right) = 0 \tag{10}$$

where σ_{eq} is the Hershey-Hosford equivalent stress defined in Eq. (4), σ_{M} is the flow stress of the matrix material according to Eq. (5), q_1,q_2,q_3 are the Tvergaard parameters, σ_{h} is the hydrostatic stress, and f is the void volume fraction. The evolution of void volume fraction is defined as

$$\dot{f} = \dot{f}_{\mathrm{g}} + \dot{f}_{\mathrm{n}} + \dot{f}_{\mathrm{s}} = (1-f)\mathrm{tr}\mathbf{D}^{\mathrm{p}} + A_{\mathrm{n}}\dot{p} + k_{\mathrm{s}} f \kappa(\boldsymbol{\sigma}')\frac{\boldsymbol{\sigma}' : \mathbf{D}^{\mathrm{p}}}{\sigma_{\mathrm{eq}}} \tag{11}$$

where $\dot{f}_{\mathrm{g}}$ is the void growth rate, $\dot{f}_{\mathrm{n}}$ is the void nucleation rate and $\dot{f}_{\mathrm{s}}$ represents the contribution from void softening in shear to the porosity evolution [38]. The parameters A_{n} and k_{s} govern void nucleation and voids softening in shear, respectively. Furthermore, $\boldsymbol{\sigma}'$ is the deviatoric stress tensor, $\mathbf{D}^{\mathrm{p}}$ is the plastic rate-of-deformation tensor defined by the associated flow rule and $\kappa(\boldsymbol{\sigma}')$ is a function of the second and third invariant of the deviatoric stress tensor, J_2 and J_3, respectively, viz.

$$\kappa(\boldsymbol{\sigma}') = 1 - \frac{27}{4}\frac{J_3^2}{J_2^3} \tag{12}$$

By including the term for void softening in shear in the evolution equation, the physical meaning of the void volume fraction f is lost and it should be interpreted as a damage parameter, as suggested by Nahshon and Hutchinson [38]. The reader is referred to Dæhli et al. [37] for a detailed account of the porous plasticity model used in the localization analyses.

5. Calibration

5.1. Calibration of hardening parameters

The calibration procedure follows a similar approach as employed in e.g. Mohr and Marcadet [5]. The uniaxial tension tests were used to obtain an initial estimate of the hardening parameters. A spreadsheet was used to fit two of the three hardening terms to the true stress-strain curve up to necking. Inverse modelling of the NT10 tests by use of the

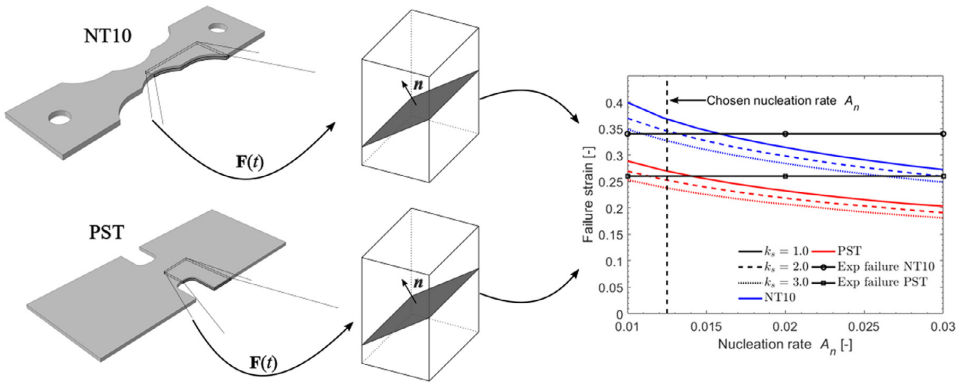

Fig. 13. Calibration approach for the porous plasticity model parameters A_n and k_s. The plot shows data for the temper T6 calibration.

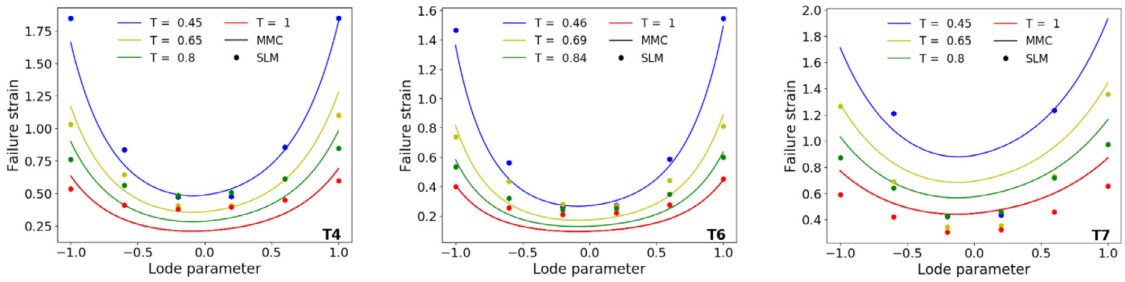

Fig. 14. Comparison between results from the localization analyses (SLM) and the calibrated MMC fracture model.

Table 3
Material parameters of the extended Voce hardening rule.

Temper	σ_0 (MPa)	Q_1 (MPa)	C_1	Q_2 (MPa)	C_2	Q_3 (MPa)	C_3
T4	135.0	19.04	87.05	142.22	10.06	75.00	3.08
T6	245.1	6.45	438.98	109.39	11.13	2.58	9.05
T7	152.8	3.76	2316.10	57.11	38.34	25.81	4.59

optimization tool LS-OPT [39] was then employed to calibrate the hardening parameters. The initial estimate was used as a starting point in the optimization, where the first hardening term was kept fixed and the second and third hardening terms could change. Sequential FE simulations were then conducted with different hardening parameters where LS-OPT employed a genetic optimization algorithm to find the optimal set of parameters. The force-displacement curves from the NT10 tests were used as targets in the optimizations. The finite element model employed is presented in Section 4.4 and the calibrated hardening parameters are displayed in Table 3. The force-displacement and logarithmic strain-displacement curves from the simulations are plotted as solid lines together with the experiments as crosses for the two notch tension tests in Fig. 12. The good agreement between the simulations and experiments for both tests illustrates the validity of the calibrated plasticity model.

5.2. Calibration of the MMC fracture model

The predictive capability of the localization analyses relies on an accurate description of the material behaviour inside and outside the imperfection band. The plasticity model used outside the band was calibrated as described in the previous section. For the porous plasticity model used inside the band, the parameters introduced by Tvergaard [36] were given standard values, i.e., $q_1 = 1.5$, $q_2 = 1.0$, $q_3 = q_1^2 = 2.25$.

The nucleation rate A_n and the void shearing parameter k_s were calibrated based on localization analyses following the process depicted in Fig. 13, whereas the initial void volume fraction f_0 was set to zero. The deformation gradient $\mathbf{F}(t)$ was extracted from the critical element in the through-thickness centre of an NT10 and a PST simulation and assigned as boundary conditions in localization analyses. A series of localization analyses with varying nucleation rate A_n and void shearing parameter k_s was conducted. According to Nahshon and Hutchinson [38], the void shearing parameter is suggested to be in the range $1 \leq k_s \leq 3$ for structural alloys, thus three values within this range were investigated: $k_s = \{1.0,\ 2.0,\ 3.0\}$. The optimal value of A_n was found when localization occurred for a strain outside the band similar to the experimental failure strain for a given k_s, as depicted in the plot in Fig. 13. The optimal value of k_s was not searched for and the calibrated value of k_s was chosen from the three values investigated. The experimental failure strain was taken from the critical element in a simulation based on both global and local measurements from DIC results. In general, failure was found to initiate just before the final dip in the force levels, as it was assumed that strain localization initiated at this point. The plot in Fig. 13 shows the results from the localization analyses for temper T6 where the opti-

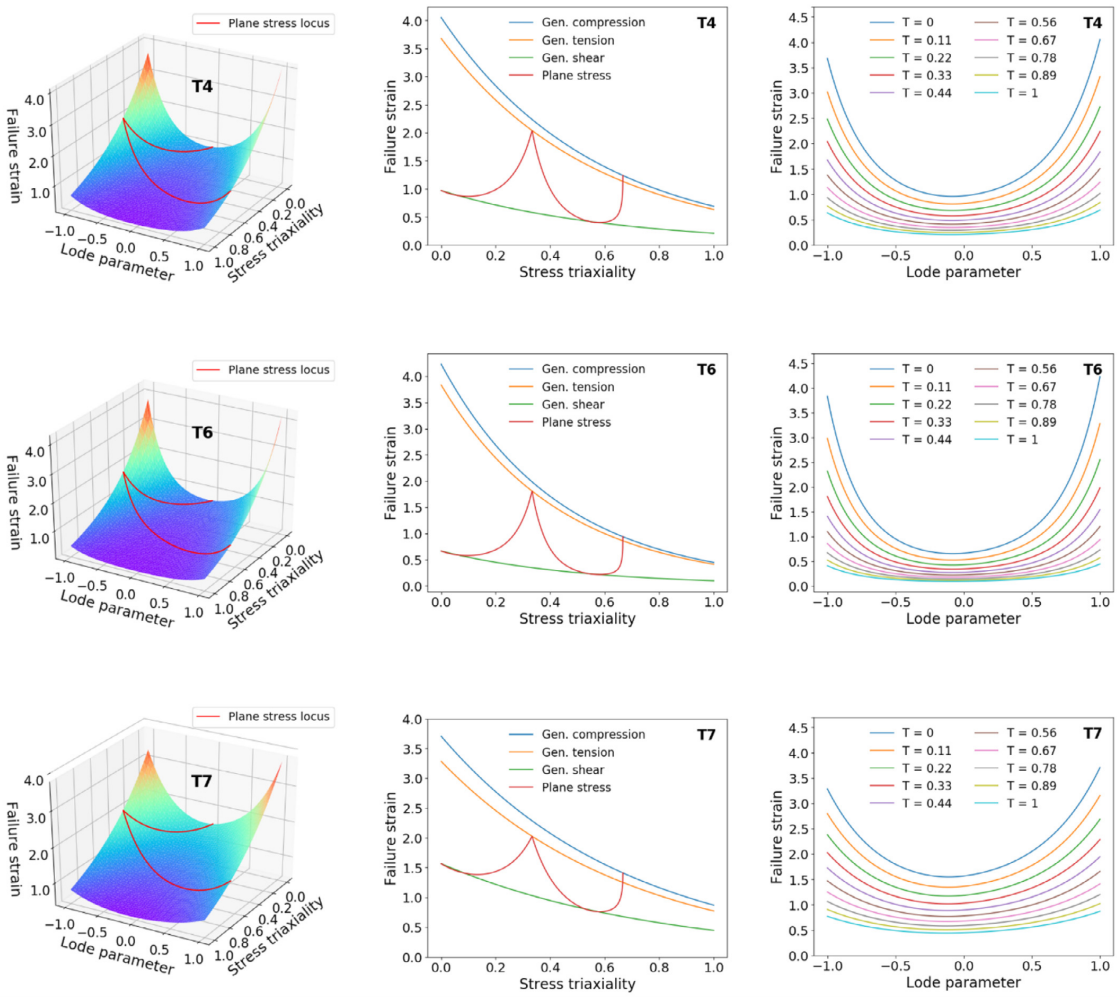

Fig. 15. Failure loci of the MMC fracture model for the three different tempers of AA6016.

Table 4
Calibrated values of the parameters in the porous plasticity model.

Temper	A_n	k_s
T4	0.006	2.0
T6	0.0125	2.0
T7	0.005	2.0

mal value of the nucleation rate A_n is depicted. The calibrated values of the parameters in the porous plasticity model are given in Table 4.

With the metal and porous plasticity models calibrated, localization analyses with proportional loading conditions were conducted, i.e., assigning a deformation where the stress triaxiality T and the Lode parameter L are constant during the entire simulation. From these analyses, failure strains covering a considerable region of the stress space were obtained, even if localization was not achieved for all the applied stress states. The parameters of the MMC fracture model were finally optimized against this cloud of points in a Python script. Approximately 100 points were used in each optimization to ensure a solid basis for the identification. The basin-hopping algorithm [40] available in the SciPy package [41] was employed to determine the optimal set of model parameters. The algorithm aims to find the global minimum of a cost function, here defined as the difference between the failure strains calculated with MMC fracture model and localization analyses for a wide range of stress states. Within the global stepping algorithm, a local minimization is carried out using a sequential least squares programming (SLSQP) method [42]. Approximately 60 basin-hopping iterations were performed to find the optimal set of parameters using the default parameters of the algorithm (the reader is referred to [41] for more details upon these numerical aspects). The calibrated parameters are given in Table 5.

The calibrated MMC fracture model and the target points calculated by the localization analyses (given the abbreviation SLM) are shown in Fig. 14 for selected values of the stress triaxiality. From the figure it is evident that the main trends are captured in the calibration of the fracture

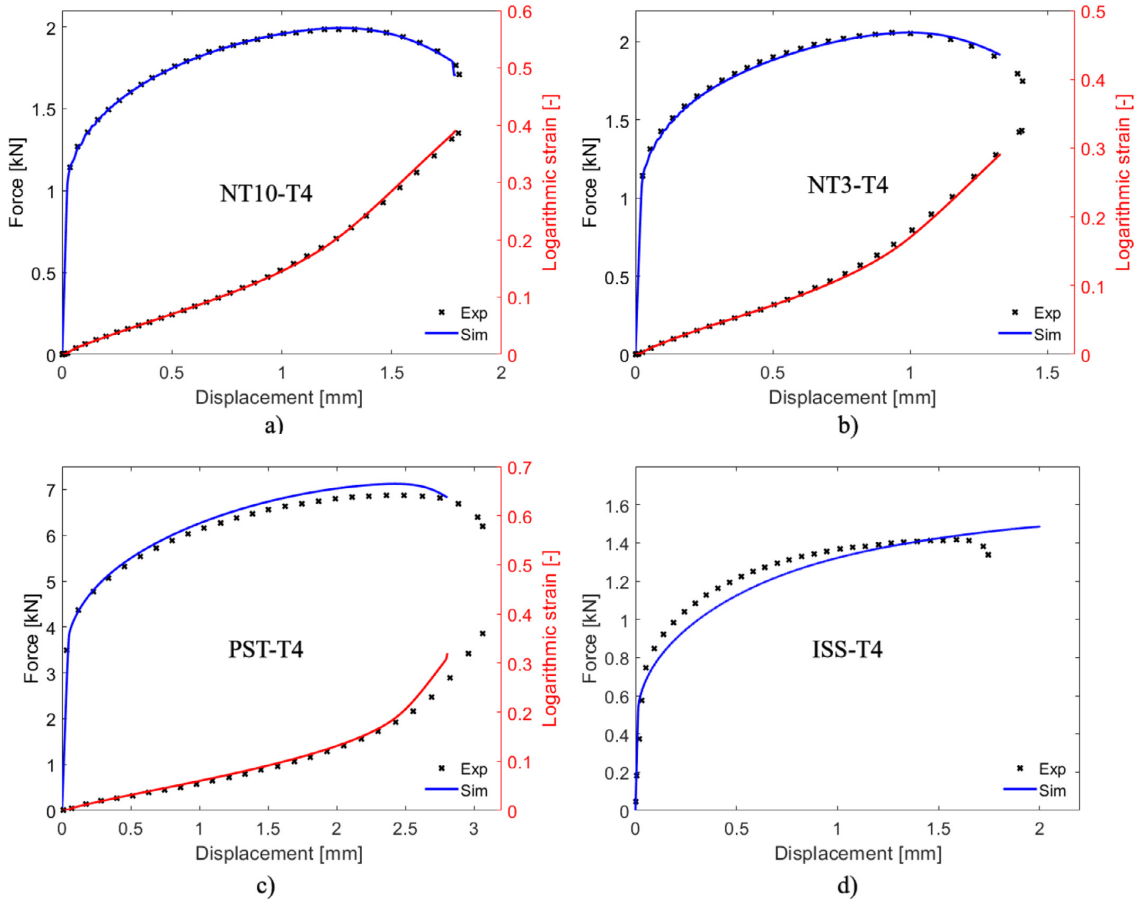

Fig. 16. Comparison between experimental (crosses) and numerical (solid lines) force-displacement and local strain-displacement curves of temper T4: a) NT10, b) NT3, c) PST and d) ISS. All curves are plotted to fracture.

Table 5
Calibrated parameters of the modified Mohr-Coulomb fracture model based on localization analyses.

Temper	K	$\hat{C}_1$	$\hat{C}_2$	$\hat{C}_3$	$\hat{C}_4$	n
T4	0.9969	0.01000	0.5075	0.8820	1.0056	0.01122
T6	0.9988	0.01135	0.5081	0.8847	1.0066	0.01000
T7	0.9611	0.00100	0.4815	0.8672	1.0005	0.00138

model, even though the fit around generalized shear ($L = 0$) is not always good. The dependence on the stress triaxiality around $L = 0$ is small according to the localization analyses, resulting in the points for $L = \pm 0.2$ in some cases overlapping each other. This behaviour is not accurately captured by the calibrated fracture model, where an evident dependence on the stress triaxiality is seen around $L = 0$. The fit is accurate for generalized tension and compression for all three tempers. The somewhat flat failure locus predicted by the localization analyses is amongst other linked to the use of a Hershey yield surface with exponent $a = 8$. The influence of the yield surface curvature on ductile failure was investigated by Dæhli et al. [37], where Hershey yield surfaces with exponent $a = 2$ (i.e., equal to the von Mises yield surface) and $a = 8$ were investigated by use of localization analyses. The results suggest that a yield surface with $a = 8$ displays a flatter failure locus compared to the yield surface with $a = 2$. The reader is referred to Dæhli et al. [37] for further details on the influence of the yield surface curvature on ductile failure.

The results from the calibration of the MMC fracture models are shown in Fig. 15. The overall shape of the three fracture surfaces in the left column of the figure is similar, where both an evident stress triaxiality and Lode parameter dependence is seen. The monotonic decrease in ductility for increasing stress triaxiality is shown in the middle column of the figure for generalized compression ($L = 1$), generalized tension ($L = -1$) and generalized shear ($L = 0$). The rate of decrease in ductility for increasing stress triaxiality is similar for generalized compression and generalized tension for all tempers. However, the rate of decrease in ductility for increasing stress triaxiality is much lower for generalized shear, especially for tempers T4 and T6. Generalized shear exhibits the lowest ductility followed by generalized tension and generalized compression, where the difference between the two latter is small. Temper T7 exhibits a much stronger dependence on the stress triaxiality for generalized shear compared to tempers T4 and T6. This is clearly visualized in the right column where the failure loci are plotted as a function of the Lode parameter for selected values of the stress triaxiality. It should be noted that this strong stress triaxiality dependence was not predicted by the localization analyses and is a result of the calibration of the MMC

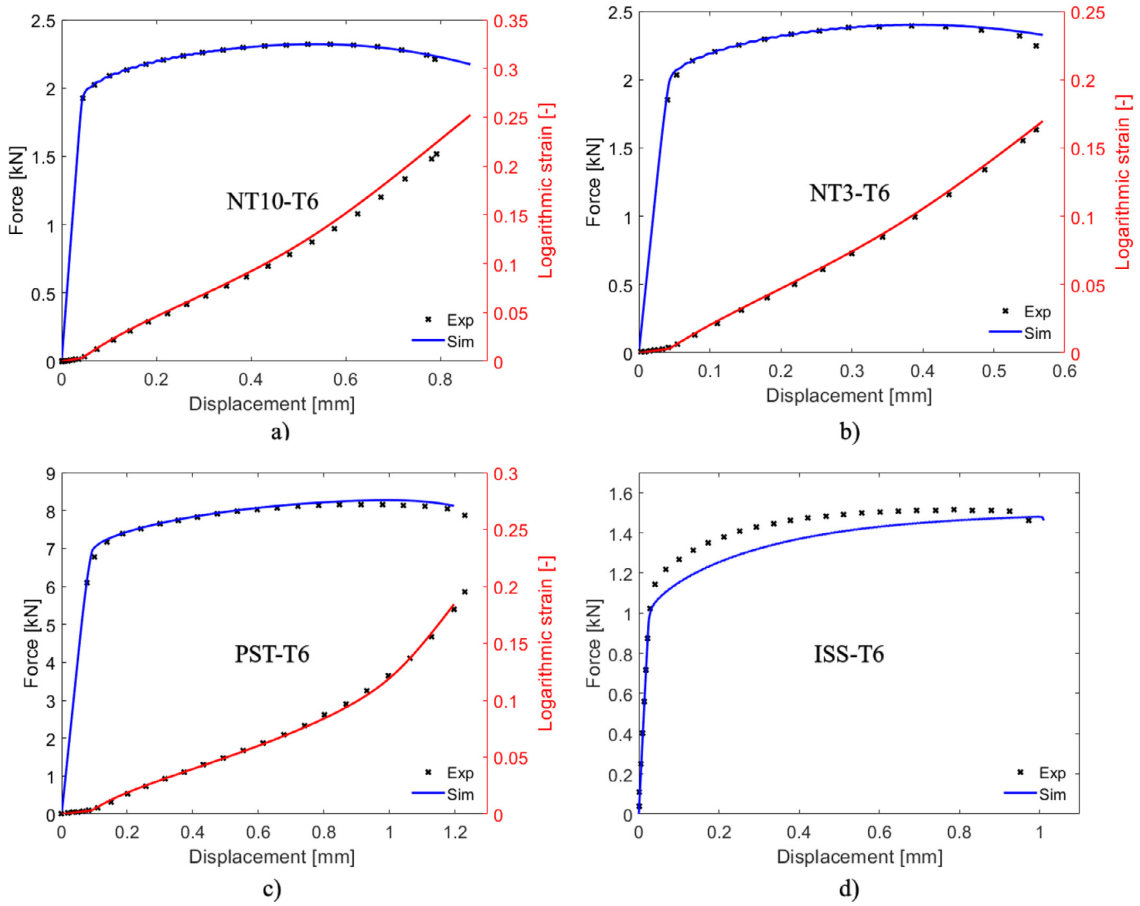

Fig. 17. Comparison between experimental (crosses) and numerical (solid lines) force-displacement and local strain-displacement curves of temper T6: a) NT10, b) NT3, c) PST and d) ISS. All curves are plotted to fracture.

fracture model. The ductility in simple shear is considerably higher for temper T7 than for temper T6, while temper T4 is somewhere in between. The asymmetry of the failure loci is evident for all tempers where the lowest ductility for selected values of the stress triaxiality is found for slightly negative values of the Lode parameter. The high ductility for $T = 0$ and $L = \pm 1$ for temper T6, higher than for both tempers T4 and T7, is somewhat peculiar. The localization analyses did not provide results for these stress states and this part of the failure locus is obtained by extrapolation. However, for the stress states achievable by experiments, the failure locus for temper T6 exhibits lower ductility than the failure loci for tempers T4 and T7.

The highest and lowest ductility on the plane stress failure locus is found for the stress states representing uniaxial tension ($L = -1$, $T = 0.33$) and plane-strain tension ($L = 0,\ T = 1/\sqrt{3}$), respectively. It is worth noting that the ductility is higher in uniaxial tension than in equi-biaxial tension ($L = 1,\ T = 0.67$) for all tempers. This difference would not be possible to express with the Hosford-Coulomb fracture model, where the ductility is forced to be equal in uniaxial and equi-biaxial tension. The cusp on the plane-stress failure locus for uniaxial tension and the valley towards simple shear ($L = 0$, $T = 0$) for all tempers categorizes these material's fracture behaviour as Lode parameter dominated. A stress triaxiality dominated fracture behaviour would exhibit higher ductility in simple shear compared to uniaxial tension, and thus no cusp would appear in the plane-strain failure locus for uniaxial tension.

6. Numerical results and discussion

6.1. Material tests

The results from the simulations of the material tests on the notch tension (NT), plane-strain tension (PST) and in-plane shear (ISS) specimens with the MMC fracture model are shown in Figs. 16–19. The experimental results are presented as discrete crosses, while the solid lines represent the simulations. By comparison of the response curves for temper T4 shown in Fig. 16, the predictions by the MMC fracture model are in general found to be good. When comparing the force-displacement curves for the four tests, the agreement for the notch tension tests is excellent, while there are some deviations for the PST and ISS tests. These deviations are expected when modelling a moderately anisotropic material with an isotropic yield surface. The onset of fracture is accurately predicted for the NT10 test, while it is slightly conservative for the NT3 and PST tests. For the ISS test, the response curves deviate already at yielding and the onset of fracture is predicted for a larger displacement than in the experiment. The reason for this deviation is linked to the

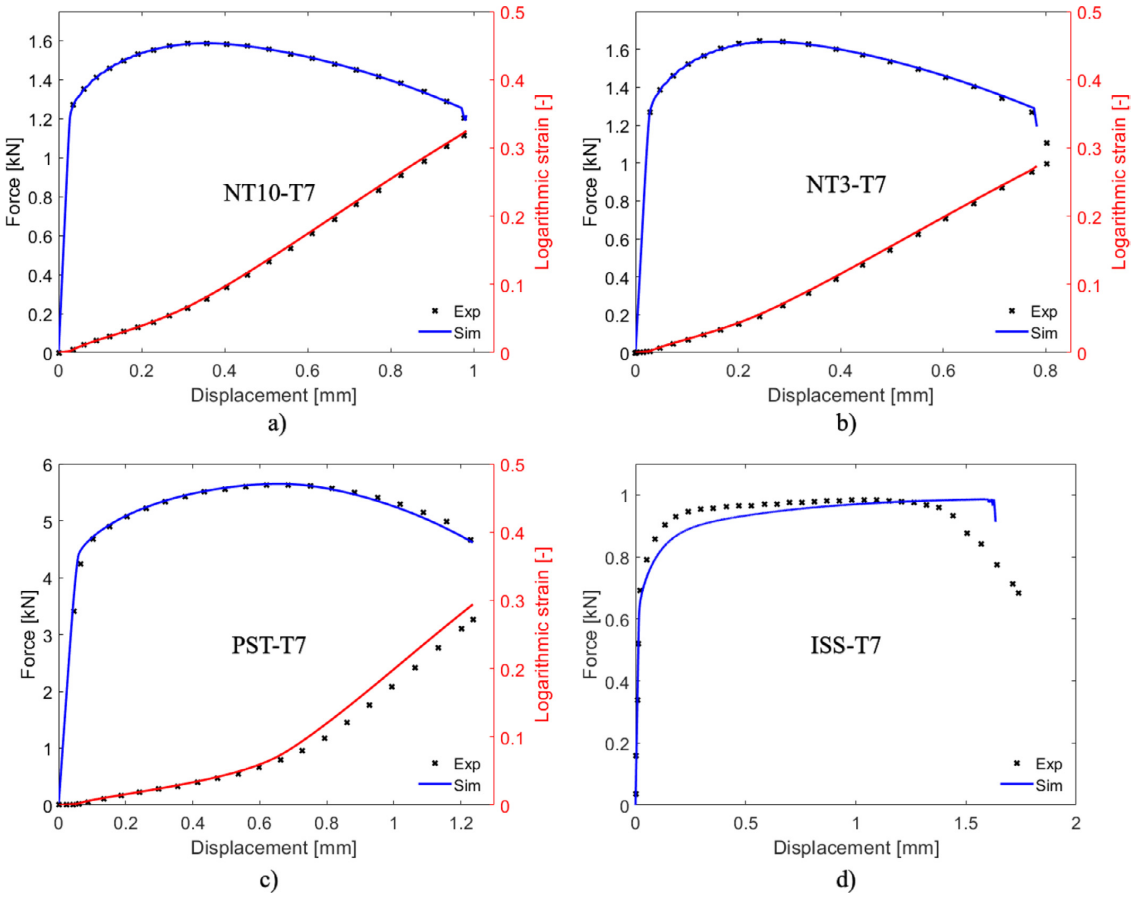

Fig. 18. Comparison between experimental (crosses) and numerical (solid lines) force-displacement and local strain-displacement curves of temper T7: a) NT10, b) NT3, c) PST and d) ISS. All curves are plotted to fracture.

texture of the alloy, requiring an anisotropic yield criterion to capture the behaviour as discussed in Achani et al. [43]. Engler et al. [28] investigated the microstructure and texture of an AA6016 sheet in temper T4 where a characteristic cube recrystallization texture was found. This texture leads to a relatively high yield stress in shear compared to uniaxial tension [43]. Thus, the yield stress in a shear test is not expected to be accurately predicted with an isotropic yield surface. Considering that the texture is not altered by the heat-treatment, this behaviour is expected for all tempers. The conflicting fracture prediction from the PST and ISS tests illustrates the difficulties of finding a set of parameters that accurately describes the onset of fracture in both tests.

The results from simulations with the MMC fracture model for temper T6 are shown in Fig. 17. The prediction of fracture in the PST test is slightly conservative, while the fracture predictions for the NT10, NT3 and ISS tests are slightly non-conservative. The impressive accuracy in the predictions of the temper T6 tests is evident as the least accurate prediction is obtained for the NT10 test, which was used in the calibration. As expected, the deviations between the force-displacement curves for the ISS test initiated already at yield. Despite this, accurate prediction on the onset of fracture is also obtained for this test.

The results from the simulations with the MMC fracture model for temper T7 are shown in Fig. 18. The agreement between the experimental and numerical response curves and the predicted onset of fracture is excellent for the NT10, NT3 and PST tests. The only notable deviation amongst these tests is the shift in the local strain for the PST tests, resulting in a slightly higher strain at the onset of fracture in the simulation compared to the experiment. As mentioned earlier, the exact onset of fracture in the ISS test is difficult to determine based on the force-displacement curves. The displacement at which the onset of fracture is predicted in the simulation appears to be a reasonable estimate when inspecting images from the test at a similar displacement.

The predictive capability of the MMC fracture model has been demonstrated in terms of global and local response parameters for four different material tests. In Fig. 19, the stress state histories extracted from simulations of the same experiments are presented. The solid lines are taken from simulations where the critical damage parameter is set artificially high and the end of the lines indicate the onset of fracture in the experiments. Fracture in the experiments was determined based on both local and global measurements for NT10, NT3 and PST tests, while global measurements were used for ISS. The dots indicate the onset of fracture predicted by the MMC fracture model. The stress states covered by the experiments include mainly negative values of the Lode parameter and positive values of the stress triaxiality. The stress state histories are taken from the through-thickness centre element for the NT10, NT3 and PST tests, which corresponds to the element subjected to the largest equivalent plastic strain. In the simulations of the ISS tests, the element

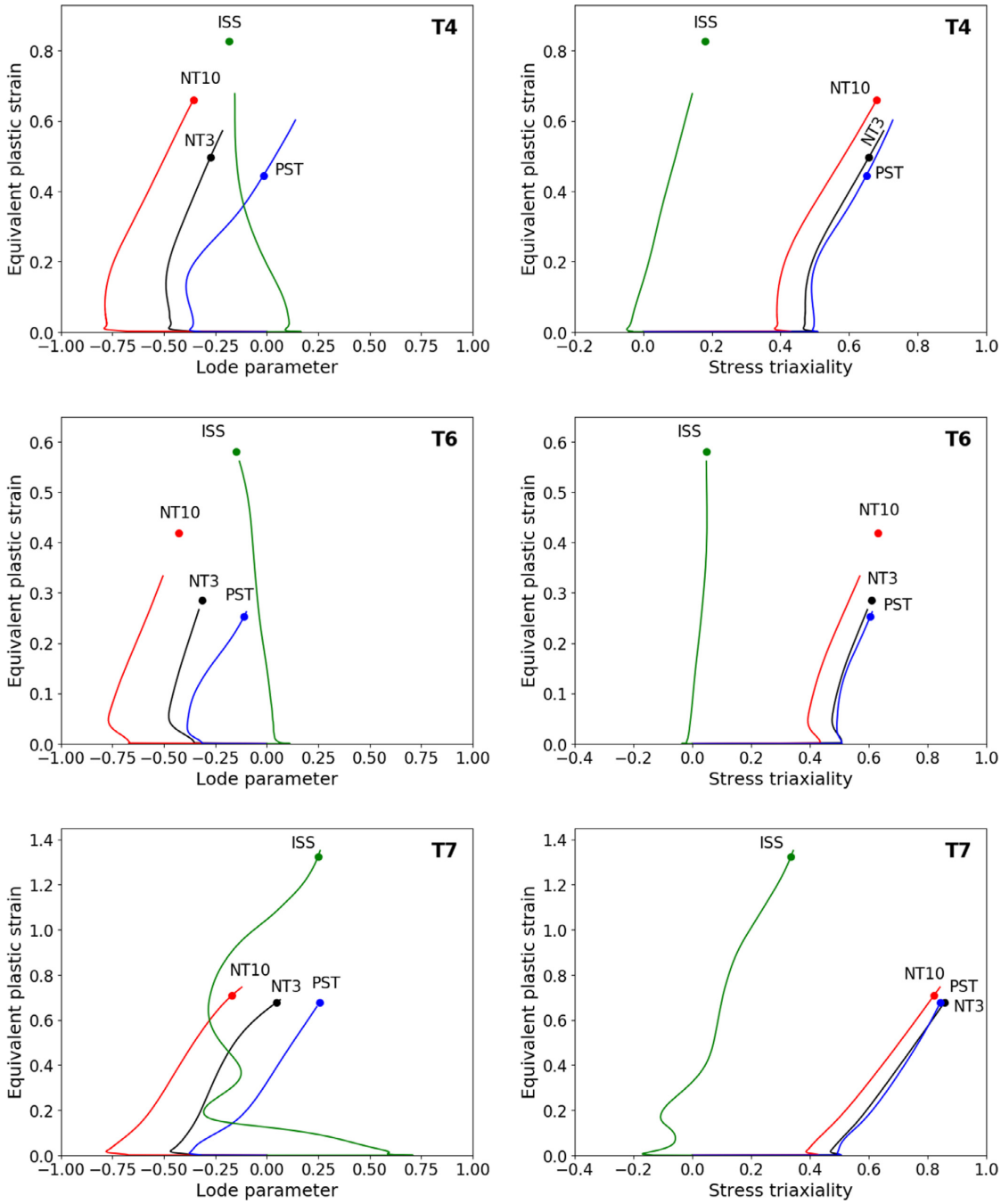

Fig. 19. Evolution of the stress state (i.e., Lode parameter and stress triaxiality) as function of the equivalent plastic strain extracted from the critical element. The predicted fracture by the MMC fracture model is indicated by the dots while the end of the solid lines gives the onset of fracture in the tests.

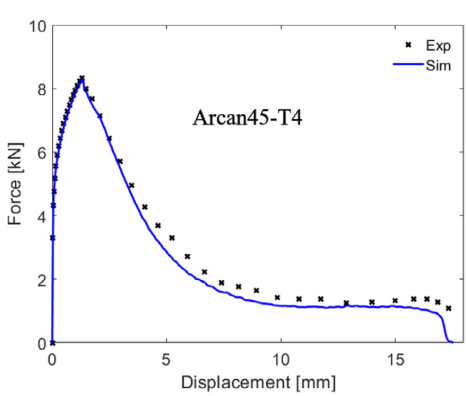

a)

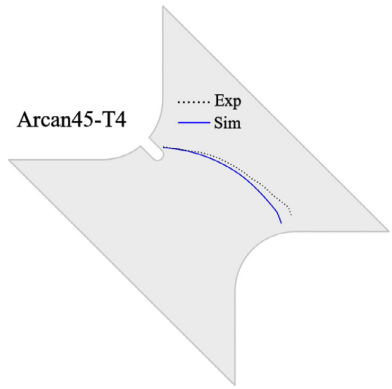

b)

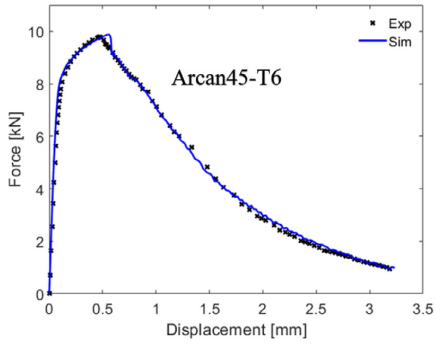

c)

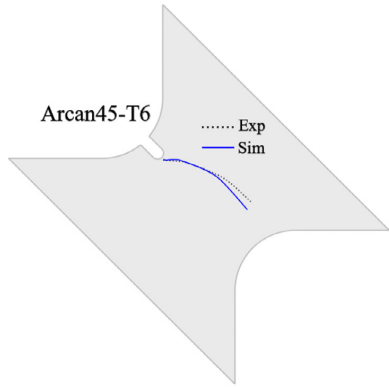

d)

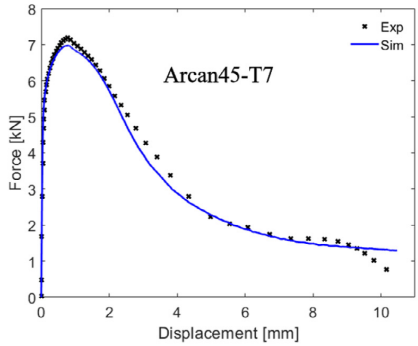

e)

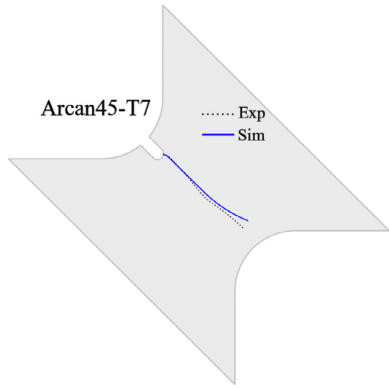

f)

Fig. 20. Experimental and numerical force-displacement curves for the Arcan45 tests in a), c) and e) and corresponding crack paths on the undeformed configuration in b), d) and f).

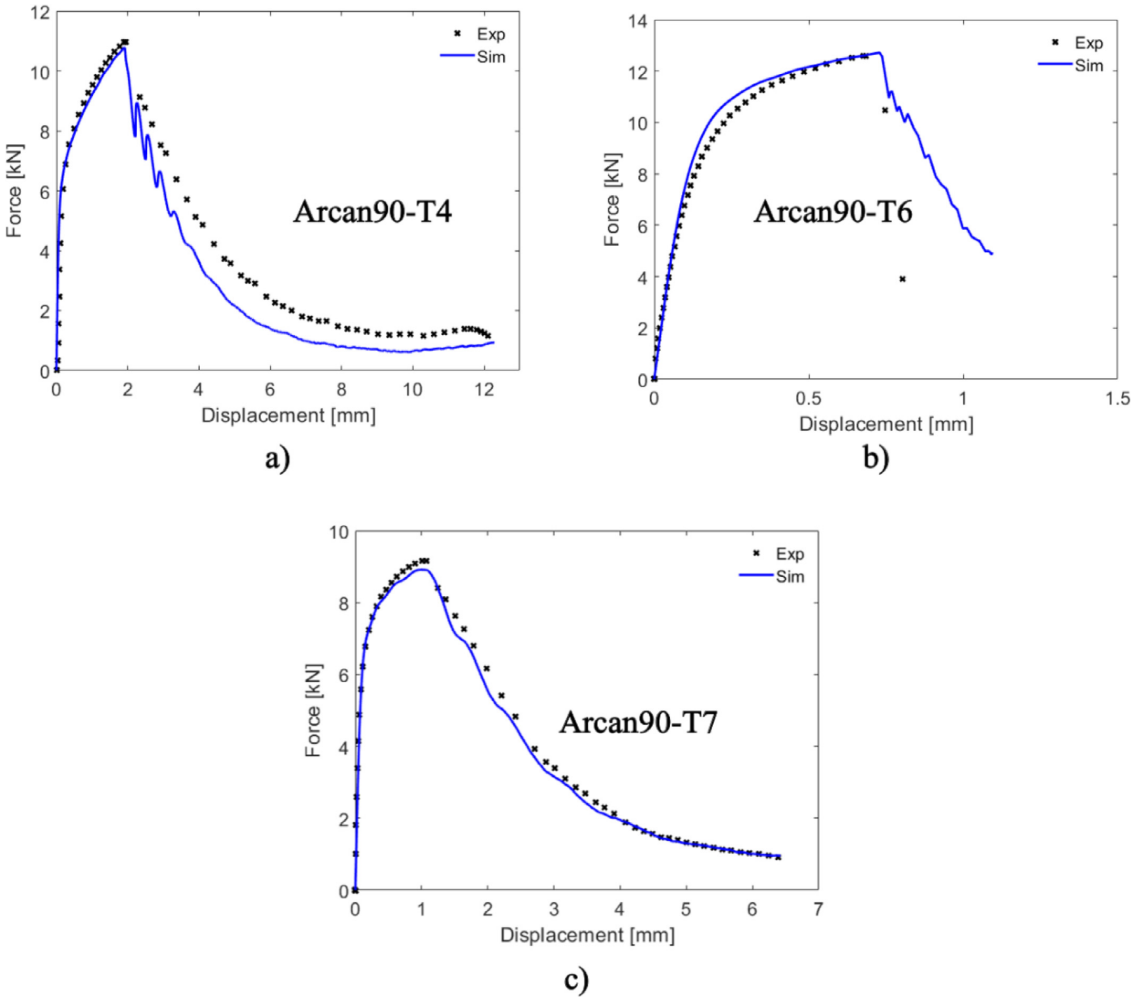

Fig. 21. Experimental and numerical force-displacement curves for the a) Arcan90-T4, b) Arcan90-T6 and c) Arcan90-T7 tests.

subjected to the largest value of the damage parameter D at the displacement of fracture in the experiment is taken as the critical element. The damage parameter was used to determine the critical element since the largest value of the equivalent plastic strain was found on the through-thickness surface within the notch. This region is heavily affected by the in-plane rotations that occur in the tests, which makes the element subjected to the largest value of equivalent plastic strain an unsuitable choice for the ISS tests. The chosen critical element in all ISS tests is located on the in-plane surface within the gauge region where strains localize. Among the eight integration points within the critical element, the one subjected to the largest value of equivalent plastic strain is chosen in all tests. When comparing the predictions by the MMC fracture model with the experimental values in Fig. 19, i.e., comparing the dots to the end point of the solid lines, the trends are similar to the ones in Figs. 16–18. By inspection of Fig. 19, it is evident that the stress state histories are quite similar among the different tempers apart from in the ISS test. The reason for this is the varying position of the critical element among the simulations of the ISS test. The difference in strength, work-hardening and ductility between the three tempers results in different deformation processes which affect the position of the critical element, emphasizing the difficulties faced with an in-plane simple shear test. Roth and Mohr [44] investigated the challenges related to determining the strain to failure for simple shear for a wide range of sheet metals. Amongst the study's conclusions, it was stated that the shape of the specimen plays a significant role and that different material properties such as strength, work-hardening and ductility require different shapes of the specimen. By inspection of the stress state histories for the ISS tests, temper T6 is closest to exhibit a proportional loading path, suggesting that the geometry of the ISS test specimen is suitable for the material properties of this temper. Ideally, both the stress triaxiality and the Lode parameter should be equal to zero all the way to fracture in a shear test. Especially the ISS test for temper T7 exhibits a loading path where T and L vary markedly throughout the deformation, making it less suitable to use as target in a calibration process. This is one of the reasons why the PST test was chosen in order to calibrate the void shearing parameter k_s in the porous plasticity model and not the ISS test. Considering the

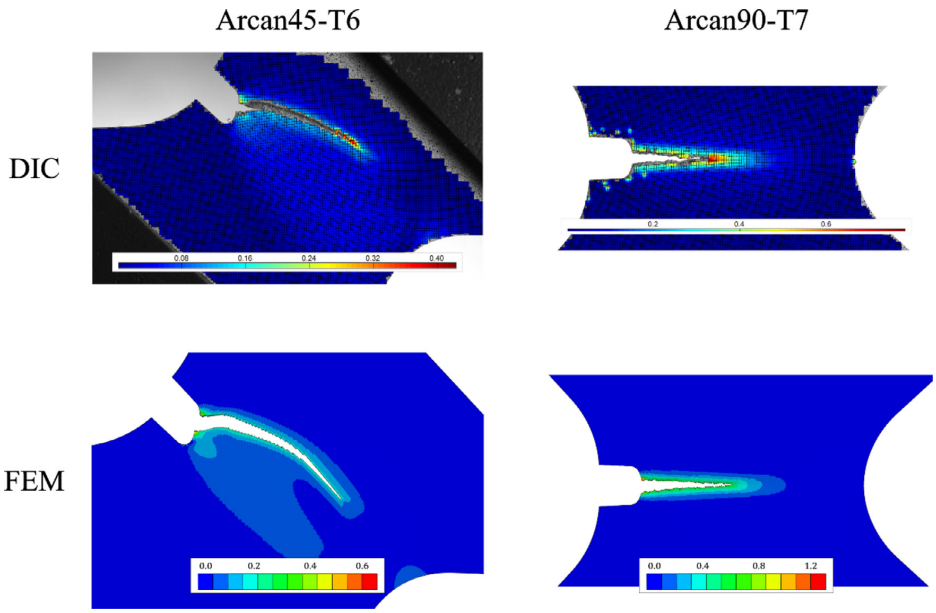

Fig. 22. The strain fields of Arcan45-T6 and Arcan90-T7 from DIC and FE simulations taken when the crack had propagated approximately halfway through the specimen.

rather simple plasticity model chosen and that only two material tests were used in the calibration, the predictions by the MMC fracture model are deemed satisfactory.

6.2. Modified Arcan tests

To further assess the predictive capabilities of the MMC fracture model, the modified Arcan tests with $\beta = 45^{\circ}$ and $\beta = 90^{\circ}$ were simulated. Here, the model's ability to predict both crack initiation and propagation is tested. In Fig. 20 the force-displacement curves from experiments and simulations of the Arcan45 tests are shown to the left, with corresponding crack paths on the undeformed configuration to the right. Despite the small inaccuracies seen in the predictions for the material tests, excellent agreement between the experimental and numerical results is seen for the Arcan45 tests, both in terms of force-displacement curves and crack paths. The onset of fracture is initiated at the correct displacement and position on the specimen for all three tempers. Additionally, the simulated crack propagation occurs mostly along the correct paths at similar velocities as the experimental ones. Even the somewhat surprising straight crack path seen in the Arcan45-T7 test was predicted accurately. The slanted fracture surface observed in the experiments was not predicted in any of the simulations. To predict slanted fracture, the through-thickness symmetry must be abandoned and a much denser mesh accompanied by a coupled damage model is most likely required [45]. However, the crack in the temper T7 simulation propagated in a tunnelling mode from initiation to complete fracture. The stress triaxiality inside the notch where fracture initiated was between 0.3 and 0.4, while the Lode parameter was approximately equal to -1 for all tempers. Just in front of the propagating crack, a region with stress triaxiality between 0.6 and 0.7 and a Lode parameter close to zero was present for all tempers.

Fig. 21 shows the experimental and numerical force-displacement curves for the Arcan90 tests. The onset of fracture was accurately predicted for tempers T4 and T7, while for temper T6 fracture occurred slightly later in the simulation than in the experiment. Additionally, there was a slight deviation in the force level in parts of the response curve before the onset of fracture for temper T6 of unknown reasons. The crack propagation was accurately predicted for tempers T4 and T7, where the agreement between the experimental and numerical response curves was good throughout the whole deformation process. The velocity of the propagating crack for temper T6 was not accurately captured in the simulations, where a lower velocity than in the tests was predicted.

The onset of fracture in the simulation was found to occur a few millimetres within the notch and not at the free surface. This occurred even though the largest value of the equivalent plastic strain was found on the free surface. However, by inspection of the stress state at the onset of fracture, the region inside the notch was found to be subjected to a higher stress triaxiality and a Lode parameter closer to zero than on the free surface. Fracture initiated in this region before propagating perpendicularly to the loading direction. The agreement between the crack pattern in the experiment and simulation was excellent for all tempers and is not shown for brevity.

The strain fields of an Arcan45-T6 and Arcan90-T7 test are shown in Fig. 22 from both DIC and FE simulations. The strain fields were taken when the crack had propagated approximately halfway through the specimen in both tests. The magnitude of the strains is consistently higher in the FE simulations than in the DIC simulations owing to the denser mesh used in the former. However, the qualitative trends are similar between the two sets of simulations for both tests. A narrow zone with localized strains in front of the propagating crack is correctly predicted in both cases. In the Arcan45-T6 test, there is a band with slightly higher strains across the specimen which is not fully developed in the FE simulations and thus only partially predicted.

7. Conclusions

This paper has presented a novel calibration procedure of the modified Mohr-Coulomb (MMC) fracture model by use of localization analyses of the imperfection band type and applied it for three tempers of

the aluminium alloy AA6016. By this approach, the onset of ductile fracture is set to coincide with strain localization. Notch tension (NT10) and plane-strain tension (PST) tests were used in the calibration of the metal and porous plasticity models assigned to the material outside and inside the imperfection band, respectively. The fracture model was validated against notch tension (NT3) and in-plane simple shear (ISS) tests in addition to two loading cases of the modified Arcan test. The goal was to assess the predictive capabilities of the proposed modelling approach, where localization analyses were used as basis to calibrate the MMC fracture model. Finite element simulations with the Hershey-Hosford plasticity model combined with the MMC fracture model were in most cases able to accurately predict the onset of fracture. For both loading cases of the modified Arcan tests, initiation and crack propagation were predicted with good accuracy in all but one simulation. Considering that only two experiments have been used in the calibration of the plasticity and fracture models, the potential of this approach is emphasized. The use of localization analyses to predict ductile fracture is an effective and well-suited tool for design of components and structures of metallic materials, where the need for an extensive test programme could be reduced.

Declaration of Competing Interest

The authors declare that they have no known competing financial interests or personal relationships that could have appeared to influence the work reported in this paper.

CRediT authorship contribution statement

Henrik Granum: Writing - original draft, Formal analysis, Investigation, Visualization. **David Morin:** Software, Methodology, Writing - review & editing. **Tore Børvik:** Conceptualization, Methodology, Writing - review & editing, Supervision. **Odd Sture Hopperstad:** Conceptualization, Methodology, Writing - review & editing, Supervision.

Acknowledgments

The authors gratefully appreciate the financial support from NTNU and the Research Council of Norway through the FRINATEK Programme, Project No. 250553 (FractAl). The authors would also like to thank Dr. Olaf Engler at Hydro Aluminium Rolled Products in Bonn, Germany, for providing the material.

References

[1] Bao Y, Wierzbicki T. On fracture locus in the equivalent strain and stress triaxiality space. International Journal of Mechanical Sciences 2003;46(1):81–98.
[2] Haltom SS, Kyriakides S, Ravi-Chandar K. Ductile failure under combined shear and torsion. Int J Solids Struct 2013;50(10):1507–22.
[3] Papasidero J, Doquet V, Mohr D. Determination of the effect of stress state on the onset of ductile fracture through tension-torsion experiments. Exp Mech 2014;54:137–51.
[4] Barsoum I, Faleskog J. Rupture mechanisms in combined tension and shear – experiments. Int J Solids Struct 2007;44(6):1768–86.
[5] Mohr D, Marcadet SJ. Micromechanically-motivated phenomenological Hosford–Coulomb model for predicting ductile fracture initiation at low stress triaxialities. Int J Solids Struct 2015;67-68:40–55.
[6] Benzerga AA, Surovik D, Keralavarma SM. On the path-dependence of the fracture locus in ductile materials–analysis. International Journal of Plasticity 2012;37:157–70.
[7] Morin D, Dæhli LE, Børvik T, Benallal A, Hopperstad OS. Numerical study of ductile failure under non-proportional loading. European Journal of Mechanics / A Solids 2019;74:221–41.
[8] Basu S, Benzerga AA. On the path-dependence of the fracture locus in ductile materials: experiments. Int J Solids Struct 2015;71:79–90.
[9] Morin D, Hopperstad OS, Benallal A. On the description of ductile fracture in metals by the strain localization theory. International Journal of Fracture 2018;209:27–51.
[10] Dunand M, Mohr D. Effect of Lode parameter on plastic flow localization after proportional loading at low stress triaxialities. J Mech Phys Solids 2014;66(1):133–53.
[11] Gruben G, Morin D, Langseth M, Hopperstad OS. Strain localization and ductile fracture in advanced high-strenght steel sheets. European Journal of Mecanics A / Solids 2017;61:315–29.
[12] Bergo S, Morin D, Børvik T, Hopperstad OS. Micromechanics-based identification of a fracture model for three structural steels. Eng Fract Mech 2020;224:106803.
[13] Wierzbicki T, Bao Y, Lee Y-W, Bai Y. Calibration and evaluation of seven fracture models. International Journal of Mechanical Sciences 2005;47:719–43.
[14] Li H, Fu MW, Lu J, Yang H. Ductile fracture: experiments and computations. International Journal of Plasticity 2011;27:147–80.
[15] Gruben G, Hopperstad OS, Børvik T. Evaluation of uncoupled ductile fracture criteria for the dual-phase steel Docol 600DL. International Journal of Mechanical Sciences 2012;63:133–46.
[16] Bai Y, Wierzbicki T. A comparative study on three groups of ductile fracture loci in the 3D space. Eng Fract Mech 2015;125:147–67.
[17] Morin D, Kaarstad BL, Skajaa B, Hopperstad OS, Langseth M. Testing and modelling of stiffened aluminium panels subjected to quasi-static and low-velocity impact loading. Int J Impact Eng 2017;110:97–111.
[18] Kristoffersen M, Costas M, Koenis T, Brøtan V, Paulsen CC, Børvik T. On the ballistic perforation resistance of additive manufactured AlSi10Mg aluminium plates. Int J Impact Eng 2020;137:103476.
[19] Bai Y, Wierzbicki T. Application of extended Mohr-Coulomb criterion to ductile fracture. International Journal of Fracture 2010;161:1–20.
[20] Dunand M, Mohr D. On the predictive capabilities of the shear modified Gurson and the modified Mohr-Coulomb fracture models over a wide range of stress triaxialities and Lode angles. J Mech Phys Solids 2011;59:1374–94.
[21] Gorji MB, Mohr D. Predicting shear fracture of aluminium 6016-T4 during deep drawing: combining Yld-2000 plasticity with Hosford-Coulomb fracture model. International Journal of Mechanical Sciences 2018;137:105–20.
[22] Zhang S, Lu Y, Shen Z, Zhou C, Lou Y. Prediction of ductile fracture for Al6016-T4 with ductile fracture criterion: experiment and simulation. International Journal of Damage Mechanics 2019;0:1–23.
[23] Lou Y, Huh H, Lim S, Pack K. New ductile fracture criterion for prediction of fracture forming limit diagrams of sheet metals. Int J Solids Struct 2012;49(25):3605–15.
[24] eCorr User Manual. https://www.ntnu.edu/kt/ecorr [accessed: 2020-04-10].
[25] Granum H, Aune V, Børvik T, Hopperstad OS. Effect of heat-treatment on the structural response of blast-loaded aluminium plates with pre-cut slits. Int J Impact Eng 2019;132:103306.
[26] Erice B, Roth CC, Mohr D. Stress-state and strain-rate dependent ductile fracture of dual and complex phase steel. Mechanics of Materials 2018;116:11–32.
[27] Gruben G, Fagerholt E, Hopperstad OS, Børvik T. Fracture characteristics of a cold-rolled dual-phase steel. European Journal of Mechanics A/Solids 2011;30:204–18.
[28] Engler O, Schäfer C, Myhr OR. Effect of natural ageing and pre-straining on strength and anisotropy in aluminium alloy AA 6016. Materials Science & Engineering A 2015;639:65–74.
[29] Gruben G, Hopperstad OS, Børvik T. Simulation of ductile crack propagation in dual-phase steel. International Journal of Fracture 2013;180:1–22.
[30] Hershey AV. The plasticity of an isotropic aggregate of anisotropic face-centered cubic crystals. J Appl Mech 1954;21(3):241–9.
[31] Hosford WF. A generalized isotropic yield criterion. J Appl Mech 1972;39:607–9.
[32] Hosford WF. On the crystallographic basis of yield criterion. Textures and Microstructures 1996;26-27:479–93.
[33] AbaqusVersion 6.14 dassault systèmes. Providence, RI, USA: Simula Corp.; 2013.
[34] Rice JR. The localization of plastic deformation. In: 14th International Congress of Theoretical and Applied Mechanics; 1976. p. 207–20.
[35] Gurson AL. Continuum theory of ductile rupture by void nucleation and growth, 1. Yield criteria and flow rules for porous ductile media. J Eng Mater Technol 1977;99(1):2–15.
[36] Tvergaard V. Influence of voids on shear band instabilities under plane strain conditions. International Journal of Fracture 1981;17(4):389–407.
[37] Dæhli LEB, Morin D, Børvik T, Hopperstad OS. Influence of yield surface curvature on the macroscopic yielding and ductile failure of isotropic porous plastic materials. Journal of Mechanics and Physics of Solids 2017;107:253–83.
[38] Nahshon K, Hutchinson JW. Modification of the Gurson model for shear failure. European Journal of Mechanics –A/Solids 2008;27(1):1–17.
[39] LS-OPT, 2018. LS-OPT Support Site. http://lsoptsupport.com/ [accessed: 2020-09-08].
[40] Wales DJ, Doyle JPK. Global Optimization by Basin-Hopping and the Lowest Energy Structures of Lennard-Jones Clusters containing up to 110 Atoms. The Journal of Physical Chemistry A 1997;101(28):5111–16.
[41] SciPy, The SciPy community. https://docs.scipy.org/doc/scipy/reference/optimize.html [accessed: 2020-09-08].
[42] Kraft D. A software package for sequential quadratic programming. Technical report dfvlr-fb 88-28. Cologne, Germany: German Aerospace Center – Institute for Flight Mechanics; 1998.
[43] Achani D, Lademo OG, Engler O, Hopperstad OS. Evaluation of constitutive models for textured aluminium alloys using plane-strain tension and shear tests. International Journal of Material Forming 2011;4(2):227–41.
[44] Roth CC, Mohr D. Determining the strain to fracture for simple shear for a wide range of sheet metals. International Journal of Mechanical Sciences 2018;149:224–240.
[45] Nielsen KL, Felter CL. Parameter window for assisted crack tip flipping: studied by a shear extended Gurson model. Int J Solids Struct 2019;171:135–45.

DEPARTMENT OF STRUCTURAL ENGINEERING
NORWEGIAN UNIVERSITY OF SCIENCE AND TECHNOLOGY

N–7491 TRONDHEIM, NORWAY
Telephone: +47 73 59 47 00

"Reliability Analysis of Structural Systems using Nonlinear Finite Element Methods",
C. A. Holm, 1990:23, ISBN 82-7119-178-0.

"Uniform Stratified Flow Interaction with a Submerged Horizontal Cylinder",
Ø. Arntsen, 1990:32, ISBN 82-7119-188-8.

"Large Displacement Analysis of Flexible and Rigid Systems Considering Displacement-Dependent Loads and Nonlinear Constraints",
K. M. Mathisen, 1990:33, ISBN 82-7119-189-6.

"Solid Mechanics and Material Models including Large Deformations",
E. Levold, 1990:56, ISBN 82-7119-214-0, ISSN 0802-3271.

"Inelastic Deformation Capacity of Flexurally-Loaded Aluminium Alloy Structures",
T. Welo, 1990:62, ISBN 82-7119-220-5, ISSN 0802-3271.

"Visualization of Results from Mechanical Engineering Analysis",
K. Aamnes, 1990:63, ISBN 82-7119-221-3, ISSN 0802-3271.

"Object-Oriented Product Modeling for Structural Design",
S. I. Dale, 1991:6, ISBN 82-7119-258-2, ISSN 0802-3271.

"Parallel Techniques for Solving Finite Element Problems on Transputer Networks",
T. H. Hansen, 1991:19, ISBN 82-7119-273-6, ISSN 0802-3271.

"Statistical Description and Estimation of Ocean Drift Ice Environments",
R. Korsnes, 1991:24, ISBN 82-7119-278-7, ISSN 0802-3271.

“Properties of concrete related to fatigue damage: with emphasis on high strength concrete”,
G. Petkovic, 1991:35, ISBN 82-7119-290-6, ISSN 0802-3271.

"Turbidity Current Modelling",
B. Brørs, 1991:38, ISBN 82-7119-293-0, ISSN 0802-3271.

"Zero-Slump Concrete: Rheology, Degree of Compaction and Strength. Effects of Fillers as Part Cement-Replacement",
C. Sørensen, 1992:8, ISBN 82-7119-357-0, ISSN 0802-3271.

"Nonlinear Analysis of Reinforced Concrete Structures Exposed to Transient Loading",
K. V. Høiseth, 1992:15, ISBN 82-7119-364-3, ISSN 0802-3271.

"Finite Element Formulations and Solution Algorithms for Buckling and Collapse Analysis of Thin Shells",
R. O. Bjærum, 1992:30, ISBN 82-7119-380-5, ISSN 0802-3271.

"Response Statistics of Nonlinear Dynamic Systems",
J. M. Johnsen, 1992:42, ISBN 82-7119-393-7, ISSN 0802-3271.

"Digital Models in Engineering. A Study on why and how engineers build and operate digital models for decisison support",
J. Høyte, 1992:75, ISBN 82-7119-429-1, ISSN 0802-3271.

"Sparse Solution of Finite Element Equations",
A. C. Damhaug, 1992:76, ISBN 82-7119-430-5, ISSN 0802-3271.

"Some Aspects of Floating Ice Related to Sea Surface Operations in the Barents Sea",
S. Løset, 1992:95, ISBN 82-7119-452-6, ISSN 0802-3271.

"Modelling of Cyclic Plasticity with Application to Steel and Aluminium Structures",
O. S. Hopperstad, 1993:7, ISBN 82-7119-461-5, ISSN 0802-3271.

"The Free Formulation: Linear Theory and Extensions with Applications to Tetrahedral Elements
with Rotational Freedoms",
G. Skeie, 1993:17, ISBN 82-7119-472-0, ISSN 0802-3271.

"Høyfast betongs motstand mot piggdekkslitasje. Analyse av resultater fra prøving i Veisliter'n",
T. Tveter, 1993:62, ISBN 82-7119-522-0, ISSN 0802-3271.

"A Nonlinear Finite Element Based on Free Formulation Theory for Analysis of Sandwich Structures",
O. Aamlid, 1993:72, ISBN 82-7119-534-4, ISSN 0802-3271.

"The Effect of Curing Temperature and Silica Fume on Chloride Migration and Pore Structure of High Strength Concrete",
C. J. Hauck, 1993:90, ISBN 82-7119-553-0, ISSN 0802-3271.

"Failure of Concrete under Compressive Strain Gradients",
G. Markeset, 1993:110, ISBN 82-7119-575-1, ISSN 0802-3271.

"An experimental study of internal tidal amphidromes in Vestfjorden",
J. H. Nilsen, 1994:39, ISBN 82-7119-640-5, ISSN 0802-3271.

"Structural analysis of oil wells with emphasis on conductor design",
H. Larsen, 1994:46, ISBN 82-7119-648-0, ISSN 0802-3271.

"Adaptive methods for non-linear finite element analysis of shell structures",
K. M. Okstad, 1994:66, ISBN 82-7119-670-7, ISSN 0802-3271.

"On constitutive modelling in nonlinear analysis of concrete structures",
O. Fyrileiv, 1994:115, ISBN 82-7119-725-8, ISSN 0802-3271.

"Fluctuating wind load and response of a line-like engineering structure with emphasis on motion-induced wind forces",
J. Bogunovic Jakobsen, 1995:62, ISBN 82-7119-809-2, ISSN 0802-3271.

"An experimental study of beam-columns subjected to combined torsion, bending and axial actions",
A. Aalberg, 1995:66, ISBN 82-7119-813-0, ISSN 0802-3271.

"Scaling and cracking in unsealed freeze/thaw testing of Portland cement and silica fume concretes",
S. Jacobsen, 1995:101, ISBN 82-7119-851-3, ISSN 0802-3271.

"Damping of water waves by submerged vegetation. A case study of laminaria hyperborea",
A. M. Dubi, 1995:108, ISBN 82-7119-859-9, ISSN 0802-3271.

"The dynamics of a slope current in the Barents Sea",
Sheng Li, 1995:109, ISBN 82-7119-860-2, ISSN 0802-3271.

"Modellering av delmaterialenes betydning for betongens konsistens",
Ernst Mørtsell, 1996:12, ISBN 82-7119-894-7, ISSN 0802-3271.

"Bending of thin-walled aluminium extrusions",
Birgit Søvik Opheim, 1996:60, ISBN 82-7119-947-1, ISSN 0802-3271.

"Material modelling of aluminium for crashworthiness analysis",
Torodd Berstad, 1996:89, ISBN 82-7119-980-3, ISSN 0802-3271.

"Estimation of structural parameters from response measurements on submerged floating tunnels",
Rolf Magne Larssen, 1996:119, ISBN 82-471-0014-2, ISSN 0802-3271.

“Numerical modelling of plain and reinforced concrete by damage mechanics”,
Mario A. Polanco-Loria, 1997:20, ISBN 82-471-0049-5, ISSN 0802-3271.

“Nonlinear random vibrations - numerical analysis by path integration methods”,
Vibeke Moe, 1997:26, ISBN 82-471-0056-8, ISSN 0802-3271.

"Numerical prediction of vortex-induced vibration by the finite element method",
Joar Martin Dalheim, 1997:63, ISBN 82-471-0096-7, ISSN 0802-3271.

"Time domain calculations of buffeting response for wind sensitive structures",
Ketil Aas-Jakobsen, 1997:148, ISBN 82-471-0189-0, ISSN 0802-3271.

"A numerical study of flow about fixed and flexibly mounted circular cylinders",
Trond Stokka Meling, 1998:48, ISBN 82-471-0244-7, ISSN 0802-3271.

"Estimation of chloride penetration into concrete bridges in coastal areas",
Per Egil Steen, 1998:89, ISBN 82-471-0290-0, ISSN 0802-3271.

"Stress-resultant material models for reinforced concrete plates and shells",
Jan Arve Øverli, 1998:95, ISBN 82-471-0297-8, ISSN 0802-3271.

"Chloride binding in concrete. Effect of surrounding environment and concrete composition",
Claus Kenneth Larsen, 1998:101, ISBN 82-471-0337-0, ISSN 0802-3271.

"Rotational capacity of aluminium alloy beams",
Lars A. Moen, 1999:1, ISBN 82-471-0365-6, ISSN 0802-3271.

"Stretch Bending of Aluminium Extrusions",
Arild H. Clausen, 1999:29, ISBN 82-471-0396-6, ISSN 0802-3271.

"Aluminium and Steel Beams under Concentrated Loading",
Tore Tryland, 1999:30, ISBN 82-471-0397-4, ISSN 0802-3271.

"Engineering Models of Elastoplasticity and Fracture for Aluminium Alloys",
Odd-Geir Lademo, 1999:39, ISBN 82-471-0406-7, ISSN 0802-3271.

"Kapasitet og duktilitet av dybelforbindelser i trekonstruksjoner",
Jan Siem, 1999:46, ISBN 82-471-0414-8, ISSN 0802-3271.

"Etablering av distribuert ingeniørarbeid; Teknologiske og organisatoriske erfaringer fra en norsk ingeniørbedrift",
Lars Line, 1999:52, ISBN 82-471-0420-2, ISSN 0802-3271.

"Estimation of Earthquake-Induced Response",
Símon Ólafsson, 1999:73, ISBN 82-471-0443-1, ISSN 0802-3271.

"Coastal Concrete Bridges: Moisture State, Chloride Permeability and Aging Effects"
Ragnhild Holen Relling, 1999:74, ISBN 82-471-0445-8, ISSN 0802-3271.

"Capacity Assessment of Titanium Pipes Subjected to Bending and External Pressure",
Arve Bjørset, 1999:100, ISBN 82-471-0473-3, ISSN 0802-3271.

“Validation of Numerical Collapse Behaviour of Thin-Walled Corrugated Panels”,
Håvar Ilstad, 1999:101, ISBN 82-471-0474-1, ISSN 0802-3271.

“Strength and Ductility of Welded Structures in Aluminium Alloys”,
Miroslaw Matusiak, 1999:113, ISBN 82-471-0487-3, ISSN 0802-3271.

“Thermal Dilation and Autogenous Deformation as Driving Forces to Self-Induced Stresses in High Performance Concrete”,
Øyvind Bjøntegaard, 1999:121, ISBN 82-7984-002-8, ISSN 0802-3271.

“Some Aspects of Ski Base Sliding Friction and Ski Base Structure”,
Dag Anders Moldestad, 1999:137, ISBN 82-7984-019-2, ISSN 0802-3271.

"Electrode reactions and corrosion resistance for steel in mortar and concrete",
Roy Antonsen, 2000:10, ISBN 82-7984-030-3, ISSN 0802-3271.

"Hydro-Physical Conditions in Kelp Forests and the Effect on Wave Damping and Dune Erosion. A case study on Laminaria Hyperborea",
Stig Magnar Løvås, 2000:28, ISBN 82-7984-050-8, ISSN 0802-3271.

"Random Vibration and the Path Integral Method",
Christian Skaug, 2000:39, ISBN 82-7984-061-3, ISSN 0802-3271.

"Buckling and geometrical nonlinear beam-type analyses of timber structures",
Trond Even Eggen, 2000:56, ISBN 82-7984-081-8, ISSN 0802-3271.

”Structural Crashworthiness of Aluminium Foam-Based Components”,
Arve Grønsund Hanssen, 2000:76, ISBN 82-7984-102-4, ISSN 0809-103X.

“Measurements and simulations of the consolidation in first-year sea ice ridges, and some aspects of mechanical behaviour”,
Knut V. Høyland, 2000:94, ISBN 82-7984-121-0, ISSN 0809-103X.

”Kinematics in Regular and Irregular Waves based on a Lagrangian Formulation”,
Svein Helge Gjøsund, 2000-86, ISBN 82-7984-112-1, ISSN 0809-103X.

”Self-Induced Cracking Problems in Hardening Concrete Structures”,
Daniela Bosnjak, 2000-121, ISBN 82-7984-151-2, ISSN 0809-103X.

"Ballistic Penetration and Perforation of Steel Plates",
Tore Børvik, 2000:124, ISBN 82-7984-154-7, ISSN 0809-103X.

"Freeze-Thaw resistance of Concrete. Effect of: Curing Conditions, Moisture Exchange and Materials",
Terje Finnerup Rønning, 2001:14, ISBN 82-7984-165-2, ISSN 0809-103X

"Structural behaviour of post tensioned concrete structures. Flat slab. Slabs on ground",
Steinar Trygstad, 2001:52, ISBN 82-471-5314-9, ISSN 0809-103X.

"Slipforming of Vertical Concrete Structures. Friction between concrete and slipform panel",
Kjell Tore Fosså, 2001:61, ISBN 82-471-5325-4, ISSN 0809-103X.

"Some numerical methods for the simulation of laminar and turbulent incompressible flows",
Jens Holmen, 2002:6, ISBN 82-471-5396-3, ISSN 0809-103X.

“Improved Fatigue Performance of Threaded Drillstring Connections by Cold Rolling”,
Steinar Kristoffersen, 2002:11, ISBN: 82-421-5402-1, ISSN 0809-103X.

"Deformations in Concrete Cantilever Bridges: Observations and Theoretical Modelling",
Peter F. Takâcs, 2002:23, ISBN 82-471-5415-3, ISSN 0809-103X.

"Stiffened aluminium plates subjected to impact loading",
Hilde Giæver Hildrum, 2002:69, ISBN 82-471-5467-6, ISSN 0809-103X.

"Full- and model scale study of wind effects on a medium-rise building in a built up area",
Jónas Thór Snæbjørnsson, 2002:95, ISBN82-471-5495-1, ISSN 0809-103X.

“Evaluation of Concepts for Loading of Hydrocarbons in Ice-infested water”,
Arnor Jensen, 2002:114, ISBN 82-417-5506-0, ISSN 0809-103X.

”Numerical and Physical Modelling of Oil Spreading in Broken Ice”,
Janne K. Økland Gjøsteen, 2002:130, ISBN 82-471-5523-0, ISSN 0809-103X.

”Diagnosis and protection of corroding steel in concrete”,
Franz Pruckner, 20002:140, ISBN 82-471-5555-4, ISSN 0809-103X.

“Tensile and Compressive Creep of Young Concrete: Testing and Modelling”,
Dawood Atrushi, 2003:17, ISBN 82-471-5565-6, ISSN 0809-103X.

“Rheology of Particle Suspensions. Fresh Concrete, Mortar and Cement Paste with Various Types of Lignosulfonates”,
Jon Elvar Wallevik, 2003:18, ISBN 82-471-5566-4, ISSN 0809-103X.

“Oblique Loading of Aluminium Crash Components”,
Aase Reyes, 2003:15, ISBN 82-471-5562-1, ISSN 0809-103X.

“Utilization of Ethiopian Natural Pozzolans”,
Surafel Ketema Desta, 2003:26, ISSN 82-471-5574-5, ISSN:0809-103X.

“Behaviour and strength prediction of reinforced concrete structures with discontinuity regions”, Helge Brå, 2004:11, ISBN 82-471-6222-9, ISSN 1503-8181.

“High-strength steel plates subjected to projectile impact. An experimental and numerical study”, Sumita Dey, 2004:38, ISBN 82-471-6282-2 (printed version), ISBN 82-471-6281-4 (electronic version), ISSN 1503-8181.

“Alkali-reactive and inert fillers in concrete. Rheology of fresh mixtures and expansive reactions.”
Bård M. Pedersen, 2004:92, ISBN 82-471-6401-9 (printed version), ISBN 82-471-6400-0 (electronic version), ISSN 1503-8181.

“On the Shear Capacity of Steel Girders with Large Web Openings”.
Nils Christian Hagen, 2005:9 ISBN 82-471-6878-2 (printed version), ISBN 82-471-6877-4 (electronic version), ISSN 1503-8181.

”Behaviour of aluminium extrusions subjected to axial loading”.
Østen Jensen, 2005:7, ISBN 82-471-6873-1 (printed version), ISBN 82-471-6872-3 (electronic version), ISSN 1503-8181.

”Thermal Aspects of corrosion of Steel in Concrete”.
Jan-Magnus Østvik, 2005:5, ISBN 82-471-6869-3 (printed version), ISBN 82-471-6868 (electronic version), ISSN 1503-8181.

”Mechanical and adaptive behaviour of bone in relation to hip replacement.” A study of bone remodelling and bone grafting.
Sébastien Muller, 2005:34, ISBN 82-471-6933-9 (printed version), ISBN 82-471-6932-0 (electronic version), ISSN 1503-8181.

“Analysis of geometrical nonlinearities with applications to timber structures”.
Lars Wollebæk, 2005:74, ISBN 82-471-7050-5 (printed version), ISBN 82-471-7019-1 (electronic version), ISSN 1503-8181.

“Pedestrian induced lateral vibrations of slender footbridges”,
Anders Rönnquist, 2005:102, ISBN 82-471-7082-5 (printed version), ISBN 82-471-7081-7 (electronic version), ISSN 1503-8181.

“Initial Strength Development of Fly Ash and Limestone Blended Cements at Various Temperatures Predicted by Ultrasonic Pulse Velocity”,
Tom Ivar Fredvik, 2005:112, ISBN 82-471-7105-8 (printed version), ISBN 82-471-7103-1 (electronic version), ISSN 1503-8181.

“Behaviour and modelling of thin-walled cast components”,
Cato Dørum, 2005:128, ISBN 82-471-7140-6 (printed version), ISBN 82-471-7139-2 (electronic version), ISSN 1503-8181.

“Behaviour and modelling of selfpiercing riveted connections”,
Raffaele Porcaro, 2005:165, ISBN 82-471-7219-4 (printed version), ISBN 82-471-7218-6 (electronic version), ISSN 1503-8181.

”Behaviour and Modelling og Aluminium Plates subjected to Compressive Load”,
Lars Rønning, 2005:154, ISBN 82-471-7169-1 (printed version), ISBN 82-471-7195-3 (electronic version), ISSN 1503-8181.

”Bumper beam-longitudinal system subjected to offset impact loading”,
Satyanarayana Kokkula, 2005:193, ISBN 82-471-7280-1 (printed version), ISBN 82-471-7279-8 (electronic version), ISSN 1503-8181.

“Control of Chloride Penetration into Concrete Structures at Early Age”,
Guofei Liu, 2006:46, ISBN 82-471-7838-9 (printed version), ISBN 82-471-7837-0 (electronic version), ISSN 1503-8181.

“Modelling of Welded Thin-Walled Aluminium Structures”,
Ting Wang, 2006:78, ISBN 82-471-7907-5 (printed version), ISBN 82-471-7906-7 (electronic version), ISSN 1503-8181.

”Time-variant reliability of dynamic systems by importance sampling and probabilistic analysis of ice loads”,
Anna Ivanova Olsen, 2006:139, ISBN 82-471-8041-3 (printed version), ISBN 82-471-8040-5 (electronic version), ISSN 1503-8181.

“Fatigue life prediction of an aluminium alloy automotive component using finite element analysis of surface topography”.
Sigmund Kyrre Ås, 2006:25, ISBN 82-471-7791-9 (printed version), ISBN 82-471-7791-9 (electronic version), ISSN 1503-8181.

”Constitutive models of elastoplasticity and fracture for aluminium alloys under strain path change”,
Dasharatha Achani, 2006:76, ISBN 82-471-7903-2 (printed version), ISBN 82-471-7902-4 (electronic version), ISSN 1503-8181.

“Simulations of 2D dynamic brittle fracture by the Element-free Galerkin method and linear fracture mechanics”,
Tommy Karlsson, 2006:125, ISBN 82-471-8011-1 (printed version), ISBN 82-471-8010-3 (electronic version), ISSN 1503-8181.

“Penetration and Perforation of Granite Targets by Hard Projectiles”,
Chong Chiang Seah, 2006:188, ISBN 82-471-8150-9 (printed version), ISBN 82-471-8149-5 (electronic version), ISSN 1503-8181.

"Deformations, strain capacity and cracking of concrete in plastic and early hardening phases",
Tor Arne Hammer, 2007:234, ISBN 978-82-471-5191-4 (printed version), ISBN 978-82-471-5207-2 (electronic version), ISSN 1503-8181.

"Crashworthiness of dual-phase high-strength steel: Material and Component behaviour", Venkatapathi Tarigopula, 2007:230, ISBN 82-471-5076-4 (printed version), ISBN 82-471-5093-1 (electronic version), ISSN 1503-8181.

"Fibre reinforcement in load carrying concrete structures",
Åse Lyslo Døssland, 2008:50, ISBN 978-82-471-6910-0 (printed version), ISBN 978-82-471-6924-7 (electronic version), ISSN 1503-8181.

"Low-velocity penetration of aluminium plates",
Frode Grytten, 2008:46, ISBN 978-82-471-6826-4 (printed version), ISBN 978-82-471-6843-1 (electronic version), ISSN 1503-8181.

"Robustness studies of structures subjected to large deformations",
Ørjan Fyllingen, 2008:24, ISBN 978-82-471-6339-9 (printed version), ISBN 978-82-471-6342-9 (electronic version), ISSN 1503-8181.

"Constitutive modelling of morsellised bone",
Knut Birger Lunde, 2008:92, ISBN 978-82-471-7829-4 (printed version), ISBN 978-82-471-7832-4 (electronic version), ISSN 1503-8181.

"Experimental Investigations of Wind Loading on a Suspension Bridge Girder",
Bjørn Isaksen, 2008:131, ISBN 978-82-471-8656-5 (printed version), ISBN 978-82-471-8673-2 (electronic version), ISSN 1503-8181.

"Cracking Risk of Concrete Structures in The Hardening Phase",
Guomin Ji, 2008:198, ISBN 978-82-471-1079-9 (printed version), ISBN 978-82-471-1080-5 (electronic version), ISSN 1503-8181.

"Modelling and numerical analysis of the porcine and human mitral apparatus",
Victorien Emile Prot, 2008:249, ISBN 978-82-471-1192-5 (printed version), ISBN 978-82-471-1193-2 (electronic version), ISSN 1503-8181.

"Strength analysis of net structures",
Heidi Moe, 2009:48, ISBN 978-82-471-1468-1 (printed version), ISBN 978-82-471-1469-8 (electronic version), ISSN1503-8181.

"Numerical analysis of ductile fracture in surface cracked shells",
Espen Berg, 2009:80, ISBN 978-82-471-1537-4 (printed version), ISBN 978-82-471-1538-1 (electronic version), ISSN 1503-8181.

"Subject specific finite element analysis of bone – for evaluation of the healing of a leg lengthening and evaluation of femoral stem design",
Sune Hansborg Pettersen, 2009:99, ISBN 978-82-471-1579-4 (printed version), ISBN 978-82-471-1580-0 (electronic version), ISSN 1503-8181.

"Evaluation of fracture parameters for notched multi-layered structures",
Lingyun Shang, 2009:137, ISBN 978-82-471-1662-3 (printed version), ISBN 978-82-471-1663-0 (electronic version), ISSN 1503-8181.

"Modelling of Dynamic Material Behaviour and Fracture of Aluminium Alloys for Structural Applications"
Yan Chen, 2009:69, ISBN 978-82-471-1515-2 (printed version), ISBN 978-82 471-1516-9 (electronic version), ISSN 1503-8181.

"Nanomechanics of polymer and composite particles"
Jianying He 2009:213, ISBN 978-82-471-1828-3 (printed version), ISBN 978-82-471-1829-0 (electronic version), ISSN 1503-8181.

"Mechanical properties of clear wood from Norway spruce"
Kristian Berbom Dahl 2009:250, ISBN 978-82-471-1911-2 (printed version) ISBN 978-82-471-1912-9 (electronic version), ISSN 1503-8181.

"Modeling of the degradation of TiB_2 mechanical properties by residual stresses and liquid Al penetration along grain boundaries"
Micol Pezzotta 2009:254, ISBN 978-82-471-1923-5 (printed version) ISBN 978-82-471-1924-2 (electronic version) ISSN 1503-8181.

"Effect of welding residual stress on fracture"
Xiabo Ren 2010:77, ISBN 978-82-471-2115-3 (printed version) ISBN 978-82-471-2116-0 (electronic version), ISSN 1503-8181.

"Pan-based carbon fiber as anode material in cathodic protection system for concrete structures"
Mahdi Chini 2010:122, ISBN 978-82-471-2210-5 (printed version) ISBN 978-82-471-2213-6 (electronic version), ISSN 1503-8181.

"Structural Behaviour of deteriorated and retrofitted concrete structures"
Irina Vasililjeva Sæther 2010:171, ISBN 978-82-471-2315-7 (printed version) ISBN 978-82-471-2316-4 (electronic version) ISSN 1503-8181.

"Prediction of local snow loads on roofs"
Vivian Meløysund 2010:247, ISBN 978-82-471-2490-1 (printed version) ISBN 978-82-471-2491-8 (electronic version) ISSN 1503-8181.

"Behaviour and modelling of polymers for crash applications"
Virgile Delhaye 2010:251, ISBN 978-82-471-2501-4 (printed version) ISBN 978-82-471-2502-1 (electronic version) ISSN 1503-8181.

"Blended cement with reducted CO_2 emission – Utilizing the Fly Ash-Limestone Synergy",
Klaartje De Weerdt 2011:32, ISBN 978-82-471-2584-7 (printed version) ISBN 978-82-471-2584-4 (electronic version) ISSN 1503-8181.

"Chloride induced reinforcement corrosion in concrete" Concept of critical chloride content – methods and mechanisms.
Ueli Angst 2011:113, ISBN 978-82-471-2769-9 (printed version) ISBN 978-82-471-2763-6 (electronic version) ISSN 1503-8181.

"A thermo-electric-Mechanical study of the carbon anode and contact interface for Energy savings in the production of aluminium".
Dag Herman Andersen 2011:157, ISBN 978-82-471-2859-6 (printed version) ISBN 978-82-471-2860-2 (electronic version) ISSN 1503-8181.

"Structural Capacity of Anchorage Ties in Masonry Veneer Walls Subjected to Earthquake". The implications of Eurocode 8 and Eurocode 6 on a typical Norwegain veneer wall.
Ahmed Mohamed Yousry Hamed 2011:181, ISBN 978-82-471-2911-1 (printed version) ISBN 978-82-471-2912-8 (electronic ver.) ISSN 1503-8181.

"Work-hardening behaviour in age-hardenable Al-Zn-Mg(-Cu) alloys".
Ida Westermann , 2011:247, ISBN 978-82-471-3056-8 (printed ver.) ISBN 978-82-471-3057-5 (electronic ver.) ISSN 1503-8181.

"Behaviour and modelling of selfpiercing riveted connections using aluminium rivets".
Nguyen-Hieu Hoang, 2011:266, ISBN 978-82-471-3097-1 (printed ver.) ISBN 978-82-471-3099-5 (electronic ver.) ISSN 1503-8181.

"Fibre reinforced concrete".
Sindre Sandbakk, 2011:297, ISBN 978-82-471-3167-1 (printed ver.) ISBN 978-82-471-3168-8 (electronic ver) ISSN 1503:8181.

"Dynamic behaviour of cablesupported bridges subjected to strong natural wind".
Ole Andre Øiseth, 2011:315, ISBN 978-82-471-3209-8 (printed ver.) ISBN 978-82-471-3210-4 (electronic ver.) ISSN 1503-8181.

"Constitutive modeling of solargrade silicon materials"
Julien Cochard, 2011:307, ISBN 978-82-471-3189-3 (printed ver). ISBN 978-82-471-3190-9 (electronic ver.) ISSN 1503-8181.

"Constitutive behavior and fracture of shape memory alloys"
Jim Stian Olsen, 2012:57, ISBN 978-82-471-3382-8 (printed ver.) ISBN 978-82-471-3383-5 (electronic ver.) ISSN 1503-8181.

“Field measurements in mechanical testing using close-range photogrammetry and digital image analysis”
Egil Fagerholt, 2012:95, ISBN 978-82-471-3466-5 (printed ver.) ISBN 978-82-471-3467-2 (electronic ver.) ISSN 1503-8181.

“Towards a better under standing of the ultimate behaviour of lightweight aggregate concrete in compression and bending”,
Håvard Nedrelid, 2012:123, ISBN 978-82-471-3527-3 (printed ver.) ISBN 978-82-471-3528-0 (electronic ver.) ISSN 1503-8181.

“Numerical simulations of blood flow in the left side of the heart”
Sigrid Kaarstad Dahl, 2012:135, ISBN 978-82-471-3553-2 (printed ver.) ISBN 978-82-471-3555-6 (electronic ver.) ISSN 1503-8181.

“Moisture induced stresses in glulam”
Vanessa Angst-Nicollier, 2012:139, ISBN 978-82-471-3562-4 (printed ver.) ISBN 978-82-471-3563-1 (electronic ver.) ISSN 1503-8181.

“Biomechanical aspects of distraction osteogensis”
Valentina La Russa, 2012:250, ISBN 978-82-471-3807-6 (printed ver.) ISBN 978-82-471-3808-3 (electronic ver.) ISSN 1503-8181.

“Ductile fracture in dual-phase steel. Theoretical, experimental and numerical study”
Gaute Gruben, 2012:257, ISBN 978-82-471-3822-9 (printed ver.) ISBN 978-82-471-3823-6 (electronic ver.) ISSN 1503-8181.

“Damping in Timber Structures”
Nathalie Labonnote, 2012:263, ISBN 978-82-471-3836-6 (printed ver.) ISBN 978-82-471-3837-3 (electronic ver.) ISSN 1503-8181.

“Biomechanical modeling of fetal veins: The umbilical vein and ductus venosus bifurcation”
Paul Roger Leinan, 2012:299, ISBN 978-82-471-3915-8 (printed ver.) ISBN 978-82-471-3916-5 (electronic ver.) ISSN 1503-8181.

“Large-Deformation behaviour of thermoplastics at various stress states”
Anne Serine Ognedal, 2012:298, ISBN 978-82-471-3913-4 (printed ver.) ISBN 978-82-471-3914-1 (electronic ver.) ISSN 1503-8181.

“Hardening accelerator for fly ash blended cement”
Kien Dinh Hoang, 2012:366, ISBN 978-82-471-4063-5 (printed ver.) ISBN 978-82-471-4064-2 (electronic ver.) ISSN 1503-8181.

“From molecular structure to mechanical properties”
Jianyang Wu, 2013:186, ISBN 978-82-471-4485-5 (printed ver.) ISBN 978-82-471-4486-2 (electronic ver.) ISSN 1503-8181.

“Experimental and numerical study of hybrid concrete structures”
Linn Grepstad Nes, 2013:259, ISBN 978-82-471-4644-6 (printed ver.) ISBN 978-82-471-4645-3 (electronic ver.) ISSN 1503-8181.

“Mechanics of ultra-thin multi crystalline silicon wafers”
Saber Saffar, 2013:199, ISBN 978-82-471-4511-1 (printed ver.) ISBN 978-82-471-4513-5 (electronic ver). ISSN 1503-8181.

“Through process modelling of welded aluminium structures”
Anizahyati Alisibramulisi, 2013:325, ISBN 978-82-471-4788-7 (printed ver.) ISBN 978-82-471-4789-4 (electronic ver.) ISSN 1503-8181.

“Combined blast and fragment loading on steel plates”
Knut Gaarder Rakvåg, 2013:361, ISBN978-82-471-4872-3 (printed ver.) ISBN 978-82-4873-0 (electronic ver.). ISSN 1503-8181.

“Characterization and modelling of the anisotropic behaviour of high-strength aluminium alloy”
Marion Fourmeau, 2014:37, ISBN 978-82-326-0008-3 (printed ver.) ISBN 978-82-326-0009-0 (electronic ver.) ISSN 1503-8181.

“Behaviour of threated steel fasteners at elevated deformation rates”
Henning Fransplass, 2014:65, ISBN 978-82-326-0054-0 (printed ver.) ISBN 978-82-326-0055-7 (electronic ver.) ISSN 1503-8181.

“Sedimentation and Bleeding”
Ya Peng, 2014:89, ISBN 978-82-326-0102-8 (printed ver.) ISBN 978-82-326-0103-5 (electric ver.) ISSN 1503-8181.

“Impact against X65 offshore pipelines”
Martin Kristoffersen, 2014:362, ISBN 978-82-326-0636-8 (printed ver.) ISBN 978-82-326-0637-5 (electronic ver.) ISSN 1503-8181.

“Formability of aluminium alloy subjected to prestrain by rolling”
Dmitry Vysochinskiy, 2014:363,, ISBN 978-82-326-0638-2 (printed ver.) ISBN 978-82-326-0639-9 (electronic ver.) ISSN 1503-8181.

“Experimental and numerical study of Yielding, Work-Hardening and anisotropy in textured AA6xxx alloys using crystal plasticity models”
Mikhail Khadyko, 2015:28, ISBN 978-82-326-0724-2 (printed ver.) ISBN 978-82-326-0725-9 (electronic ver.) ISSN 1503-8181.

“Behaviour and Modelling of AA6xxx Aluminium Alloys Under a Wide Range of Temperatures and Strain Rates”
Vincent Vilamosa, 2015:63, ISBN 978-82-326-0786-0 (printed ver.) ISBN 978-82-326-0787-7 (electronic ver.) ISSN 1503-8181.

“A Probabilistic Approach in Failure Modelling of Aluminium High Pressure Die-Castings”
Octavian Knoll, 2015:137, ISBN 978-82-326-0930-7 (printed ver.) ISBN 978-82-326-0931-4 (electronic ver.) ISSN 1503-8181.

“Ice Abrasion on Marine Concrete Structures”
Egil Møen, 2015:189, ISBN 978-82-326-1034-1 (printed ver.) ISBN 978-82-326-1035-8 (electronic ver.) ISSN 1503-8181.

“Fibre Orientation in Steel-Fibre-Reinforced Concrete”
Giedrius Zirgulis, 2015:229, ISBN 978-82-326-1114-0 (printed ver.) ISBN 978-82-326-1115-7 (electronic ver.) ISSN 1503-8181.

“Effect of spatial variation and possible interference of localised corrosion on the residual capacity of a reinforced concrete beam”
Mohammad Mahdi Kioumarsi, 2015:282, ISBN 978-82-326-1220-8 (printed ver.) ISBN 978-82-1221-5 (electronic ver.) ISSN 1503-8181.

“The role of concrete resistivity in chloride-induced macro-cell corrosion”
Karla Horbostel, 2015:324, ISBN 978-82-326-1304-5 (printed ver.) ISBN 978-82-326-1305-2 (electonic ver.) ISSN 1503-8181.

“Flowable fibre-reinforced concrete for structural applications”
Elena Vidal Sarmiento, 2015-335, ISBN 978-82-326-1324-3 (printed ver.) ISBN 978-82-326-1325-0 (electronic ver.) ISSN 1503-8181.

“Development of chushed sand for concrete production with microproportioning”
Rolands Cepuritis, 2016:19, ISBN 978-82-326-1382-3 (printed ver.) ISBN 978-82-326-1383-0 (electronic ver.) ISSN 1503-8181.

“Withdrawal properties of threaded rods embedded in glued-laminated timer elements”
Haris Stamatopoulos, 2016:48, ISBN 978-82-326-1436-3 (printed ver.) ISBN 978-82-326-1437-0 (electronic ver.) ISSN 1503-8181.

“An Experimental and numerical study of thermoplastics at large deformation”
Marius Andersen, 2016:191, ISBN 978-82-326-1720-3 (printed ver.) ISBN 978-82-326-1721-0 (electronic ver.) ISSN 1503-8181.

“Modeling and Simulation of Ballistic Impact”
Jens Kristian Holmen, 2016:240, ISBN 978-82-326-1818-7 (printed ver). ISBN 978-82-326-1819-4 (electronic ver.) ISSN 1503-8181.

“Early age crack assessment of concrete structures”
Anja B. Estensen Klausen, 2016:256, ISBN 978-82-326-1850-7 (printed ver). ISBN 978-82-326-1851-4 (electronic ver.) ISSN 1503-8181.

“Uncertainty quantification and sensitivity analysis for cardiovascular models”
Vinzenz Gregor Eck, 2016:234, ISBN 978-82-326-1806-4 (printed ver.) ISBN 978-82-326-1807-1 (electronic ver.) ISSN 1503-8181.

“Dynamic behaviour of existing and new railway catenary systems under Norwegain conditions”
Petter Røe Nåvik, 2016:298, ISBN 978-82-326-1935-1 (printed ver.) ISBN 978-82-326-1934-4 (electronic ver.) ISSN 1503-8181.

“Mechanical behaviour of particle-filled elastomers at various temperatures”
Arne Ilseng, 2016-295, ISBN978-82-326-1928-3 (printed ver.) ISBN 978-82-326-1929-0 (electronic ver.) ISSN 1503-8181.

“Nanotechnology for Anti-Icing Application”
Zhiwei He, 2016:348, ISBN 978-82-326-2038-8 (printed ver.) ISBN 978-82-326-2019-5 (electronic ver.) ISSN 1503-8181.

“Conduction Mechanisms in Conductive Adhesives with Metal-Coated Polyer Spheres”
Sigurd Rolland Pettersen, 2016:349, ISBN 978-326-2040-1 (printed ver,) ISBN 978-82-326-2041-8 (electronic ver.) ISSN 1503-8181.

“The interaction between calcium lignosulfonate and cement”
Alessia Colombo, 2017:20, ISBN 978-82-326-2122-4 (printed ver.) ISBN 978-82-326-2123-1 (electronic ver.) ISSN 1503-8181.

“Behaviour and Modelling of Flexible Structures Subjected to Blast Loading”
Vegard Aune, 2017:101, ISBN 978-82-326-2274-0 (printed ver.) ISBN 978-82-326-2275-7 (electronic ver.) ISSN 1503-8181.

“Behaviour of steel connections under quasi-static and impact loading”
Erik Løhre Grimsmo, 2017:159, ISBN 978-82-326-2390-7 (printed ver.) ISBN 978-82-326-2391-4 (electronic ver.) ISSN 1503-8181.

“An experimental and numerical study of cortical bone at he macro and Nano-scale”
Masoud Ramenzanzadehkoldeh,, 2017:208, ISBN 978-82-326-2488-1 (printed ver.) ISBN 978-82-326-2489-8 (electronic ver.) ISSN 1503-8181.

“Optoelectrical Properties of a Novel Organic Semiconductor: 6,13-Dichloropentacene”
Mao Wang, 2017:130, ISBN 978-82-326-2332-7 (printed ver.) ISBN 978-82-326-2333-4) (electronic ver.) ISSN 1503-8181.

“Core-shell structured microgels and their behavior at oil and water interface”
Yi Gong, 2017:182, ISBN 978-82-326-2436-2 (printed. ver.) ISBN 978-82-326-2437-9 (electronic ver.) ISSN 1503-8181.

“Aspects of design of reinforced concrete structures using nonliear finite element analyses”
Morten Engen, 2017:149, ISBN 978-82-326-2370-9 (printed ver.) ISBN 978-82-326-2371-6 (electronic ver.) ISSN 1503-8181.

“Numerical studies on ductile failure of aluminium alloys”
Lars Edvard Dæhli, 2017:284, ISBN 978-82-326-2636-6 (printed ver.) ISBN 978-82-326-2637-3 (electronic ver.) ISSN 1503-8181.

“Modelling and Assessment of Hydrogen Embrittlement in Steels and Nickel Alloys”
Haiyang Yu, 2017:278, ISBN 978-82-326-2624-3 (printed. ver.) ISBN 978-82-326-2625-0 (electronic ver.) ISSN 1503-8181.

“Network arch timber bridges with light timber deck on transverse crossbeams”
Anna Weronika Ostrycharczyk, 2017:318, ISBN 978-82-326-2704-2 (printed ver.) ISBN 978-82-326-2705-9 (electronic ver.) ISSN 1503-8181.

“Splicing of Large Glued Laminated Timber Elements by Use of Long Threated Rods”
Martin Cepelka, 2017:320, ISBN 978-82-326-2708-0 (printed ver.) ISBN 978-82-326-2709-7 (electronic ver.) ISSN 1503-8181.

“Thermomechanical behaviour of semi-crystalline polymers: experiments, modelling and simulation”
Joakim Johnsen, 2017-317, ISBN 978-82-326-2702-8 (printed ver.) ISBN 978-82-326-2703-5 (electronic ver.) ISSN 1503-8181.

“Small-Scale Plasiticity under Hydrogen Environment”
Kai Zhao, 2017:356, ISBN 978-82-326-2782-0 (printed ver.) ISBN 978-82-326-2783-7 (electronic er.) ISSN 1503-8181.

“Risk and Reliability Based Calibration of Structural Design Codes”
Michele Baravalle, 2017:342, ISBN 978-82-326-2752-3 (printed ver,) ISBN 978-82-326-2753-0 (electronic ver.) ISSN 1503-8181.

“Dynamic behaviour of floating bridges exposed to wave excitation”
Knut Andreas Kvåle, 2017:365, ISBN 978-82-326-2800-1 (printed ver.) ISBN 978-82-326-2801-8 (electronic ver.) ISSN 1503-8181.

“Dolomite calcined clay composite cement – hydration and durability”
Alisa Lydia Machner, 2018:39, ISBN 978-82-326-2872-8 (printed ver.). ISBN 978-82-326-2873-5 (electronic ver.) ISSN 1503-8181.

“Modelling of the self-excited forces for bridge decks subjected to random motions: an experimental study”
Bartosz Siedziako, 2018:52, ISBN 978-82-326-2896-4 (printed ver.). ISBN 978-82-326-2897-1 (electronic ver.) ISSN 1503-8181.

“A probabilistic-based methodology for evaluation of timber facade constructions”
Klodian Gradeci, 2018:69, ISBN 978-82-326-2928-2 (printed ver.) ISBN 978-82-326-2929-9 (electronic ver.) ISSN 1503-8181.

“Behaviour and modelling of flow-drill screw connections”
Johan Kolstø Sønstabø, 2018:73, ISBN 978-82-326-2936-7 (printed ver.) ISBN 978-82-326-2937-4 (electronic ver.) ISSN 1503-8181.

“Full-scale investigation of the effects of wind turbulence characteristics on dynamic behavior of long-span cable-supported bridges in complex terrain”
Aksel Fenerci, 2018 100, ISBN 9978-82-326-2990-9 (printed ver.) ISBN 978-82-326-2991-6 (electronic ver.) ISSN 1503-8181.

“Modeling and simulation of the soft palate for improved understanding of the obstructive sleep apnea syndrome”
Hongliang Liu, 2018:101, ISBN 978-82-326-2992-3 (printed ver.) ISBN 978-82-326-2993-0 (electronic ver.) ISSN 1503-8181.

“Long-term extreme response analysis of cable-supported bridges with floating pylons subjected to wind and wave loads”.
Yuwang Xu, 2018:229, ISBN 978-82-326-3248-0 (printed ver.) ISBN 978-82-326-3249-7 (electronic ver.) ISSN 1503-8181.

“Reinforcement corrosion in carbonated fly ash concrete”
Andres Belda Revert, 2018:230, ISBN 978-82-326-3250-3 (printed ver.) ISBN 978-82-326-3251-0 (electronic ver.) ISSN 1503-8181.

“Direct finite element method for nonliear earthquake analysis of concrete dams including dam-water-foundation rock interaction”
Arnkjell Løkke, 2018:252, ISBN 978-82-326-3294-7 (printed ver.) ISBN 978-82-326-3295-4 (electronic ver.) ISSN 1503-8181.

“Electromechanical characterization of metal-coated polymer spheres for conductive adhesives”
Molly Strimbeck Bazilchuk, 2018:295, ISBN 978-82-326-3380-7 (printed. ver.) ISBN 978-82-326-3381-4 (electrical ver.) ISSN 1503-8181.

“Determining the tensile properties of Artic materials and modelling their effects on fracture”
Shengwen Tu, 2018:269, ISBN 978-82-326-3328-9 (printed ver.) ISBN 978-82-326-3329-6 (electronic ver.) ISSN 1503-8181.

“Atomistic Insigth into Tranportation of Nanofluid in Ultra-confined Channel”
Xiao Wang, 2018:334, ISBN978-82-326-3456-9 (printed ver.) ISBN 978-82-326-3457-6 (electronic ver.) ISSN 1503-8181.

“An experimental and numerical study of the mechanical behaviour of short glass-fibre reinforced thermoplastics”.
Jens Petter Henrik Holmstrøm, 2019:79, ISBN 978-82-326-3760-7 (printed ver.) ISBN 978-82-326-3761-4 (electronic ver.) ISSN 1503-8181.

“Uncertainty quantification and sensitivity analysis informed modeling of physical systems”
Jacob Sturdy, 2019:115, ISBN 978-82-326-3828-4 (printed ver.) ISBN 978-82-326-3829-1 (electric ver.) ISSN 1503-8181.

“Load model of historic traffic for fatigue life estimation of Norwegian railway bridges”
Gunnstein T. Frøseth, 2019:73, ISBN 978-82-326-3748-5 (printed ver.) ISBN 978-82-326-3749-2 (electronic ver.) ISSN 1503-8181.

“Force identification and response estimation in floating and suspension bridges using measured dynamic response”
Øyvind Wiig Petersen, 2019:88, ISBN 978-82-326-3778-2 (printed ver.) ISBN 978-82-326-377-9 (electronic ver.) ISSN 1503-8181.

“Consistent crack width calculation methods for reinforced concrete elements subjected to 1D and 2D stress states”
Reignard Tan, 2019:147, ISBN 978-82-326-3892-5 (printed ver.) ISBN 978-82-326-3893-2 (electronic ver.) ISSN 1503-8181.

“Nonlinear static and dynamic isogeometric analysis of slender spatial and beam type structures”
Siv Bente Raknes, 2019:181, ISBN 978-82-326-3958-8 (printed ver.) ISBN 978-82-326-3959-5 (electronic ver.) ISSN 1503-8181.

“Experimental study of concrete-ice abrasion and concrete surface topography modification”
Guzel Shamsutdinova, 2019:182, ISBN978-82-326-3960-1 (printed ver.) ISBN 978-82-326-3961-8 (electronic ver.) ISSN 1503-8181.

“Wind forces on bridge decks using state-of-the art FSI methods”
Tore Andreas Helgedagsrud, 2019:180, ISBN 978-82-326-3956-4 (printed ver.) ISBN 978-82-326-3957-1 (electronic ver.) ISSN 1503-8181.

“Numerical Study on Ductile-to-Brittle Transition of Steel and its Behavior under Residual Stresses”
Yang Li, 2019:227, ISBN 978-82-326-4050-8 (printed ver.) ISBN 978-82-326-4015-5 (electronic ver.) ISSN 1503-8181.

“Micromechanical modelling of ductile fracture in aluminium alloys”
Bjørn Håkon Frodal, 2019:253, ISBN 978-82-326-4102-4 (printed ver.) ISBN 978-82-326-4103-1 (electronic ver.) ISSN 1503-8181.

“Monolithic and laminated glass under extreme loading: Experiments, modelling and simulations”
Karoline Osnes, 2019:304, ISBN 978-82-326-4204-5 (printed ver.) ISBN 978-82-326-4205-2 (electronic ver.) ISSN 1503-8181.

“Plastic flow and fracture of isotropic and anisotropic 6000-series aluminium alloys: Experiments and numerical simulations “
Susanne Thomesen, 2019:312, ISBN 978-82-326-4220-5 (printed ver.), ISBN 978-82-326-4221-2 (electriniv ver.) ISSN 1503-8181

“Stress-laminated timber decks in bridges”
Francesco Mirko Massaro, 2019:346, ISBN 978-82-326-4288-5 (printed ver.), ISBN 978-82-326-4289-2 (electronic ver.) ISSN 1503-8181

“Connections between steel and aluminium using adhesive bonding combined with self-piercing riveting: Testing, modelling and analysis”
Matthias Reil, 2019:319, ISBN 978-82-326-4234-2 (printed ver.), ISBN 978-82-326-4235-9 (electronic ver.) ISSN 1503-8181

“Designing Polymeric Icephobic Materials”
Yizhi Zhuo, 2019:345, ISBN 978-82-326-4286-1 (printed ver.), ISBN 978-82-326-4287-8 (electronic ver.) ISSN 1503-8181

“Fundamental Mechanisms of Ice Adhesion”
Rønneberg, Sigrid 2020:87, ISBN 978-82-326-4527-8 (printed version) ISBN 978-82- 326-4524-5 (electronic version) ISSN 1503-8181

“Mechanical modeling of the polymeric coating on a subsea pipeline” Vestrum, Ole 2020:105, ISBN 978-82-326-4562-6 (printed version) ISBN 978-82- 4563-3 (electronic version ISSN 1503-8181

“Conceptual form-finding in structural engineering” Marcin Luczkowski 2020: “Self-assembled superstructures of magnetic nanoparticles: advanced nanofabrication and enhanced mechanical properties”

Verner Håkonsen 2020:271, ISBN 978-82-326-4890-0 (printed version) ISBN 978-82- 326-4891-7 (electronic version) ISSN 1503-8181

“Micromechanical modelling of fracture in ductile alloys with applications to high-strength steel”
Sondre Bergo 2020:313, ISBN 978-82-326-4974-7 (printed version) ISBN 978-82-326-4975-4 (electronic version) ISSN 1503-8181

“Fracture in wood of Norway spruce - Experimental and numerical study” Katarzyna Ostapska 2020:314, ISBN 978-82-326-4976-1 (printed version) ISBN 978- 82-326-4977-8 (electronic version) ISSN 1503-8181

“Dynamic anti-icing surfaces (DAIS)” Feng Wang 2020:330 ISBN 978-82-326-5006-4 (printed version) ISBN 978-82-326-5007-1 (electronic version) ISSN 1503-8181

“«Multiaxial Fatigue analysis of offshore mooring chains, considering the effects of residual stresses and corrosion pits» Ershad P. Zarandi 2020:337 ISBN 978-82-326-5020-0 (printed version) ISBN 978-82-326-5021-7 (electronic version) ISSN 1503-8181

“Production and documentation of frost durable high-volume fly ash concrete: air entrainment, cracking and scaling in performance testing” Andrei Shpak 2020:366 ISBN 978-82-326-5078-1 (printed version) ISBN 978-82-326-5079-8 (electronic version) ISSN 1503-8181

ISBN 978-82-326-5094-1 (printed ver.)
ISBN 978-82-326-5095-8 (electronic ver.)
ISSN 2703-8084 (online)
ISSN 1503-8181 (trykt utg.)

NTNU

Norwegian University of
Science and Technology